Stellar Activity and Radial Velocities in M Dwarfs

Dissertation
zur Erlangung des mathematisch-naturwissenschaftlichen Doktorgrades
“Doctor rerum naturalium”
der Georg-August-Universität Göttingen

im Promotionsprogramm PROPHYS
der Georg-August University School of Science (GAUSS)

vorgelegt von
Erik N. Johnson
aus Walnut Creek, California, USA

Göttingen, 2023

Betreuungsausschuss

Prof. Dr. Ansgar Reiners, Institut für Astrophysik, Georg-August-Universität Göttingen

Prof. Dr. Stefan Dreizler, Institut für Astrophysik, Georg-August-Universität Göttingen

Prof. Dr. Hardi Peter, Abteilung Sonne und Heliosphäre, Max-Planck-Institut für Sonnensystemforschung

Mitglieder der Prüfungskommission

Referent: Prof. Dr. Stefan Dreizler
Institut für Astrophysik, Georg-August-Universität Göttingen

Korreferent: Prof. Dr. Hardi Peter
Abteilung Sonne und Heliosphäre, Max-Planck-Institut für Sonnensystemforschung

2. Korreferent: Prof. Dr. Artie Hatzes
Thüringer Landessternwarte Tautenburg, Friedrich-Schiller-Universität Jena

Weitere Mitglieder der Prüfungskommission:

Prof. Dr. Wolfram Kollatschny
Institut für Astrophysik, Georg-August-Universität Göttingen

Prof. Dr. Andreas Tilgner
Institut für Astrophysik, Georg-August-Universität Göttingen

Prof. Dr. Natalie Krivova
Abteilung Sonne und Heliosphäre, Max-Planck-Institut für Sonnensystemforschung

Tag der mündlichen Prüfung: 28. Juni 2024

We do these things not because they are easy, but because they are hard.

–John F. Kennedy

Audentes Fortuna iuvat.

Fortune favors the bold.

–Latin proverb

Abstract

Stellar activity is one of the principal obstacles to achieving sub 1 $\mathrm{m\,s^{-1}}$ radial velocity precision in exoplanet detection surveys. Understanding how stellar activity affects the stellar environment is crucial to mitigating or eliminating unexpected radial velocity excursions that mask planetary signals. We look at the two extreme ends of stellar activity in M dwarfs.

First, we characterize over 14,000 spectra from 345 M dwarfs of the CARMENES[1] Guaranteed Time Observations (GTO) sample and quantify a quiet sample within that set of stars. We were able to reduce the interfering effects of molecular line continuum contamination on measurement methods by normalizing the effect out. In so doing we developed a new measurement method, the Molecular Normalized Index (MNI). This allowed us to detail the behavior of Ca II IRT (InfraRed Triplet), Hα, Na I $D_{1\&2}$, and He I D_3 from the quietest stars to the point where emission in these profiles becomes dominant. We found that Hα profiles can be well explained by the combination of an emission and absorption profile. From this we also noticed a significant gap separating out the low activity stars, with Hα profiles in absorption or with low wing emission, from emission profile stars. This gap may be related to the rapid spin down hypothesis. We observed that, for the quietest stars, the Hα absorption strongly correlates with stellar effective temperature. Given the prevailing thought that Hα in M dwarfs should respond to stellar activity induced chromospheric heating by first becoming more absorptive before filling in and going into emission, this strong correlation with effective temperature for the maximally absorptive stars should not occur. We also find no evidence for this initial increase in Hα absorption. We therefore present a modified model in which the Hα absorption that correlates with the effective temperature is due to a basal amount of chromospheric heating that is unlikely to be related to the heating by stellar activity that causes Hα emission. The result of this is that as a quiet star gains active chromospheric regions the wider Hα emission profile of these regions will combine with the Hα absorption from what remains of the quiet chromosphere.

Second, we examine the extreme other end of stellar activity in M dwarfs by examining the extremely active, young, rapidly rotating star, GJ 3270. We simultaneously observed this star for a total of 7.7 h with photometric and spectroscopic instruments. We combined our data with TESS observations conducted roughly one month prior to our observation period. We found two large flares during our observation period, one of which released

[1]Calar Alto high-Resolution search for M dwarfs with Exoearths with Near-infrared and optical Échelle Spectrographs.

3.6×10^{32} erg of energy and had a post-flare co-rotating feature. We tracked this feature for 90 minutes through the asymmetries it caused in the chromospheric activity indicators. We concluded that this feature was likely similar to post-flare arcadal loops on the Sun. To sum up our results we found that the chromosphere of M dwarfs is likely heated by a mechanism that is not related to stellar activity and on active M dwarfs that individual active regions can be tracked as they rotate across the stellar disk.

Contents

1. Introduction **1**

1.1. Measuring Light . . . 1

1.1.1. Spectroscopy . . . 1

1.1.2. Spectrographs . . . 3

1.1.3. Spectral lines . . . 4

1.1.3.1. Black body spectrum . . . 4

1.1.3.2. Formation of spectral lines . . . 6

1.1.3.3. Line broadening . . . 8

1.1.4. Forbidden line transitions . . . 11

1.2. Exoplanet detection . . . 11

1.2.1. Direct imaging . . . 12

1.2.2. Gravitational microlensing . . . 13

1.2.3. Transit method . . . 13

1.2.4. Radial velocity . . . 16

1.3. Stellar classification . . . 17

1.3.1. Spectral types . . . 17

1.3.2. Luminosity classes . . . 19

1.3.3. M dwarfs . . . 19

1.4. Stellar structure . . . 20

1.4.1. Stellar atmospheres . . . 23

1.4.2. Origin of stellar magnetic fields . . . 24

1.5. Stellar Activity . . . 25

1.5.1. Photospheric phenomena: spots and faculae . . . 26

1.5.2. Chromospheric Activity . . . 28

1.6. Chromospheric activity indicators . . . 29

1.6.1. Calcium . . . 29

1.6.2. Hydrogen . . . 31

1.6.3. Sodium . . . 34

1.6.4. Helium . . . 34

2. Observations and data reduction **37**

2.1. Observations . . . 37

2.2. Data selection and reduction . . . 37

2.3. PHOENIX and MARCS model spectra . . . 38

2.4. Reference stars . . . 39

3. Methods **41**
3.1. Index . . . 41
3.2. Gaussian fitting . . . 44
3.3. pFWHM . . . 45
3.4. Variability as an indicator of activity . . . 46
3.5. Selection of an initial sample . . . 47
3.6. Evaluating the index . . . 48
3.6.1. Parameters for improvement . . . 51
3.7. Molecular Normalized Index (MNI) . . . 51
3.7.1. Evaluating the MNI . . . 53
3.7.2. Modifying the low activity I sample . . . 56
3.7.3. Metallicity . . . 61
3.7.4. Summary . . . 61

4. Results **63**
4.1. Hα . . . 63
4.2. Ca II IRT . . . 64
4.3. Na I $D_{1\&2}$ . . . 70
4.4. He I D_3 . . . 73

5. Discussion **77**
5.1. Determining reference stars . . . 77
5.2. Hα . . . 78
5.3. Ca II IRT . . . 84
5.4. Comparison to previous works . . . 87
5.5. Proposal for line formation across the M dwarf sequence . . . 88
5.6. Discrepancies in modeling molecule rich atmospheres . . . 91

6. Conclusions from chapters 3 to 5 **93**

7. High cadence spectroscopic and photometric observations of a post-flare co-rotating feature on GJ 3270 **95**
7.1. Introduction . . . 95
7.2. Observations and data reduction . . . 98
7.2.1. Ground-based photometry . . . 98
7.2.2. Space-based *TESS* photometry . . . 99
7.2.3. CARMENES spectra . . . 101
7.3. Stellar parameters . . . 102
7.4. Analysis . . . 105
7.4.1. Flare energy estimation . . . 106
7.4.2. Flare model . . . 106
7.4.3. Spectroscopic index definition . . . 107

7.5. Results . . . 108
7.5.1. Photometry . . . 108
7.5.1.1. SNO and MuSCAT2 . . . 109
7.5.1.2. *TESS* . . . 110
7.5.2. Spectroscopy . . . 113
7.5.2.1. Chromospheric index time series . . . 113
7.5.2.2. Hα wing indices . . . 114
7.5.2.3. Doppler shifted emission . . . 116
7.5.3. Spectroscopy versus photometry . . . 120
7.6. Discussion . . . 121
7.6.1. Flaring rates and energies . . . 122
7.6.2. Localization of flare 2 region . . . 122
7.6.3. Minor flares . . . 123
7.6.4. Rotational modulation and Doppler shifts of activity indicators . . 124
7.6.5. Comparison of flare 1 and 2 . . . 125
7.6.6. Ejection of material . . . 126
7.7. Conclusions . . . 127

8. Summary & future work 129

A. Appendix 133
A.1. Wavelength ranges for index and MNI . . . 133
A.2. Median Activity Indicator Table . . . 139

Bibliography 147

List of Figures

1.1. Fraunhofer lines 2
1.2. Blackbody spectra 5
1.3. Spectral line formation 7
1.4. Line saturation 10
1.5. Direct image of HR8799 14
1.6. Gravitational Microlensing event 15
1.7. Transit of WASP-96b 15
1.8. Radial velocity illustration 16
1.9. The HR diagram 18
1.10. PP chain fusion process 21
1.11. CNO cycle fusion process 22
1.12. Energy transfer in stars of differing masses 22
1.13. Structural elements of the Sun 23
1.14. Butterfly sunspot diagram 26
1.15. Effect of spots on spectral lines 27
1.16. Calcium K mosaic of the Sun 28
1.17. Grotrian diagram of calcium I 30
1.18. Hα absorption profiles 32
1.19. Hα emission profiles 33
1.20. Asymmetric Hα profile 33
1.21. Intermediate Hα profile 34

3.1. Progression of Hα line profiles by spectral type 43
3.2. Gaussian fitting of J14257+236W 44
3.3. Gaussian fitting to star J03133+047 45
3.4. Index v. variability 47
3.5. Designating the I sample 48
3.6. Comparison of Hα index ($\widetilde{I_\mathrm{T}}$) to normalized core flux 49
3.7. Comparison of reference star Hα values to models 50
3.8. Comparison of Hα reference values to models, Gauss fitting regions and reference region index 52
3.9. Reference star index compared to Gaussian fits of Hα 52
3.10. Regions used in the calculation of the index and MNI 53
3.11. Comparison of the index and MNI on reference stars and models for Hα . 54
3.12. Reference stars compared to Gaussian fits and MNI of Hα 55
3.13. Toy model simulation to test index and MNI 56

3.14. Comparing the index and MNI on the I sample . . . 57
3.15. MNI and variability . . . 58
3.16. The N sample . . . 59
3.17. N sample and rotation . . . 59
3.18. MNI and Kürster Index . . . 60
3.19. Metallicity . . . 62

4.1. Comparing N and I samples . . . 65
4.2. MNI and pFWHM . . . 65
4.3. MNI and Hα core flux . . . 66
4.4. Core flux and pFWHM for Hα . . . 66
4.5. Ca II IRT MNI by $T_{\rm eff}$ . . . 67
4.6. Ca II IRT line shape evolution with core flux and pFWHM for N sample . . . 67
4.7. Ca II IRT line shape evolution with core flux and pFWHM for full sample 68
4.8. Comparison of active and quiet spectra for Ca II IRT) . . . 69
4.9. Comparison of active and quiet spectra for different spectral sub-types (Hα) 69
4.10. Comparison of Hα and Ca II IRT MNI values . . . 70
4.11. Na I D_1 MNI vs $T_{\rm eff}$ . . . 71
4.12. Na I D_1 MNI values for the Hα N sample . . . 71
4.13. Na I D_1 low activity sample . . . 72
4.14. Na I D_1 vs Hα MNI . . . 73
4.15. Na I D_1 vs Ca II IRT MNI . . . 74
4.16. He I D_3 MNI vs $T_{\rm eff}$, N sample . . . 74
4.17. He I D_3 MNI vs $T_{\rm eff}$, full sample . . . 75
4.18. He I D_3 compared to Hα MNI values . . . 76

5.1. MNI of N sample M1.0V spectral sub-type . . . 79
5.2. Comparison of sets of reference stars by spectral sub-type . . . 80
5.3. Comparison of reference stars by rotation period . . . 81
5.4. Hα double Gauss toy model compared to observed CARMENES spectra 82
5.5. Hα profile toy model . . . 83
5.6. Graphical interpretation of the N and I sample . . . 85
5.7. Models and late type M dwarfs . . . 91

7.1. SNO and MuSCAT2 light curves . . . 100
7.2. TESS lightcurve . . . 101
7.3. Periodogram of combined TESS and SNO V data . . . 103
7.4. Phase-folded lightcurves with Hα . . . 104
7.5. GLS power of half and full rotation periods . . . 104
7.6. Lightcurves of minor flaring . . . 109
7.7. Timing of major flare . . . 110
7.8. Flare energy vs Peak Luminosity . . . 112
7.9. Activity indicators and flaring . . . 114
7.10. Double Gaussian fitting of flare profile . . . 115

7.11. Wing indices and flare after effects 116
7.12. Comparison of the flare to activity minimum in Hα 117
7.13. Flare in He I D_3 118
7.14. Locating the flaring active region 119
7.15. Doppler shift of excess flare emission 120

A.1. Regions used in calculation of Ca II IRT MNI and index 134
A.2. Progression of CARMENES reference M dwarf Ca II IRT spectra from M0.0V at the bottom to M6.0V at the top. 135
A.3. Regions used to calculate the Na I $D_{1\&2}$ MNI and index 136
A.4. Line profile of by spectral type 137
A.5. line profile of He I D_3 by spectral type 138
A.6. Display of the calculation regions used in this work for He I D_3. Red is the He I D_3 measurement region. Blue and green denote the regions that the He I D_3 index is referenced to. Yellow represents the regions used for calculating the index of the reference regions. 139

List of Tables

2.1. Model parameters. 39
2.2. List of initial reference stars by spectral type. 40

3.1. Parameters of $I(S) = mS + b$ models for models and reference regions . . 51
3.2. Parameters of trend fits for Fig. 3.15. 'Active' is fit with a black line, the others with a green line. 57

5.1. Comparison of reference star selections by spectral type. R is the ranking value as calculated by Eq. 5.1 78

7.1. Start time, duration, and exposure time at time of flare of photometric observations. SNO: S, MuSCAT2: M. 99
7.2. GJ 3270 basic properties. 105
7.3. Vacuum wavelength ranges adopted for index definition 108
7.4. Parameters of flares 1 and 2a. 111
7.5. Parameters of *TESS* flares. 112
7.6. Parameters of double Gaussian fit. 115
7.7. Indicator energies for flare 2. 121
7.8. Enhancement factor of flare 2 from flare 1 by photometric band. 125
7.9. Expected vs. observed activity indicator response to flare 1 126

A.1. Hα wavelength ranges of concern 133
A.2. Ca II IRT wavelength ranges of concern 134
A.3. Na I D_1 wavelength ranges of concern 134
A.4. Na I D_2 , wavelength ranges of concern 134
A.5. He I D_3 wavelength ranges of concern 136
A.6. Activity indicator MNI values 1. 140
A.7. Activity indicator MNI values 2. 141
A.8. Activity indicator MNI values 3. 142
A.9. Activity indicator MNI values 4. 143
A.10. Activity indicator MNI values 5. 144
A.11. Activity indicator MNI values 6. 145
A.12. Activity indicator MNI values 7. 146

1. Introduction

This work consists of two main components that sum up the efforts taken during my doctoral program. The first part deals with the behavior of chromospheric activity indicators over the spectral range of M0V to M6V in the CARMENES GTO sample. The second part is a chapter comprising a published work (Johnson et al. 2021, A&A, 651,A105) that is placed as an unaltered unit. The only modifications taken pertained to the sizing of the figures so that they would better fit the format of this thesis. This work contends with the discovering of a co-rotating post-flare feature on the rapidly rotating M dwarf GJ 3270. As this paper uses the royal we pronoun throughout and cannot be altered we will do the same in all other parts of this thesis. Any acknowledgements of work done by others will be announced in chapter introductions.

1.1. Measuring Light

The two main methods of measuring light in astronomy are photometry and spectroscopy. As we use both ground-based and space-based photometry in our paper on GJ 3270 we will, to avoid unnecessarily repeating ourselves, only cover spectroscopy in this introduction.

1.1.1. Spectroscopy

Humanity has been aware of the effects of refraction, such as rainbows, for millennia. It was not until Sir Isaac Newton, in the mid 17$^{\text{th}}$ century, that the effect was scientifically described. He placed a prism into a beam of sunlight and produced an artificial rainbow- a spectrum (Newton & Innys 1730). This discovery would be critical for the development of spectroscopy and astronomy in the subsequent centuries. By the late 18$^{\text{th}}$ century, William Herschel found that light passing through the prism would affect a thermometer nearest the red section of the produced spectrum. Herschel realized that the prism must have split off light that was invisible to the human eye but could confer heat (Herschel 1800). He called them 'calorific rays' which would be re-designated as infrared radiation in the 19$^{\text{th}}$ century.

A few decades after Herschel had published his findings on calorific rays in 1800, Joseph Fraunhofer, with his background in fine optical instrument manufacture, discovered that the colors split off by passing sunlight through a prism would have tiny dark lines interrupting what had previously been thought were continuous colors. He described 570 lines (Fig. 1.1) with the most prominent features being designated A through H (Fraunhofer 1817) with K being added on later. It would later be found out that some of these spectral lines were due to the Earth's atmosphere but some, such as the D line, were not, and are still in the astrophysical nomenclature today. What Fraunhofer and his contemporary, William Hyde Wollaston, who had noted gaps in the spectrum independently of Fraunhofer, had discovered was the first evidence for absorption lines (Hyde Wollaston 1802).

During the 19th century it was realized that each of these lines corresponded to the wavelength of an emission line from a known element except for one. Therefore it was thought that this element was indigenous to the Sun and was named after the Greek name for the Sun, *Helios*. Helium was eventually isolated on Earth but the name stuck. Spectroscopy has led to other false discoveries, such as the case with Nebulium. These discoveries ultimately led to a greater understanding of what processes drive the illumination of the universe and has become the primary technique for humanity to investigate astrophysical objects (Thomson 1871).

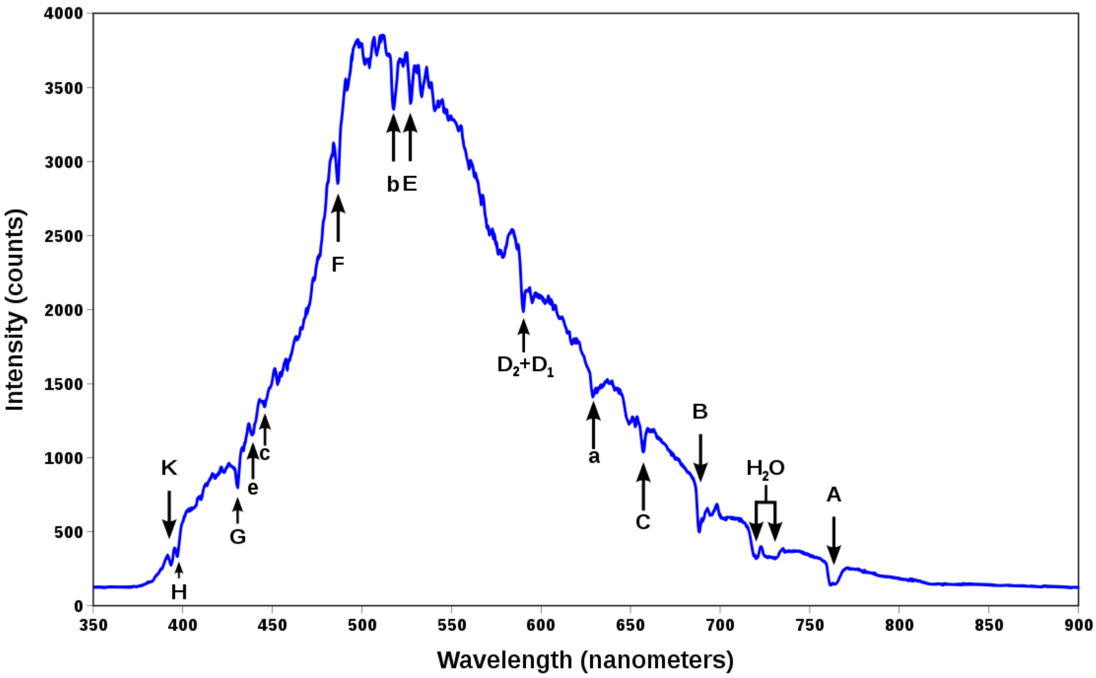

Figure 1.1.: Fraunhofer noted distinct features in the spectrum of the Sun and labeled them alphabetically from longer to shorter wavelengths. These features are now known as the Fraunhofer lines. Credit Eric Bajart via Wikimedia Commons used by CC BY-SA 4.0

1.1.2. Spectrographs

Most astrophysical spectrographs consist of five components. The first is the pathway to let light into the instrument. This can be done by either having an aperture directly at the focus of the telescope or to have a fiber optical cable from the focus to the instrument. The second component is a collimator that parallelizes the incoming beam onto the third component, the dispersing element (Gray 2008). The dispersing element can be a prism or, in modern spectrographs, some form of diffraction grating (Jacquinot 1954). The diffraction grating splits the incoming light into its component wavelengths, creating a spectrum. The fourth component, a focusing element or camera, focuses the spectrum onto the fifth element, a detector. Historically the detector was a photographic plate but these have largely been replaced by digital detectors such as Charged Coupled Devices (CCD). The main trade off in designing spectrographs is that the higher resolution comes at a cost of requiring more light or in astrophysics limiting the brightness of observable targets (Gray 2008).

A common type of modern spectrograph is an échelle spectrograph. Modern spectrographs used in exoplanet surveys operate on a design and methodology pioneered by the ELODIE spectrograph (Baranne et al. 1996). ELODIE was particularly noted for its capacity for simultaneous calibration. These échelle spectrographs are cross dispersed and use an échelle grating, hence the name of the device. This grating uses a large groove spacing design with a high blaze angle. In the case of ELODIE, the blaze angle was set at 76° (Baranne et al. 1996). This high blaze angle allows for the majority of the light to be concentrated at higher diffraction orders. A cross disperser is used to take this high order diffracted light and stack it into a 2D configuration which is ideal for modern digital detectors. The major benefit of this design is that it allows for a large wavelength coverage in a relatively compact device (Gray 2008). The resultant spectrum, however, still needs to be calibrated to be useful.

The wavelength solution can be calibrated in a number of ways. The most inexpensive way is to use the absorption lines present in the atmosphere of the Earth as a wavelength guide. These telluric lines have a large wavelength coverage and known wavelengths so the wavelength of the lines in the stellar spectrum can be calculated (Griffin & Griffin 1973). The downside of this approach is that telluric line positions can be shifted due to atmospheric conditions, such as wind, which limits the precision of the wavelength solution. Additionally the number of lines in a particular section of spectrum that the observer is interested in may not be sufficient for the task. Alternatively the light, from the telescope, can be passed through a gas cell. This gas, at first hydrogen fluoride (Campbell & Walker 1979) but now usually iodine (Marcy & Butler 1992), imparts an additional known absorption spectrum into the observed stellar spectrum, allowing wavelengths of stellar lines to be calculated. The issue with this approach is that the gas cell spectrum can interfere with features from the stellar spectrum. This can be ameliorated by one observation done with the gas cell in and one without but this costs twice the observation time. Hollow cathode lamps, on the other hand, use an emission spectrum in another channel to calibrate. This provides an easy to calculate wavelength solution but can be an issue if a stellar line is too close to a bright emission line from the lamp. This can cause some light to bleed into the stellar spectrum. With CARMENES[1] (Quirrenbach et al. 2012), wavelength solutions are calibrated using Fabry-Pérot interferometers and hollow cathode lamps to improve the wavelength solution in addition to providing drift correction. This allows for both accuracy (wavelength calibration) and precision (drift correction). The Fabry-Pérot provides evenly spaced lines that cover the entire spectral range (Bauer et al. 2015). Lastly, the most accurate calibration method is to use a laser frequency comb which outputs a finely, and evenly, spaced set of lines, in frequency space, that looks vaguely like a comb, hence the name (Debus et al. 2021). This precision comes at a cost as the devices are very expensive and complex.

Spectrographs intended for exoplanet surveys, such as HARPS[2] (Mayor et al. 2003) and CARMENES need to be as stable as possible in order to obtain the desired less than 1 m/s precision. This requires all optical elements to be incredibly stable as any movement will cause an apparent shift greater than requirements. Even the air and ambient temperature changes can affect the precision so the instruments are placed inside temperature controlled vacuum vessels.

1.1.3. Spectral lines

1.1.3.1. Black body spectrum

In the mid 19$^{\text{th}}$ century, Gustav Kirchhoff theorized that an idealized radiator would be in thermodynamic equilibrium with its surroundings, absorb all electromagnetic radiation incident upon it and have no reflective properties. He described such an object as a black body and the continuous spectrum resultant from such a body emitting radiation would be black body, or thermal, radiation. This radiation is also known as cavity radiation as the best attempts of realizing a theoretical black body in the physical world involved the use of a cavity with a blackened interior and only one viewing port. This minimized interaction with the outside world (Kirchhoff 1860). While black bodies are theoretical concepts, the spectra of many stars can be approximated by black body radiation. However, stellar spectra show features such as atomic and molecular lines, which can cause strong deviations from a black body spectrum. The effective temperature of a star is defined to be the total radiation given off by that star as equal to the total radiation a black body would admit with a temperature T. Wien's displacement law (Eqn. 1.1) describes the point of maximum flux density for a black body of given temperature. Adopting the stellar effective temperature, it can be used to estimate the intensity maximum of stellar radiation (Karttunen et al. 2014).

[1]Calar Alto high-Resolution search for M dwarfs with Exoearths with Near-infrared and optical Échelle Spectrographs.

[2]High Accuracy Radial velocity Planet Searcher

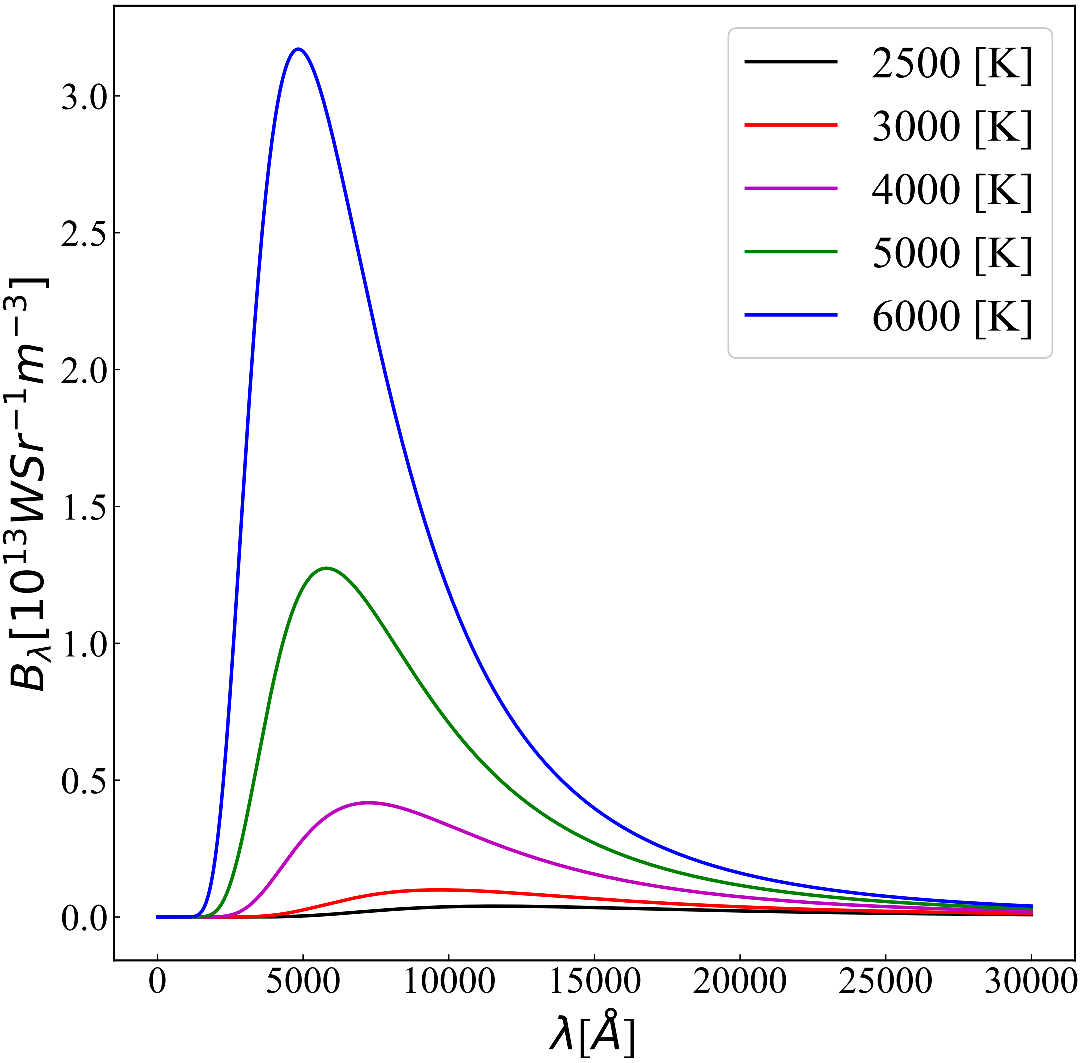

Figure 1.2.: Blackbody spectra for objects ranging from 2500 K to 6000 K.

$$\lambda_{max} T = 2.89777 \times 10^{-3}\,\mathrm{m\,K}. \tag{1.1}$$

The first attempt to, mathematically, describe the spectrum of a black body, the Rayleigh-Jeans approximation, fit the low energy portion of the spectrum well but predicted that black bodies would emit infinite amounts of ultraviolet radiation. It was therefore called the *ultraviolet catastrophe* and classical physics could not appropriately address the issue. The Rayleigh-Jeans approximation is given in equation 1.2 where $B_\lambda(T)$ is the spectral radiance at a particular wavelength, k_B is the Boltzmann constant, c is the speed of light,

λ is the wavelength and T is the temperature[3].

$$B_\lambda(T) = \frac{2ck_BT}{\lambda^4}. \tag{1.2}$$

It took Max Planck, with the assumption that the energy of light was quantized, that a solution to the ultraviolet catastrophe was found (Planck 1900). The Planck equation

$$B_\lambda(T,\lambda) = \frac{2hc^2}{\lambda^5}\frac{1}{e^{\frac{hc}{k_BT\lambda}} - 1} \tag{1.3}$$

successfully reproduced the sharp dropoff in emitted radiation a blackbody experiences toward the high energy end of the spectrum (Fig. 1.2). From this equation the blackbody flux equation can be derived

$$F = \sigma T^4. \tag{1.4}$$

Integrating the blackbody flux over the surface area of a sphere gives us the luminosity

$$L = 4\pi R^2 \sigma T^4 \tag{1.5}$$

which is one of the most widely used equations in astrophysics.

1.1.3.2. Formation of spectral lines

The realization that light could be quantized led Niels Bohr to postulate that the energy levels of the atom were discrete and the transitions of electrons from high energy states to low energy states would produce the emission spectra observed from heated gas lamps (Bohr 1913). This discrete amount of energy would equate to the wavelength of the emitted light. The first success in this was in explaining the Rydberg formula for the spectrum of hydrogen and is given in equation 1.6 where R_H is the Rydberg constant and n_x indicates the energy level (Rydberg 1890). This, for the first time allowed for the prediction of spectra of atoms rather than the spectra needing to be empirically described. Following this, there were fewer claims of new elements being discovered in exotic environments (such as coronium or nebulium) as these were either rare or highly ionized transitions of known elements

$$\frac{1}{\lambda_{\text{vac}}} = R_H\left(\frac{1}{n_1^2} - \frac{1}{n_2^2}\right). \tag{1.6}$$

As shown in Figure 1.3, a continuous spectra is seen when observing a dense, hot gas directly. The formation of a continuous spectra can arise through a variety of mechanisms but in the case of stars the energy distribution of the continuum approximates

[3] For future equations in this work λ will, unless otherwise noted, always refer to wavelength. T will refer to temperature, h the Planck's constant, c the speed of light.

Figure 1.3.: Formation of spectral lines. Direct view of a source produces a continuous spectrum. View of a source through a cloud of cooler gas produces an absorption spectrum. View of that same gas cloud not back dropped by a source produces an emission spectrum. Credit Openstax *Astronomy* by CC-BY 4.0.

that of a black body curve. In hot stars the bound-free absorption of hydrogen can affect the shape (Gray 2008). In cooler stars the absorption of the negative hydrogen ion strongly affects the shape of the continuum (Branscomb & Pagel 1958; Wildt 1939). In very cool stars strong absorption from molecular bands can completely mask the classical continuum (Allard & Hauschildt 1995). Such spectra are referred to as being a pseudo-continuum. Other features can be induced through absorption of various lines within the hydrogen or helium atoms such as the Balmer or Paschen discontinuities (Gray 2008).

If a cloud of gas is between a continuous source and the observer, this cloud can absorb some of the continuous spectrum and the energy is subsequently re-emitted in all directions. The absorbed wavelengths correspond to specific electron transitions within the atoms/ions/molecules of that cloud. This causes less of the continuous spectrum to be observed at that wavelength by the observer creating an absorption line. If this same cloud is viewed without the background continuous source then those same lines would be viewed in emission Gray (2008). This represents a basic two-layer model of a stellar atmosphere but in reality the situation is more complicated.

Spectral lines are formed as a series of contribution functions that can be affected by the environment of the atmospheric layer they are formed in (Jefferies 1968). The contribution function gives us how much each layer of the atmosphere is contributing to the line formation (Magain 1986). This also gives us a convenient way of probing those environments. The fundamental parameter that affects spectral lines is the temperature gradient. If the temperature, and thus the magnitude of the contribution function, decreases with altitude then the line will appear in absorption. If the contribution function increases with altitude then the line will appear in emission (Linsky et al. 1979). Lines will also vary with temperature depending on the transition constraints of the upper and lower electron levels. For instance if the temperature of a gas is insufficient to populate the originating electron level with an electron then no line can form. If the temperature gradient is such that the destination electron level is populated more than the originating level, an emission line will be observed. This can be calculated using the Boltzmann equation. If the atom is ionized then there would either be no line or an emission line depending on the degree of ionization. This can be calculated using the Saha equation (Gray 2008).

Pressure can affect the formation of a line as well. As more atoms, in the process of undergoing a line transition, are influenced by other nearby atoms or molecules, the energy of the transitions can be affected. This tends to broaden the line (Gray 2008). A subtype of pressure broadening that particularly affects hydrogen lines is the linear Stark effect, in which nearby ions create an electric field that can split the energy levels of the hydrogen atom. This broadening effect is particularly noteworthy on hot, early type, stars that have many ions in their atmospheres (Sobel'Man et al. 1995).

The quantity of absorbing atoms in an atmosphere also has a strong effect on the formation and even existence on spectral lines as if there are no atoms capable of absorbing a particular wavelength then no absorption occurs. As the number of absorbing atoms starts to increase the line growth is proportional to the increase in the optical depth, the integral of attenuation cross section and number density from the outside to the point in question, usually denoted by τ, of the surrounding atmosphere. In this stage the line is referred to as being weak or optically thin. If the optical depth of the atmosphere continues to grow, the line becomes saturated where the linear relationship between optical depth and absorption are no longer linear. At this point the line is now optically thick and referred to as a strong line Fig. 1.4. Observationally weak lines are Gaussian in shape and their growth is mostly constrained to the line core. As the line strengthens wings will broaden noticeably. This process is referred to as the curve of growth (Gray 2008).

1.1.3.3. Line broadening

After the temperature the most common environmental effect on a spectral line is broadening. We will discuss the prominent causes of broadening in M dwarf atmospheres but for a more complete treatment we refer to Böhm-Vitense (1992); Foukal (2004) and Gray (2008). The fundamental width of a line is defined by the Heisenberg uncertainty principle in that the lifetime of an electron in an excited state and the energy difference between the transition states can not be precisely known (Hubeny & Mihalas 2015). This *natural broadening* leads to a Lorentzian profile (wider wings and narrower peak when compared to a Gaussian) with a width on the order of 10^{-4}Å (Rutten 2003).

Another broadening process that leads to the formation of a Lorentzian profile is that of *pressure broadening* also known as collisional broadening. This arises from the direct interaction of atomic or molecular species in the gas. LTE conditions exist when a localized patch of gas has sufficient interaction between particles that a single temperature is a good approximation (Reid & Hawley 2005a). Stellar interiors and the photosphere are frequently approximated, in literature, using LTE. Above the photosphere, in the chromosphere, this approximation no longer holds. This is due to the decrease in pressure resulting in a decrease in particle collisions. These conditions make the LTE approximation progressively inappropriate (Gray 2008).

Due to the random motions of atoms in a gas in the radial direction of an observer the observed wavelength of a transition can be altered. For an atom moving toward an observer the wavelength is observed to be shorter, or bluer. For an atom moving away the wavelength with be observed to be longer, or redder (Sobel'Man et al. 1995). This Doppler shift can be calculated with Eq. 1.7 where V_r is the velocity in the radial direction of the observer (Doppler 1842).

$$\frac{V_r}{c} = \frac{\Delta\lambda}{\lambda} \tag{1.7}$$

Taken together the random motions of the gas will follow the Maxwellian distribution of velocities and will give rise to a *thermal broadening* term. The magnitude of this broadening is given by Eq. 1.8 where m is the mass of the atomic species in question.

$$\Delta\lambda = \frac{\lambda}{c}\frac{2kT}{m} \tag{1.8}$$

The observational consequence of this is that lighter atoms, like hydrogen ($\Delta\lambda \approx 0.25$Å), are more affected than heavier atoms, like calcium ($\Delta\lambda \approx 0.02$Å).

Bulk motions of a gas can also lead to a Doppler shift as any motion along the observers radial of light emitting gas will. Replacing V_r with V_s in Eq. 1.7 for the speed of sound can place an upper limit on the expected value of this *turbulent broadening* term. Mihalas (1978) estimate that V_s for the solar chromosphere was about 8km s^{-1}. This leads to a broadening of 0.1Å for Ca II HKand 0.18Å for Hα.

Taken together the thermal and turbulent broadening are referred to as the *Doppler broadening* and amount to 0.1Å of broadening for calcium lines and 0.3Å for Hα. The line profile of lines shaped by Doppler broadening can be well represented by a Gaussian profile and is referred to as the Doppler core of the line. If pressure broadening is dominant, a Lorentzian profile is generally a better fit. When both pressure broadening and Doppler broadening are important a Voigt profile is generally a better fit.

An object's rotation can also lead to broadening effects as the oncoming and retreating hemispheres of the object will have difference Doppler shifts. This *rotational broadening* is proportional to the rotational velocity of the object multiplied by the sine of its inclination to the observer. As we cover in Chapter 7 the rotational broadening of rapidly rotation M dwarfs can be impressive with a broadening in excess of 1Å (Newton et al. 2016; Johnson et al. 2021). On the slowest rotating M dwarfs this broadening term is negligible.

Spectral lines can also be affected by being within an electric or magnetic field. The *Stark effect* can broaden and eventually split the spectral lines of a gas in a strong electric

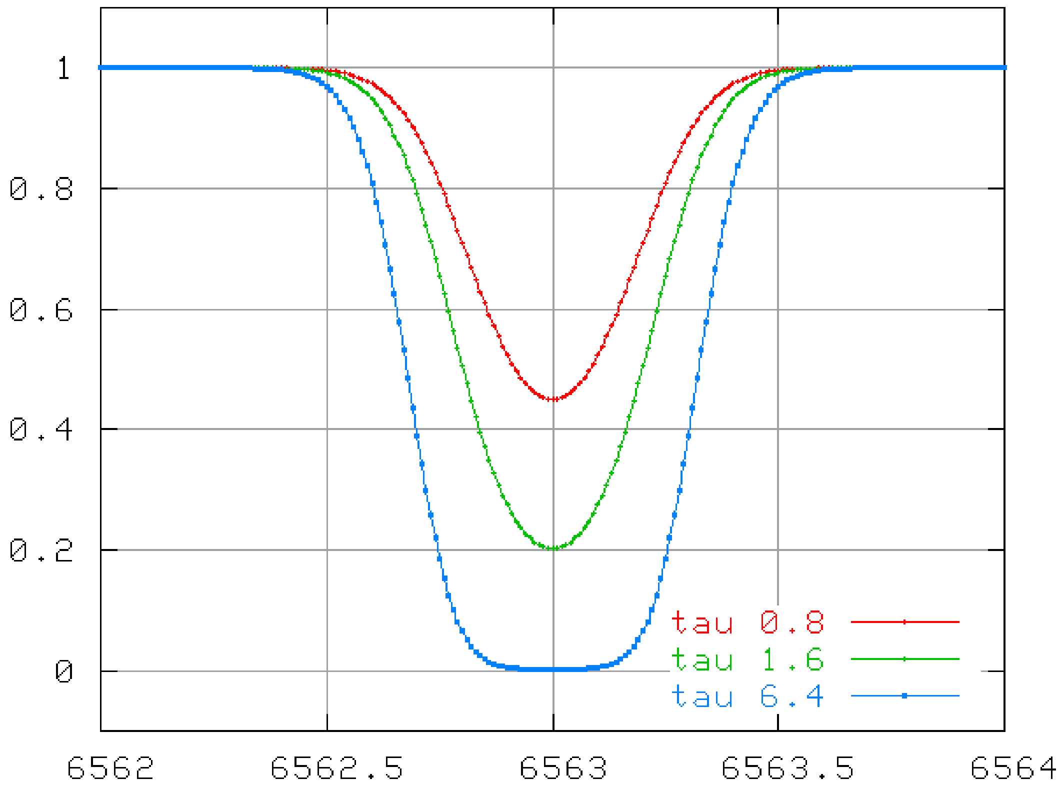

Figure 1.4.: Line saturation. Spectral line profiles as a function of increasing optical depth (tau), as described in Section 1.1.3.2. The figure illustrates the transition from an optically thin, weak, line, in which the doubling of the optical depth results in a doubling of the absorption, to optically thick, where the doubling of optical depth does not result in the doubling of absorption. At this point the line has begun to become saturated and is considered a strong line. Credit Michael Richmond under a Creative Commons License.

field (Fulcher 1915). The operating mechanism is that the positively charged nucleus of the atom will move in the opposite direction to the negatively charged electron and this will either add or detract energy from the transition of the electron between states. In a mild electric field this will broaden the line but in extreme cases will split the line into multiple discrete lines. The *Zeeman effect*, like the Stark effect, broadens and eventually splits the spectral line (Robinson 1980; Saar 1988; Shulyak et al. 2017; Böhm-Vitense 1992). The Zeeman effect works on the dipole moment of an atom and the angular momentum of the electrons within that atom, allowing for more energy levels for the electron to transition from thereby broadening and eventually splitting the line (Zeeman 1896). While nature has many processes that can broaden spectral lines our instruments also contribute as no spectrograph has infinite resolving power. This will induce broadening by effectively smoothing the line profile. This *instrumental broadening* accounts for about 0.07Å of line broadening in the region around Hα using the CARMENES instrument.

1.1.4. Forbidden line transitions

The occurrence of an electron transition producing an observed line is given by the electronic selection rules and the probability of that transition taking place. The electronic selection rules state that the spin of the electron cannot change. The change in the total orbital angular momentum can be -1,0 or 1 but cannot transition from 0 to 0. Similarly the total angular momentum change can be -1, 0 or 1 but not transition from 0 to 0 (Atkins et al. 2018). Lastly the initial and final wave functions must change parity. The transitions that would break these rules are considered forbidden (Gray 2008). The word forbidden, however, should be taken a bit loosely and is more akin to the transition being very unlikely. The most prominent forbidden transition is the O III 5777Å line which gives some nebulae their greenish color. This transition was first thought to be a new element (nebulium) but was later found to be the aforementioned transition of oxygen (Huggins & Miller 1864; Bowen 1927).

In higher pressure environments, this transition cannot be observed as the time it takes for a transition to occur is vastly greater than the time between interactions of the oxygen atom with another atom which can bump the electron out of the originating energy state. Usually the only way out of these metastable states is to be excited back up to a higher energy state or collisionally de-excited through interaction with another atom (Böhm-Vitense 1992). These meta stable states can also be populated by collisional excitation from another state if the temperature of the medium is sufficient to cover the difference between the lower energy state and that of the meta stable state. Conversely to the forbidden lines, the strongest lines of a particular atom are those that transition to the ground state, or lowest energy level, of the atom. These lines are referred to as resonant lines and are usually quite prominent in a spectrum. Notable examples of resonant lines are Ly-α,Na I $D_{1\&2}$, and Ca II HK (Morton 1990).

1.2. Exoplanet detection

Two of the most compelling reasons for humanity to study astronomy throughout the ages was either to get closer to whatever deity (or deities) they believed in or to try to answer whether or not there was anything like us or another Earth out there. In ancient times the first planets were noticed by eye as points of light that moved against the background of stars. These were called 'wandering stars'-'planets' by the ancient Greeks. They were able to identify 5 planets and ascribed them the names of their pantheon of gods. Later the Romans took the same naming convention and ascribed the planets their names of the same pantheon of gods. Names that they are still known by today: Mercury, Venus, Mars, Jupiter and Saturn. During the 19th century telescopes had become large enough to detect two additional planets, Uranus and Neptune. The 20th century added diminutive Pluto to our pantheon of planets. Pluto remained until the 2000s when it was demoted to the status of dwarf planet, with the discovery of like-sized objects with similar orbits around the Sun.

By the early 1980s the distribution of solar system planets had a distinct pattern in which the types of planets were organized. The small, terrestrial planets, like Earth, exist close to the Sun followed by the massive gas giants (Jupiter and Saturn) with Uranus and Neptune taking up next with the small icy planets, like Pluto at the furthest edge of the system. When the first planets, in 1992, were discovered around another star they were nothing that we expected. The planets were small and rocky but they orbited a neutron star (Wolszczan & Frail 1992). This corpse of a massive star that had gone supernova had probably destroyed any solar system it previously had, so it has been theorized that they formed from the debris leftover from the supernova. Podsiadlowski (1993), however, argues for a white dwarf merger event as a more likely progenitor to planet formation in this system.

The first planet around a Sun-like star, 51 Pegasi b, was also not like anything in our own system. 51 Pegasi b has a mass about half that of Jupiter, but orbited so close as to have a year of only 4.23 days with a semi-major axis of only 0.05 astronomical units (Mayor & Queloz 1995). This was the first discovery of a 'hot Jupiter'- a gas giant that orbits extremely close to its host star. Needless to say this discovery caused not a small amount of consternation among those working on planet formation as this style of system was radically different from our own. This consternation grew with additional discoveries of such systems but was allayed with additional discoveries of more systems more akin to our own, systems that had planets in stable, circular orbits relatively far from their stars. We have yet to find a system that is a direct analog of our own as this is only now entering the detection regimes of the newest instruments. The discovery of hot Jupiters was a observational bias in that, due to their mass and proximity, they had the most effect upon their host stars. In 2003 (Hatzes et al. 2003) the planet γ Cephei b was announced which confirmed a disputed planetary discovery from 1988 (Campbell et al. 1988). This is arguably the first exoplanet discovered but, due to the long time it took to confirm the discovery, is not usually considered as such. The discovery of these and subsequent exoplanets occurred through use of four primary techniques: Direct imaging, gravitational microlensing, transits and radial velocity. We will briefly discuss each method, going a little more in depth on the radial velocity method as that is the most pertinent to working with CARMENES data, but refer to Bozza et al. (2016) and Perryman (2018) for a more complete description.

1.2.1. Direct imaging

What may seem the most straight-forward method of detecting an exoplanet-taking a picture- is, in actuality, one of the most difficult. The main issue is that the angular separation of a planet from its host star is usually exceptionally small and at those separations the brightness difference between the host star and the planet can be on the order of 10^9 in the visual band. Thus far the best technique is to use a coronagraph to blot out the light from the host star in the infrared and to target young star systems where the planets would still be hot from their formation (Fig. 1.5). In the most favorable of conditions the contrast between the star and planet can be reduced to a factor of 100 (Colloquium et al. 2006). Even with this, however, the closest confirmed planet, using this method, to its host star is β Pictoris b, a 12.7 Jupiter mass planet with the semi-major axis similar to that of Saturn (Lagrange et al. 2009).

1.2.2. Gravitational microlensing

While the direct imaging method may be the most technically difficult to achieve, the gravitational microlensing method is the most dependent on luck. The stars literally have to align just right and be observed doing so in order to make a discovery. The process relies on general relativity's prediction that massive objects bend the fabric of space-time. Light traveling through this disturbed region will bend along with space-time, in effect creating a very large lens (Gould 2000). This works on the same principal as gravitational macrolensing, just with the angular resolution amplification still below the telescope's resolving threshold, in which a large galaxy will amplify a background object, like a quasar, making it large and bright enough to be observed on Earth. The smaller scale version happens when a planet-bearing star system passes in front of a background star, relative to us, there is a possibility that both the parent star and the planet will lens the background light, making it appear brighter. Analysis of the light curve can determine the mass, radius and semi-major axis of the planet (Fig. 1.6). The benefits of this method are that it allows for extremely distant planet detection, potentially extragalactic (An et al. 2004). Microlensing can also detect small planets close to their stars, to the point of detecting Earth mass planets around Sun-like stars, the downside of this method is that it is a one time event and, given that the distances can be potentially extra-galactic in nature (Dai & Guerras 2018), prevents follow-up with other detection methods (Bozza et al. 2016).

1.2.3. Transit method

The transit method of exoplanet detection is done by measuring the small dip in light caused by a planet passing in between the star's photosphere and Earth (Konacki et al. 2003). This small dip is directly related to the radius of the planet (Fig. 1.7). However, due to a number of potential false positives any light curve that exhibits a dip can only be described as a planetary candidate and must be confirmed by other methods (Bozza et al. 2016). This detection method is also affected by stellar activity as star spots can also create an irregular light curve. While this method can be achieved with ground based telescopes, it is far more effective using space-based telescopes that can focus on an area of sky for an extended period of time and without the interference of the atmosphere. With the Kepler and TESS space telescopes this method has resulted in the majority of exoplanet discoveries (Bozza et al. 2016; Ricker et al. 2022).

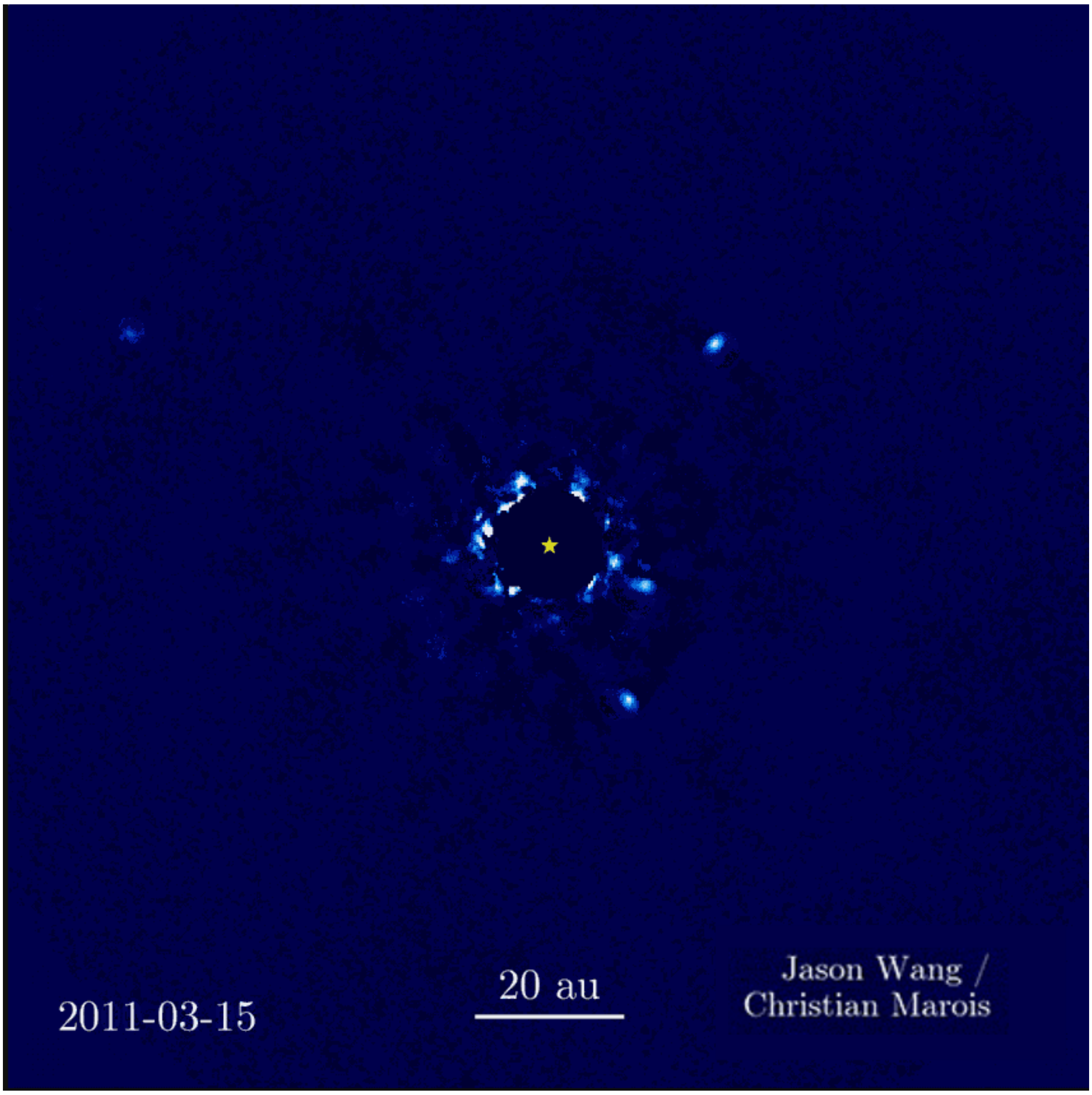

Figure 1.5.: HR8799 system. Detection of an exoplanet via direct imaging. Modified from NASA, Credit: Jason Wang and Christian Marois, via Creative Commons License.

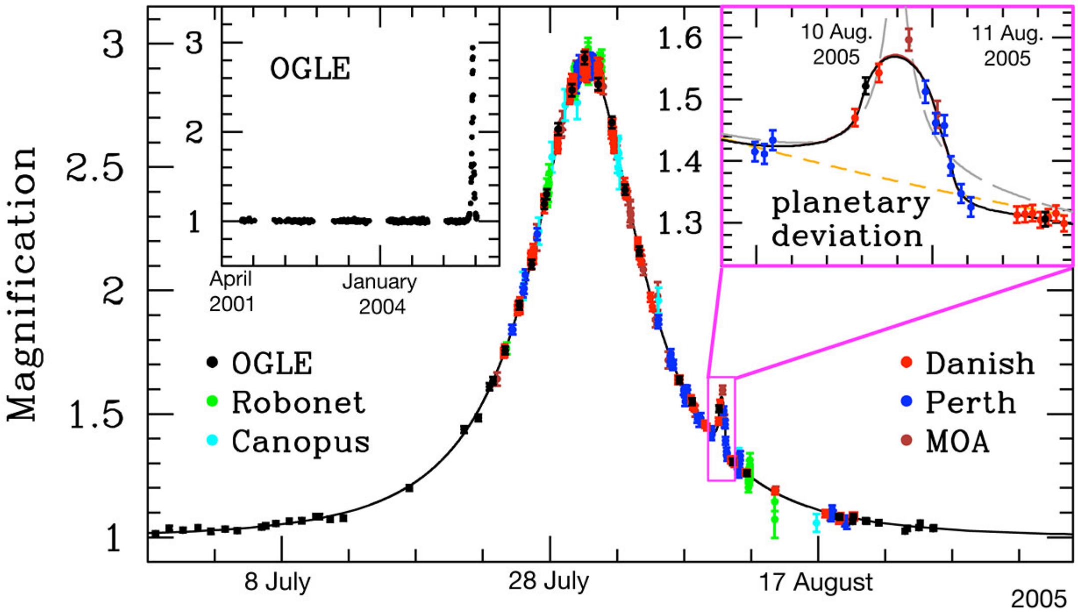

Figure 1.6.: Gravitational Microlensing event. Credit ESO, data from OGLE under CC BY-SA 4.0 Source: ESO.

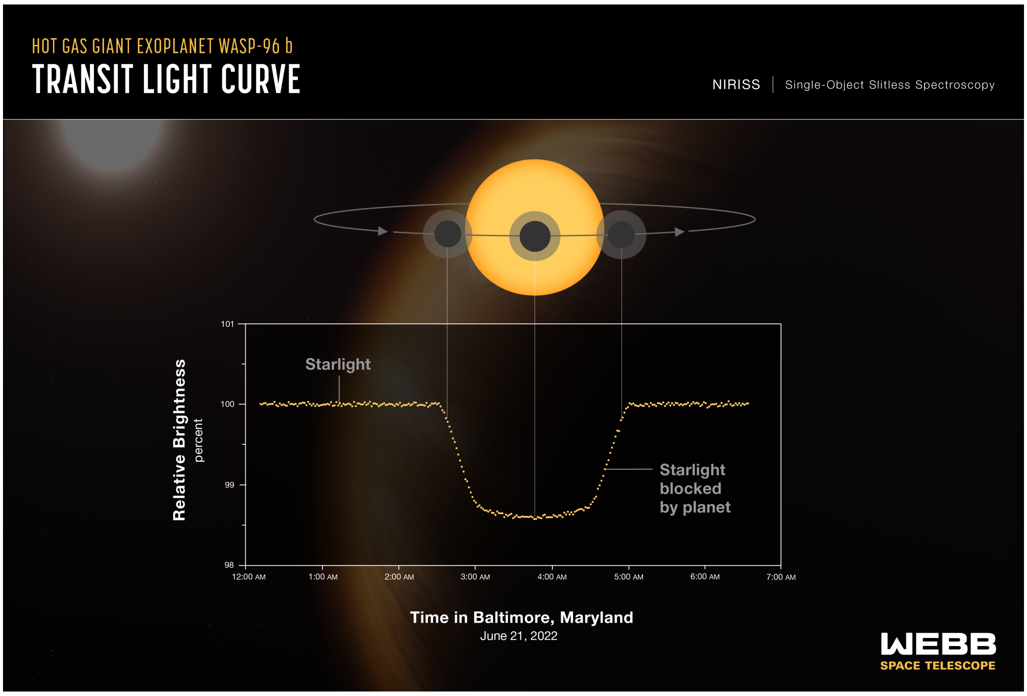

Figure 1.7.: Transiting exoplanet WASP-96b photometric profile. Credit ESA, NASA, CSA, and STScI used under CC-BY 3.0. Source: ESA.

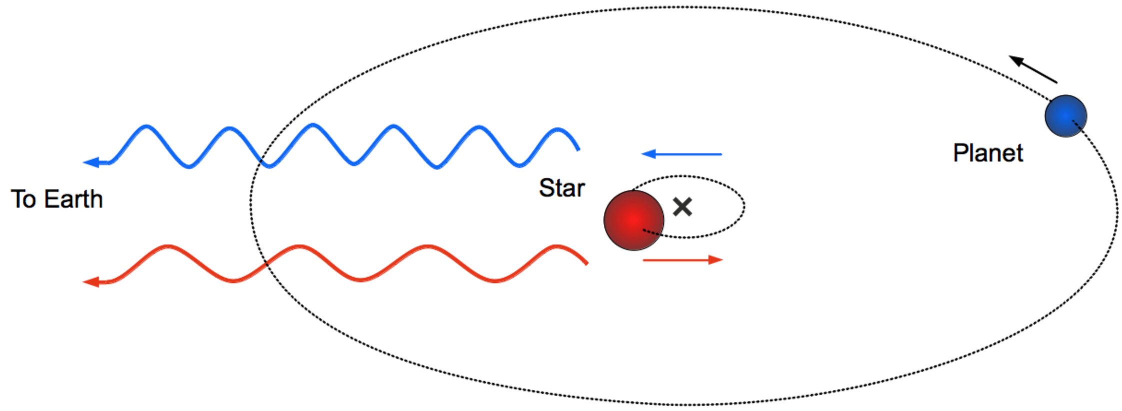

Figure 1.8.: Radial velocity signature imparted upon a star by an orbiting planet.Credit Tenefifi Wikimedia Commons under CCO 1.0 license.

1.2.4. Radial velocity

The aforementioned first planet discovered around a Sun-like star, 51 Pegasi b, was discovered using the radial velocity method. This process works by detecting the red or blue Doppler shift of stellar spectral features caused by an orbiting planet inducing a small velocity on its host star (Fig. 1.8). The magnitude of this velocity is directly related to the mass-ratio of the star-planet system and is given with equation 1.9. K refers to the semi amplitude, G is the gravitational constant, P refers to the period, M_P the mass of the planet, M_* the mass of the star, i the inclination and e the orbital eccentricity. This method is the method most often employed to confirm transit planetary candidates. Doing so gives us a mass, from the amplitude of the radial velocity signal induced on the star, and a radius, from the amount of stellar light occulted by the planet, thereby allowing for a rough categorization of these planets via their densities (Perryman 2018).

$$K = \left(\frac{2\pi G}{P}\right)^{\frac{1}{3}} \frac{M_p \sin i}{(M_p + M_*)^{\frac{2}{3}}} \frac{1}{\sqrt{1-e^2}} \tag{1.9}$$

The radial velocity method is among the more technically challenging methods to successfully employ, especially when looking for Earth analogs. Earth induces a roughly $0.1\,\mathrm{m\,s^{-1}}$ velocity on the Sun (Perryman 2018; Seager 2010). This level of precision is achievable by only the newest of ultra stabilized spectrographs like ESPRESSO (Pepe et al. 2021). This, however, does not account for variability of stars, such as stellar activity, that can further complicate detection efforts. Thus finding Earth-mass planets around Sun like stars has been beyond our technical capabilities until very recently. Lower mass stars also have the added benefit of being cooler and their habitable zones being closer to the star (Kasting et al. 1993; Kopparapu et al. 2013). Thereby an Earth-mass planet, in the habitable zone, would induce an apparent velocity of $1\,\mathrm{m\,s^{-1}}$ (Endl et al. 2003) on the star. This is beneficial not only for the higher chance of detection but also due to the shorter orbital periods of these planets as more complete orbits can be observed in a shorter time. In order to detect this motion, spectrographs have to be extremely stable in temperature and pressure while using a precise wavelength reference. Some of the first instruments of this nature are HIRES (Vogt et al. 1994), UVES (Dekker et al. 2000) and HARPS (Mayor et al. 2003) and worked mostly in the range of 400 to 800nm. Now instruments such as CARMENES (Quirrenbach et al. 2010) , CRIRES+ (Dorn et al. 2016) and SPIRou (Donati et al. 2018) are attempting to reach $1\,\mathrm{m\,s^{-1}}$ precision in the infrared. Even with such an instrument the detection can be disrupted by the star itself. Stellar activity can induce apparent velocity deviations on the order of several hundred meters per second. These can be caused by cool spots changing the nature of the integrated stellar spectrum to flares that can temporarily alter a star's spectrum to that of a much hotter star. In the attempt to find an Earth-analog it is therefore imperative to know the instrument and the star extremely well (Bozza et al. 2016).

1.3. Stellar classification

Stellar classification has been an enterprise undertaken by humanity since the earliest days of written records and most likely before, as it was important to know which stars indicated planting and harvesting times. In ancient Greece, Hipparchus was the fist recorded effort to classify all stars. He did so by judging how bright they were to his eye. The brightest stars were called first magnitude and the dimmest sixth. This system has survived, in part, to the modern day as the magnitude system. It wasn't until the advent of spectroscopy in the early to mid 1800s as an effective tool to study stars that stellar classification could take the next step toward the system we utilize today.

1.3.1. Spectral types

The origin of the modern spectral classification system came from the Draper system which arranged stars according to the strength of their hydrogen lines from A, with the strongest lines, to M, with the weakest. This system also included non-stellar objects like planetary nebulae. In the early 20th century, with the understanding that the hydrogen line strength increased and decreased according to the temperature of the stellar photosphere, Annie Jump Cannon reordered the stellar classification letters of the Draper system into the modern orientation of O B A F G K M with O (Fig. 1.9) being the hottest (*early*) and M being the coolest (*late*) (Cannon & Pickering 1912). Additionally she subdivided each class with numerals to create finer classifications of stars. While this system was later amended with newer information, such as the addition of brown dwarf classifications of L T Y, this Harvard system has been the default spectral classification system for the last hundred years (Johnson & Morgan 1953; Morgan et al. 1943). This system, as well as the knowledge of the absolute magnitude of stars, allowed Ejnar Hertzsprung and Henry Russell to develop the HR diagram which made effective study of the evolution of

Figure 1.9.: The Hertzsprung-Russel diagram detailing the characteristics of stars on their evolution from the main sequence to stellar remnant. Credit ESO used under CC-BY 4.0

stars possible (Hertzsprung 1909; Russell 1914) and did away with the notion, still from the Kelvin-Helmholtz era, that the brighter stars were younger and evolved into cooler, smaller stars as they contracted from losing heat (Bradt 2008).

1.3.2. Luminosity classes

While the Harvard system sorts stars based on which lines are present, it was noted that these lines did not always appear to have the same shape. In some stars the lines were extremely broad and shallow while in others almost needle-like. This was found to be caused by the physical size of the star rather than by its mass and temperature. The larger the star is the lower the density of the gas at the photosphere. This reduces the effect of thermal and pressure broadening on the spectral line making them appear thinner than a smaller star of the same temperature. The different classes were denoted by roman numerals with class I being hypergiants and supergiants (later split into Ia and Ib), class II being bright giants, class III giants, class IV subgiants, class V dwarfs and VI (or sd) for sub dwarfs. Main sequence stars are classified as dwarfs so our Sun would be labeled as a G2V star whereas a much larger star of the same surface temperature as our Sun would be a G2III as an example (Karttunen et al. 2014).

1.3.3. M dwarfs

In the bottom right of the HR diagram reside the coolest, smallest stars. In the original form of the Harvard system these stars were denoted with the letter M to indicate the very weak hydrogen lines present in their spectra. Unlike their alphabetical neighbors, the O stars, the lack of hydrogen lines in M stars is due to insufficient temperature to form the hydrogen lines rather than being so hot that all of the hydrogen is ionized. The significant difference between late type and early type stars, besides their hydrogen lines, is that these late type stars are so cool that they have abundant molecular absorption features in their spectrum. Most prominent among these features are abundant bands of TiO and VO. Kirkpatrick et al. (1991) has used these bands in order to define spectral subtypes from K5 to M9. The temperature over the M star spectral type ranges from 3850 K (M0V) to 2400 K (M9.5V) (Pecaut & Mamajek 2013). It should be noted that different models have slightly different temperature ranges but nearly all have the range between 4000 K and 2000 K (Husser et al. 2013).

The smallest M dwarfs have a radius of only 8% that of our Sun (Reid & Hawley 2005b) which makes them comparable to radius of Jupiter, although with a mass of 0.075 $M_\odot$, they are 80 times more massive than Jupiter (Chabrier & Baraffe 2000). The smallest M dwarfs have a luminosity of only $1.5{\cdot}10^{-4}\ L_\odot$ (Reid & Hawley 2005b). The smallest of the M dwarfs are also fully convective. This allows for the core to be refreshed with hydrogen from the envelope. Consequently, their lifespans can be up to 10^{13} years (Laughlin et al. 1997). At around spectral subtype M4V this fully convective nature changes to a more solar-like configuration of a radiative core and convective envelope (Chabrier & Baraffe 1997). The most massive M dwarfs are 0.6 $M_{\odot}$ with radii of 0.62 $R_{\odot}$ and luminosities of $7.2 \cdot 10^{-2}$ $L_{\odot}$ (Reid & Hawley 2005b). With a luminosity this low, even the closest M dwarf to our Sun, Proxima Centauri-M5.5V, is not visible to the human eye (Boyajian et al. 2012). Due to their low mass and long life, M dwarfs are the most common stars in the galaxy with 75% of stars within 10pc of the Sun being within this class (Henry et al. 2018). As stated in Section 1.2, their low mass and close-in habitable zone make these stars ideal targets for planet searches. Additionally lower mass stars tend to more commonly have planets (Gaidos et al. 2016). Unfortunately for any potential life on these planets, these stars are also prone to high energy flares and coronal mass ejections. We will go into more detail on this in Section 7.1.

1.4. Stellar structure

All main sequence stars, those that are converting hydrogen to helium in their cores, have three main structural elements. The core, the envelope and the atmosphere. The core comprises the interior 10% of the star and is the only region of the star that releases energy through nuclear fusion (Kippenhahn & Weigert 1990). When a star is burning, or fusing, Hydrogen into Helium in its core, called the main sequence (Hertzsprung 1909), two processes can be dominant, depending on the mass of the star. In low mass stars the proton-proton (pp) chain is dominant where initially two hydrogen atoms fuse and one of the protons becomes a neutron creating deuterium (Adelberger et al. 2011). Subsequently two deuterium atoms fuse creating Helium (Fig. 1.10). While the pp chain reaction rate is highly sensitive to temperature the other process, the CNO cycle, is even more so (Kippenhahn & Weigert 1990). In stars greater than roughly 1.5 times the mass of the Sun the core temperature approaches 15 million Kelvin and the CNO cycle becomes dominant over the pp chain (Dunlap 2021). The CNO cycle operates by using Carbon, Nitrogen and Oxygen as catalysts to facilitate fusing hydrogen into helium (Fig. 1.11) (Bethe 1939). The CNO cycle is a far more efficient energy generating process than the pp chain. The switch over between the two also changes the dominant energy transport mechanism of the core from radiative with the pp chain to convective with the CNO cycle (Bradt 2008). As the mass of a star increases to 1.5 $M_{\odot}$ the CNO cycle becomes dominant and the core becomes convective. This change is caused by a change in the temperature gradient (Bradt 2008). The convective envelope in low mass stars switches to being predominantly radiative in nature with an ever shrinking convective zone on the outer edge of the star (Fig. 1.12). This has an observational effect in that higher mass stars will have a much more rapid convective rate than low mass stars. Ultimately when a star is massive enough then the entire envelope becomes radiative (Kippenhahn & Weigert 1990).

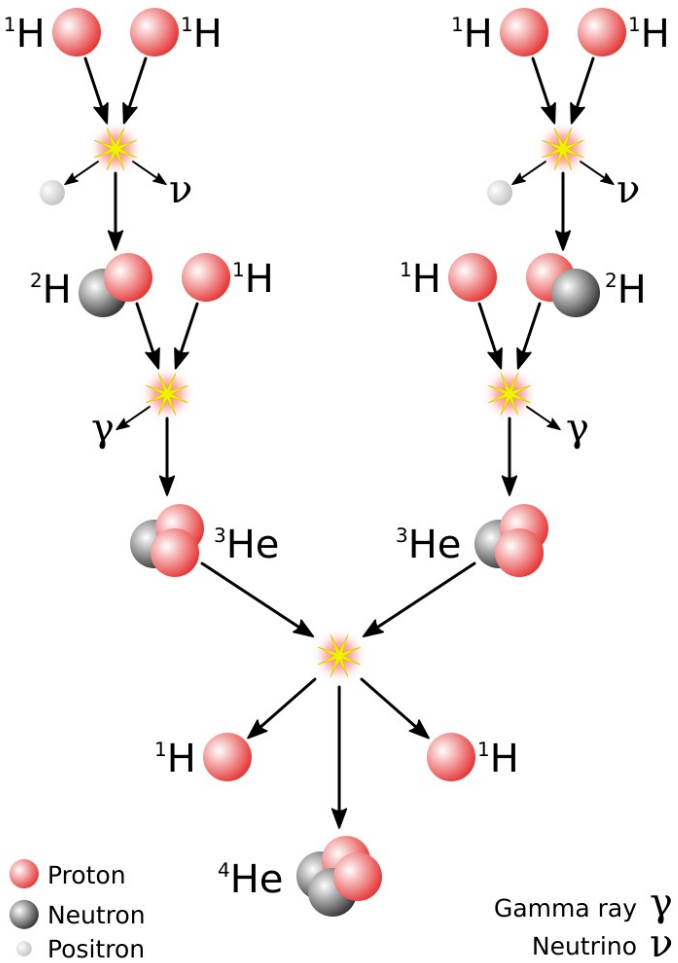

Figure 1.10.: Proton-Proton chain fusion reactions. Credit Sarang Public Domain via Wikimedia Commons

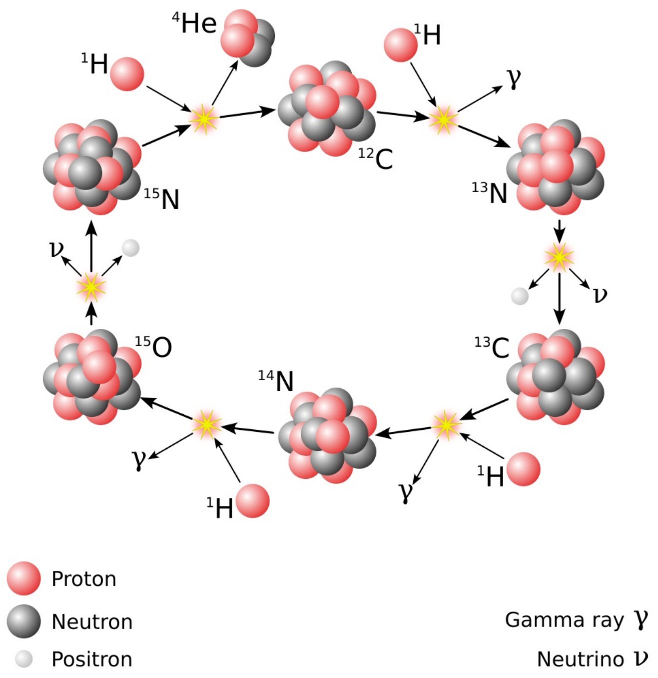

Figure 1.11.: Carbon-Nitrogen-Oxygen (CNO) hydrogen fusion catalyst process. Credit Sarang, Public Domain via Wikimedia Commons

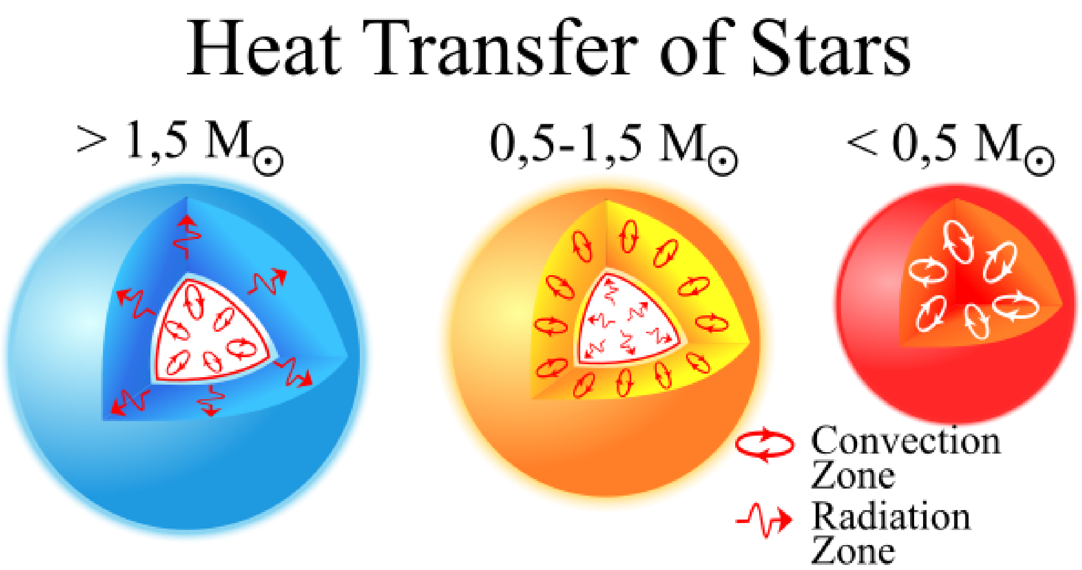

Figure 1.12.: Energy transfer in stars. High mass stars (blue) have a convective core and radiative envelope while low mass (yellow) stars have a radiative core and convective envelope. Very low mass stars (red) are fully convective. Credit Sun.org under CC-BY-SA 3.0

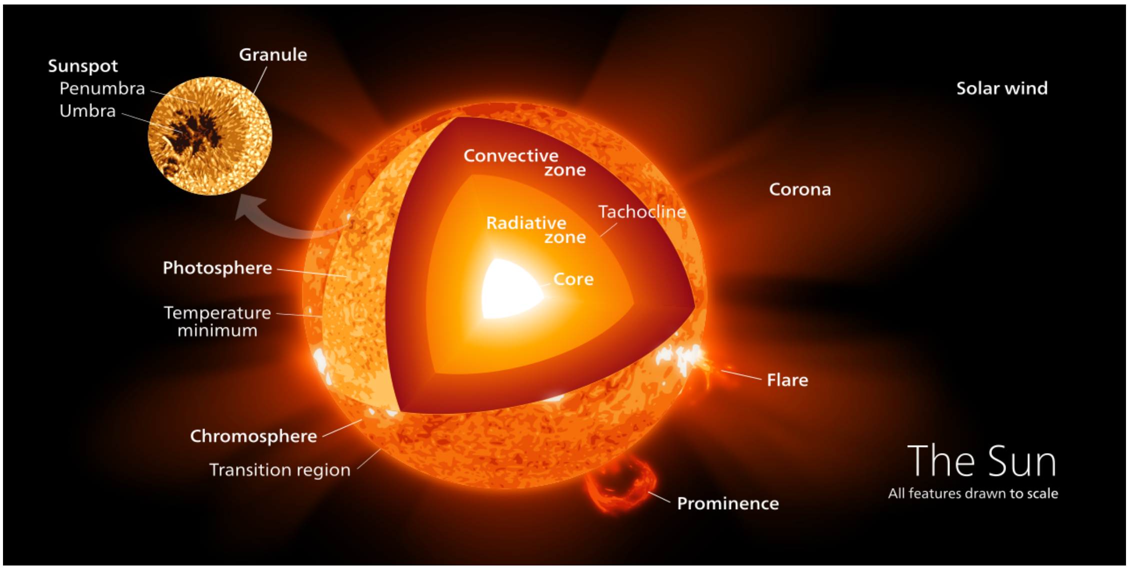

Figure 1.13.: Structural elements of the Sun and its atmosphere. Credit Kelvinsong under CC BY-SA 3.0 via Wikimedia Commons

1.4.1. Stellar atmospheres

The lowest part of the atmosphere, and the part that gives off the majority of the light is known as the photosphere (Fig. 1.13). This region, on the Sun, is roughly 400km thick and can appear as a visible surface of a star. This is due to the optical depth decreasing to the point where the majority of the photons emitted are lost to space (Carroll & Ostlie 2014). This is also the first layer that we can observe stellar activity having a visible effect in the form of sun or star spots. These are relatively cool, topologically lower regions in which the flow of plasma has been coupled to strong magnetic field lines. This disrupts the convective energy flow causing the area to cool and appear darker (Solanki 2003).The photosphere is the last layer of the star that can be approximated as being in LTE conditions. As altitude increases the density decreases and radiative transitions, rather than particle collisions, begin to dominate.

Above the photosphere, on stars of spectral type F or later, the atmosphere can be generalized to be comprised of three distinct layers; the chromosphere, the transition region and the corona. The chromosphere is the lowest and most dense of the three, and it takes its name from the red color in a solar eclipse as opposed to the white color of the outer regions and photosphere and was thusly named chromo or color in Greek (Jess et al. 2015). The structure of the chromosphere is best measured in height, temperature and pressure. As the height of the chromosphere increases the temperature reaches a minimum just above the photosphere before beginning to climb again reaching temperatures of upwards of 10,000K, simultaneously the density decreases (Mariska 1986). The chromosphere, while being less dense than the underlying photosphere, is still dense enough to produce enough photons to be visible against the photosphere (Jess et al. 2015). It is also, due to its low density nature, much more affected, and for longer duration, by energetic stellar activity phenomena than the photosphere. The chromosphere is also home to the opposite of the star spot, the chromospheric plage (Athay & Warwick 1961), or bright regions. These regions have a higher temperature than the surrounding chromosphere and frequently will have several lines such as Hα, He I D_3, Ca II IRT, Na I D_2 and others in emission (Böhm-Vitense 1992; Jess et al. 2015). The Solar chromosphere is divided between quiet and active (Vernazza et al. 1981; Rutten 2012) as they have different temperature pressure profiles, and line formation altitudes. The quiet regions of the photosphere and chromosphere are considered as part of the standard Sun by which the more variable active regions are compared. We will cover the stellar activity nature of the chromosphere in more depth in Section 1.5.2.

At the top of the chromosphere is the transition region which, as the name implies, is the transition between the relatively dense, cool chromosphere and the extremely hot low density corona. The temperature increases rapidly and the density decreases rapidly (Mariska 1992). This trend continues until reaching the corona where the temperatures exceed 1 million kelvin and the density is on the order of 10^{-12} less dense than the photosphere (Böhm-Vitense 1992; Benz et al. 1998; Shopov et al. 2008) . Due to these conditions the corona can be studied in the ultraviolet and x-ray regimes of the spectrum and involves the the emission of light from highly ionized atoms such as Fe X. Unlike the chromosphere, the corona extends for many millions of kilometers into space and is the origin of the most large scale manifestations of stellar activity such as flares, coronal mass ejections and loops (Livshits et al. 2011). We will cover these in greater detail in Section 7.1. The Corona is the origin point for the stellar wind. While chromospheres and coronae are known to exist on late type stars, B and O class stars have not been observed to have them, possibly due to the lack of an outer convection region (Simon et al. 2002).

1.4.2. Origin of stellar magnetic fields

That the upper levels of the solar atmosphere were considerably hotter than the photosphere left many perplexed as to the reason as this was an apparent violation of the 2nd law of thermodynamics (Leibacher & Stein 1982). It was therefore reasoned that some sort of heating mechanism was at play that transported energy into the upper atmosphere. The first suggestions of what this mechanism could be were put forth in the 1940s with the idea that acoustic waves (Biermann 1946; Schwarzschild 1948) or magnetohydrodynamic waves (Alfvén & Lindblad 1947) were the cause of the heating. Schrijver (1987) found that several lines exhibited basal chromospheric flux and attributed this basal flux to acoustic heating, arguing that as it was temperature dependent. Later, small scale magnetic reconnection (ie nanoflares) was considered (Parker 1988). Others suggested that the dissipation of magnetic fields could cause the phenomenon (Heyvaerts 1990). Judge & Carpenter (1998) claimed that this basal component was unlikely to be due to acoustical heating and suggested a basal magnetic component. Jefferies et al. (2006) attempted a combined explanation with a magneto-acoustic heating mechanism. Wedemeyer-Böhm et al. (2007) calculated that, for the solar chromosphere, acoustical heating, through convective overshooting, had sufficient energy to heat the chromosphere to observed temperatures. Despite the copious amount of effort the exact mechanism for the heating is not yet fully understood.

The origin of this field was a different issue altogether. It has been long observed that the faster a star rotates the more activity it tends to exhibit. This has been noted in a number of indicators- radio (Slee & Stewart 1989; McLean et al. 2012), Ca II HK (Astudillo-Defru et al. 2017; Boudreaux et al. 2022) and Hα (Newton et al. 2017) among others. The interpretation of this has been that the rotation of the star creates a dynamo out of the charged plasma in the interior of the star. Initially the generation of this dynamo was thought to originate from where the rigidly rotating core region transitioned into the differentially rotating envelope. The transition between these regions, called the tachocline, causes a large amount of shear and Parker (1955) proposed that this led to a cyclic process whereby a poloidal field would transition to a toroidal field over the course of a solar cycle and thereby create the effects that we observe in the upper solar atmosphere. The issue with this explanation is that late type M dwarfs, that are fully convective, do not have a tachocline yet are some of the most magnetically active main sequence stars known (Chabrier & Küker 2006). Some of these stars produce flares orders of magnitude larger than our Sun does (Osten et al. 2016). Additionally the later spectral types of M dwarfs are far more likely to be active as a percentage of population (West et al. 2004; Reiners et al. 2012; Jeffers et al. 2018). Due to M stars having these large scale magnetic fields yet not having a tachocline, it has been proposed that the tachocline was not required for a solar-type magnetic field (Spruit 2011). This idea was reinforced by close examination of the activity-rotation relation by Wright et al. (2018) who found that there was no evidence for any kind of disruption to the relation caused by a changeover of dynamo processes at the fully convective -radiative core boundary. Currently there is no consensus on the precise nature of magnetic field generation. The general consensus is that some sort of dynamo is at work that is tied to the rotation of the star and as a star ages and loses angular momentum, the magnetic field weakens.

1.5. Stellar Activity

Stars are far from the perfect celestial spheres the ancient Greeks and their medieval counterparts thought they were. While there had been observations in the many centuries before the renaissance that purported to refute this notion, it was not until the highly publicized discoveries of Galileo that it became well known that the Sun could be *blemished*. These blemishes, or spots, were the first sign that the Sun had other processes ongoing besides producing light and warmth for Earth. In 1843 it was observed that the numbers of these spots increase and decrease in an 11 year cycle (Schwabe 1844; Wolf 1852).

Shortly afterward, in 1859, the first evidence that the Sun could have more violent episodes came to light. Carrington reported to have seen a large flash on the sun whilst observing

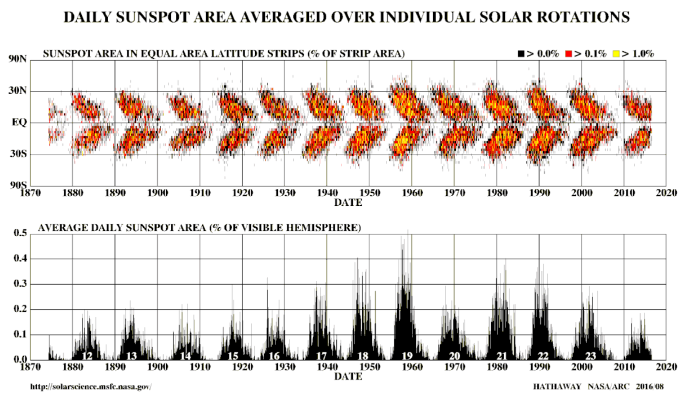

Figure 1.14.: Diagram showing the evolution of spot latitude over time. Known as the *butterfly diagram*. Credit NASA, Marshal Space Flight Center, Public Domain, via Wikimedia Commons

a sunspot cluster (Carrington 1859). A few days later there were aurorae down to low latitudes and telegraph operators reported being shocked by the electricity running through their telegraphs (Council 2008). This solar flare and subsequent coronal mass ejection had blasted an enormous quantity of charged particles into space, enhancing the already present flow of charged particles called the solar wind, and then impacting the Earth's geomagnetic field creating the aurorea and other electrical disruptions. If a similar event were to occur today it could be catastrophic to our much more technology dependent civilization (Council 2008). At the time of Carrington, however, the true scope of the event wasn't realized. It would take another half century until it was realized that the Sun had a magnetic field and the spots were significantly more magnetized than the rest of the photosphere for the study of solar, and later stellar activity to truly begin. In this section we will be covering the low altitude effects of solar and stellar activity on the Sun and M dwarf stars, namely the origin of the field, spots, plages, and chromospheric lines that are more affected by stellar activity than others, otherwise known as chromospheric activity indicators. In Section 7 we will cover the more energetic manifestations of activity in the form of flares, coronal mass ejections, prominences and loops.

1.5.1. Photospheric phenomena: spots and faculae

Sun or star spots are caused when lines of magnetic flux intersect the photosphere of a star. This causes the convecting plasma to be suppressed and thus the energy transport to be inhibited causing the area to cool so as to appear darker than the surrounding photosphere (Berdyugina 2005). The intensity of the magnetic field in these regions can be on the order of several thousand Gauss (Okamoto & Sakurai 2018). This is sufficient to cause Zeeman splitting of atomic lines in the region which was how the solar magnetic field was first discovered in the early 20th century (Hale 1908). The field intensity in these spots is thought to originate from the magnetic field lines of the star being twisted by the differential rotation of the star thereby creating magnetic flux tubes that intersect

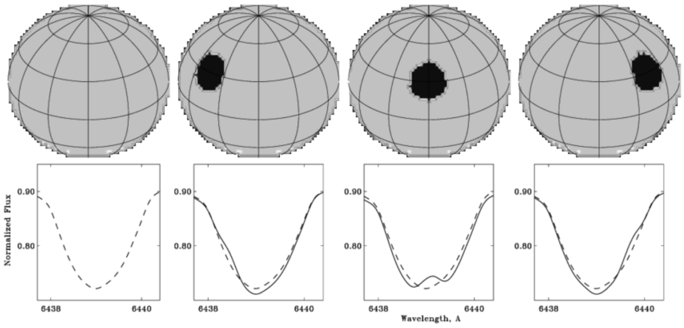

Figure 1.15.: Effect of spots on spectral lines. Credit:Berdyugina (2005), used under CC-BY 4.0

the photosphere of the star creating the spot (Parker 1955; Jouve, L. et al. 2020). These spots corotate with the rest of the star per the latitude in which they are found and can be used as a tracer of rotation. This phenomena was used to strongly suggest the presence of spots on other stars (Kron 1947; Chugainov 1966). This method is more effective on rapidly rotating stars as slower rotators run into the problem that the lifespan of the spot may be less than the rotational period of the star (Petrovay & van Driel-Gesztelyi 1997). Fast rotators, on the other hand, can suffer from line distortion issues related to their rapid rotation. When this distortion is not too great and magnetic effects on the line profiles can be observed, Doppler imaging can be done which gives an estimation of the distribution of spots on another star (Strassmeier et al. 1991; Shulyak et al. 2017). On M dwarfs, unlike the equatorial placement of spots on the Sun, the spots seem to congregate around the polar regions (Kuerster et al. 1994; Jeffers et al. 2002). Whether this is a general attribute of M dwarfs or not is still a matter of some debate. M dwarfs tend to have large toroidal and non axis symmetric polodial field components (Donati et al. 2008). On the Sun, the spots vary in location and quantity with the activity cycle. Early in the cycle they appear infrequently and near 30 degrees north or south latitude but as the cycle progresses they appear more frequently and approach the equator (Fig. 1.14). The magnetic polarity flips, the field essentially resetting itself, and the process starts anew (Weiss 1990). Searches for activity related brightness cycles on other stars have yielded mixed results with some stars showing solar-like cycles while others do not (Baliunas & Vaughan 1985; Oláh, K. et al. 2016; Fuhrmeister et al. 2023). The presence of spots, essentially a cooler area on the effective surface of the star can affect the shape of spectral lines (Fig. 1.15). This can make planet signals, for RV surveys, more difficult to detect.

Counter intuitively, the solar luminosity is the highest when the most spots are present (Willson & Hudson 1991). This is due to the spots being surrounded by faculae which are associated with smaller magnetic features than those that cause the spots (Walton et al. 2003). These features are near depressions that have been evacuated of material by magnetic pressure. This allows the material in the wall of the depression to radiate to space and as this material is deeper within the Sun than the rest of the photosphere it is hotter and thus brighter. This overrides the brightness lost by the dark spots in the magnetic flux tube itself (Spruit 1976; Berger et al. 2007; Socas-Navarro, H. & Asensio Ramos, A. 2021).

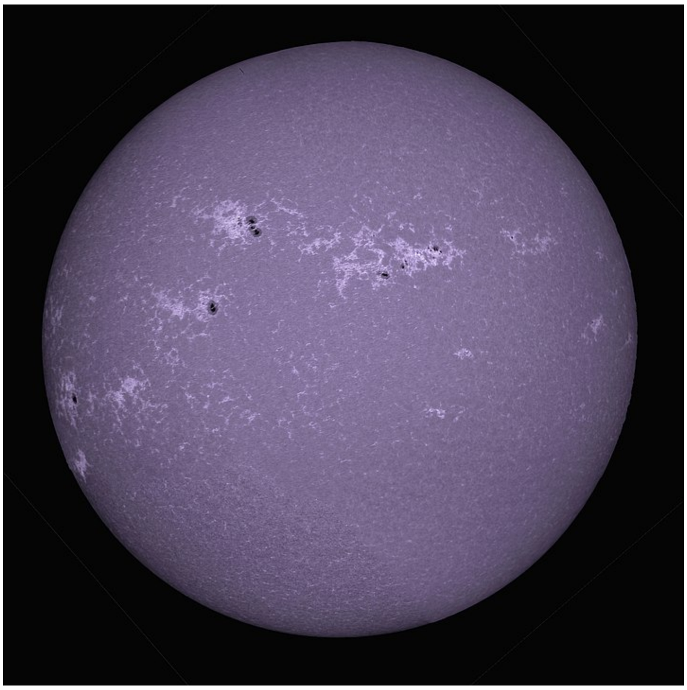

Figure 1.16.: Calcium K mosaic of the solar disk. Bright spots show location of plages. Credit John Purvis under CC BY 2.0 via Wikimedia Commons

On low-activity, Sun-like, stars the faculae are much more prevalent than the spots and dominate the luminosity cycle of the star. On more active stars the flux tubes remain large and create more spots leading to their domination of the stars luminosity variation (Radick et al. 1998).

1.5.2. Chromospheric Activity

Above the spots and their associated faculae networks are bright areas in the chromosphere called plages (Hall 2008). These regions exhibit emission of strong resonant lines (Fig. 1.16) and, together with their photospheric counterparts are called active regions. Some lines that are often observed in emission are Ca II HK (Young 1872),Hα (Joy 1947),Na I $D_{1\&2}$ (Díaz et al. 2007), and He I D_3 (Houdebine 2012), among others (Linsky 2017). The active regions co-rotate with their latitude and can be tracked around their star (Johnson et al. 2021). These regions are thought to have higher temperatures and densities than the surrounding chromosphere (Hintz et al. 2019). On the Sun the Ca II HK trace the 11 year cycle of solar activity (Wilson 1968) and this can be found on other stars as well (Robinson et al. 1989). Outside of these regions the chromosphere, on the Sun, is considered quiet, when the resonant lines are not in emission, but these areas can still have spicules—hot jets of plasma (Vernazza et al. 1981; Leenaarts et al. 2011; Rutten 2012). For the Sun Ca II HK (Wilson 1968) is the preferred activity indicator but or later type stars, such as M dwarfs, Hα (West et al. 2004) is generally the preferred as M dwarfs do not emit much flux in the blue region of the spectrum that Ca ɪɪ HK inhabits (Jeffers et al. 2018). Hα, in M dwarfs can appear in absorption or emission. It is thought that both of these states confer some level of chromospheric activity as the photospheres are too cool at those spectral types to form any Hα absorption features (Cram & Mullan 1979).

1.6. Chromospheric activity indicators

While many atomic species respond to stellar activity, the most noteworthy in the chromosphere and what we will focus on in this work, consist of hydrogen, calcium (singly ionized), sodium and to a lesser extent helium. While there are other atomic species and molecules that react to activity (Short & Doyle 1998; Linsky 2017; Schöfer et al. 2019) we will be focusing on these for this work. These atomic species can be excited to emit in one of three ways. The first way is for a recombination event to occur in which an electron recombines with an ion into an excited energy state and descends to the ground level by emitting photons. This is the pathway most preferred for lines that require a large amount of energy to activate. The second pathway is for a feeder line to absorb a photon and elevate an electron to a higher energy level. That electron can then de-excite by returning to a lower energy state by releasing a photon of the activity indicator line. The third way is for enough gas pressure to be present, at sufficient temperatures, to impart sufficient energy onto an electron through a collision. This collisional excitation is usually only for low activation lines as the gas in the chromosphere is usually not dense or hot enough to impart a large amount of ionization or excitation potential but can be for more high energy lines in specific circumstances. In the following sections any energy level and transition information are sourced from NIST[4] with specific authors indicated. The calcium line information is from Sugar et al. (1985).

1.6.1. Calcium

The Ca ɪɪ H and K lines [3969.59 Å, 3934.77 Å], henceforth Ca ɪɪ HK] (Reader et al. 1980), have been known to exist in the stellar spectra since the early 1800s, but was not until 1872 that they were first observed on the Sun in emission (Young 1872). In 1913 Ca ɪɪ HK emission cores were observed in other stars (Eberhard & Schwarzschild 1913). As solar observations of Ca ɪɪ HK progressed, it was observed that the variation in the emission strength of Ca ɪɪ HK was correlated to the number of sun spots and, thusly, to stellar activity (Livingston et al. 2007). It subsequently became the primary indicator of solar and stellar activity, so much so that Mt Wilson observatory created a special filter to measure it (Wilson 1968). The Ca ɪɪ HK lines are resonant lines of the singly ionized calcium atom. They occur as a result of a transition between the ground level (4S) and the 4P excited state. This transition has an Einstein coefficient of 1.47 ×

[4] https://www.nist.gov/pml/atomic-spectra-database

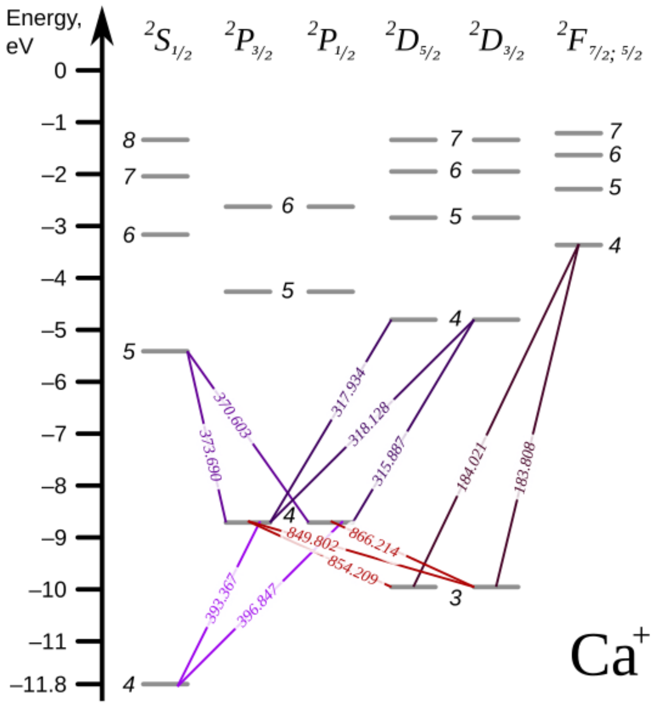

Figure 1.17.: Grotrian diagram of the Ca II ion. Shows absorption of the Ca II IRT line (3) leads to population of the Ca II HK excited levels. Credit Esmu Igors under CC BY-SA 4.0 via Wikimedia Commons.

$10^8\ s^{-1}$ (Haynes 2016) and requires 3.15 eV of energy. Coupled with the ionization of the neutral calcium atom requiring 6.11 eV it ultimately takes 9.26 eV to activate the Ca II HK lines. At 11.87eV the calcium atom is ionized to the second ionization stage. The Ca II HK lines shares their excited 4P state with another set of lines (Fig. 1.17), the Calcium Infrared Triplet (Ca II IRT 8500.36, 8544.44, 8664.52 Å). These result from a transition of the 4P excited state to the 3D level. This requires 2.45 eV and has an Einstein coefficient of $10^7\ s^{-1}$ (Haynes 2016) which is an order of magnitude less than the Ca II HK transition. The 3D level is also a metastable level in that the transition is unlikely to occur in environments where the timescale of an interaction with another particle is less than the timescale of the transition (Mallik 1997). It requires 1.7 eV to collisionally excite an electron from the Ca II ground state to the lower Ca II IRT energy level. Thus it requires 7.81 eV to see Ca II IRT in absorption. The Ca II IRT line can be seen in emission and has been studied as a proxy of the Ca II HK line for use as an activity indicator (Shine & Linsky 1972; Linsky et al. 1979). Schrijver (1987) determined that Ca II HK flux that included emission could be considered as part of a basal flux that seemed to be independent of stellar activity. They used information, along with similar results from other lines, to advocate for an acoustic basal heating model of a chromosphere.

1.6.2. Hydrogen

Hα or the first line in the Balmer series, occurs at a wavelength of 6564.63 Å (Kramida 2010), and results from the transition from the n=3 orbital to the n=2 orbital. This transition has an Einstein coefficient of $5\times10^7\ s^{-1}$ (Jitrik & Bunge 2004) and requires 1.89 eV. The n=3 excited state of this transition occurs at 12.09 eV and is not far from the ionization energy of hydrogen at 13.6 eV Kramida (2010). While Ca II HK has been the defacto standard for quantifying stellar activity on solar-like stars, for M dwarfs it suffers from the problem that, due to the low effective temperature, there is not much continuum flux at the Ca II HK wavelengths (Stauffer & Hartmann 1986; Hall 2008). This makes quantifying the Ca II HK lines either imprecise or expensive in exposure time. In lieu of Ca II HK, Hα was the obvious replacement as it had been observed in emission since 1947, so much so that these stars were given their own classification of *dMe* (Joy 1947). While all hydrogen lines respond to stellar activity, such as the Lyman series and Paschen series, the Lyman series suffered from even more of a continuum loss than Ca II HK. The Paschen series had the opposite problem, in that it was in the near infrared and out of most spectrograph wavelength coverage. Additionally the Paschen series also suffered from molecular line and telluric contamination. Hα has several advantages in M dwarfs over Ca II HK in that the continuum is much stronger and that there is no photospheric absorption of Hα due to the low effective temperature. Hα is also in the visual band making it easy to observe from ground based instruments. This allows Hα to be used as meter of chromospheric activity without having to subtract the photospheric component.

Hα appears in both absorption and emission in M dwarfs. The emission profiles were

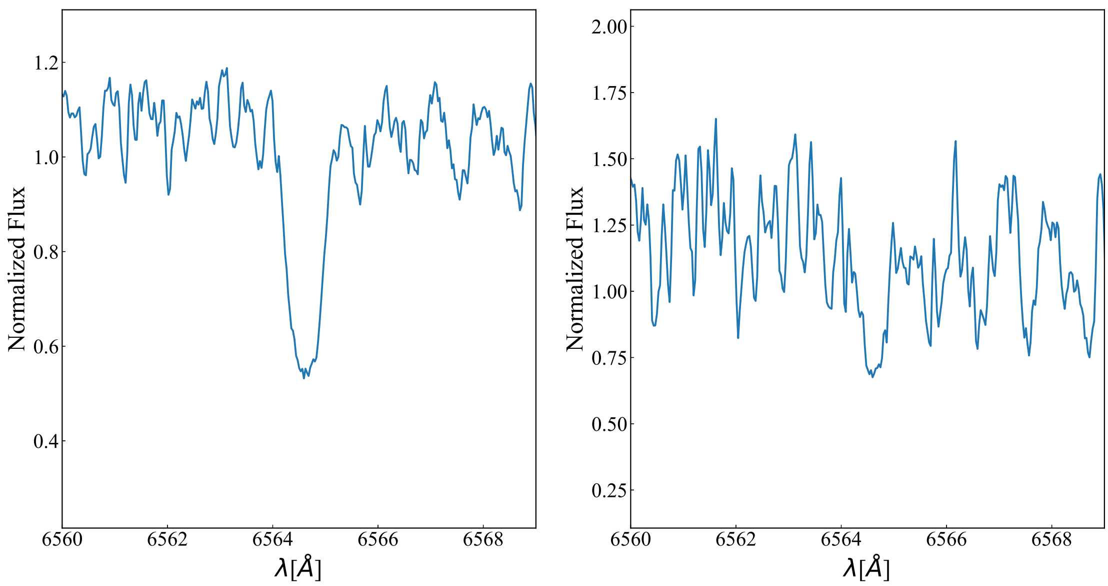

Figure 1.18.: Hα absorption profiles. Left: early type absorption profile from star J00051+457. Characterized by Hα absorption dominant over the molecular continuum. Right: Late type Hα absorption profile from star J00162+198E. Characterized by Hα absorption equivalent in magnitude to the molecular continuum.

determined to be due to stellar activity (Young et al. 1989) but when the Hα absorptive profiles were correlated with Ca II HK in emission it was the conclusion of Joy (1947) that these Hα absorptive stars were also manifestations of stellar activity. This was reinforced when Cram & Mullan (1979) simulated M star chromospheres by incrementally heating the chromosphere and observed that Hα would first go into absorption, then fill in and become emissive. More recently, Hintz et al. (2019) was able to fit active M dwarf profiles by assuming a two component model of a quiet and active chromosphere and combining them through use of a filling factor to simulate the disc integrated nature of our observations of M dwarfs.

The Hα profile, in the CARMENES sample, occurs in one of three categories. The first are absorptive profiles (Fig. 1.18) in which a prominent absorption profile can be seen. The next set are the classical emission profiles (Fig. 1.19) that led Joy (1947) to the classification of *dMe*. These emission frequently feature a central reversal centered about the line core. This central reversal can shift slightly about the center line creating asymmetric profiles (Fig. 1.20) (Fuhrmeister et al. 2018). The last category are intermediate profiles (Fig. 1.21) which exhibit wing emission and an absorption element that is still prominent but does not reach the same depth of core flux that a fully absorptive star of the same spectral type would.

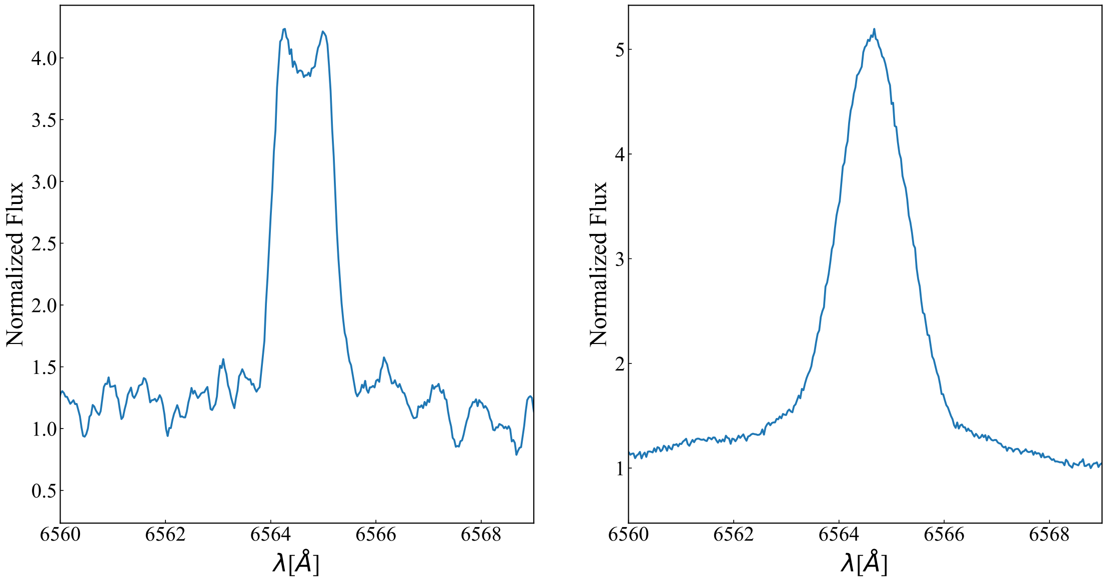

Figure 1.19.: Hα emission profiles. Left: Classic M dwarf Hα, emission profile featuring a relatively narrow emission profile from star J00162+198W. In the center a small absorptive central reversal is frequently present, especially on earlier type stars. Right: Emission profile of the very active, rapidly rotating star J12156+526. Characterized by a triangular shaped profile and the smoothing out of surrounding molecular features.

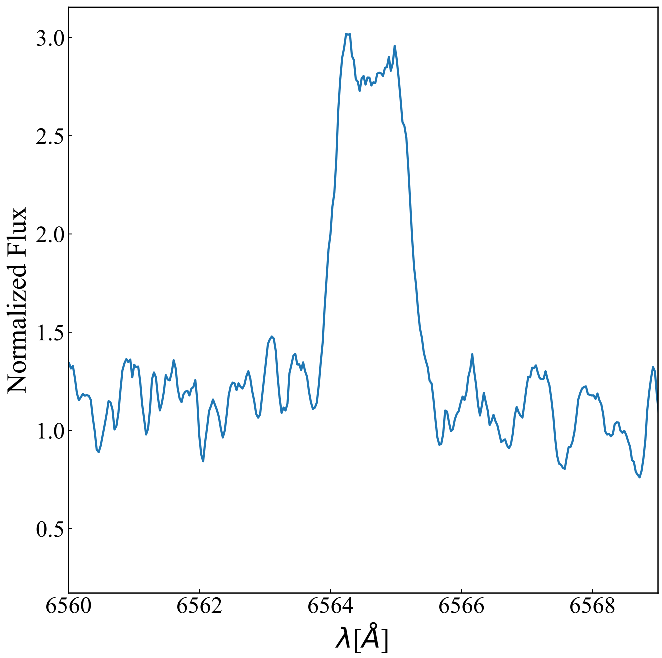

Figure 1.20.: Asymmetric Hα profile from star J05366+112. The red side of the profile is encountering more absorption than the blue side.

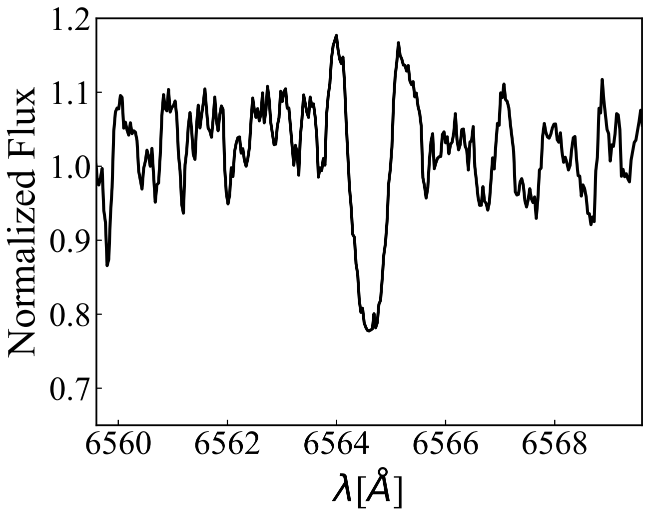

Figure 1.21.: Intermediate Hα profile from J11026+219. Characterized by enhanced emission in the wings while remaining absorptive in the core.

1.6.3. Sodium

The Na I $D_{1\&2}$ lines (5891.58, 5987.56 Å) have the least activation energy (2.1 eV) of any potential activity indicators (Juncar et al. 1981). They result from a resonant transition between the 3P excited state and the ground state of the neutral sodium atom. The transition strength is $6.15 \times 10^7 s^{-1}$ (Volz et al. 1996) The ionization energy of sodium is 6.14 eV (Juncar et al. 1981).

The sodium D lines have been studied as a potential activity indicator for the last couple of decades as it has been noted that stars with Hα in emission have sodium lines in emission as well (Giampapa et al. 1978). Houdebine et al. (2009) found that He I D_3 in emssion is associated with D line in emission. It was also found that the two lines of the doublet are well correlated with each other. Houdebine et al. (2009) also found that the line shapes change from one star to another without a determinable cause but did leave open the possibility of using the line as a chromospheric diagnostic. Díaz et al. (2007) found that Na I $D_{1\&2}$ only correlates with HK when Hα is in emission but not for stars in general. It was also discussed that the TiO band the line sits in and the large photospheric wings make accurate evaluation difficult.

1.6.4. Helium

Although nearby to sodium in wavelength space (5877.25 Å) and thus transition energy (2.11 eV, He I D_3 is quite different in nature (Martin 1973). Unlike sodium, it is the activity indicator with the highest activation energy of 20.96 eV to population the lower level and 23.07 eV, total (Martin 1973). This places it quite close to ionization energy of helium

(24.59 eV) and results from a transition between the 3D and 2P levels (Martin 1973). The transition probability is $4.2 \times 10^7 s^{-1}$ (Drake 2006). He I D_3 has been closely correlated with solar plages (Landman 1981) and is lacking in the quiet solar chromosphere. This is due to the energy required to populate the lower level is simply unavailable in these regions (Saar et al. 1997). Additionally it is not observed in absorption, in late type stars, and this indicates that non-activity related processes either do not contribute to the line or do so in a very minimal amount. Saar et al. (1997) described it as a pure activity indicator. Schöfer et al. (2019) found that helium in emission correlates well when Hα is also in emission.

Formation mechanisms for He I D_3 are still debated with the primary contestants being recombination (Hirayama 1971; Zirin 1957, 1975) , excitation or a combination thereof (Milkey et al. 1973). More recent simulations suggest it to be collisionally dominated in the upper chromosphere with a formation temperature of between 8 and 40 thousand Kelvin (Saar et al. 1997).

2. Observations and data reduction

2.1. Observations

All spectra of this work were obtained using the CARMENES[1] spectrograph. CARMENES is a fiber-fed instrument mounted on the 3.5m telescope at Calar Alto. This instrument features highly stabilized visual (VIS) and near-infrared (NIR) channels which are simultaneously operated (Quirrenbach et al. 2016). The VIS channel, which we employ for our project, has a wavelength range of 440nm (520nm - 960nm) with a spectral resolution of 94,600. The NIR channel has a range of 750nm (960nm - 1710nm) with a resolution of 80,400.

Starting 1 January, 2016 the CARMENES spectrograph is primarily employed in a search for exoearths around M dwarfs. We used data collected up until 6 September, 2021 as this was the time at which concerted effort on this thesis began. During this time frame this survey produced 14,156 spectra of 345 M dwarfs. These M dwarfs are apart of the CARMENES GTO sample and comprise the brightest stars of their respective spectral subtype within 10 pc, that were above a declination of -23°. This was the minimum declination that could be observed from the Calar Alto site and still produce scientifically valuable results (Alonso-Floriano et al. 2015; Ribas et al. 2023). While the majority of these stars are of earlier type than M5.0V, there remain some that were observed up to M9.0V. Due to this large range in spectral type and distance this entailed a large variation in apparent magnitude which affects the exposure time. Due to the requirements of the survey, however, the maximum time for any observation was limited to 30 minutes.

2.2. Data selection and reduction

Of the 14,156 spectra we had available, 13,541 were of usable quality. The majority of the rejected spectra were due to various issues with the observation and flagged in the FITS header. The remainder failed to meet the minimum S/N (Signal to Noise) threshold in the Hα order (order 93) of 7 for stars earlier than M5.0V and 1 for those M5.0V and later. We chose this dichotomy as, due to a combination of decreasing flux in the Hα order and

[1]Calar Alto high-Resolution search for M dwarfs with Exoearths with Near-infrared and optical Échelle Spectrographs.

the exposure limit, there were very few high S/N spectra for the latest spectral types. If a value was unable to be calculated then a 'nan' would be produced in its stead.

For each order in each observation we selected the middle 80% of the wavelength range and normalized the order by the median of that 80%. We did this as to minimize the effects of the larger errors at the fringes of the orders on the normalization procedure. Therefore our normalization value is based only on the middle 80% of a given order. We then compared the observed spectrum to an already barycentric corrected template spectrum of the same star to compensate for barycentric motion. This was done via generating a cross correlation function, fitting a Gaussian to the range about the maximum in the cross correlation function using the CURVE_FIT function and using the output to shift the observed spectrum. This process results in orders that comprised of normalized, barycentric corrected data in vacuum wavelengths.

2.3. PHOENIX and MARCS model spectra

In this work we use PHOENIX (Husser et al. 2013) and MARCS model spectra as a control for determining the principal effects on the spectra we are testing. The PHOENIX models were obtained from the PHOENIX webpage[2]. For the MARCS models, Denis Shulyak modified the base model specifically for this project. He used the MagneSyn code as he described in Shulyak et al. (2017) using solar abundance model atmosphere inputs from the MARCS model grid[3](Gustafsson et al. 2008). The spectra around Hα was calculated covering spectral types M0.0V (T=3850K) to M8.0V (T=2500K). $\log g$ was determined using calibrations from Kenyon & Hartmann (1995) and Golimowski et al. (2004). As TiO molecular lines are ubiquitous in the wavelength space around the Hα and since these lines increase in absorption with decreasing temperature he used three different line lists (Schwenke 1998; Plez 2012a,b) to simulate the effect of TiO on the region around Hα. The line lists were extracted from the Vienna Atomic Line Database v.3 (VALD3[4] Ryabchikova et al. 2015).

In order to obtain the best possible comparison, we split the model spectra into wavelength ranges equal to that of the orders in the CARMENES spectra and proceeded to normalize them in the same procedure as described in Section 2.2. For both sets of model spectra we assumed solar metallicity. We assumed solar metallicity as the majority of low activity stars are clustered about this value. We will discuss this in detail in Section 3.7.3. The T and $\log g$ values for the spectra are given in Table 2.1.

[2] https://phoenix.astro.physik.uni-goettingen.de/
[3] https://marcs.astro.uu.se/
[4] http://vald.astro.uu.se/~vald/php/vald.php

Table 2.1.: Model parameters.

	MARCS		PHOENIX	
SpT	$T[K]$	$\log g$	$T[K]$	$\log g$
M0.0V	3850	4.68	3900	4.5
M0.5V	3788	4.69	3800	4.5
M1.0V	3720	4.71	3700	4.5
M1.5V	3648	4.74	3600	4.5
M2.0V	3580	4.78	3600	5.0
M2.5V	3522	4.83	3500	5.0
M3.0V	3470	4.88	3500	5.0
M3.5V	3421	4.92	3400	5.0
M4.0V	3370	4.97	3400	5.0
M4.5V	3327	5.03	3300	5.0
M5.0V	3240	5.10	3200	5.0
M5.5V	3047	5.17	3000	5.0
M6.0V	2846	5.23	2800	5.0
M6.5V	2717	5.26	2700	5.0
M7.0V	2621	5.29	2600	5.0

2.4. Reference stars

Due to the number of stars and spectra available in the CARMENES archive, we found it useful, for data visualization purposes, to use a set of reference stars. Initially we will utilize the reference star list from Schöfer et al. (2019) who used an earlier version of this data set. They determined their list of reference stars by using the longest rotation period per spectral subtype as it is assumed these would be the least active stars in that spectral subtype. We will discuss the merits of this approach and introduce our own method of determining a representative star for a spectral subtype in Section 5.1. For our initial analysis, and in communication with the authors of the paper, we will utilize the most up to date version of the reference star list from Schöfer et al. (2019) given in Table 2.2. The spectral types for stars denoted with a '*' are sourced from Alonso-Floriano et al. (2015). All others sourced from Hawley et al. (1996).

Table 2.2.: List of initial reference stars by spectral type.

GJ	SpT	Karmn
548A	M0.0V	J14257+236W
740	M0.5V	J18580+059
701	M1.0V	J18051–030
625	M1.5V*	J16254+543
226	M2.0V	J06103+821
357	M2.5V	J09360–216
581	M3.0V	J15194–077
699	M3.5V*	J17578+046
447	M4.0V	J11477+008
1235	M4.5V	J19216+208
1057	M5.0V	J03133+047
1002	M5.5V	J00067–075
283	M6.0V	J07403–174

3. Methods

In this section we will introduce some of the methods of determining stellar activity in M dwarfs. We will focus only on Hα in this section. All plotted data is the median of the indicator unless otherwise specified. These methods being the index (Section 3.1), Gaussian fitting (Section 3.2), pseudo Full Width Half Maximum (pFWHM, Section 3.3) and the variability (Section 3.4) we will then select an initial sample of minimal activity stars (Section 3.5). We will discuss these methods' strengths and weaknesses (Sections 3.6 & 3.6.1) as well as any observational inconsistencies. Subsequently we will lay out requirements for an improved methodology that we will introduce in Section 3.7. Lastly we will introduce our improved index (Section 3.7), the Molecular Normalized Index (MNI) and discuss how this new process addresses the shortfalls of the other methods.

During the course of this and the following chapters, we will be discussing the relative activity level of M dwarfs. We will describe three samples within the CARMENES GTO set. The first and easiest to define is the E, or emission sample. This sample comprises M dwarfs that exhibit Hα in emission. The I sample, or initial sample, comprises our first guess as to a set of M dwarfs that exhibit minimal Hα activity. The N, new, sample reflects a refined minimal activity set of M dwarfs that we will argue represent a quiet sample.

3.1. Index

The Kürster index, I_k, (Kürster et al. 2003) and the equivalent width (EW, Williams et al. 1962) have long been used to determine the strengths of spectral lines in astrophysics and are functionally interchangeable (Zechmeister 2010). The Kürster index is given by

$$I_{\mathrm{T}} = \frac{\overline{F}_{\mathrm{T}}}{\frac{1}{2}(\overline{F}_{\mathrm{R}_1} + \overline{F}_{\mathrm{R}_2})} \tag{3.1}$$

where I refers to the index and F refers to the flux in a particular region with the overline indicating a mean flux value. The regions are designated T for the target region (in this chapter this is the Hα region but will still refer to it in the general sense as the equations will be used for other lines) with R_1 and R_2 being the reference regions. The wavelength ranges for these regions are given by Table A.1. We will keep to this notation for the rest of this work.

The Kürster index was never intended to compare late type M dwarfs against one another, as there was a concern that the influence of the molecular bands in the atmosphere of these stars would influence the measurement of the target line (Kürster et al. 2003; Rajpurohit et al. 2018). Nominally, both the index and equivalent width were originally meant for use on early type stars that had recognizable, flat continua. M dwarfs, as can be seen in Figure 3.1, can not be characterized as such. The consequence of this non ideal continuum is that the index and equivalent widths cannot be directly compared between two different M dwarfs, especially of different spectral sub-types. This problem is so pronounced that those using the equivalent width measurement method on M dwarfs will denote it as the *pseudo* Equivalent Width (pEW, Schöfer et al. 2019). Fundamentally, the measurement regions are no longer representing the continuum but rather the continuum plus the absorption from the molecular lines. These molecular lines are influenced not just by the effective temperature of the star but also by metallicity. Metallicity varies from star to star and is notoriously difficult to evaluate for M dwarfs (Passegger et al. 2022). Despite these issues, these methods are the most commonly used and thus we will use the index measurement method as our starting point in this work.

To compensate for the molecular line influence we replaced the average fluxes of the reference regions with the 90$^{\text{th}}$ percentile of the flux within those reference regions. This 90$^{\text{th}}$ percentile of the flux is often used in the study of M dwarfs as a proxy for the continuum level of the star (Schöfer et al. 2019). The intent is to be able to compare the flux of Hα to the assumed continuum level of the star in order to have a better basis of comparison between stars. The usage of this percentile is more robust than using the highest flux lines as a continuum assumption and is also more robust, in general, than using means or weighted means (Feigelson & Babu 2012). This 90$^{\text{th}}$ percentile index will be the basis of comparison for the rest of this work and, in the interest of brevity, will refer to it as the index.

The formula for this index is given by

$$\widetilde{I}_{\mathrm{T}} = \frac{\overline{F}_{\mathrm{T}}}{\frac{1}{2}(\widetilde{F}_{\mathrm{R}_1} + \widetilde{F}_{\mathrm{R}_2})} \, . \tag{3.2}$$

$\widetilde{I}_{\mathrm{T}}$ refers to the index of the target line, T. $\overline{F}_{\mathrm{T}}$ refers to the average flux of the target region. For this chapter $T = \mathrm{H}\alpha$. $\widetilde{F}_{\mathrm{R}_1}$ and $\widetilde{F}_{\mathrm{R}_2}$ refers to the 90$^{\text{th}}$ percentile flux values of the regions R_1 and R_2, respectively. The wavelength ranges for these regions are given in Table A.1. The error of the index ($\sigma_{\widetilde{I}_{\mathrm{T}}}$) is given by error propagation.

$$\sigma_{\widetilde{I}_{\mathrm{T}}} = \widetilde{I}_{\mathrm{T}} \times \sqrt{\left(\frac{\delta\overline{F}_{\mathrm{T}}}{\overline{F}_{\mathrm{T}}}\right)^2 + \left(\frac{\delta\widetilde{F}_{\mathrm{R}_1}}{\widetilde{F}_{\mathrm{R}_1} + \widetilde{F}_{\mathrm{R}_2}}\right)^2 + \left(\frac{\delta\widetilde{F}_{\mathrm{R}_2}}{\widetilde{F}_{\mathrm{R}_2} + \widetilde{F}_{\mathrm{R}_1}}\right)^2} \, , \tag{3.3}$$

where the uncertainties (δ) in the values described above are combined to estimate the error. This methodology was adapted from Johnson et al. (2021). Index values greater than 1 indicate emission, a non detection or neutrality at 1 and absorption in values greater

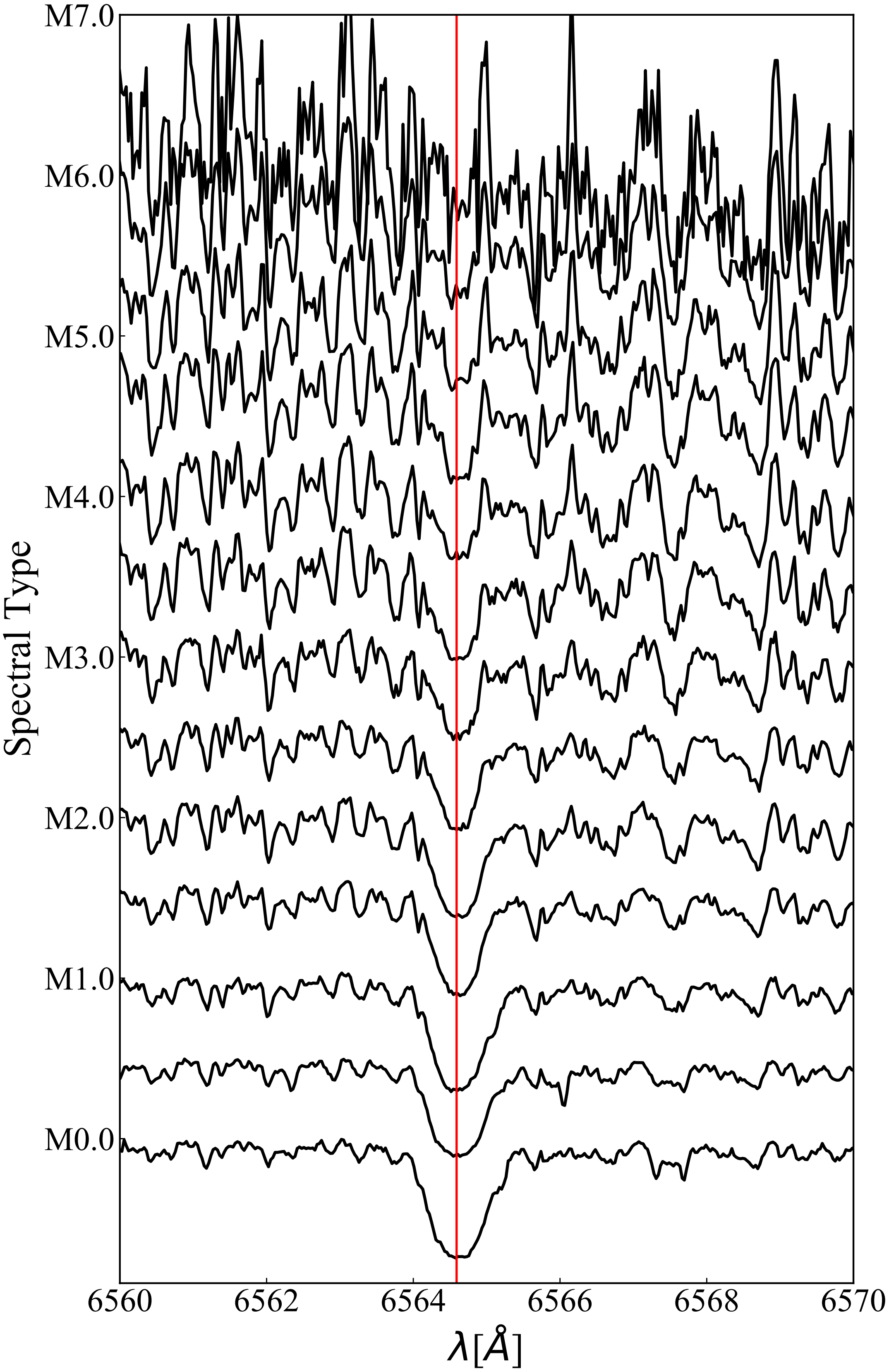

Figure 3.1.: Progression of CARMENES reference M dwarf Hα spectra from M0.0V at the bottom to M6.0V at the top.

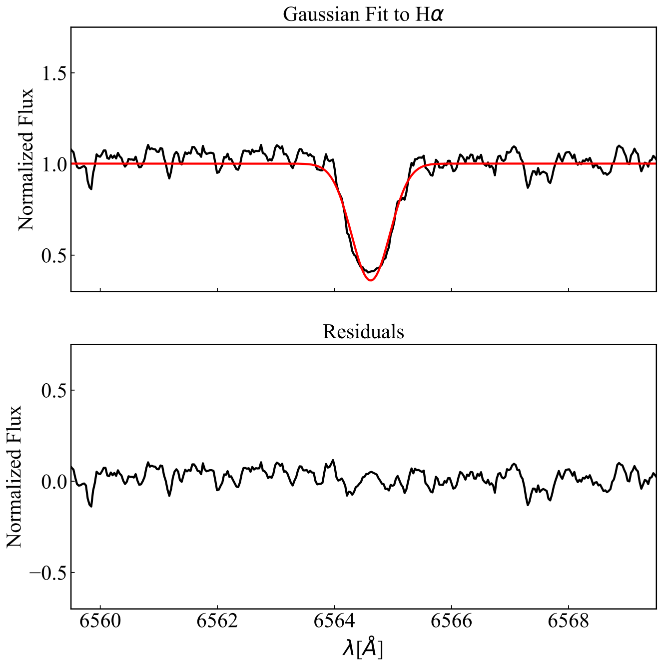

Figure 3.2.: Fitting a Gaussian to the profile of M0.0V star J14257+236W. Top: Overlay of the Gaussian fit on the original spectrum. Bottom: residual spectrum after removing the Hα Gaussian fit.

than 0 but less than 1. The equivalent width, meanwhile, measures emission in negative values, neutrality at 0 and absorption in positive values.

3.2. Gaussian fitting

One method to separate the target line from the molecule contaminated spectrum is to fit a Gaussian profile to the line and then measure either the amplitude of the fitted Gaussian or measure the index ($\widetilde{I_T}$) of the Gaussian profile. We opted for calculating the index ($\widetilde{I_T}$) of the Gaussian profile so that this index and the others calculated in this work, such as the index calculated directly from the spectrum, could be more directly compared.

In order to fit the Gaussian we used CURVE_FIT and CHISQUARE functions, to test goodness of fit, from the python SCIPY library, we constrained the center of the fit Gaussian to be within ± 0.1 Å of the line center to prevent the function from fitting any of the molecular lines in the vicinity of the target line. For early type stars this process fits the line well with only a relatively slight over-estimation of the absorptive flux (Fig. 3.2). Conversely, for stars later than M4.5V the combination of the increase in the molecular contamination and the increasingly non-Gaussian shape of the lines led to an overestimation of the absorption in absorption dominated profiles (Fig. 3.3). Due to the difficulty in getting Gaussian profiles to fit late type Hα features, we opted to use the Gaussian fits only on the reference stars.

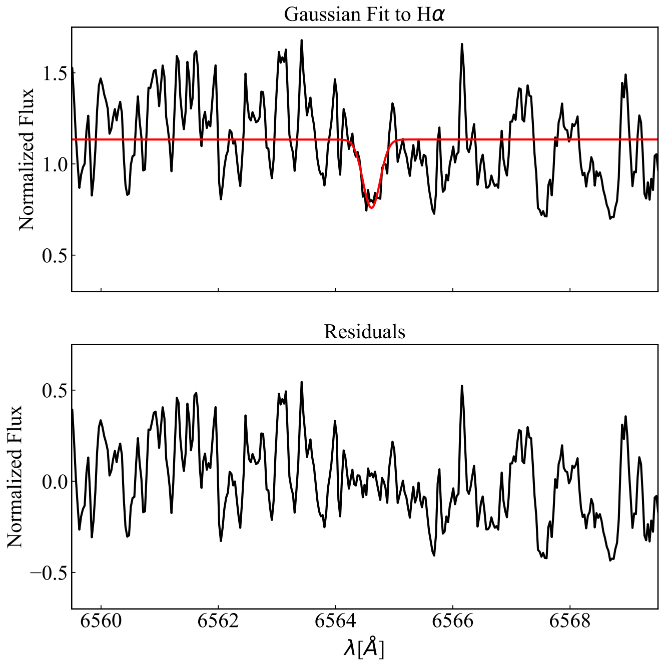

Figure 3.3.: Fitting a Gaussian to the profile of M5.0V star J03133+047. Top: Overlay of the Gaussian fit on the original spectrum. Bottom: residual spectrum after removing the Hα Gaussian fit.

For calculating the FWHM (Full Width at Half Maximum) of all spectra we had to employ a different method.

3.3. pFWHM

The FWHM of a line can be obtained by fitting a Gaussian profile to that absorption line. However, as described in Section 3.2, fitting a Gaussian profile to the lines in M dwarfs can get increasingly problematic with decreasing stellar effective temperature. In lieu of this method we chose to programmatically determine an effective FWHM value. We did this by finding the line maximum or minimum value, depending on whether the line core (λ = 6564.5Å) was in absorption or emission, then finding the point at which the line was no longer distinguishable from the molecular continuum. We will refer to the flux at λ = 6564.5Å as the Hα Line Core Flux (LCF). This point is determined by an inflection point, where the line profile, in this case Hα, inverts due to the presence of a nearby molecular line. If the line profile passes through the normalization value, as in Fig. 3.3, then 1.0 is chosen as the inflection point value for that side. This, however, incurs an uncertainty cost which is reflected in the assigned error for this value. We do this for both sides of the line profile and the distance between the maximum or minimum value and the continuum is then averaged. This gives an average value for where the line becomes indistinguishable from the continuum.

As an example, in Fig. 3.3, the left side of the line profile gives a value of 1.1 where the right side defaults to 1.0 with a higher uncertainty. This averages to 1.05 and is used along with the line core flux to determine the depth of the line. The half maximum is then calculated as the midpoint between these values.

We then find the points at which the line profile intersects the half maximum value ($\lambda_{\rm r}$,$\lambda_{\rm b}$; where r and b refer to the red and blue portions of the line profile) and measure the width. The equation for the pseudoFWHM is given by

$$pFWHM = (\lambda_{\rm r} - \lambda_{\rm b}) \tag{3.4}$$

and the associated error estimate is given by

$$\sigma_{pFWHM} = \sqrt{(\delta\lambda_{\rm b})^2 + (\delta\lambda_{\rm r})^2}. \tag{3.5}$$

Our goal for the pFWHM measurement, combined with the line core flux (λ = 6564.5Å), which we will describe in Section 3.6, is to measure how line profiles change shape over the spectral range M0V to M6V. This was particularly useful for lines that consist of two components, such as the Ca II IRT lines, with one component originating in the photosphere and the other in the chromosphere. We will elaborate on this further in Sections 4.2 and 5.3.

Like the Gaussian-fit method, described in Section 3.2, the pFWHM method had issues in measuring complex line profiles as the one shown in Figure 1.21. The problem with these composite profiles is that the program can treat it as a broad, low-emission feature or a narrow absorption feature. For these profiles we set the criterion to be that if the line core flux was above 1.0 we treat the line as a emission feature and if the line core flux was below 1.0 we would treat it as an absorption feature with the wings of the profile being the inflection point. This criterion can create a break in values of the Hα profiles centered around the 1.0 core flux value.

3.4. Variability as an indicator of activity

The variability of a chromospheric activity line is a natural method of determining the activity level of a star, as a perfectly quiescent star would have no variability. We define the variability, V, of a line as the spread between the 10$^{\rm th}$ percentile (P_{10}) of all observations of the indicator for that star from the 90$^{\rm th}$ percentile (P_{90}) value.

$$V = P_{90} - P_{10}. \tag{3.6}$$

This is similar to the method used in Schöfer et al. (2019).

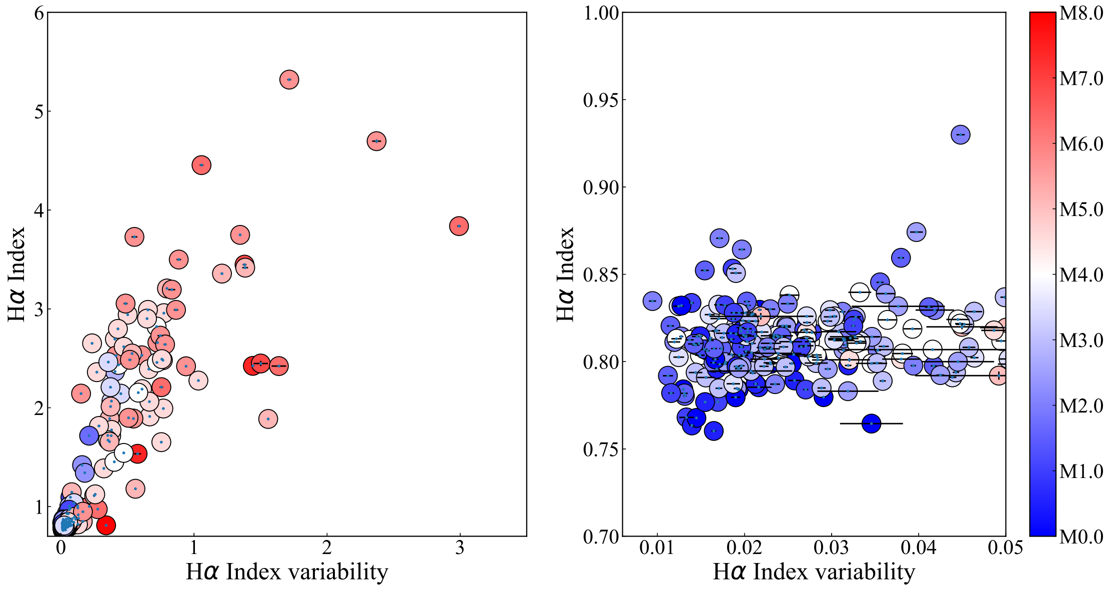

Figure 3.4.: Hα index ($\widetilde{I_T}$) vs the Hα index variability. Left: full CARMENES sample displaying a general trend of more activity leading to more variability. Right: zoomed in view of the lowest activity stars in which the aforementioned trend is no longer evident.

For the more active stars there is a direct correlation between the index ($\widetilde{I_T}$) and the variability of a star (Fig. 3.4). For the least active stars, however, this correlation no longer exists. We will discuss this dichotomy further in Section 3.7.2. The error formulation for this measurement is calculated by,

$$\sigma_V = \frac{3}{\sqrt{N}} \sqrt{\left(\frac{\delta P_{90}}{P_{90}}\right)^2 + \left(\frac{\delta P_{10}}{P_{10}}\right)^2}, \tag{3.7}$$

where the errors of the 90$^{\text{th}}$ and 10$^{\text{th}}$ percentile values are added in quadrature and divided by the root of the number (N) of observations of that star. The uncertainties (δ) are determined by the error calculation of whatever indicator is being used. In Fig. 3.4, the indicator is the index ($\widetilde{I_T}$) and its error is given by Eq. 3.3. The formulation of the error of a percentile was adapted from Stuart et al. (1999).

3.5. Selection of an initial sample

Our initial goal is to select a set of stars in the CARMENES sample that represent the least active stars. As we mentioned in Section 3.1, the index ($\widetilde{I_T}$) has a neutral point of 1 where a line is neither in emission or absorption and constitutes a non detection. Values below this mean the line has net absorption. Therefore the logical, initial, low activity sample would be any stars with an index ($\widetilde{I_T}$) value less than one. We define this set of

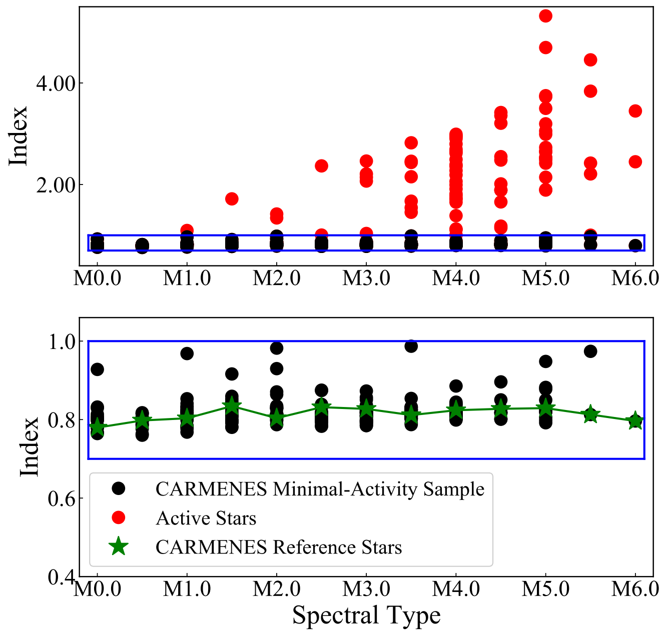

Figure 3.5.: Hα index ($\widetilde{I_T}$) vs spectral subtype. Top: Full sample with the low-activity I sample highlighted by the blue box. Bottom: I sample with aforementioned blue box for context. Green stars depict the index values of the CARMENES reference set of stars.

stars as the I sample. The average index ($\widetilde{I_T}$) values for the full CARMENES survey and highlighted those that are less than one. The reference stars (Section 2.4) agree well with this selection being low-activity.

3.6. Evaluating the index

The initial impression of using the index ($\widetilde{I_T}$) to determine the quiet sample (Section 3.5) was quite good. The relatively constant level of absorption across the spectral subtypes meets the expectation of models such as that described by Cram & Mullan (1979). However, when comparing the values of the reference stars in Figure 3.5 to the Hα spectra in Figure 3.1, we can see a discrepancy. The Hα line decreases in strength, both in width and depth, as the stellar effective temperature decreases. The corresponding index ($\widetilde{I_T}$) value, however, does not. In fact, the index ($\widetilde{I_T}$) value appears stable up to the M6.0V reference star, which is the latest spectral type for which a low Hα activity spectrum, with sufficient signal to noise, that could be identified. We can see this trend in Figure 3.6, where the line core flux (LCF, for Hα the LCF is the flux at λ = 6564.5Å), is rising toward the continuum for the range M0V-M5V, whereas the corresponding index ($\widetilde{I_T}$) values do not appreciably change. The line core flux by spectral type can be described with the linear function by

$$F(S) = 0.06S + 0.38 \tag{3.8}$$

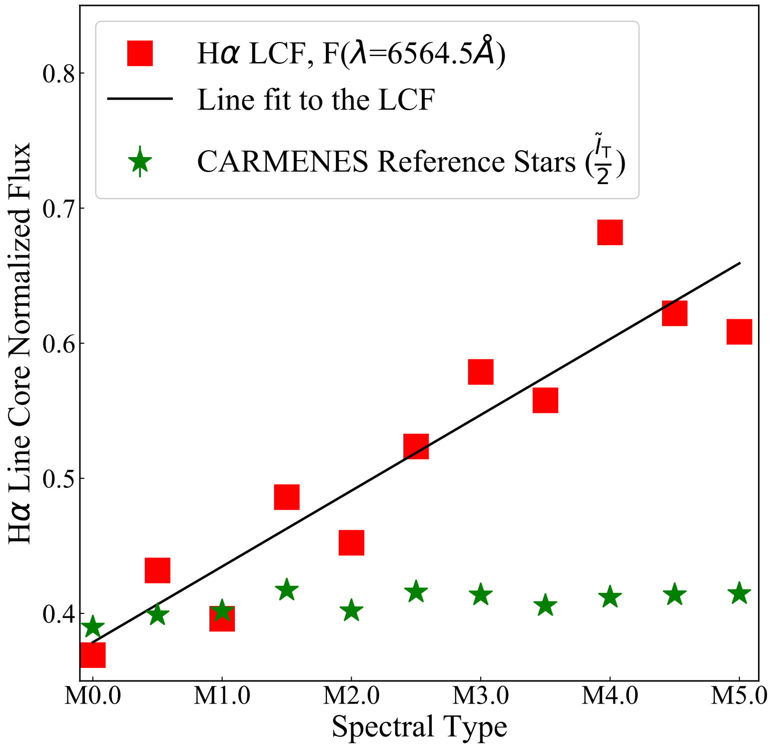

Figure 3.6.: Hα core normalized flux by spectral subtype. Red squares indicate the normalized flux values of the core which steadily rise toward the continuum until M5.0V. Green stars indicate the Hα index values for the CARMENES reference stars divided by two in order to be visualized together with the flux values. The fit of the line, F(S), is given by Eq. 3.8

.

where S is the numerical spectral subtype.

We can also compare whether the trend in the index ($\widetilde{I}_T$) values of the reference stars is related to trends present in the reference regions. We do this by evaluating the reference regions with their own index. For this we used the same equation format as the index ($\widetilde{I}_T$) but use different regions to calculate the reference indexes ($\widetilde{I}_{\mathrm{R}_1}$, $\widetilde{I}_{\mathrm{R}_2}$). These equations are given by

$$\widetilde{I}_{\mathrm{R}_1} = \frac{\overline{F}_{\mathrm{R}_1}}{\frac{1}{2}(\widetilde{F}_{\mathrm{R}_2} + \widetilde{F}_{\mathrm{C}_1})} \tag{3.9}$$

$$\widetilde{I}_{\mathrm{R}_2} = \frac{\overline{F}_{\mathrm{R}_2}}{\frac{1}{2}(\widetilde{F}_{\mathrm{R}_1} + \widetilde{F}_{\mathrm{C}_2})} \,. \tag{3.10}$$

with C_1 and C_2 being new reference regions required to make the reference region indexes (wavelength ranges for $\widetilde{I}_T$, $\widetilde{I}_{\mathrm{R}_1}$ and $\widetilde{I}_{\mathrm{R}_2}$ are listed in Table A.1). The error calculation follows the same format as Eq. 3.3. It can be seen that, initially, the index ($\widetilde{I}_T$) values of the reference stars, with Hα, do not match the trend in the reference regions (Fig. 3.7).

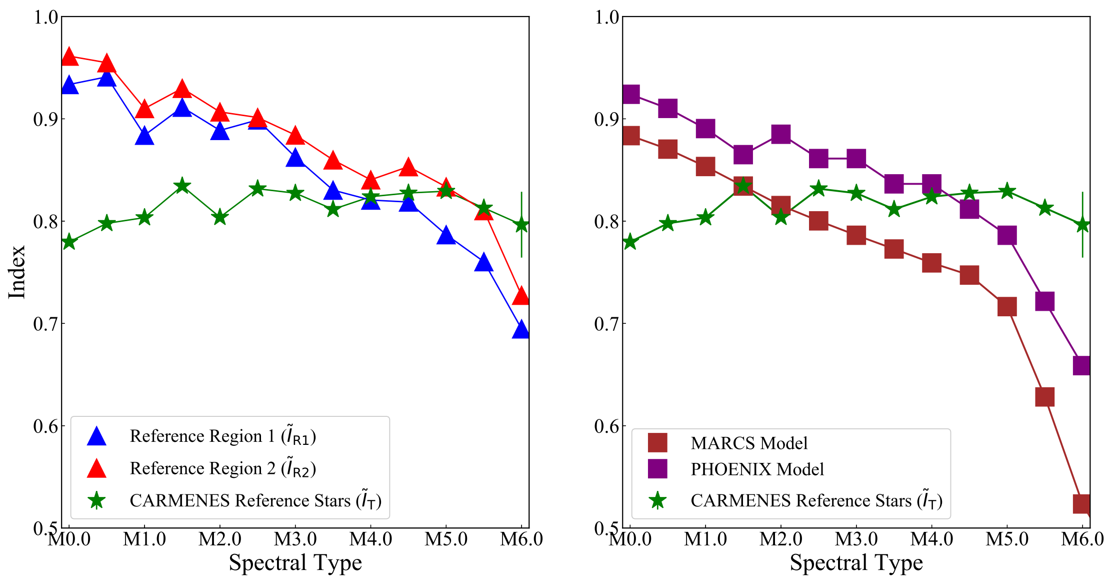

Figure 3.7.: *Left*: Comparison of the CARMENES reference star Hα index ($\widetilde{I}_T$) to the index of the reference regions that are used in calculating the Hα index ($\widetilde{I}_T$). *Right*: Comparison of the index ($\widetilde{I}_T$) of the reference stars to the index ($\widetilde{I}_T$) of the Hα region in PHOENIX and MARCS models. Note that the trend of the reference star indexes are not similar to either but the trend of the models is very similar to trend in the reference regions.

The values, however, converge toward the later spectral sub-types but still differ slightly. The reference region index trend is similar to the index ($\widetilde{I_T}$) of the Hα region in the PHOENIX and MARCS models. In both those models chromospheric Hα is not modeled as they only handle LTE conditions - so effectively they only model the photosphere. Their models also suggest that Hα does not form in even an M0V photosphere, and thus these models give an example of the Hα region without Hα being present. This makes them ideal to compare the index ($\widetilde{I_T}$) of our reference regions.

To further investigate if the discrepancy is due to a confluence of effects from the molecular lines and Hα, we fit the Hα line of the median spectra of the reference stars (Fig. 3.1) with a Gaussian, as described in Section 3.2. We then subtract this fitted Gaussian profile from the reference star spectrum to generate a residual spectrum that is without the Hα line. In Figure 3.8 we compare the index ($\widetilde{I_T}$) values of the residuals from our Gaussian fits to that of the reference stars with Hα, the models and the reference regions.

We find that the trend exhibited by the reference regions, models and residuals all agree very well with each other. We present the fits of the reference regions and models in Table 3.1. While the values are not an exact match, the trends are almost identical.

Since the Gaussian fits of Hα are of the form shown in Figure. 3.3, red line, we can calculate an index of the Gaussian fit in the same manner as we calculate the index for the original spectrum. When we compare the index ($\widetilde{I_T}$) of the Gaussian fits of Hα to the Hα index ($\widetilde{I_T}$) of the reference stars (Fig. 3.9), it can be seen that they differ considerably

Table 3.1.: Parameters of $I(S) = mS + b$ models for models and reference regions

Fitted item	m	b
Reference region 1	-0.04	0.95
Reference region 2	-0.03	0.97
MARCS model	-0.07	0.95
PHOENIX model	-0.02	0.90
Reference stars	-0.00	0.80

from one another. However, the trend of the Hα Gaussian fits closely resembles the decay of the Hα profile going toward later spectral sub-types seen in Figure 3.1 and the trend of the line core flux in Figure 3.6. We can therefore conclude that a) the reference regions and models are a good approximation of the Hα region without Hα and b) the index ($\widetilde{I_T}$) does not accurately reflect the 'true' value of Hα in low-activity stars but is a combination of the influence of Hα and the increasing strength of molecular lines toward later spectral sub-types. We define the 'true' value of Hα as the value Hα would have if the star consisted of a blackbody with the same temperature as the star's effective temperature. The chromosphere has the same properties as the chromosphere of the star, but Hα is the only line present.

3.6.1. Parameters for improvement

Each of the different methods covered in this section have their own benefits and drawbacks. In order to develop a new method we should set out what an idealized measurement should be. Firstly, and most importantly, the value of the measured line should be accurate and not differ with a changing continuum, or in this case pseudocontinuum. Secondly, it should not be reliant on models, reference stars or multiple observations in order to function properly. Lastly, it would be preferable that the new method would be easy to implement and comparable to existing methods for earlier type stars.

3.7. Molecular Normalized Index (MNI)

In Section 3.6, we concluded that the Hα index ($\widetilde{I_\mathrm{T}}$), in the reference stars, was a combination of the Hα signal, the signal from the molecular absorption and the continuum. We also showed that the residuals of subtracting the Hα Gaussian fit from the spectra closely resembled the indexes of the calibration regions ($\widetilde{I_{R_1}}$,$\widetilde{I_{R_2}}$) (Fig. 3.8) used in the calculation of the Hα index.

Therefore, if we average the indexes from these calibration regions and divide that value from the Hα index ($\widetilde{I_\mathrm{T}}$), Eq. 3.2, we should be able to reduce the influence of the molec-

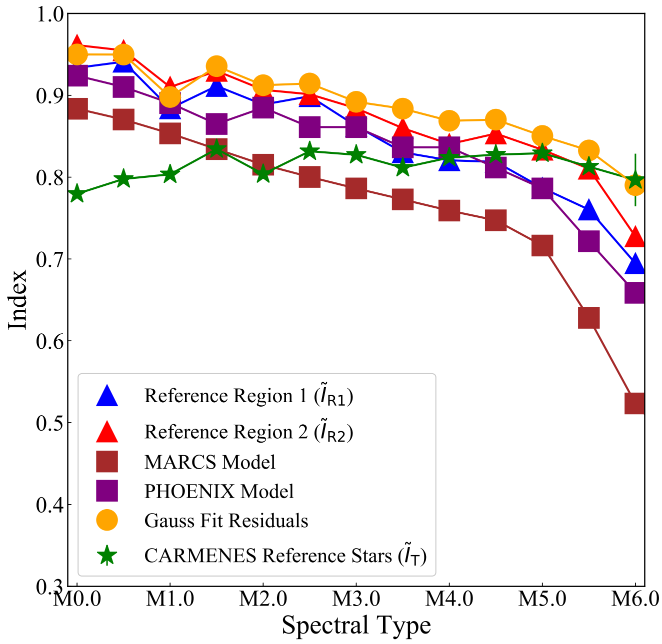

Figure 3.8.: Comparison of the reference star Hα index ($\widetilde{I_T}$) to the reference regions, models and the Gauss fit residuals from Figs. 3.2 & 3.3. Note that the trends of the regions without Hα are a very close match while the reference star index trend does not match at all.

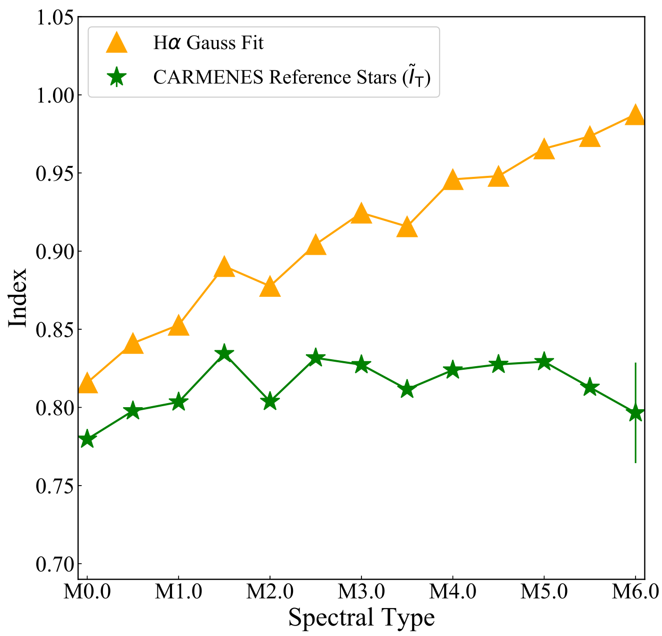

Figure 3.9.: Comparison of the reference star Hα index ($\widetilde{I_T}$) values to the index values of the Hα Gaussian fits described in Section 3.2

.

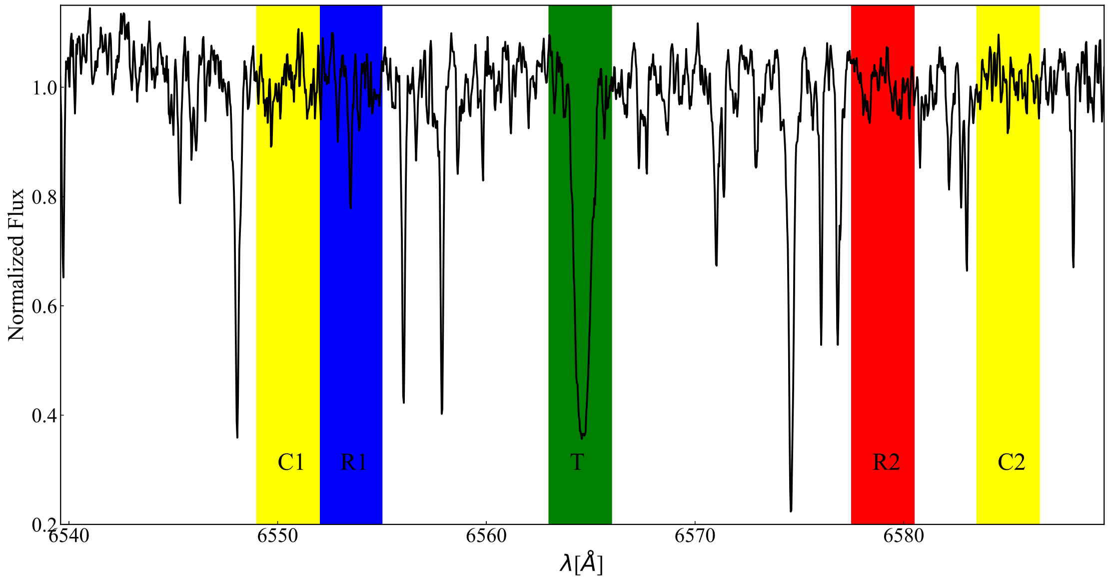

Figure 3.10.: Display of the calculation regions used in this work for Hα. Green is the Hα measurement region. Blue and red denote the regions that the Hα index is referenced to. Yellow are the regions used for calculating the index of the reference regions in Figs. 3.7 & 3.8.The width of the regions was the largest possible, whilst remaining close to the target region, without incorporating large features such as other atomic lines that could affect the measurement.

ular absorption on the Hα measurement (Eq. 3.11). The regions of note are given in Figure 3.10 and listed in Table A.1.

As this measurement effectively normalizes out the influence of the molecular absorption from the Hα index ($\widetilde{I}_T$) we designated this new measurement the Molecular Normalized Index (MNI). The error in this measurement is given in Equation 3.12 with δ referring to the uncertainty in a measurement and σ referring to the calculated error in the MNI measurement.

$$\mathrm{MNI} = \frac{\widetilde{I}_T}{\frac{1}{2}(\widetilde{I}_{R_1} + \widetilde{I}_{R_2})}, \tag{3.11}$$

$$\sigma_{\mathrm{MNI}} = \mathrm{MNI} \times \sqrt{\left(\frac{\delta\widetilde{I}_T}{\widetilde{I}_T}\right)^2 + \left(\frac{\delta\widetilde{I}_{R_1}}{\widetilde{I}_{R_1} + \widetilde{I}_{R_2}}\right)^2 + \left(\frac{\delta\widetilde{I}_{R_2}}{\widetilde{I}_{R_2} + \widetilde{I}_{R_1}}\right)^2}. \tag{3.12}$$

3.7.1. Evaluating the MNI

One of the first things to note with the MNI is that, effectively, it is an index of other indexes. Since the index has a neutrality point of 1.0 (Eq. 3.2), when the limit of the MNI (Eq. 3.11) is taken as the calibration regions approach 1.0 (as in applying the MNI

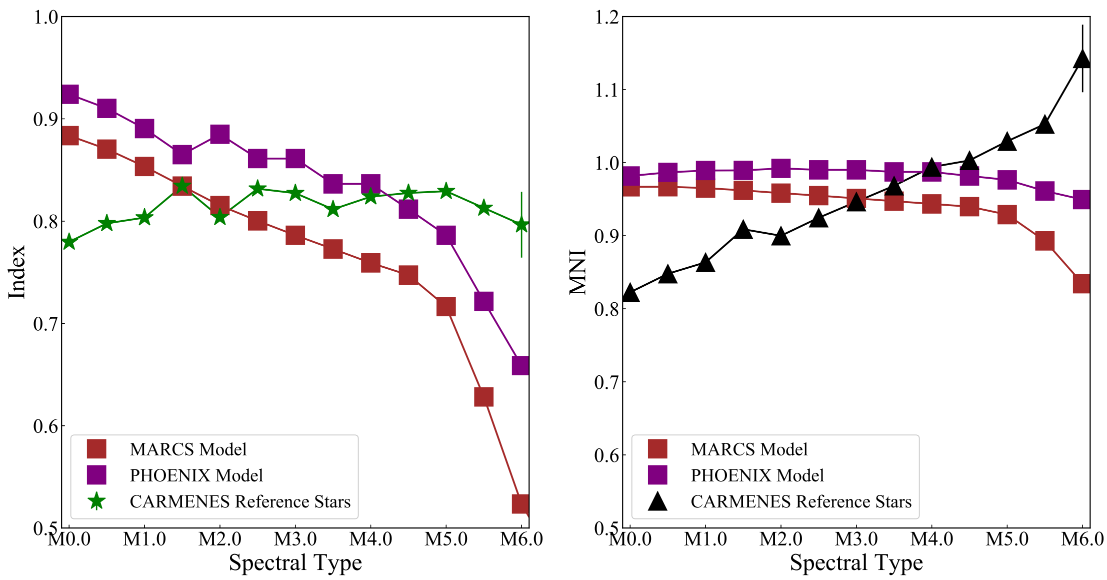

Figure 3.11.: Comparison of the Hα index of the reference stars (green stars) and models (*left*, squares) to that of the MNI (black triangles) to the same (*right*). Note in the MNI of the models that, for stars earlier than M5.0V, the normalization is close to the neutrality value for the index and MNI of 1.0.

measurement to earlier type stars with few molecular absorption features) the original index ($\widetilde{I}_T$) is recovered as shown by

$$\lim_{\widetilde{I}_{\mathrm{R}_1},\widetilde{I}_{\mathrm{R}_2}\to 1} \frac{\widetilde{I}_{\mathrm{T}}}{\frac{1}{2}(\widetilde{I}_{\mathrm{R}_1}+\widetilde{I}_{\mathrm{R}_2})} = \frac{\widetilde{I}_{\mathrm{T}}}{\frac{1}{2}(1+1)} = \widetilde{I}_{\mathrm{T}}\,, \tag{3.13}$$

Therefore the MNI, when applied on M dwarfs, is comparable to the index ($\widetilde{I}_T$) applied to early type star. Effectively, the MNI is a correction factor to deal with the issue that the reference regions can no longer be assumed to be equivalent as the local continuum flux is no longer equivalent between the reference regions.

In Figure 3.8 we compared the Hα index ($\widetilde{I}_T$) from the CARMENES reference stars to the index of the models, calibration regions and residual spectra from the Hα Gauss fitting. In Figure 3.11 we compared the index ($\widetilde{I}_T$) of the reference stars to the index of the models and the MNI of the reference stars compared to the MNI of the models. Firstly we see that, unlike the Hα index ($\widetilde{I}_T$), the Hα MNI value goes from a strong absorption signal in the M0.0V reference star to almost no absorption by the M5.0V reference star. This trend resembles the deterioration of the Hα profiles in Figure 3.1 and the decreasing depth of the line core flux in Figure 3.6. The second feature of note is that the MNI of the models, which do not have Hα in their spectra, is nearly at the neutrality point of 1.0. This would be the value expected of a non-detection of Hα. This trend begins to degrade after M5.0V, however, and we will touch on this issue in Section 5.6.

In Fig. 3.12 we compare the values of the median Hα index ($\widetilde{I}_T$), Gauss fit of Hα, and the

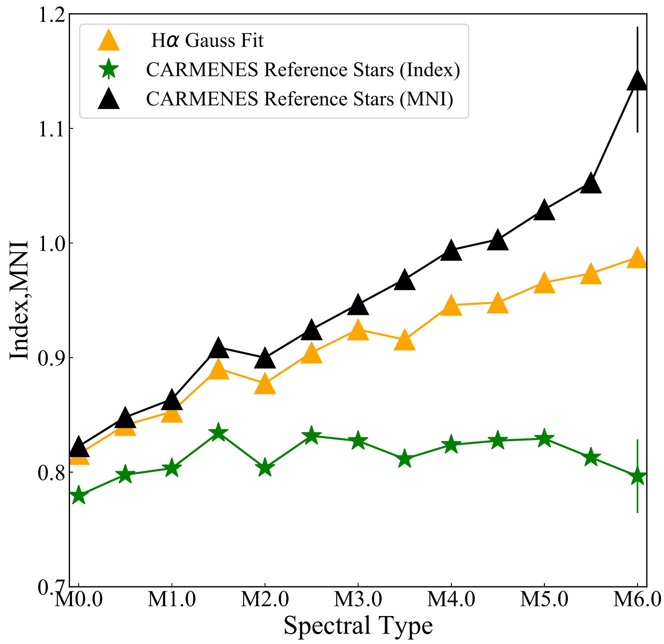

Figure 3.12.: Comparison of MNI (black triangles) to the index of the Gauss fits (orange triangles) to the index of the reference stars (green stars). Note the similarity in trends between the MNI and the Gauss fits.

Hα MNI values of the reference stars. It can be seen that the MNI follows the Gaussian fit values more closely than the index ($\widetilde{I_T}$) for early M stars. This correlation weakens as the spectral sub type approaches M6.0V. Generally, the Gaussian fit displays more absorption than the MNI values. We suspect this is due to the issue discussed in Section 3.2, where the Hα profile becomes less and less Gaussian in shape, owing to the interference of molecular features, toward later spectral sub-types. This results in the fitting program overestimating the absorption. We therefore suspect that the MNI better reflects the decay of the Hα profile over the range M0V to M6V than the Gaussian fit, but we cannot rule out that the MNI might be overcorrecting for the differences in reference regions.

Lastly, we designed a toy model to simulate the spectrum around Hα to test the MNI vs the index ($\widetilde{I_T}$). We did this by generating a small Gaussian profile, similar to what would be observed in an M5.0V star, and measuring the index and MNI values of this profile. They both returned a value of 0.98 (to be referred to as the 'true value' of the test) as the 'continuum' was flat (Eq. 3.13). We then generated a 'molecular' line list of 1000 random line locations between 6550 Å and 6580 Å and generated Gaussian profiles. Initially we assigned each 'molecular' line with an amplitude of 1 (Molecular Factor Enhancement, MFE=1). We then took the index ($\widetilde{I_T}$) and MNI of this step, then increased the amplitude by 1. We repeated this process until we had reached an amplitude of 11. We chose 11 as the maximum value, as going to 12 made a significant number of the simulated molecular lines go below 0 flux and thus created an unphysical situation. At this point we observed the resultant simulated spectrum and removed from consideration any sets

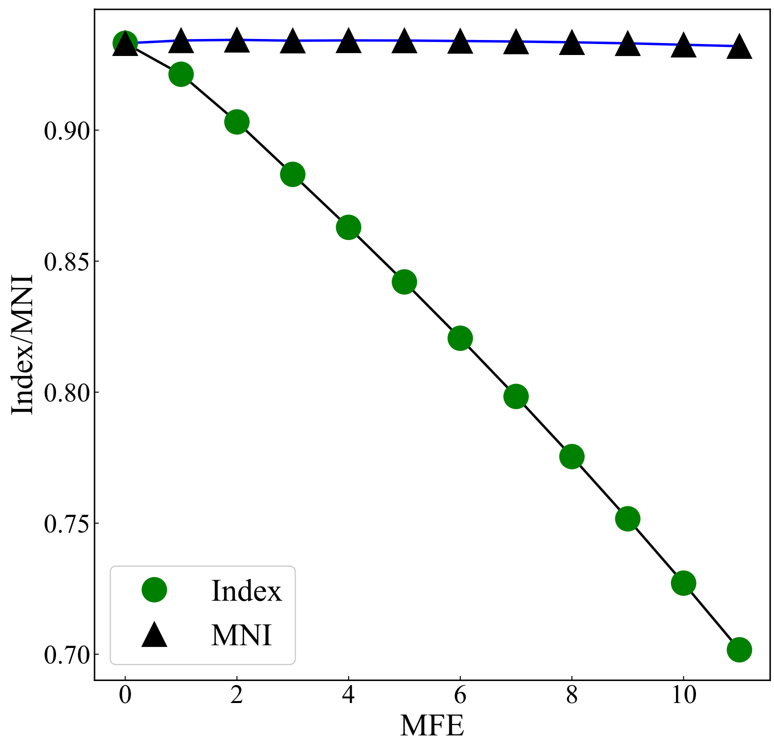

Figure 3.13.: Index (circles) and MNI (triangles) values from a simulated M dwarf spectrum in which the amplitude of 1000 simulated molecular lines increases by 1 in factor (MFE) for each step.

that had formed large absorption bands (which are not present near Hα) and any that have absorption lines that had negative values as this is not physical. All the remaining sets showed approximately the same profile as in Figure 3.13, in that the index ($\widetilde{I_T}$) lost between 30 and 40% of its original value while the MNI lost between 2 and 5%.

3.7.2. Modifying the low activity I sample

In Section 3.5 we defined an initial low-activity selection (the I sample) as any star with a median index ($\widetilde{I_T}$) below 1.0 - which indicates an overall absorption dominated profile. This selection of stars, however, included profiles such as Figure 1.21 which has significant emission in its profile, despite the large absorption trough in the center. When we apply the MNI method to this set of stars (Fig. 3.14), it can be seen that what was an irregular, roughly horizontal, band of stars, using the index ($\widetilde{I_T}$) method, is now a band of stars losing Hα absorption as it approaches the M6.0V reference star. This is what corresponds well to the decay of the Hα profile in Figure 3.1.

Based on this refinement we can consider refining our I sample. In Figure 3.15, it can be seen that the variability of this band of stars is the lowest of the sample. Additionally,

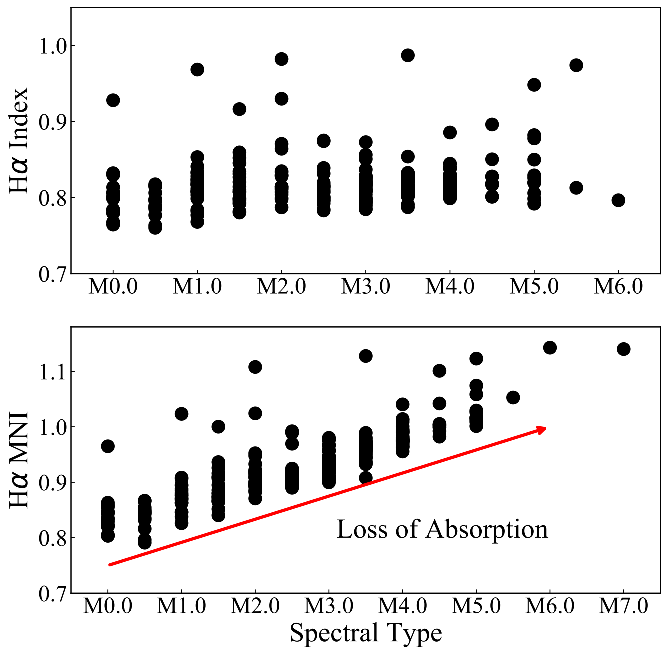

Figure 3.14.: Comparison of the low activity sample in the index (*top*) and the MNI (*bottom*). Note the distinct loss of absorption strength in the MNI values when moving from early to late M dwarfs.

the trend, when looking at each individual spectral type, is significantly different from the more active stars. We tabulate the trend fits of the low activity, spectral-type dominated trends and the trend of the active stars in Table 3.2 where m is the slope of the trend and b is the MNI axis intercept.

We can now define the MNI - based sample (N sample) with the goal of selecting only stars that can be considered quiet in that they show no signs of Hα emission in their spectra. This sample is bounded on the lower end by the trend in the loss of absorption and, on the higher end by the uptick in variability and emission. We show the upper bound in Fig. 3.16 as this is the boundary line of the N sample. The stars above this

Table 3.2.: Parameters of trend fits for Fig. 3.15. 'Active' is fit with a black line, the others with a green line.

Spectral type	m	b
M0, M0.5	1.13	0.82
M1, M1.5	0.84	0.86
M2, M2.5	0.39	0.9
M3, M3.5	0.15	0.94
M4, M4.5	0.28	0.97
Active	2.33	0.9

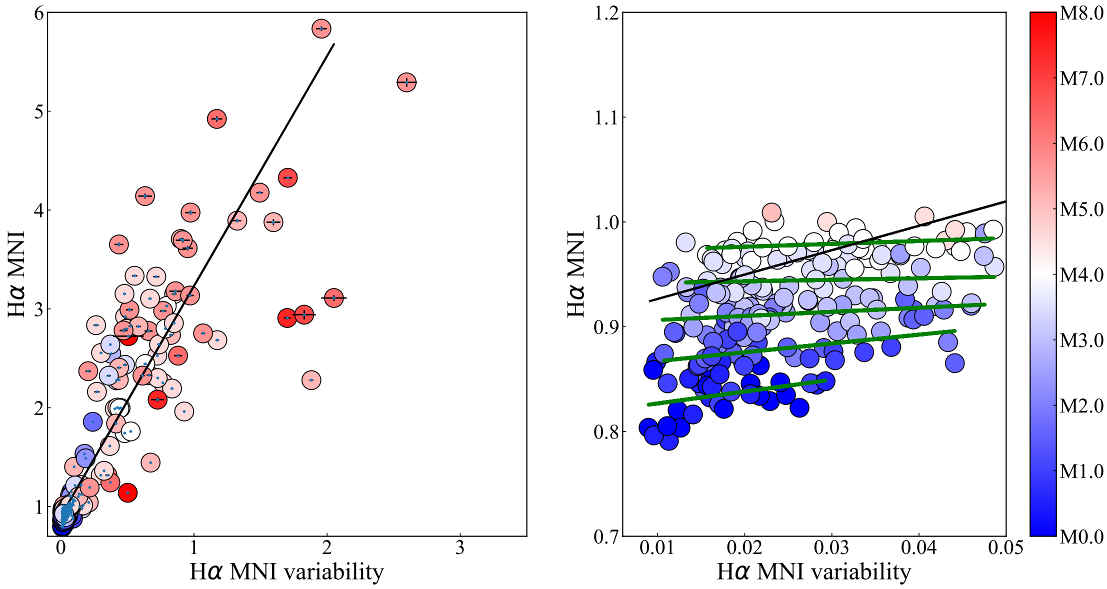

Figure 3.15.: MNI variability for the full sample (*left*) and low activity sample (*right*). The black line is the fit for the activity sample whereas the green lines are fits for each spectral subtype of the low activity sample. Note the stratification in the low activity sample.

line, except for the M5.5V star, are excluded from the N sample as they show some signs of activity. By comparing Figure 3.4 to Figure 3.15 as well as the plots in Figure 3.14, we demonstrate that the usage of the MNI method has made the identification of these quiet stars considerably easier than it would have been with the index. It should be noted that we left the M5.5V star in the N sample as it was the only one relatively close to the boundary line, in our sample, for that spectral type. The equations bounding the quiet sample are given by

$$\begin{aligned} \mathrm{MNI}_U &= 0.034S + 0.87 \\ \mathrm{MNI}_L &= 0.038S + 0.75 \end{aligned} \tag{3.14}$$

where MNI_U and MNI_L refer to the upper and lower bounds for the MNI value per S spectral subtype. We can check this by placing the sample into a log(MNI)-log(rotation) plot (Fig. 3.17). There are five M5V+ stars that have MNI 1.0 and above, which have enhanced variability. We have taken a more liberal approach and included these in the N sample as, there are not many in the sample in that spectral type range that would qualify and the majority of the spectra of these stars do appear to be in line with what would be expected from the spectra shown in Fig. 3.1. Therefore these stars are most likely to found in a non-active state. In Figure 3.18, we compare the Kürster index to the MNI. They perform equivalently until about M2.0V, at which point they begin to diverge. This divergence is due to the aforementioned non-uniform increase in molecular features in the later type M dwarfs which results in the the reference regions no longer being equivalent.

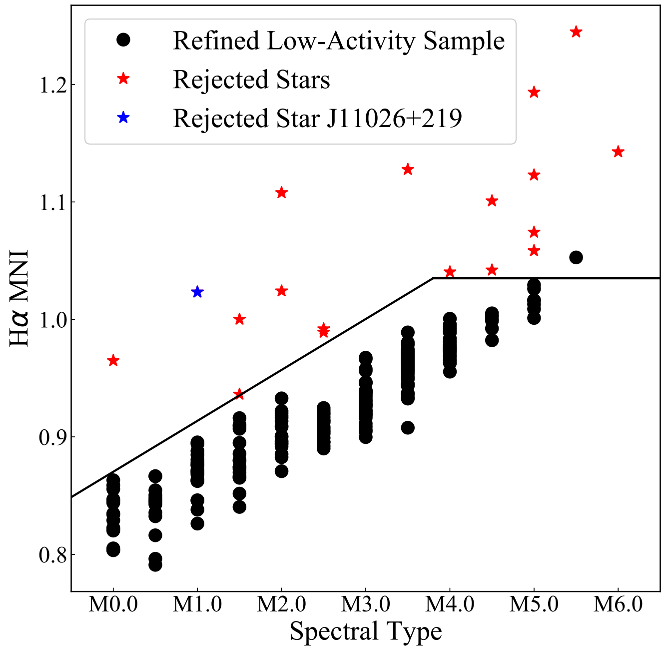

Figure 3.16.: Definition of the N sample (black dots) from the I sample (black dots plus stars). The blue star, referring to J11026+219, has a Hα intermediate profile (Fig. 1.21).

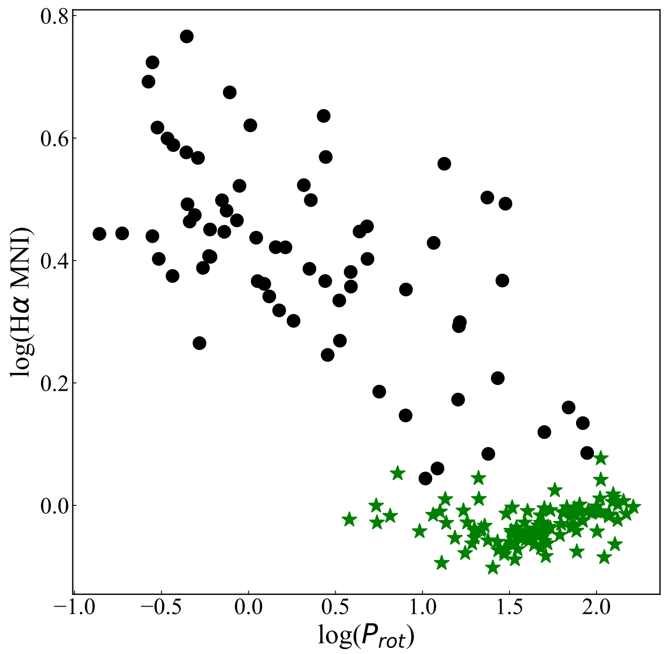

Figure 3.17.: Log-log plot of activity vs rotation. Pictured full CARMENES sample with the N sample denoted by green stars.

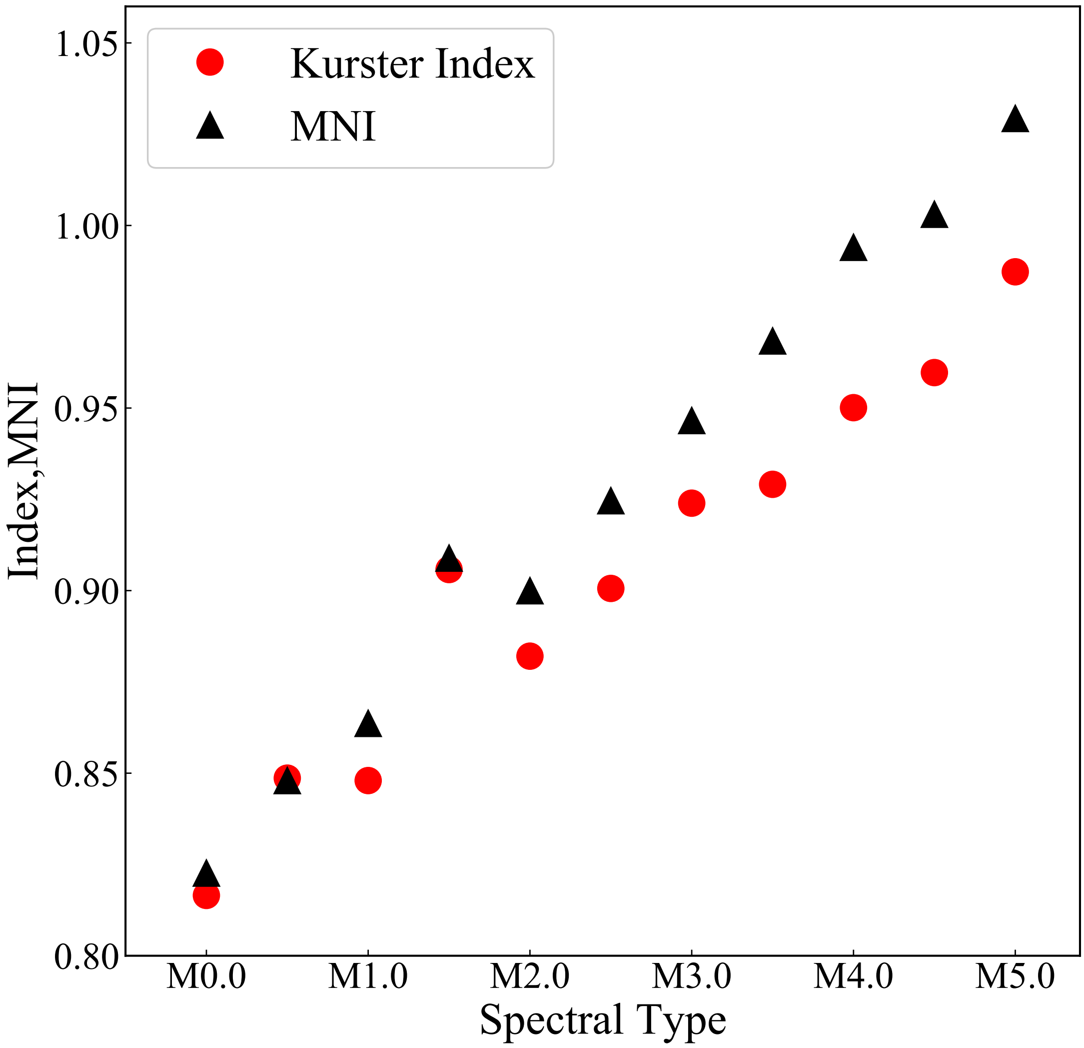

Figure 3.18.: MNI, black, compared to the Kürster index,red, when applied to the CARMENES reference stars. The MNI and the Kürster index perform equivalently to each other until about M2.0V at which point they begin to diverge from another.

3.7.3. Metallicity

A natural question arises when presenting a new measurement method with respect to spectral lines: How does the metallicity of the star affect the measurement? As the MNI is just a combination of three indexes. If each index has a systemic bias toward a particular attribute, in this case metallicity, then that same systemic bias would be inherited by the MNI. We can therefore expect the MNI to be no more susceptible to the effects of metallicity than the index. A more detailed investigation into this issue quickly runs into a few problems. In Figure 3.19 (Cifuentes et al. 2020; Passegger et al. 2022) it can be seen, in the left hand panel, that a strong dichotomy exists between the least active stars and the more active stars in that nearly all of the more active stars are shown as being more metal poor than the Sun. This is not logically consistent, seeing as the younger a star is, both the more active it is and the more metal rich it should be. Therefore we can conclude that stellar activity likely biases the metallicity measurement.

Looking to the right panel of Figure 3.19, it can be seen that, unlike the active stars, the N sample is more centered about solar metallicity. The only oddity here is that for spectral sub-types, M0.0V to M1.5V are skewed toward super-solar metallicities. This, like the active stars skewing toward low metallicities, is counter-intuitive. These low-activity, early-type stars should be on the older side of our sample, perhaps much older than the Sun. This should skew this sample toward lower metallicity values rather than higher ones. With these oddities in the metallicity determination of the CARMENES M dwarf sample we therefore conclude that we cannot definitively determine if metallicity has an effect on the MNI measurement. This being said, we can constrain the effect to the width of the band of low-activity stars shown in Figure 3.16. Within this band, we cannot, thus far, isolate the different effects of temperature and metallicity. We can conclude that, with respect to metallicity, we do not expect any difference in measurement quality between the MNI and the index.

3.7.4. Summary

In Section 3.6.1, we set out four attributes for a better measurement technique. We primarily wanted a measurement that would reflect the observed loss in Hα absorption across multiple spectral subtypes in our I sample. In Figures 3.12 and 3.14 we showed that the MNI performs markedly better than the index. Secondly, we wanted a measurement that could be performed on a single spectrum without need of reference stars, models or rotation periods. Since the MNI is an index of an index, it has no more complicated of requirements than the index method itself. Similarly the MNI is not much more complex than the index to implement. It is only more complex in that an index must be calculated three times for every MNI value generated. The MNI can allow M dwarf star's features to be directly compared to earlier type stars in that it is essentially a compensation for a non-ideal continuum. It returns a value that the index would have returned for the same

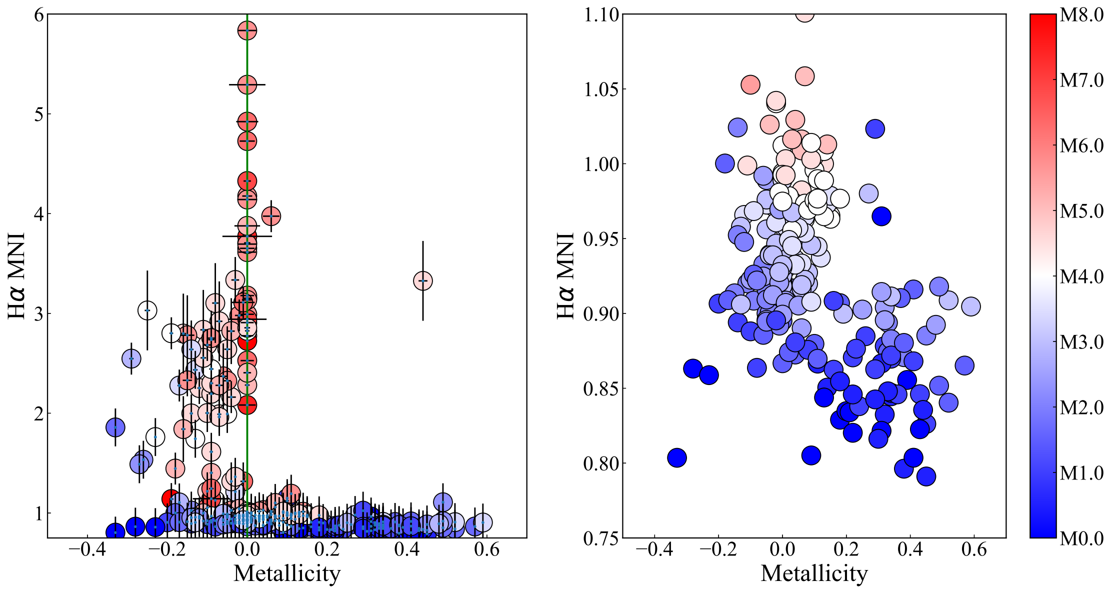

Figure 3.19.: Comparison of median MNI values to the metallicity. The vertical line, green, denotes solar values. *Left*: Full CARMENES sample. Note that the active stars nearly all have solar or sub-solar metallicities (Cifuentes et al. 2020; Passegger et al. 2022). *Right*: N sample shows a slight skewing toward super - solar metallicities.

strength line in a more ideal continuum. When comparing the MNI to the Kürster index, the two methods are comparable from M0V to M2V. After M2V they diverge. This is likely due to the strong increase in molecular absorption in the Hα region at this effective temperature. Overall the MNI seems to be a slightly improved version of the Kürster index that is beneficial for studying late type M dwarfs with Hα in absorption. Consequently this suggests that the Kürster index is effective at comparing stars of different spectral types up to M2V. This work also shows that Kürster index is much more suitable for comparing chromospheric features of stars with different spectral types than originally thought.

4. Results

In this section we will examine the application of the MNI method to the chromospheric activity indicators in the N sample of the CARMENES survey. We will start by continuing our coverage of Hα, then proceeding to Ca II IRT, Na I $D_{1\&2}$ and ending with He I D_3. We will be focusing on the evolution of the lines from M0V to M5.5V M dwarfs, including the evolution of the line profile itself. We will also look at the interface of the low activity I sample with that CARMENES stars that arefully active with Hα in emission. We designate this set as the E sample.

4.1. Hα

In Section 3.7, we set up two low activity samples. The I sample, defined by the index, I_{T}, (Fig. 3.5) and one, the N sample, defined by the MNI (Fig. 3.14). We plotted these two sets side by side in Figure 4.1. Instead of plotting by spectral type, we plotted the two indicators against effective temperature (T_{eff}, Cifuentes et al. 2020). We also used the variability (Fig. 3.15) measurement as a modifier to the marker size as a proxy for activity. Figure 4.1 shows that once the larger variability stars in the I sample are removed, as we did in defining the N sample, the stars are confined to a tight band that is strongly correlated to the effective temperature. It can also be seen that after M2.5V the rate of absorption loss increases considerably. The equations for these two regimes are given by

$$\begin{aligned} M(T)_{>\mathrm{M2.5V}} &= -0.00031T + 1.993 \\ M(T)_{<\mathrm{M2.5V}} &= -0.00017T + 1.51. \end{aligned} \tag{4.1}$$

where T is the effective temperature and M is the MNI value. It should be noted that the increased size of the markers for late type stars may not be exclusively caused by increased activity but also longer exposure times and lower S/N for the Hα order, all of which act to increase the apparent variability of the star.

We can also use the MNI in conjunction with other measurement methods given in Section 3. In Figure 4.2, we compare the MNI to the pFWHM (described in Section 3.3) for both the full sample and the interface region between the lower and higher activity stars. It can be seen that for the lower activity stars, the effective width of the Hα line decreases in a linear fashion with decreasing effective temperature (increasing spectral sub-type). This linear decrease is given by

$$M(f) = -0.575f + 1.379 \tag{4.2}$$

where f is the pFWHM value.

When comparing the active, E, sample to the quiet, N, sample on a spectral type by spectral type basis, the E sample is 0.7 Å broader than the N sample. The E sample also decreases in width with spectral type, similar to what would be expected of the Wilson-Bappu effect,which is the correlation between spectral type and the width of an emission line (Wilson & Vainu Bappu 1957; Stauffer & Hartmann 1986), but the correlation is much weaker than that of the N sample. Between the I sample, which includes some stars that show very weak emission, and the fully emissive E sample, there exists a large gap bounded by the lines given by

$$\begin{aligned} U(f) &= -0.473f + 1.732 \\ L(f) &= -0.457f + 1.279. \end{aligned} \tag{4.3}$$

Here U is the equation for the upper bound and L for the lower, with f being the pFWHM. To further look into this gap (Fig. 4.2), we compared the normalized line core flux of Hα to the MNI. Figure 4.3 shows that, for the full sample, the line core flux (LCF) increases in a linear fashion. Here the I sample can be identified by spectral type but the E sample can not. It can be seen that a gap exists between the I and E samples. The normalized flux is not susceptible to having a gap as the pFWHM could be, as we described in Section 3.3. Therefore, this gap appears to be physical, and not an artifact of the pFWHM measurement. As such, out of the 333 stars that had spectra of sufficient quality to calculate an MNI, 218 (65.5%) are quiet and 115 (34.5%) are active. Schöfer et al. (2019) found, out of 333 usable stars in the same sample, that 96 (29%) were active in Hα. The discrepancy between these two values is most likely due to differing methods used. Schöfer et al. (2019) used a spectral subtraction method with a cutoff pseudo equivalent width of -0.3 Å. Many of the stars we classified as active in our analysis were not so in Schöfer et al. (2019). Even if we excluded the five potentially active M5+ stars we would still have a discrepancy of 14 stars more active than Schöfer et al. (2019). Interestingly, when we calculated the active percentage using the I sample (Section 3.5), we would have classified 92 (27.2%) as active.

4.2. Ca II IRT

The Ca II IRT lines are, like Hα, an oft-used chromospheric activity indicator in M dwarfs (Martin et al. 2017). Unlike Hα, however, the Ca II IRT retains a strong photospheric component that can complicate measurements. As the name implies, the Ca II IRT has three lines. In the CARMENES instrument two of the lines (B [8544.44 Å] and C [8664.52 Å]) lie close to the order boundaries, which makes them difficult to implement with the MNI method and can expose the measurement to higher uncertainties due to the fringing effects. We therefore chose the A [8500.36 Å] line as the best candidate to implement the MNI method on. The measurement regions utilized are given in Figure A.1 and the wavelength ranges are listed in Table A.2.

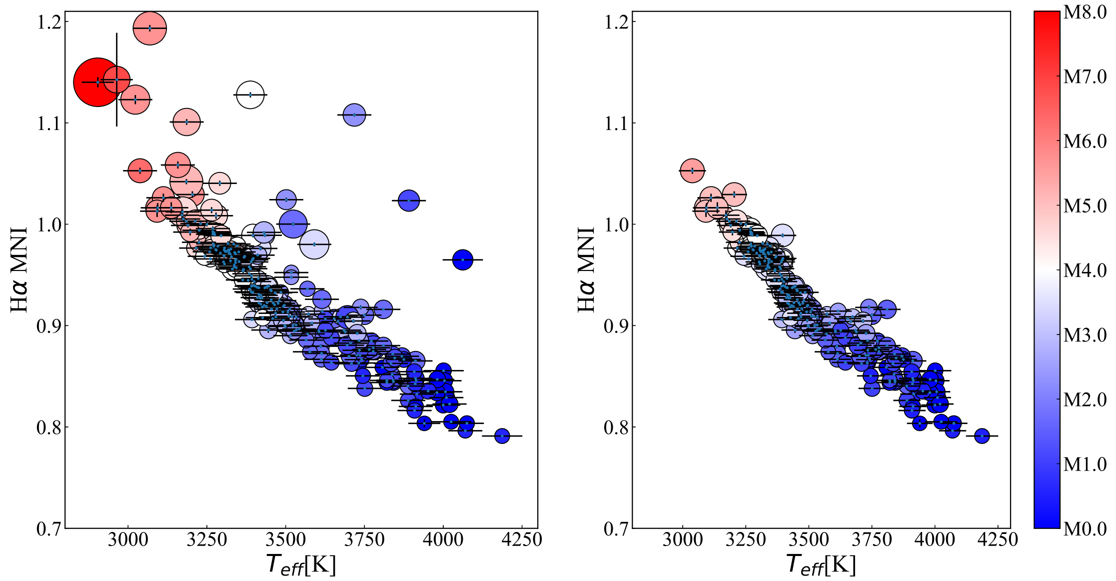

Figure 4.1.: Median Hα MNI values for the I sample (*left*) and the N sample (*right*) vs effective temperature. Marker size denotes variability, with the larger marker indicating more variability.

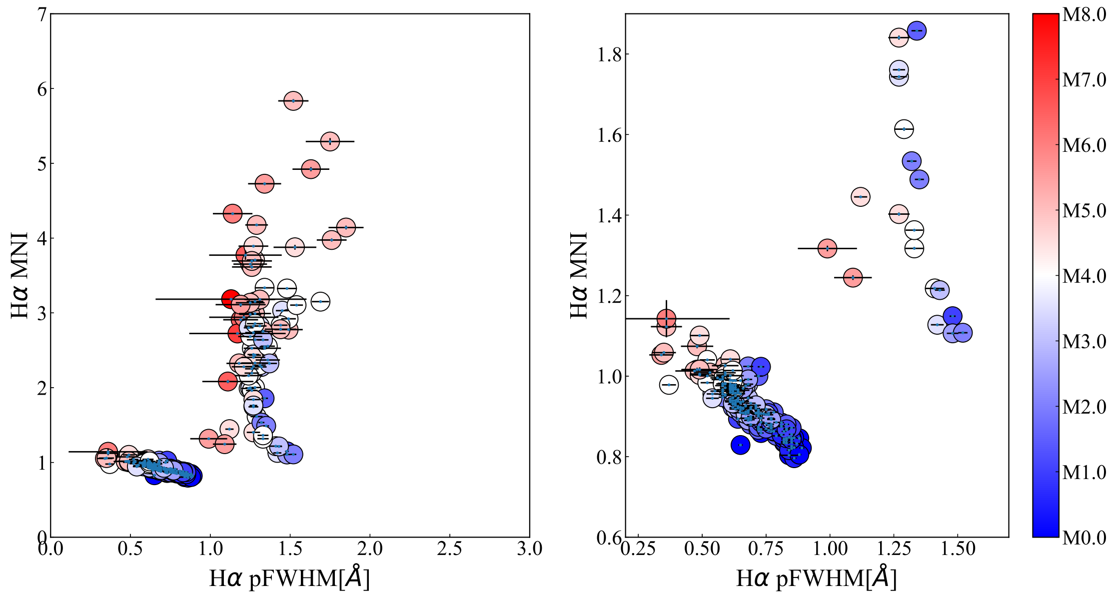

Figure 4.2.: Comparison of median MNI values to median pFWHM values for full sample (*left*) and the interface between the I sample and lower E sample (*right*). Note the gap between the two groups in addition to the width difference in the Hα profile between those stars that are in emission and absorption.

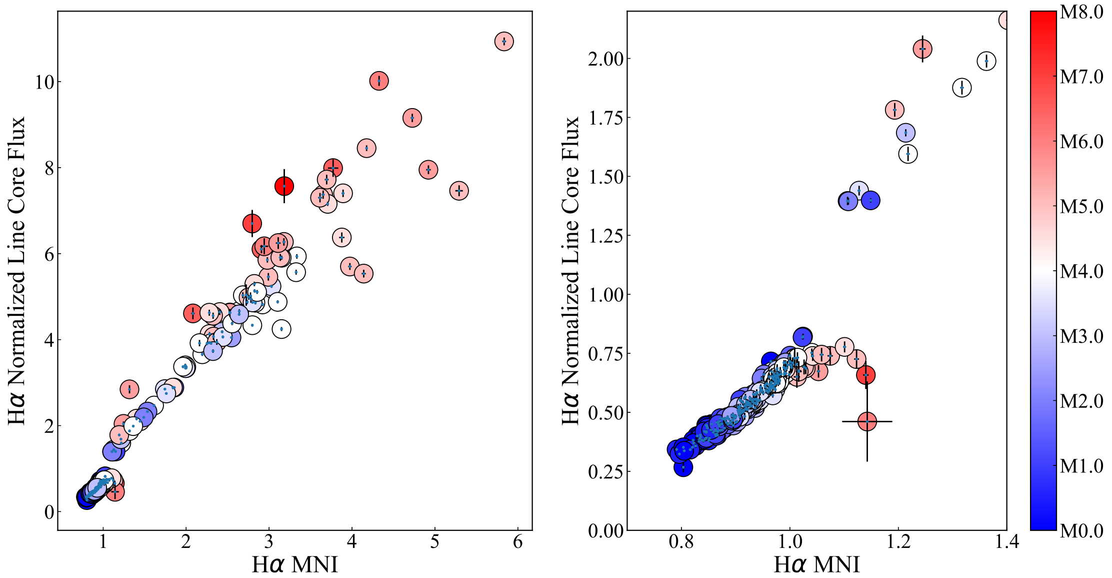

Figure 4.3.: Median core flux values vs median MNI values for the full sample (*left*) and the interface between the I sample and the lower E sample (*right*). Note the gap between the two groups.

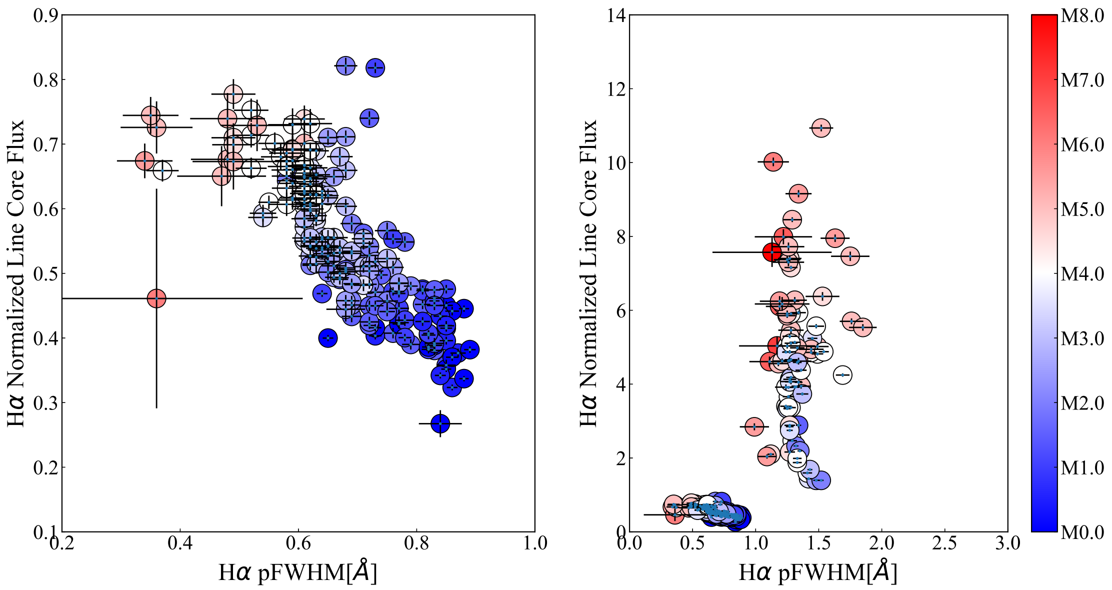

Figure 4.4.: Comparison of the median line core flux to the median pFWHM for the I sample (*left*) and the full sample (*right*).

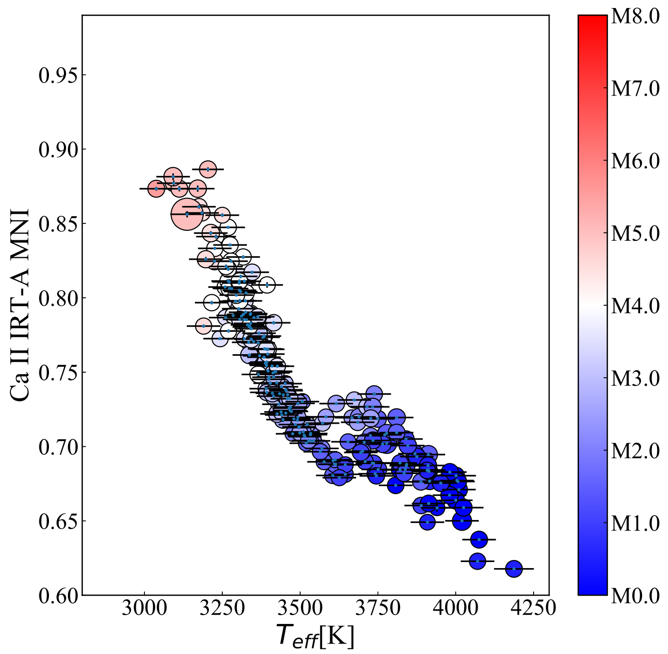

Figure 4.5.: Median MNI values for Ca II IRT vs $T_{\rm eff}$ for the N sample. Marker size denotes variability.

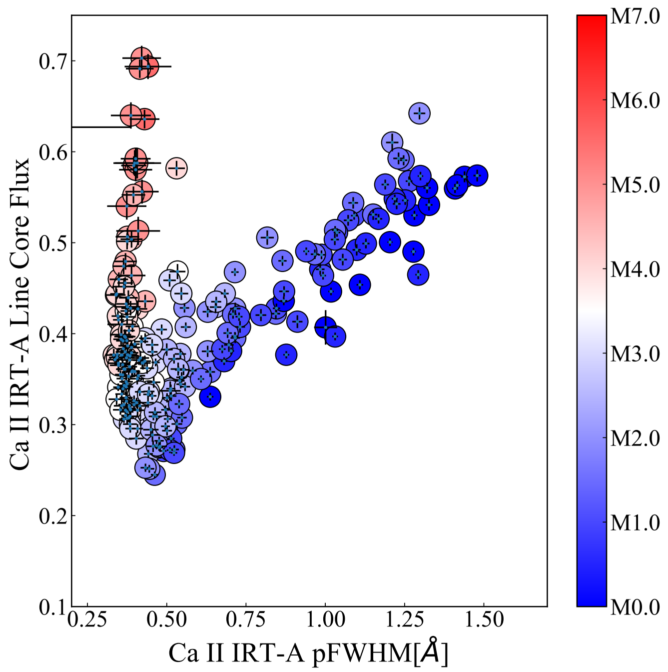

Figure 4.6.: Ca II IRT core flux versus pFWHM median values. Illustrates the change in the shape of the Ca II IRT line from early type stars (blue) to late type (red).

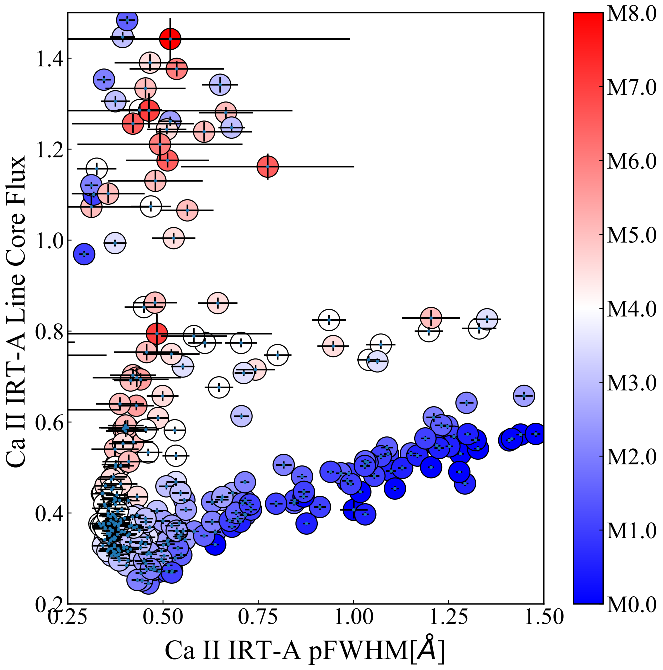

Figure 4.7.: Core flux vs pFWHM for Ca II IRT-A median values for the full sample.

In Figure 4.5, it can be seen that the Ca ii IRT follows a similar pattern to Hα in that the general trend is toward lower absorption with decreasing effective temperature. The line pinches out, or is no longer detectable, by M5.5V. The most notable feature is a short halt of the trend in absorption decrease between M1.0V and M2.0V, forming a prominent kink. To investigate this kink further, we look at the line core flux vs the pFWHM (Fig. 4.6). This is a proxy for line shape and it demonstrates that the line starts out, at M0.0V, as broad and shallow which narrows and deepens until M2.0V at which point the line stays narrow and quickly becomes shallow again before reaching the molecular continuum by M5.5V. This can be observed in Figure A.2 as well. This is contrary to the predictions of the PHOENIX model that shows the photospheric Ca ii IRT line remaining prominent past M5.5V. In the CARMENES data, as shown in Figure. A.2, we find no evidence for Ca ii IRT past M5.5V.

Figure 4.6 shows the line shape evolution for the Hα N sample. In Figure 4.7 we expand on Figure 4.6 to show the full sample. Here it can be seen that as a star becomes more active, its position in this plot moves along the same pathway as the line evolution by increasing spectral type. If we compare spectra of the same spectral subtype in N sample and E sample configurations (Fig. 4.8), we can see that the activity directly fills in the absorption dip. This is in contrast to Hα, where the first noticeable signs of activity come from increased wing emission (Fig. 4.9, 1.21). Figure 4.10 shows that the N sample is tightly correlated between Hα and Ca ii IRT. The E sample is less well correlated but in general, if a star is active in Hα then it is so with Ca ii IRT.

Overall the line behavior makes Ca ii IRT difficult to use to differentiate N and E, and

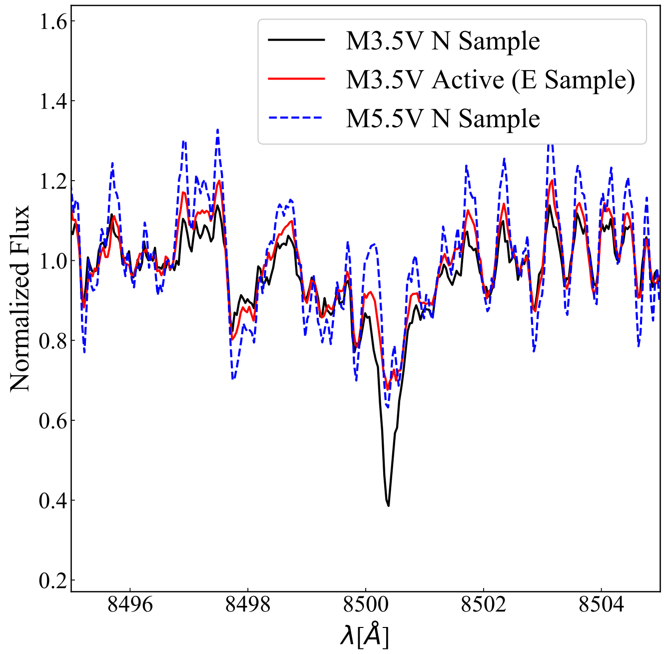

Figure 4.8.: Comparison of active and quiet Ca II IRT-A profiles. Black line is a M3.5V probable quiescent star. Red line is an M3.5V active star. Dotted blue line is a probable quiescent M5.5V star. Note that the active M3.5V and quiet M5.5V have very similar Ca II IRT-A core flux values.

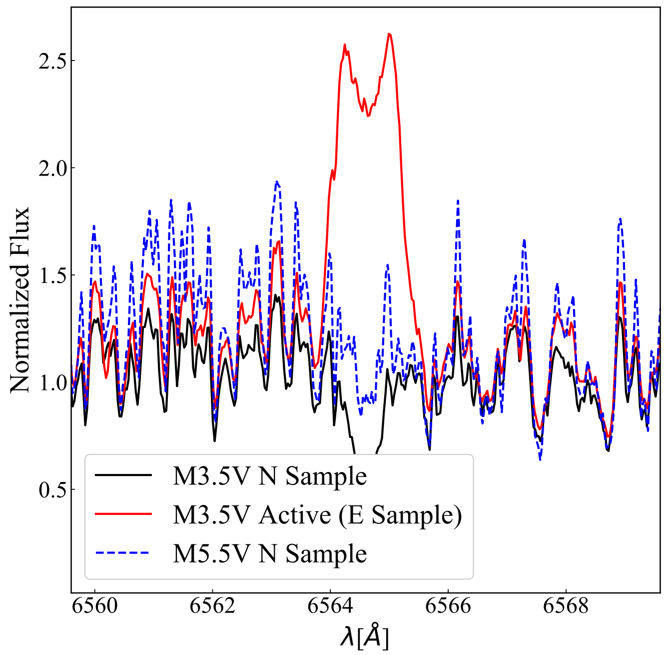

Figure 4.9.: Comparison of active and quiet Hα profiles. Black line is a M3.5V probable quiescent star. Red line is an M3.5V active star. Dotted blue line is a probable quiescent M5.5V star.

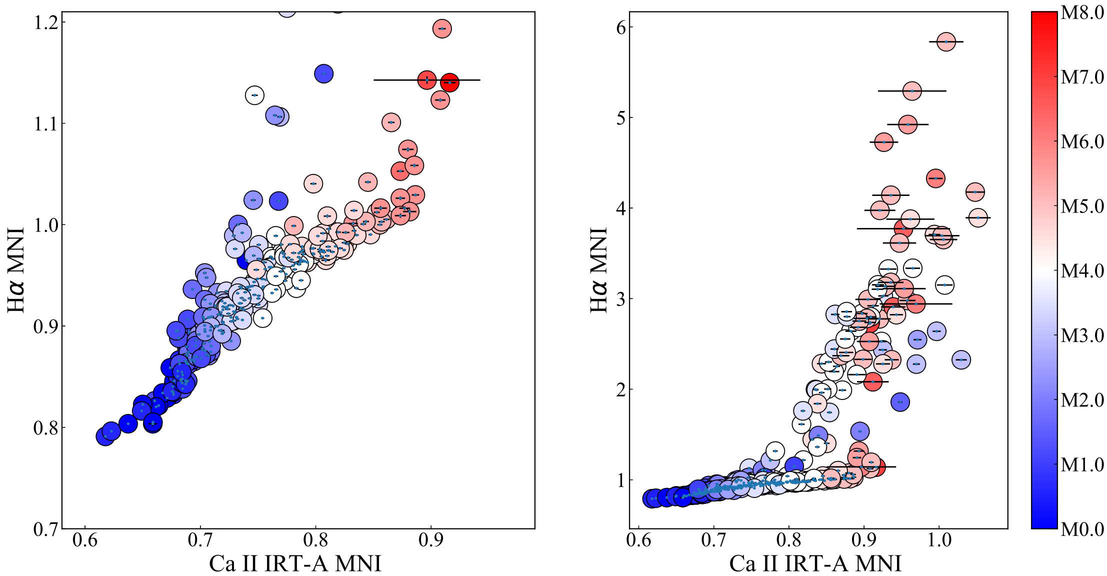

Figure 4.10.: Hα vs Ca II IRT median MNI values. *Left*: Zoom in of the lowest activity stars. *Right*: full sample.

thus we used the Hα N sample in this analysis to classify activity. We tried using the variability of Ca II IRT to differentiate the samples with an initial value of 0.15. This corresponded to 213 (64%) inactive stars. To match the Hα inactive sample we had to change the variability cutoff to 0.1535. Due to the difficulty in differentiating varying levels of activity, it is our conclusion that Hα is the more useful activity indicator.

4.3. Na I $D_{1\&2}$

The Na I $D_{1\&2}$ lines, with an activation energy of 2.1 eV, have long been considered a prime candidate for a low level activity indicator (Andretta et al. 1997). Many authors, however, have encountered issues, such as a proper definition of a pseudo-continuum, telluric contamination and low flux in late type M dwarfs, in employing the D lines as an indicator (Díaz et al. 2007; Johnson et al. 2021). We encountered our own issues as well, starting with the photospheric component of the D lines. With the CARMENES instrument the order width gets smaller with decreasing wavelength to the point that the entire order, that contains the D lines, is affected by the photospheric component (Fig. A.3). We nevertheless attempted to compensate for this by looking for the contrast between the photospheric component and the chromospheric component. The wavelength ranges are listed in Appendix Tables A.3 & A.4. As the results for Na I D_1 and Na I D_2 are similar, we present the results for Na I D_1.

The result of this application of the MNI is shown in Figure 4.11. As with Hα and Ca II IRT, the majority of active stars are later than M3V. Looking at the Hα N sam-

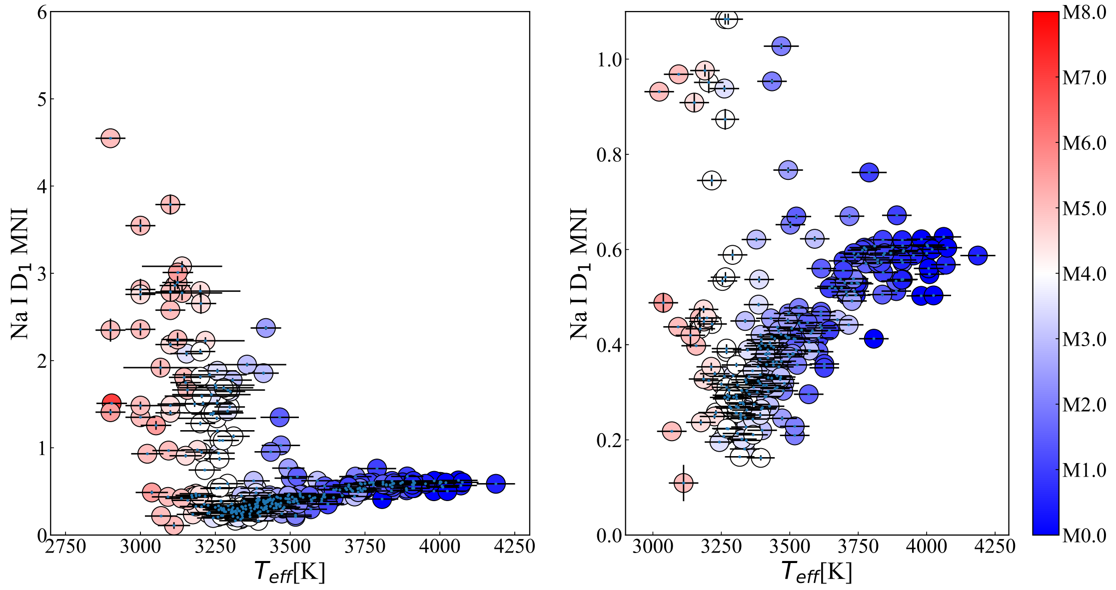

Figure 4.11.: Median MNI values for Na I D_1 vs effective temperature. *Left:* full sample. *Right:* Zoomed in view of the least active stars

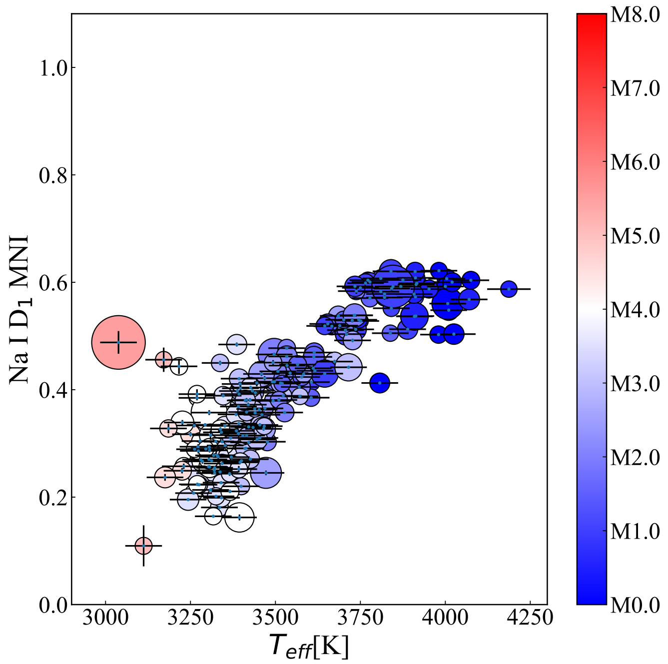

Figure 4.12.: Median MNI values for Na I D_1 vs effective temperature. Marker size denotes variability. Displayed are the Hα N sample.

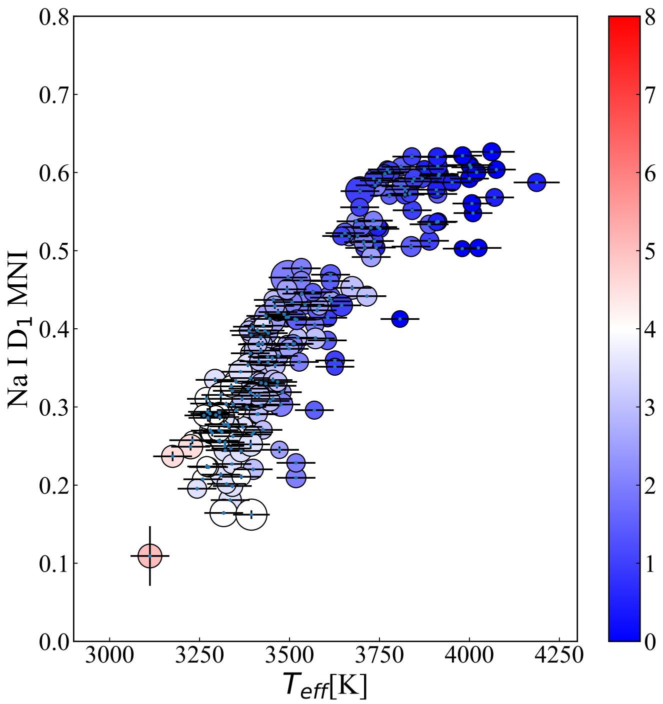

Figure 4.13.: Median MNI values for Na I D_1 vs effective temperature. Marker size denotes variability. Displayed are the Na I D_1 low activity sample.

ple (Fig. 4.12), we can observe a strong dependence on effective temperature. Initially, the ratio of the core to the wings (in essence the ratio of the chromospheric component of the line to the photospheric component) holds steady or slightly increases with temperature. After 3750 K, this ratio quickly declines. Isolating the low activity sample for Na I $D_{1\&2}$ was, at first glance, more straight forward than it was for Ca II IRT. It was soon realized, however, that telluric airglow can have a major impact on the presentation of the sodium lines.

The telluric airglow can affect the MNI measurement if the telluric emission line is in any of the measurement regions. If this occurs often enough it can also affect the variability. In several instances this caused what would otherwise be viewed as a low activity star, by the median MNI, to have the variability of a much more active star. We classified these stars as *indeterminate*. Out of 322 stars with sufficiently good spectra to analyze, we determined 175 stars to be low activity, 123 as active and 24 as indeterminate (Fig. 4.13). If all the indeterminate stars are low activity, as we suspect based on Hα, then the distribution comes to 199 (61.8%) low activity and 123 (38.2%) as active.

We conclude that using the Na I $D_{1\&2}$ lines as activity indicators in hopes of detecting lower level activity is not effective, and with the aforementioned issues their use as an activity indicator in general is of limited usefulness. In comparing Hα to Na I D_1 (Fig. 4.14) the scatter in the active branch is much larger than that of Hα and Ca II IRT. Similarly, this can be seen with Ca II IRT as well (Fig. 4.15). Gomes da Silva et al. (2011) found the

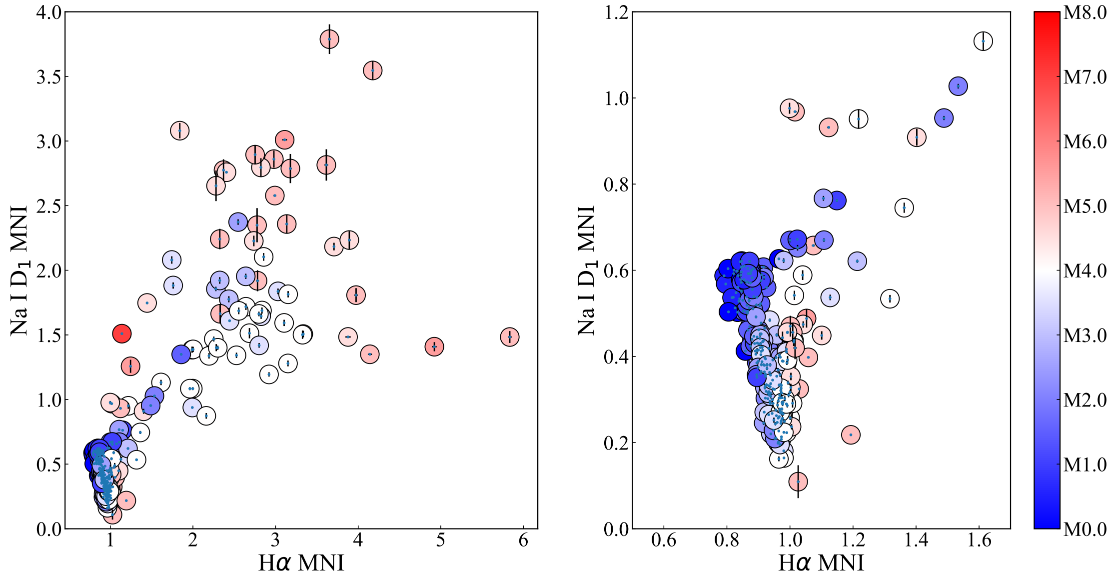

Figure 4.14.: Median MNI values for Na I D_1 versus median MNI values for Hα. *Left:* Full sample. *Right:* Zoomed in area showing lowest activity stars.

Na I $D_{1\&2}$ lines to be the most variable of the lines that they were studying, but did not mention compensating for telluric airglow which, as we have demonstrated, can cause a star to appear more active than it actually is.

4.4. He I D_3

With an activation energy of 23.07 eV, we did not expect to observe any signal from He I D_3 [5877.3Å] in the Hα derived N sample. It was therefore unexpected when a slight trend toward increased absorption with decreasing effective temperature was detected (Fig. 4.16). In Figures A.5 and A.6, it can be seen that this trend is not due to the He I D_3 line but rather that the He I D_3 line is in the wing of the Na I $D_{1\&2}$ lines' photospheric component. As with Na I $D_{1\&2}$, the change in this photospheric component over the range of M dwarfs can impart a small signal on the He I D_3 measurement. The change in the continuum and depth of molecular lines can introduce normalization issues as well. The wavelength ranges used for the calculation of the He I D_3 index and MNI are given in Table A.5.

This small effect, however, becomes insignificant when measuring more active stars (Figs. 4.17 and 4.18). Once the chromospheres of active stars are sufficiently energized to generate measurable levels of He I D_3 the correlation with Hα becomes significant. This can be seen by the fewer active stars in He I D_3 than Hα (79 active for He I D_3 compared to 115 active for Hα). We therefore conclude that while He I D_3 is of little use in the low activity sample, it is a good discriminator between moderately and acutely active stars. That Hα,

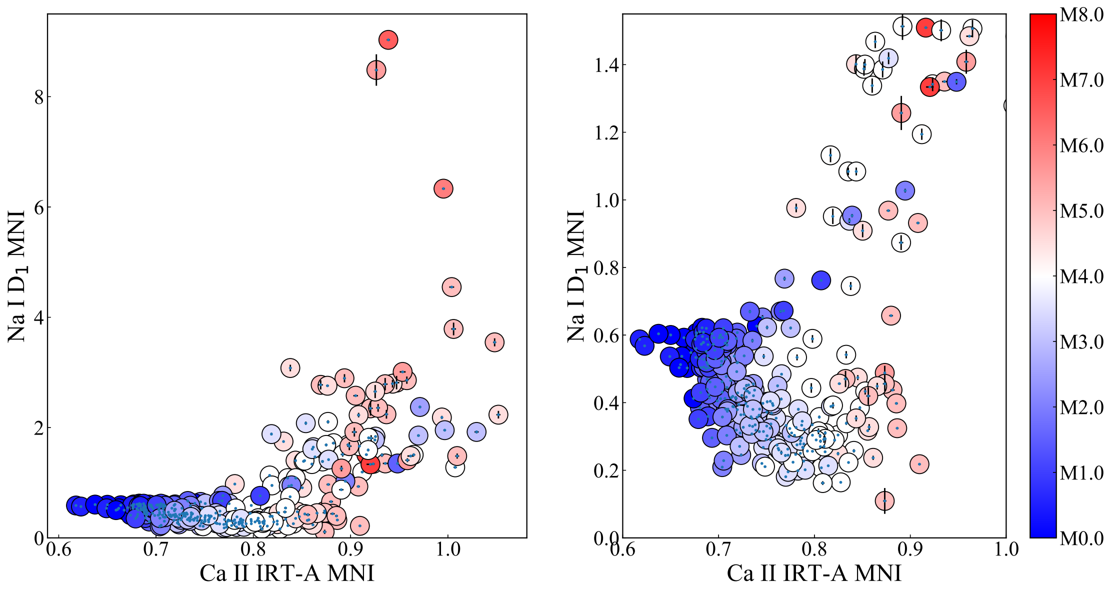

Figure 4.15.: Median MNI values for Na I D_1 versus median Ca II IRT values. *Left:* Full sample. *Right:* Zoomed in area showing lowest activity stars.

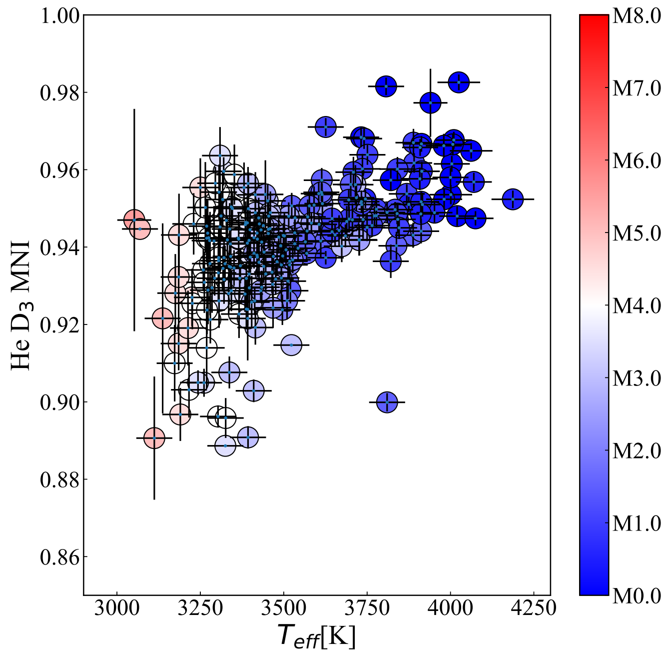

Figure 4.16.: Median MNI values for He I D_3 vs T_{eff}.

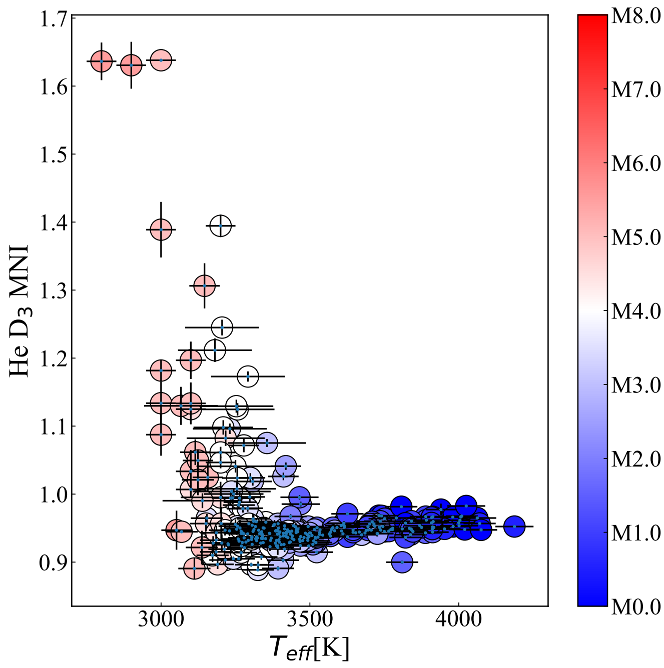

Figure 4.17.: Median MNI values for He I D_3 vs effective temperature for the full sample.

Ca II IRT, and Na I $D_{1\&2}$ correlate well in terms of number of active stars and He I D_3 does not, agree well with the findings of Gomes da Silva et al. (2011) and Schöfer et al. (2019). As He I D_3 is the only activity indicator with a significantly different number of active stars, this supports the conclusions of Saar et al. (1997) and Hintz et al. (2019), among others, in that He I D_3 has different formation conditions and altitude than the rest of the activity indicators in this work.

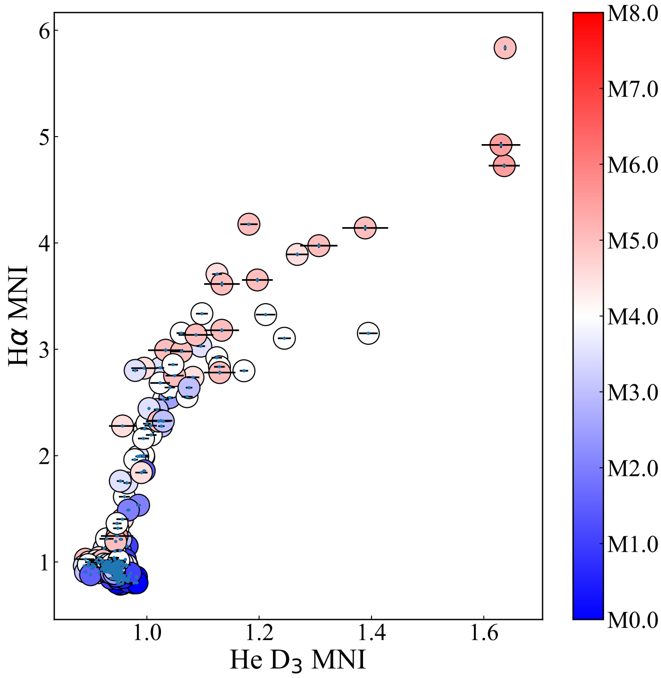

Figure 4.18.: Median MNI values for Hα vs He I D_3 median MNI values.

5. Discussion

In this chapter we will place our results into context with previous works and theory. We will begin by comparing our results to that of Schöfer et al. (2019) who worked on an earlier version of the CARMENES data set. Following this we will discuss our Hα and Ca II IRT results and present a proposal for an updated model of line formation in M dwarfs. Lastly we will analyze the application of the MNI to model photospheres of M dwarfs.

5.1. Determining reference stars

In Section 2.4, we discussed how determining a set of reference stars for each spectral subtype can be a useful exercise in a number of applications. Principal among these are spectral subtraction techniques such as those employed by Schöfer et al. (2019) and Montes et al. (1997). We also noted that the best, current, method of using the stars with the longest rotation periods was logical, but was prone to the problem that rotation periods in M dwarfs with long rotation periods are very difficult to determine (Popinchalk et al. 2021). This effectively biases the sample to the longest *known* rotation periods rather than the longest actual periods.

In Section 4.1 we showed that, for the N sample, there is a strong relation between effective temperature and Hα absorption. In Figure 5.1 we show how this relation looks over the span of one spectral subtype, in this case M1.0V. By fitting a line to this trend, we fit the Hα absorption loss over one spectral subtype. This fit takes into account the Hα absorption, T_{eff} and the variability. We decided not to include metallicity in this selection process due to the known issues involved in this measurement. To determine our new set of reference stars we use

$$R = \sqrt{[\frac{(T_m - T_*)}{10K}]^2 + (100V)^2 + [100(\mathrm{MNI}_m - \mathrm{MNI}_*)]^2}. \tag{5.1}$$

R is the ranking value of the star. T_m is the median temperature of the sample, T_* is the temperature of the star in question, V corresponds to the variability of the MNI (defined in Section 3.4). This captures the amount of absorption in the line. In Figure 5.1, it can be seen that the pre-existing reference star (green star) is in a similar position to that of our suggested reference star (red star).

Table 5.1.: Comparison of reference star selections by spectral type. R is the ranking value as calculated by Eq. 5.1

	CARMENES Reference		MNI Reference	
SpT	Karmn	R	Karmn	R
M0.0V	J14257+236W	3.48	J07393+021	2.17
M0.5V	J18580+059	2.95	J12312+086	1.51
M1.0V	J18051–030	11.44	J13209+342	2.73
M1.5V	J16254+543	10.18	J13457+148	2.08
M2.0V	J06103+821	4.07	J10289+008	2.11
M2.5V	J09360–216	3.0	J11421+267	2.07
M3.0V	J15194–077	2.65	J19084+322	1.9
M3.5V	J17578+046	10.77	J14310–122	1.68
M4.0V	J11477+008	6.97	J09447–182	2.67
M4.5V	J19216+208	7.78	J17033+514	4.34
M5.0V	J03133+047	12.85	J18165+048	6.57
M5.5V	J00067–075	13.36	J00067–075	13.36
M6.0V	J07403–174	...	J07403–174	...

Expanding this process to the the full low-activity sample (Fig. 5.2), shows that, except for subtypes M1.5V and M2.5V, the two methods produce consistent results. We tabulate our results in Table 5.1. Similarly if we plot the two sets of reference stars of rotation period against spectral sub-type (Fig. 5.3) it can be seen that, for the stars that have rotation periods, Eqn. 5.1 selects longer rotators as well. It should be noted that spectral sub-types that do not have a red star displayed indicates that the star selected by the MNI method did not have a known rotation period. The least active stars are also the slowest rotators with the least amount of rotational variability which makes determining a rotational period extremely difficult. The benefits of using this methodology over using the rotational periods are twofold. First we are less likely to bias a spectral subtype by selecting a star that is on the extreme end of the temperature range for that subtype. Our method selects the most representative star (midpoint of the absorption-temperature relation) for that subtype. Second, on a purely practical side, it removes the need for having rotation periods to determine a reference star and thus saves on observing time.

5.2. Hα

The Hα absorption in the lowest activity M dwarfs has been taken as a sign of activity as it requires a chromosphere that is hotter than the photosphere to produce. This implies the chromosphere was heated and was thus assumed to be caused by the same mechanism that causes more energetic forms of stellar activity. Cram & Mullan (1979) described the process of Hα line formation as an initial increase in Hα absorption to a point of

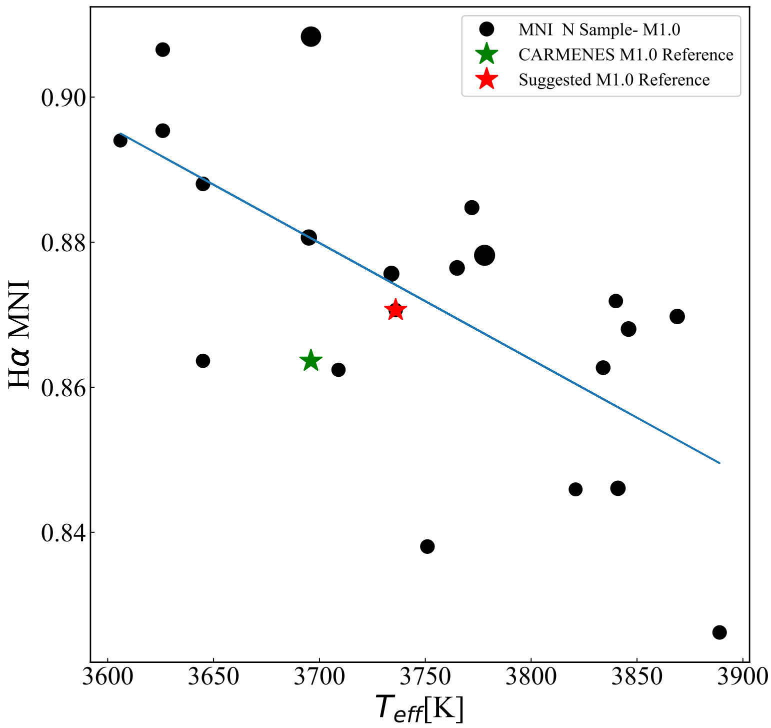

Figure 5.1.: M1.0V N sample stars comparing the MNI to the effective temperature. The blue line denotes the trend of cooling temperatures over the spectral type. The green star represents the CARMENES reference star for this spectral type. The red star marks the suggested reference star based on the MNI information. Marker size denotes variability.

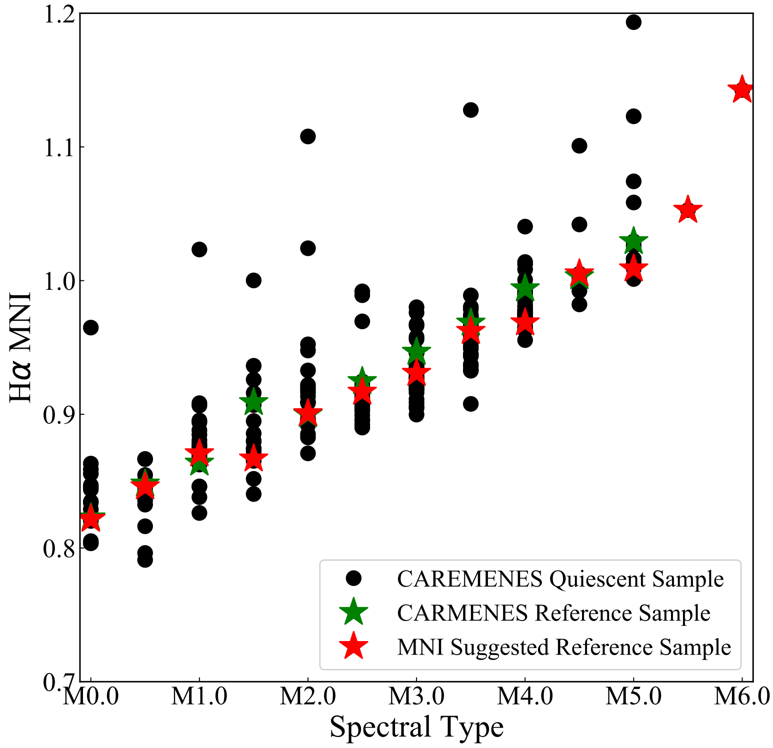

Figure 5.2.: Median MNI values for the N sample (black dots) with the CARMENES reference stars overlaid in green stars and the MNI suggested reference stars in red stars.

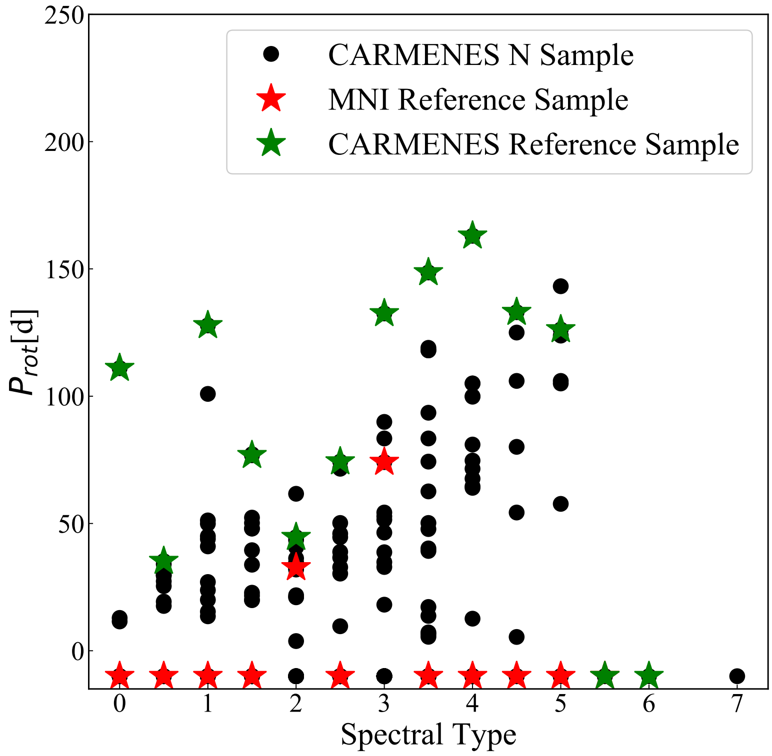

Figure 5.3.: Period values for the N sample with CARMENES reference stars marked in green stars and MNI suggested reference stars in red stars. Stars at the bottom of the plot with negative day periods are those without a known period.

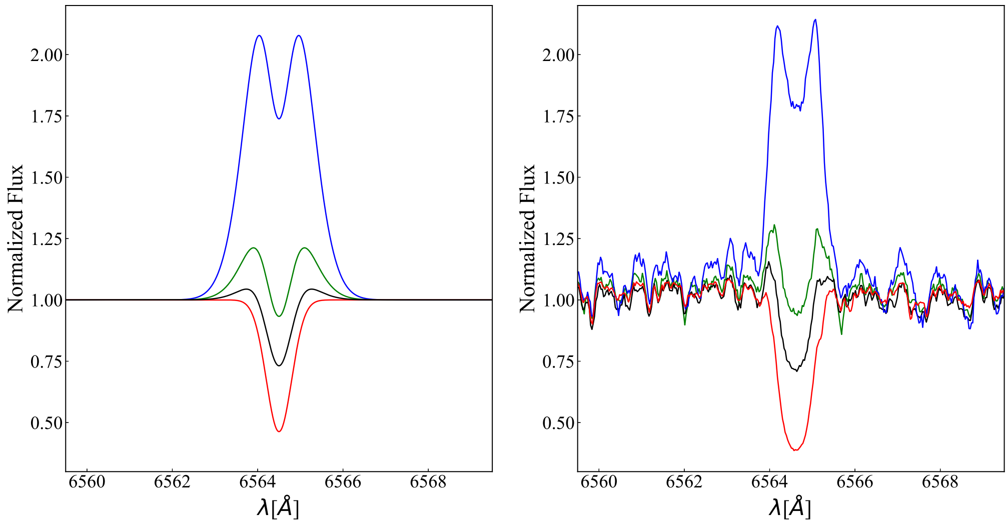

Figure 5.4.: *left*: Simulated Hα profiles using a two component Gaussian approximation. The emission component has a FWHM of 1.4 Å and the absorptive component has a FWHM of 0.7 Å. These values are roughly equivalent to an M3.5V star from the CARMENES sample. *Right*: Observed profiles from CARMENES spectra.

maximum Hα absorption and then a filling in of this absorption with emission until a classic *dMe* profile is produced. This creates a system where one would expect both a slightly and mildly active star to have the same profile, creating the issue of differentiating one from the other. However, as we have shown in Figure 4.1, there is a strong relation between the amount of Hα absorption and the effective temperature of the star. Similarly the variability of a star is directly related to the level of activity of the star until it reaches the least active stars (Fig. 3.15) which was also noted by Schöfer et al. (2019). In the least active stars the variability is stratified by spectral type (Fig. 4.1), indicating that the previously strong relation with activity, thought to be due to magnetic effects, no longer exists. This relation also cannot be due to any noise limitation as it includes both high S/N and low S/N stars.

The Hα line core flux and the pFWHM (Figs. 4.2, 4.3) both show a distinct delineation between the E sample and the N sample. Fig. 4.2 shows that the width of the Hα line is, on average, 0.7 Å different between the N and E samples, for a given spectral type. The Hα profile toy model (Fig. 5.4) shows that the different observed profiles could be reproduced using a two component model. One component consisting of a relatively thin absorption profile and another of a relatively wide emission profile. Additionally Figure 5.5 illustrates that if every profile were equally likely, then there should not be a gap between the N and E samples. We can, therefore, draw a few inferences from these data.

Firstly the absorption seen in Hα seems to be driven by a different process than what causes Hα emission. That the amount of this absorption is dictated by the stellar effective temperature is indicative that this is an intrinsic property of the star rather than being an

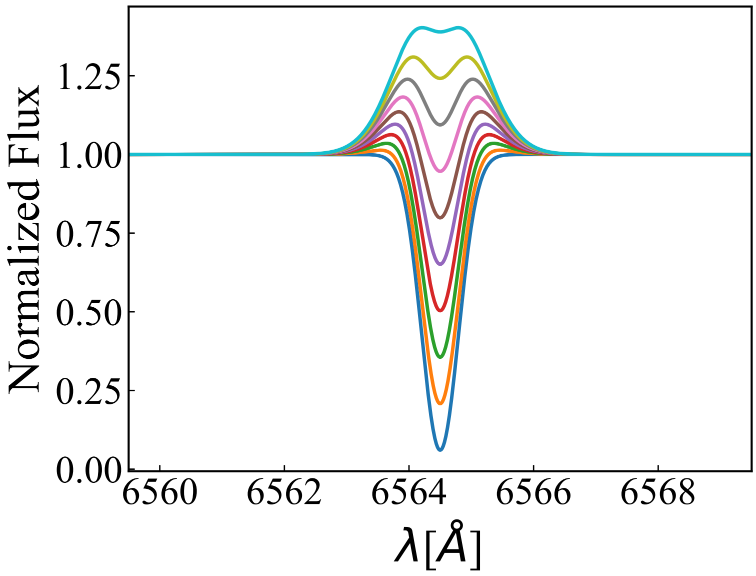

Figure 5.5.: Two component Hα simulation. Emission component has a FWHM of 1.4 Å and stars at zero amplitude to create a fully absorptive profile. The absorption component has a width of 0.7 Å and starts at max amplitude. Each step removes amplitude from the absorptive component and adds the same amount of amplitude to the emissive component. All other parameters of the Gaussians were held constant.

effect of activity. The loss of this absorption over the spectral range of M stars can be interpreted as the cooling of the chromosphere over the same range. Eventually, after M6.0V, the quiet chromosphere is no longer hot enough to absorb any Hα photons and the line disappears in quiet stars.

Secondly, the gap between the activity branch stars and the quiescent stars, suggests that the transition from a star with Hα in emission to a quiescent, Hα absorptive, star occurs rapidly. With the assumption that Hα line profile can be thought of as a composite between absorptive and emissive components and the knowledge that the absorptive component is the signature of the quiet chromosphere, we can conclude that the central reversal seen in many active M dwarfs is due to the relative amount of quiet and active chromospheres with a minimal amount of self absorption. This would explain the frequently observed asymmetries in the Hα profile in that different distributions of active and quiet regions would move the center of the quiet and active components relative to one another, creating an asymmetry. These asymmetries, therefore, should occur less frequently on slower rotating stars as the range of available radial velocities that a surface element can have reduces. On late type M dwarfs (later than M5.5V) the central reversal should be rare to non-existant as there would be no quiet chromosphere capable of absorbing Hα photons. The only exception to this is if the star has developed a lot of active regions and the radiation from these regions is enough excite the hydrogen in the surrounding quiet chromosphere to be able to absorb some Hα, photons, in which case the reversal should be small and irregular.

Lastly, we can refine our understanding of how the Hα profile evolves. We usually describe the Hα as profile *filling in* as it has been assumed that as the activity level increases, Hα first goes from neutrality into absorption. A maximum absorption value is reached then emission counter acts the absorption first then goes into emission. With the knowledge that Hα is likely a two component line profile and the emissive component is wider than the absorptive component, filling in is difficult. Starting as a fully absorptive star the first signs of activity would be in the wings of Hα which would become elevated and variable, as we observe. Concurrently the bottom of the absorption trough would rise up but the overall amount of absorption would only slightly decrease. This results in the apparent effect of the absorption profile being *lifted up* until it becomes a central reversal in a classically active dMe star profile. Overall this analysis of Hα corroborates the work done by Hintz et al. (2019) in that they found for inactive M dwarfs a single temperature-pressure profile could replicate the observed profiles while for active stars a minimum of two temperature-pressure profiles were required. Integration of the two profiles was done via a filling factor. A visual description of the different stages of Hα profile evolution can be found in Figure 5.4, in which we show that what adding a wide emission feature to a reducing narrow absorption feature would produce. With this we can state that we do not observe any evidence that supports the Cram & Mullan (1979) description of Hα first going into absorption from neutrality. Our findings are much more in line with Schrijver (1987) acoustical heating model and description of Ca II HK as having basal chromospheric flux.

5.3. Ca II IRT

Unlike Hα, the Ca II IRT exists as a combination photospheric and chromospheric line in a quiet M0.0V star. Like Hα however, the absorption, in the quiescent sample, decreases as the effective temperature decreases. A difference with Hα is that the decrease in absorption is not linear. It appears as if the loss of absorption in the line pauses for spectral types M1.0V and M1.5V.

Our hypothesis for why this is, is that as the photosphere and chromosphere cool, the photospheric component loses the Ca II IRT absorption prior to the chromosphere. Since the photospheric component is collisionally broadened this results in the width of the line decreasing. As the chromosphere cools, however, it becomes *more* conducive to Ca II IRT formation and, being less collisionally broadened than the photosphere, the line deepens. The net result of these two effects is that the deepening of the chromospheric component offsets the loss of the width in the photospheric component and thus, the loss of absorption appears to pause. The chromospheric component is at its deepest at the M2.5V spectral sub-type. From M3.0V on, the line, now very thin after the complete loss of the photospheric component, quickly recedes. By M5.5V the line is no longer discernible from the molecular continuum. PHOENIX models do not show this early loss

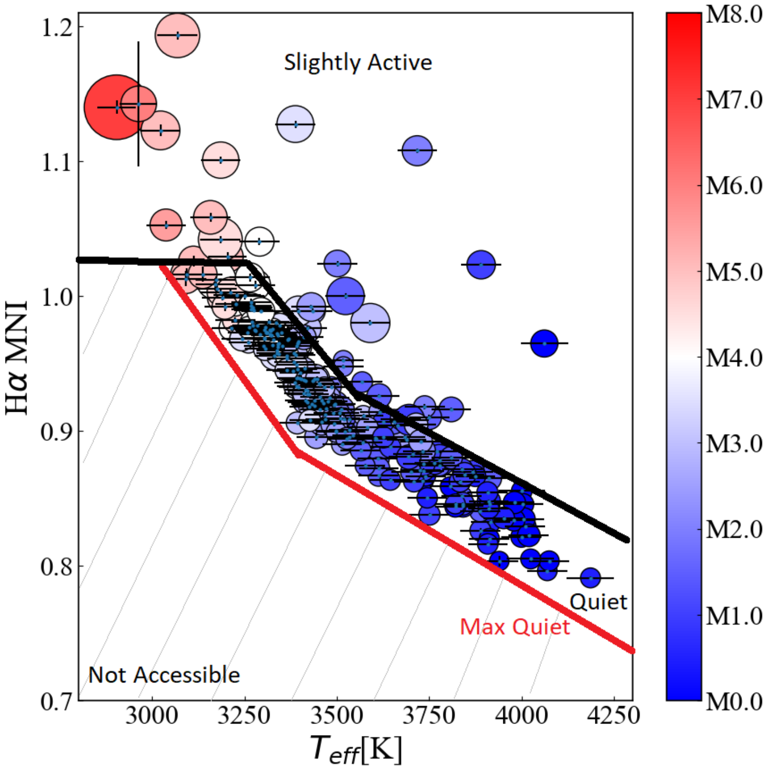

Figure 5.6.: Median Hα MNI vs T_{eff}. Regions separated by type of activity. In the gray area no stars are observed to have Hα absorption values. The red line indicates the maximum Hα absorption values and represent the value of an activity devoid star. The clustering of stars between the red and black lines represents the functionally quiet stars. These stars are mostly at the quiet values and the thickness of the band is probably due to stellar variables such as metallicity. Small amounts of activity can also be added to the width of this band, denoted by slight emission in wings and a raising of the core flux, but anything but the most minor and occasional activity would bump the star up into the next region *slightly active*. This slightly active region consists of profiles resembling Fig. 1.21 and is the first area that exhibits clear signs of wing emission and a substantially higher core flux.

of a photospheric component and continue to show evidence of the Ca II IRT line well past the point we can no longer differentiate it from the continuum. This suggests that there is some issue with modeling this line in M dwarfs and cannot aid us in determining the underlying causes of the observed line behavior.

Ca II IRT, unlike Hα, does seem to fill in as the activity level increases (Fig. 4.8). In early type stars this is seen as a thin emission spike in the middle of the photospheric absorption trough. In late type stars it is seen as less than normal absorption in mildly active stars, due to the now thinner overall profile, or a thin emission line in very active stars. There does not seem to be a width dichotomy between active and quiescent line profiles as we have seen in Hα. This could be due a number of effects. Firstly calcium is less susceptible to thermal broadening than Hα as it is more massive. Secondly, calcium forms lower in the chromosphere than Hα and, as such, is less susceptible to a change in chromospheric temperature gradient. Lastly, the narrower temperature tolerance of the Ca II ion in that if the temperature is too high then nearly all of the Ca II ions ionize to Ca III. Whatever the source of this effect is, it does have a confounding effect on activity determination, particularly for early type stars. This can be observed in Figure 4.6 as the line shape of a mildly active star is virtually identical to a earlier type quiescent star. Due to this problem we can conclude that the Ca II IRT lines do not perform as well as Hα in the role of chromospheric activity indicators.

Not being as good of an activity indicator as Hα, however, does not mean that Ca II IRT does not have an impact on activity determination. In Figure 1.17, the transition from ground singly ionized calcium to the lower energy level of Ca II IRT is a forbidden transition. Therefore the Ca II IRT levels can only be populated by a transition from the excited state, which would release a Ca II IRT photon, or by collisional excitation. In order to be in absorption the collisional excitation population method would have to be the dominant method of populating the Ca II IRT levels. This has the result that every time a Ca II IRT photon is absorbed the excited state becomes populated. From this higher state the electron has two options in order to release energy. The first is to descend back into the Ca II IRT level which would release a Ca II IRT photon again or, by an order of magnitude more likely, it will drop down to the Ca II ground level, releasing a Ca II HK photon. This will cause the Ca II HK line to appear to be more in emission that it otherwise would, with an over enhancement of the K vs H line due to two Ca II IRT lines feeding the K line to one Ca II IRT feeding the H line. As Ca II HK is frequently used as an activity indicator this process would make quiescent M dwarfs to appear more active than they actually are. This effect, however, should be removed after M5.5V, as there no longer is a Ca II IRT line to pump the excited state. Therefore quiescent late type stars should not exhibit Ca II HK emission. This mechanism corresponds well the findings of Schrijver (1987) that found Ca II HK emission was part of their described basal flux for the line and to the findings of Rauscher & Marcy (2006) who observed an enhancement of the K vs H line of Ca II HK for the lowest activity stars.

5.4. Comparison to previous works

As the MNI is a new indicator a direct conversion to previous works is not feasible. We can, however, compare results. The subject of chromospheric activity in M dwarfs has been studied extensively as it is viewed as a subject critical to understand in order to mitigate stellar radial velocity variability in exoplanet surveys in addition to having implications for the habitability of any planets found. Numerous authors have used a variety of data sets and methods to explore this subject (e.g., Stauffer & Hartmann 1986; Reid et al. 1995; Alonso-Floriano et al. 2015; Hodgkin et al. 1995; Gaidos et al. 2014; Jeffers et al. 2018; Newton et al. 2017; West et al. 2015; Reiners & Basri 2010; Lépine et al. 2013; Schöfer et al. 2019; Montes et al. 1997, among many others). The results were generally mixed on the specifics (e.g. which indicator correlated with which at a certain activity phase) but agreed on big picture items. One of the points of agreement is that as later spectral types are analyzed the percentage of active stars increases. Second, that all M dwarfs are in some fashion active. Lastly, the model of Cram & Mullan (1979) accurately displays the activity evolution of the Hα line. From our use of exclusively high resolution CARMENES spectra and the development of the MNI we agree with the first and disagree with the last two of these points. In the next section (Sec. 5.5) we will detail our contrast to the Cram & Mullan (1979) model. Here we will discuss some issues that previous authors, through no intrinsic fault, may have encountered that may have masked the results we have discussed in this work.

1. Use of low resolution spectra. Low resolution spectra R < 10,000 act to smear out the flux of a particular feature over a certain spectral range. This would effectively obliterate spectra such as featured in Fig. 1.21 and all that would be observed would be a flat line as the MNI or index value of these profiles are close to 1.0. This would lead the observer to conclude that Hα was not present in the spectrum and that this was observational support of an extremely low activity or quiet M dwarf by the prevailing model. Stauffer & Hartmann (1986) mentioned this exact concern and called for studies to be done at higher resolution.

2. Too broad of integration windows. The larger the integration window, the more the effect molecular absorption has on the index or equivalent width. For these methods any integration window larger than 1.5Å will encounter issues. At 3Å we found that the increase in molecular absorption over spectral types M0-M5 nearly balanced the decrease in Hα absorption over the same spectral range.

3. Methods not sensitive to low activity or quiet stars. The spectral subtraction technique employed by Schöfer et al. (2019) and Montes et al. (1997) are not sensitive to low activity stars as their methods subtract out their least active spectra to measure the emission more clearly. This work has shown that these methods are, in actuality, more effective than their authors suggest they are. This is due to the prevailing thought that Hα absorption still indicates some level of activity and therefore the subtraction was removing some of the activity that they were trying to measure. Whereas if our findings are correct they are actually subtracting a zero or near zero

activity state thereby yielding the full emission value that the target star is displaying.

While these are the main issues that we identified they are not an exhaustive list. The realization of both this work and reading of previous works is that the intricate atmospheres of M dwarfs are not to be underestimated in their complexity and methods that work on earlier type stars may not on M dwarfs without some modification. This should be particularly stressed on M dwarfs later than M5V, where additional factors, such as dust formation, can further complicate the spectra.

5.5. Proposal for line formation across the M dwarf sequence

The current model for stellar activity in M dwarfs is that, due to the fact that Ca II HK is always in emission, all M dwarfs are in some way active. This was reinforced by modeling showing that Hα would first go into absorption before filling in and going into emission as the activity level increases (Cram & Mullan 1979). It also suggested that the central reversal of Hα is due to self absorption. This model can explain the surface level observations of Ca II HK, Ca II IRT and Hα but has more difficulty in explaining the specifics.

Firstly, this model has difficulty explaining the observed distribution of Hα absorptive M dwarfs. It would be expected that there would be a fairly even distribution of stars of any spectral type of reaching the Hα maximum absorption and those that have not yet reached it or have gone past it. Rather, what we observe is that a large clump of the least active stars (slowest rotators) clump at certain Hα absorption values. The space between these maximum Hα absorption points and the clearly active Hα emission profiles is populated exclusively by stars exhibiting emission in the wings of Hα with a deep absorptive core such as shown in Fig. 1.21. We consider it likely that, due to the low spectral resolution available to some authors, the details of these profiles were not able to be resolved. If the flux of the emission wings and the central absorptive core were to be smeared out in anyway they would appear as a continuous function. Even the MNI method records the profile in Fig. 1.21 at a value of near 1.0. We also observe that the activity-induced variability of these stars is at a minimum level and not a continuation of the trend observed in the active stars. If these stars were a continuation of the same activity that produces the emission stars this trend should have continued into this group.

Secondly, the model has difficulty explaining the Hα intermediate profiles that have pronounced wing emission with a deep central reversal or that these profiles are preferentially seen in early type M dwarfs. It also does not explain why there is a difference in the widths of the profiles from the narrow absorption profile stars to the wide emission profile stars.

Our new model attempts to explain these issues and it rests on three assumptions: 1) All M dwarfs have a chromosphere that, without any stellar activity, is hotter than the photosphere through mechanisms such as acoustical heating. 2) Hα emission and absorption occur in different areas similar to active and quiet chromosphere on the Sun. 3) There is sufficient energy in the chromosphere in early to mid M dwarfs to collisionally excite the lower levels of the Ca II IRT transition.

We would also like to refer back to our running definition of stellar activity as *any magnetically induced excursion from the temperature-pressure profile of a star* and couple this with the observations from the previous sections to define four useful terms pertaining to different activity states of stars. We endeavor to do this as many terms such as quiet and active are often used but poorly defined. This frequently leads to confusion and disagreements where none should exist. We, therefore, propose the following definitions:

1. Zero Chromosphere (ZC) star: This star would, as the name suggests, be without a chromosphere in that there would be no chromospheric heating and the temperature would continue to drop with altitude beyond the photosphere. These stars are entirely theoretical in nature as none have ever been identified. Many refer to this as the only quiet star as they view any chromospheric heating as a form of activity. We disagree with this view as certain methods of chromospheric heating, such as acoustic waves, are a function of the stellar mass and thus part of the basic temperature-pressure profile of the star, not an excursion from it. On a more practical note, it does not seem logical to us to define all stars ever observed as active as this is then a label without a purpose.

2. Quiet star: Our definition of a quiet star, already touched on above, would be any star whose temperature pressure profile is dominated by basic stellar parameters (mass, effective temperature, log g). No magnetically active regions are present. This would include any star existing at the basal flux level in Schrijver (1987) and our N sample of stars. Chromospheric activity indicators in these stars would have a flux determined by the effective temperature of the star and not significantly vary from that state.

3. Active star: These stars have their temperature pressure profiles severely affected by magnetically active regions. Emission in chromospheric lines is ubiquitous and variable with the emission flux varying on timescales of minutes to hours. This would correspond to our E sample.

4. Intermediate star: These stars have a rough equivalence between quiet and active chromosphere. Profiles, such as Fig. 1.21, show both strong absorption and emission features. This state is rare in M dwarfs and is likely a short lived state in the evolution of the star. This would correspond to the stars that positioned between the N and E samples.

Under these assumptions and definitions it can be argued that:

1. The decreasing amount of Ca II IRT and Hα absorption from early to late M dwarfs is due to a decrease in the temperature of the chromosphere over these spectral types with early type chromospheres being hotter and more able to absorb Hα.

2. We propose that the Ca II HK emission in the quiet stars is influenced by absorption from the Ca II IRT lines via a shared upper energy level. As the transition strength of the Ca II HK transition is an order of magnitude higher than that of the Ca II IRT transition, the majority of these electrons will release an Ca II HK photon as they descend to the ground state of the Ca II ion. This creates a radiative imbalance that presents as apparent low level emission. This would also explain why Ca II HK, Hα, and Ca II IRT are correlated when Hα is in absorption as they are all driven by the temperature-pressure profile of a quiet chromosphere. This would also explain the disconnect when comparing He I D_3 to Ca II HK in that there was not a good correlation until the sample was reduced to stars that also showed Hα in emission, at which point the correlation was strong (Houdebine et al. 2009; Gomes da Silva et al. 2011).

3. The change in the trend of the variability-activity relation between that of the active stars and the Hα absorption dominated stars indicates that the absorption dominated stars form a set of quiet M dwarfs in the CARMENES sample. It would also explain why these stars are so difficult to get reliable rotation periods on as there are few, if any spots, and have very long rotation periods.

4. The central reversal may not be due to self absorption, or not entirely, but rather may be the result of the integration of the quiet (absorptive) and active(emission) regions into one spectra. This would, if correct, also result in the observed preference for intermediate profiles to exist in early type M dwarfs, as they have larger absorption profiles to make that combination more likely to occur. This would also account for the observed reduction in size of active star central reversals with both activity and increasing spectral type as in both cases the amount and the ability of the quiet chromosphere to absorb Hα would be negatively impacted.

5. Hα asymmetries are due to an asymmetric distribution of the active and quiet regions. As these distributions shift with both rotational phase and time, thereby shifting the centroid of the respective profile, the relative position of the absorptive profile to the emission profile would change and create an asymmetry in the overall line profile.

This model comes with a few predictions: since the maximum Hα and Ca II IRT absorption amount is decreasing over the spectral types M0.0V to M5.5V we would expect that no Hα or Ca II IRT absorption would be observed after M6.0V and without Ca II IRT in absorption there should no longer be anomalous Ca II HK emission. Hα would behave in these stars much like He I D_3 does in the early type stars in that it is either in emission or not present. Additionally on Hα emission stars the central reversal will become increasingly small and more erratic as the effective temperature decreases. Once the quiet chromosphere loses the ability to absorb Hα only the regions directly adjacent to active

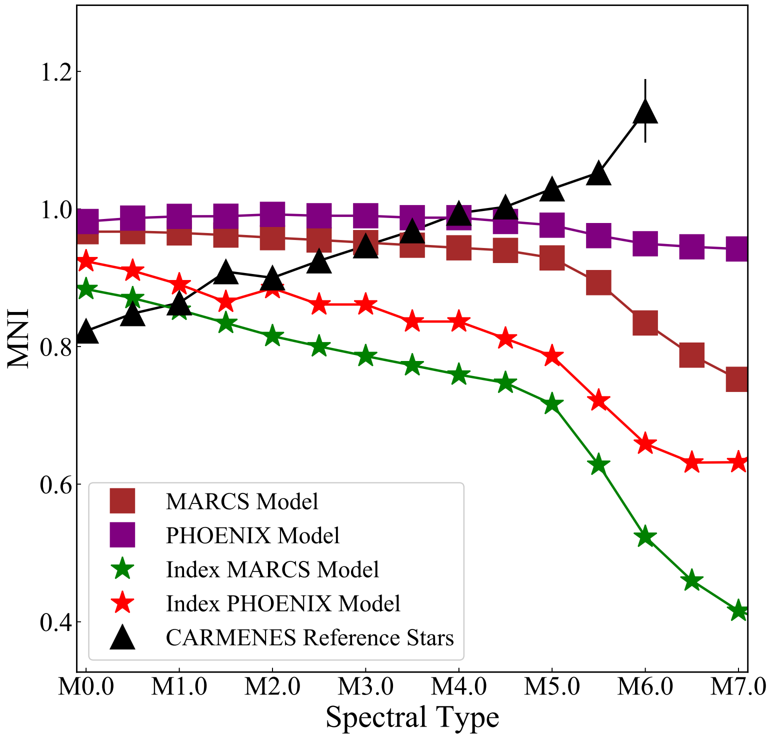

Figure 5.7.: Hα MNI and index values for MARCS and PHOENIX models after M5.0V. The black triangles, and squares are MNI values whilst the red and green stars are index values.

regions would get enough leaked radiation to be able to absorb Hα. This type of absorption would not result in a cohesive absorption profiles but in many widely distributed, small, absorption profiles thereby creating an erratic, ragged appearance to late type Hα profiles.

This model, if correct, would also give a benefit to exoplanet surveys encountering mildly active stars in that the asymmetries of the Hα profile would roughly correlate to the distribution of active regions and spots. This has a potential to be modeled in order to eliminate or reduce spot induced RV jitter.

5.6. Discrepancies in modeling molecule rich atmospheres

The PHOENIX and MARCS models were of invaluable assistance in verifying that the MNI method was effective at eliminating the molecular influence on the Index (Fig. 3.13), as they provided a Hα-less spectrum to test our reference regions against. However, toward later spectral subtypes, we noticed that the MNI values started deviating from the neutrality expectation which we did not see in the CARMENES sample. Expanding the evaluation to spectral types later than that available in quiescence for CARMENES (Fig. 5.7) made us aware that the MNI values continued to deteriorate. Compared to the index, however, the MNI still performed better but the excursion was concerning. We returned to our simulations (Section 3.7.1, Fig. 3.13) and reviewed some of the rejected runs and found that the pattern most closely matched simulations where we had overestimated the width of the molecular lines. This led to the merging of the lines and complete loss of any remnant continuum upon which the MNI and index depends resulting in the observed performance. We then attempted to replicate this by using the CARMENES coadded spectra that are effectively an average spectra of all observations for that star. We found that this issue did not present itself in any of the coadded spectra. As we looked at progressively later spectral types (M8, M9) we found that the signal to noise ratio decreased to the point that the continuum was effectively replaced by noise. So while measuring an emission line in reference to noise is of little use, except for, perhaps, providing a lower bound on the observed emission, we did not observe the same falloff in values as we did in the models of the same spectral type. Our conclusion from this is that the models may be overestimating the parameters of the molecular lines and that caution should be used in measuring Hα in very late type spectra.

6. Conclusions from chapters 3 to 5

We presented a new method for measuring chromospheric lines in M dwarfs, the MNI. This method allows for M dwarf chromospheric activity to be compared to that of earlier type stars directly as well as other M dwarfs with different levels of molecular contamination.

Using the MNI, we determined that, for the lowest activity stars in the CARMENES sample, the chromospheric absorption in Hα and the Ca II IRT is dependent on the stellar effective temperature rather than being tied to stellar activity effects. This results in a trend that, as the stellar temperature decreases, so does the absorption in these two lines. The lines cease to be discernible from the background at spectral types later than M5.5V.

We were also able to determine that Na I D$_2$ was severely limited in its potential use due to telluric air glow and loss of the surrounding continuum prior to the point where any low levels of stellar activity would be a useful indicator. He I D$_3$ proved to be a better indicator but not for low level activity stars. Rather He I D$_3$ is best suited for separating low and high activity stars. Ca II IRT is better suited than He I D$_3$ at determining activity in very low activity stars, but suffers from a fill-in problem in which it is difficult to discern a quiescent star from a very low activity star and a star of a different spectral subtype. The presence of Ca II IRT, however, presents an interesting issue in that it may artificially inflate the detected emission from Ca II HK, thereby causing a star to be perceived as being more active than it actually is. Overall, Hα is the preferred activity indicator as it can delineate the difference between very low level active and quiescent M dwarfs. We also showed that there exists a gap between the lowest activity stars and the more active stars which suggest that the time frame in which a M dwarf goes from displaying an active emission profile to that of a quiet absorption profile is very short.

We demonstrated that Hα can be modeled by a two component system with one component representing a quiet, thin, Hα absorptive profile and, the second component, an active, wide, emission profile. The combination of these two profiles can reproduce all observed Hα line profiles. That these two components have different widths causes the line, when moving from quiescence to activity, to appear to lift up rather than fill in. That these two components represent quiet and active chromospheres allows for the possibility of determining RV influence by measuring the relative RV deviation of the quiet to the emissive components.

Overall our most consequential conclusions are that we find no supporting evidence for the Cram & Mullan (1979) description of Hα going into absorption first before going into emission with increasing activity level. In contrast we find a basal amount of Hα, Ca II IRT and Na I $D_{1\&2}$ absorption that is strongly correlated with stellar effective temperature and can be considered as quiet. These findings are more in line with the conclusions of Schrijver (1987) and a mass-dependent acoustical heating model for the basal flux. Accordingly we put forth a model that describes the evolution of the various activity indicator line profiles. We also put forth a hypothesis regarding a proposed mechanism for Ca II IRT to pump the excited energy levels of Ca II HK through the sharing of an upper energy level. This mechanism would explain why Schrijver (1987) observed Ca II HK emission as part of their basal flux. This, however, should be effectively modeled with NLTE chromospheric models to confirm.

7. High cadence spectroscopic and photometric observations of a post-flare co-rotating feature on GJ 3270

This chapter contends with the discovering of a co-rotating post-flare feature on the rapidly rotating M dwarf GJ 3270. It has been already published in Astronomy and Astrophysics (Johnson et al. 2021, A&A, 651,A105)] under an open license. Here we present the main body of the work, adapted to fit the format of this thesis. All content remains qualitatively identical to the original. For the content of the appendix, authors list and acknowledgements we refer to the A&A website[1]. As a function of working in a consortium this chapter is more of a collaborative effort than the second chapter but still is, in the vast majority, my work. Besides the extensive review efforts provided by the members of the CARMENES consortium, the contributions of note should be to Stefan Czesla and Birgit Fuhrmeister who added a lot of feedback and assistance with building the model that estimated the flare energy. Carlos Cardona Guillen also contributed to the stellar parameters section by narrowing down some details of GJ 3270, particularly the age and moving group.

7.1. Introduction

This chapter contains the paper published with Astronomy and Astrophysics (A&A 651, A105-2021) under an open license. The main content of the paper is in this chapter unchanged except for the formatting of the figures, which have been changed to fit the format of this thesis. The abstract and appendixes of the paper are not included and can be found on the publishers website as well as arxiv (Johnson et al. 2021). As a function of working in a consortium this chapter is more of a collaborative effort than the second chapter but still is, in the vast majority, my work. Besides the extensive review efforts provided by the members of the CARMENES consortium the contributions of note should be to Stefan Czesla and Birgit Fuhrmeister who added a lot of feedback and assistance with building the model that estimated the flare energy. Carlos Cardona Guillen also

[1] https://www.aanda.org/articles/aa/full_html/2021/07/aa40159-20/aa40159-20.html

contributed to the stellar parameters section by narrowing down some details of GJ 3270, particularly the age and moving group.

As a result of their ubiquity, low mass, and close-in habitable zones, M dwarfs have garnered the interest of exoplanet surveys hunting Earth-like analogs. Some of these stars, however, are also known to have exceptional levels of stellar activity (Gizis et al. 2000; Khodachenko et al. 2007; Yelle et al. 2008; O'Malley-James & Kaltenegger 2017; Guarcello et al. 2019). These high levels of stellar activity cannot only make planet detection more difficult, but also call into question the habitability of any planets found around these stars (Johnstone et al. 2019; Tilley et al. 2019). The ionizing radiation and high energy particles released can erode or completely strip the atmosphere of an otherwise habitable planet. This process is particularly concerning for planets around M dwarfs because the habitable zone of these stars is much closer in. Particularly energetic events have been proposed as triggers of extinction events on Earth (Lingam & Loeb 2017). Therefore, knowing the frequency, energy, and history of these events on the host star is critical to understanding the habitability potential of a given exoplanet.

Stellar activity manifests itself on our Sun most prominently in the form of sunspots, plages, flares, and coronal mass ejections (CMEs – Strassmeier 1993; Benz & Güdel 2010). Stellar activity is usually more extreme in younger, faster-rotating stars (Appenzeller & Mundt 1989; Kiraga & Stepien 2007; Newton et al. 2016; Guarcello et al. 2019). Additionally the proportion of active to quiet stars in the M spectral type is higher than in other types of stars (West et al. 2008; Reiners et al. 2012; Jeffers et al. 2018). This effect is even more pronounced for late M dwarfs. It has been proposed, for M dwarfs later than ~M4, that this is due to the geometry of a the magnetic field of a star, which prevents ejection of material and inhibits the magnetic breaking of the star and its transition to a lower activity state (Barnes 2003; Reiners & Mohanty 2012).

While starspots on M dwarfs can often be studied from rotational modulation in photometric time series (Kron 1952; Barnes et al. 2015), the most noticeable feature of stellar activity in either photometry or spectroscopy are stellar flares (Budding 1977). Stellar flares result from a release of energy caused by magnetic reconnection in the upper atmosphere (Hawley & Pettersen 1991; Haisch et al. 1991; Hilton et al. 2010; Benz & Güdel 2010). This reconnection forces free electrons to follow the magnetic field lines into the chromosphere and photosphere. In the chromosphere, the release of X-rays and enhancement in the chromospheric lines is commonly observed. Upward flows of chromospheric material can also occur as heated material rises into the upper atmosphere. This phenomenon is referred to as chromospheric evaporation (Fisher et al. 1985; Abbett & Hawley 1999). The photosphere reacts by extremely rapid increase in brightness in the affected area (impulsive phase) followed by an exponential decay back to pre-flare brightness (decay phase) once the electron bombardment has ceased (Segura et al. 2010). The decay phase may last minutes to hours and in very rare cases days (Osten et al. 2016; Kuerster & Schmitt 1996). Post-flare arcades and additional minor reconnection events are common during this phase (Gopalswamy 2015). In cool stars flares are more noticeable at shorter wavelengths owing to the contrast of the typical temperatures of flares of

$\sim 10^4$ K (Kowalski et al. 2018; Fuhrmeister et al. 2018) and the host star of $\sim 10^3$ K. As the flare-affected region cools during the decay phase, this contrast fades, thereby leading to a change in the continuum slope over the course of the flare duration (Segura et al. 2010).

In spectra, flares are usually detected through enhancement of chromospheric lines, particularly the Balmer lines and those of singly ionized calcium (Hawley & Pettersen 1991; Crespo-Chacón et al. 2006; Fuhrmeister et al. 2008; Schmidt et al. 2011; Fuhrmeister et al. 2018). As opposed to the photometric flare signature of a near-immediate peak at the flare onset, spectroscopically observed flares may not have a peak for many tens of minutes into the event (Benz & Güdel 2010). Line profiles of chromospheric lines can also undergo broadening and exhibit both red and blue asymmetries in response to a flare (Fuhrmeister et al. 2018).

Line asymmetries are thought to vary during the course of a flare. However as a consequence of the random nature of observing a stellar flare, the most common detection is through chance observations during a survey. By their very nature these observations only show a moment in time of the progression of the flare. It is therefore difficult to ascertain in which phase an observation catches the flare, making the assignment of a phase to any observed line asymmetry impossible. In general blue asymmetries are assumed to occur in the pre-flare or rise phase and are indicative of chromospheric evaporation or other bulk upward plasma motions. Red asymmetries, on the other hand, are thought to be associated with coronal rain and the decay phase (Fuhrmeister et al. 2018).

The energies of stellar flares can vary dramatically with the magnitude of the flare and wavelength. The most energetic flares can emit 10^{37} erg in X-rays that can be an order of magnitude more energetic than that observed in visible wavelengths for the same flare (Kuerster & Schmitt 1996). Günther et al. (2020) estimated the bolometric energy of the largest M dwarf flares to be $10^{36.9}$ erg. These estimates, however, are usually based on the assumption that the flare is a blackbody, which may not be a good approximation. On the Sun the largest flares are three orders of magnitude lower in X-rays (Kane et al. 2005). The total energy released in the Carrington Event, the most powerful flare yet recorded, was estimated to be ~10^{33} erg (Aulanier et al. 2013). The smallest solar flares have been reported with energies as low as 10^{23} erg (Parnell & Jupp 2000).

The largest, longest-lasting solar flares are frequently associated with a CME. The velocity of this ejected mass can vary from 60 to 3200 $\mathrm{km\,s^{-1}}$ with masses on the order of 10^{12} kg (Benz & Güdel 2010). While CMEs are relatively easy to detect on our Sun, particularly if they directly impact Earth, they are far more difficult to detect on other stars and none have yet been conclusively identified (Vida et al. 2019a; Leitzinger et al. 2020). This primarily results from their diffuse nature and being outshined by the host star. Therefore, CMEs are easiest to observe in shorter wavelengths where the contrast is the highest. Coronal mass ejections are thought to produce large, asymmetric blue line asymmetries in Balmer lines as detectable indicators (Vida et al. 2019a). If the shift in the asymmetry corresponds to a velocity of at least 10 % of the stellar escape velocity, we can be reasonably confident that a CME has occurred. These CMEs are frequently associated with prominence ejections. Munro et al. (1979) found that as much as 70 %

of solar CMEs have an ejected prominence at their core. It is known that the mass of a prominence depends on the strength of the magnetic field of the host star (Villarreal D'Angelo et al. 2018). M dwarfs are known to have much stronger magnetic fields than the Sun (Shulyak et al. 2019) and thereby can presumably host much larger prominences. Cho et al. (2016) detect a large prominence prior to a flaring event on the Sun using high cadence spectroscopy.

While flaring is fundamentally random in nature, the odds of observing a flare increases when observing the more active fast-rotating stars due to the rotation-activity relation. The MEarth survey identified a number of stars whose rotational periods are thought to be less than a day (Berta et al. 2012). One of these stars, GJ 3270, is a M4.5 V star with a $v \sin i$ greater than 30 km s^{-1}and a rotation period shorter than 10 h (e.g., West et al. 2015; Kesseli et al. 2018).

In this paper, we analyze a series of flares that were observed on the ultra-fast-rotating M dwarf GJ 3270, which we observed on 15 December 2018, utilizing high cadence, simultaneous spectroscopy and photometry. In Section 7.2 we provide details on the instruments and the reduction of the data. In Section 7.3 we discuss the stellar parameters of GJ 3270. Section 7.4 we introduce the methods used to analyze the data. In Section 7.5 we present the results of our analysis, then discuss these results in Section 7.6.

7.2. Observations and data reduction

We present the instruments and data reduction used in this paper. The simultaneous, ground-based, photometry is discussed first followed by the long-baseline SuperWASP data. We then discuss the *TESS* data reduction followed up by the spectroscopic data provided by CARMENES.

7.2.1. Ground-based photometry

We obtained multiband photometry of GJ 3270 simultaneously with the MuSCAT2 instrument, mounted at the 1.52 m Telescopio Carlos Sáchez in the Teide Observatory (Narita et al. 2019), and the T150 and T90 Ritchie-Chrétien telescopes of the Observatorio de Sierra Nevada (SNO). The MuSCAT2 instrument has a field of view (FOV) of 7.4 × 7.4 arcmin. This instrument was designed to carry out multicolor simultaneous photometry. In our run, we used the r (full width at half maximum; FWHM: 1240 Å, henceforth r), i (FWHM: 1303 Å, henceforth i), and z_s (FWHM: 2558 Å) bands, which we refer to as r, i, and z bands in the following. The data that we utilized were preprocessed using the MuSCAT2 data pipeline, detailed in Parviainen et al. (2020).

The T150 and T90 telescopes at SNO were used to obtain simultaneous photometry in the Johnson B (FWHM: 781 Å) and V (FWHM: 991 Å) filters. The telescopes are equipped

Table 7.1.: Start time, duration, and exposure time at time of flare of photometric observations. SNO: S, MuSCAT2: M.

Filter	Start JD	Duration [h]	Exp. time [s]	Total Obs#
S B	2458468.304	5.0	30[a]	379
S V	2458468.298	8.6	30[b]	669
M r	2458468.398	5.59	22	941
M i	2458468.399	5.59	12	1755
M z	2458468.399	5.59	6	3093

a60 s during the first 3 hs; b100 s during the first and 60 s for the following 2 h.

with similar CCD cameras (VersArray 2k × 2k). Their FOVs are 7.9 × 7.9 arcmin^2 and 13.2 × 13.2 arcmin^2, respectively (Rodríguez et al. 2010). During the readout, we applied 2 × 2 binning for the T150 camera and no binning for the T90 camera.

Each CCD frame was corrected for bias and flat field and, subsequently, light curves were extracted by applying synthetic aperture photometry. All frames cover a number of suitable comparison stars for differential photometry. Different aperture sizes were tested to choose the best size for our observations. The normalization was done by dividing the light curve by its median value. The start time, duration, and exposure times of each photometric run are given in Table 7.1. Excerpts of the final normalized light curves, showing the two most prominent flaring events, are shown in Fig 7.1.

The Super-Wide Angle Search for Planets (SuperWASP, Pollacco et al. 2006) survey is a transiting planet survey conducted from two robotic observatories (located in La Palma, Spain, and Sutherland, South Africa), each with a setup of eight wide-angle cameras. The observations are done through a broadband filter covering 400–700 nm. GJ 3270 was monitored by the SuperWASP program from 2008 to 2014, culminating in ~57 000 observations over six seasons, each lasting about three months. Data were reduced by the SuperWASP team and detrended using methods designed to preserve variations of astrophysical origin, as detailed in Tamuz et al. (2005). As we utilized SuperWASP data for the sole purpose of analyzing dominant periodicities, associated with the stellar rotation and not for flaring analysis, we filtered the SuperWASP light curves iteratively to remove 4.0σ outliers.

7.2.2. Space-based *TESS* photometry

GJ 3270 was observed in Sector 5 by the *Transiting Exoplanet Survey Satellite* (*TESS*; Ricker et al. 2015) in two-minute cadence mode between 15 November and 11 December 2018. These observations ended five days prior to the beginning of our campaign. We used the *TESS* light curves available at Mikulski Archive for Space Telescopes.Utilizing

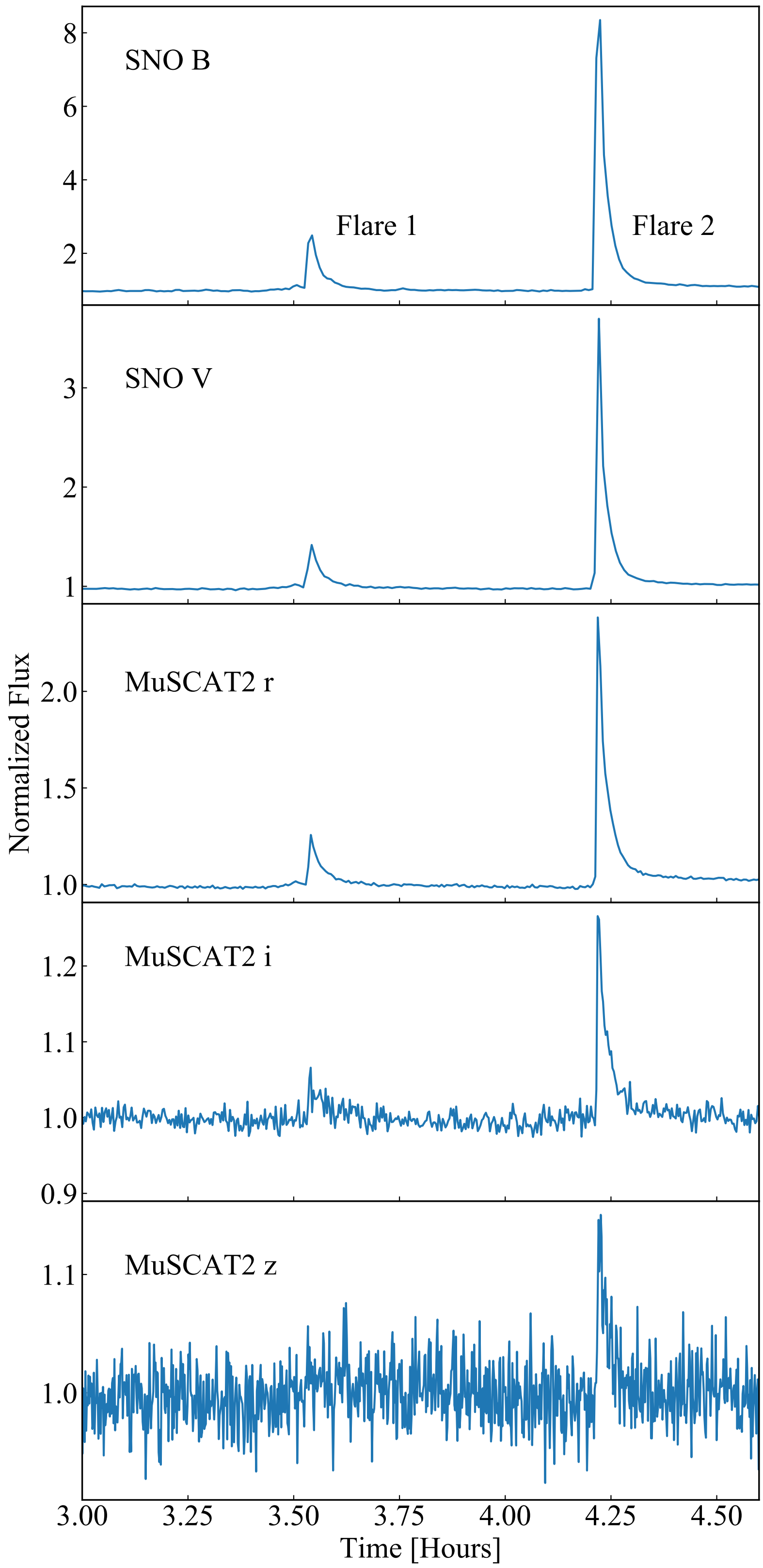

Figure 7.1.: The SNO observations normalized light curves in V and B band are shown in the top two panels. The normalized light curves of the MuSCAT2 data, in r, i, and z bands, are represented in the bottom three panels.

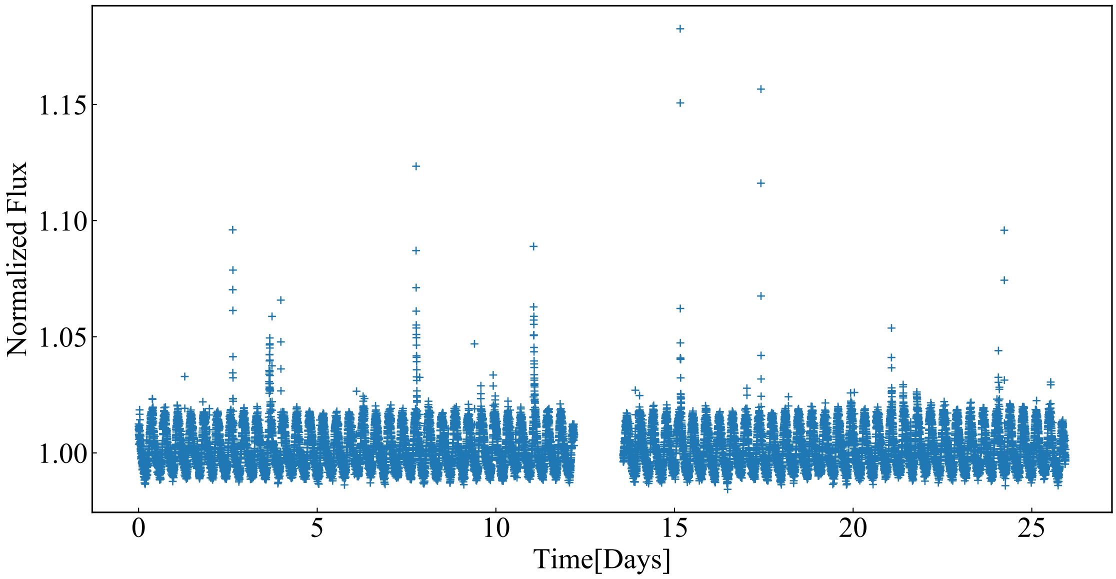

Figure 7.2.: *TESS* light curve of GJ 3270 from sector 5 observations. At least 22 flares occurred during this time span. Rotation of ˜0.3 d can be seen by inspection of the non-flaring light curve.

the PDCSAP data, we removed the data points flagged as low-quality by the *TESS* pipeline (Jenkins et al. 2016) prior to our analysis. The *TESS* light curve is given in Fig. 7.2.

7.2.3. CARMENES spectra

CARMENES[2] is a fiber-fed, highly stabilized spectrograph mounted at the Calar Alto 3.5 m telescope. The instrument has a visual (VIS) and near-infrared (NIR) channel, which are operated simultaneously (Quirrenbach et al. 2016). The VIS channel operates between 520 nm and 960 nm and the NIR channel between 960 nm and 1710 nm at spectral resolutions of 94,600 and 80,400, respectively.

Our observations of GJ 3270 were carried out on 15 December 2018 and comprise 28 VIS and NIR spectra, which each have an exposure time of 15 min. The spectral time series covers a total of 7.7 h. All spectra were reduced using the `caracal` pipeline, which relies on the flat-relative optimal extraction (Zechmeister et al. 2014; Caballero et al. 2016). In Table **??**, we give the central time of the observations and the duration since the first observation, and assign an observation number, which is used to refer to the spectra in the following.

[2] Calar Alto high-Resolution search for M dwarfs with Exoearths with Near-infrared and optical Échelle Spectrographs.

7.3. Stellar parameters

GJ 3270 has been placed in several young associations. In particular, it was proposed to be a member of the AB Doradus moving group by Bell et al. (2015). Cortés-Contreras et al. (2017a) proposed GJ 3270 as a member of the Local Association, also known as the Pleiades moving group (Eggen 1983). These groups range in age from 20 Myr to 300 Myr. The *ROSAT* All Sky Survey measured X-ray emission to be $\log(L_x) = 28.3\,\mathrm{erg\,s^{-1}}$ (Voges et al. 1999). This value is too low for the younger groups but is compatible for those from similar objects in AB Dor. Lithium 6708 Å was not detected in our spectra. This indicates that the age of GJ 3270 must be greater than about 50 Myr (Zickgraf et al. 2006). Therefore our age range for GJ 3270 is 50 Myr to 300 Myr with a most probable age of ~150 Myr as a member of AB Doradus. In color-magnitude diagrams GJ 3270 is not significantly over-luminous (Cifuentes et al. 2020). This indicates that it is nearly, or already on, the main sequence, as is expected for low-mass stars older than 100 Myr. Therefore, we can use main-sequence relations to determine its stellar parameters.

Using multiwavelength photometry from the blue optical to the mid-infrared, Cifuentes et al. (2020) estimate a T_{eff} of 3100±50 K for of GJ 3270. Using magnitude values only from Zacharias et al. (2013) and the color-temperature relations from Cox (2000), Reid & Hawley (2005a), and Pecaut & Mamajek (2013), we were able to confirm this value. However, owing the fast rotation and youth of GJ 3270, we assume a conservative ±200 K uncertainty when using T_{eff} in calculations. We chose a PHOENIX model spectra (Husser et al. 2013) with $T_{\mathrm{eff}} = 3100$ K, $\log g = 5.0$, and solar metallicity for our template spectra.

Cifuentes et al. (2020) also estimate the luminosity of GJ 3270 to be $0.00642 \pm 0.00003\, L_\odot$. With the mass-luminosity relationship in Eq. 7.1 (Schweitzer et al. 2019),

$$\frac{L}{L_\odot} = 0.163 \left(\frac{M}{M_\odot} \right)^{2.22\pm0.22} , \tag{7.1}$$

we determine the mass to be $0.25 \pm 0.07\, M_\odot$, which is consistent with the findings of Cifuentes et al. (2020).

Five days prior to our SNO and MuSCAT2 observations, *TESS* ended its observation of GJ 3270. We searched for periodic signals in the combined data set of the *TESS*, SNO, and MuSCAT2 photometric data using the generalized Lomb–Scargle periodogram (GLS, Zechmeister & Kürster 2009). The resulting power spectrum is shown in Fig. 7.3. The most significant signal is found at a period of 0.369829 ± 0.0000036 d (frequency ~2.70 $\mathrm{d^{-1}}$), which we interpret as the stellar rotation period and, henceforth, denote it by . The *TESS* light curve phase-folded to is shown in Fig 7.4. We consider the other formally highly significant peak at about 0.1848 d, which is very close to the rotational period reported by West et al. (2015) and Schöfer et al. (2019), a semi-period of the first because its power is about four times lower and nearly half the value of . The West et al. (2015) period determination was based on MEarth data prior to 2011. Interestingly, an analysis

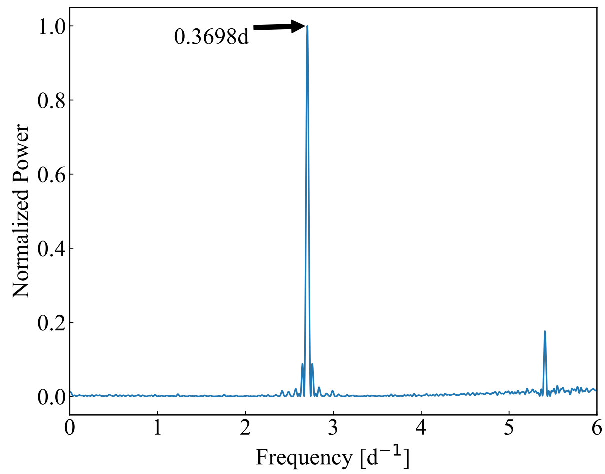

Figure 7.3.: Generalized periodogram of combined TESS and SNO V data. The power level of a 10^{-3} FAP is 0.0219.

of the SuperWASP light curves, which span several seasons, shows an evolution in the dominant periodicity from 0.1849 d before 2011 to 0.3697 d after 2013, as illustrated in Figure 7.5.

This evolution of dominant periodicity was previously described in Basri & Nguyen (2018) and Schöfer et al. (2019). They proposed a geometrical solution to the periodicity shifts. The simplest, solution being two spots 180 deg apart on the stellar surface. In Sections 7.6.2 and 7.6.3 we show evidence for two active regions on opposite hemispheres of GJ 3270. These regions, however, are traced using chromospheric activity indicators that are indicative of faculae or plague features more than spots. While we surmise that the periodicity shifts can arise from any bimodal surface, or near surface, heterogeneity that varies in relative strength over time, the driving mechanism is behind this phenomenon remains unclear. We consider this issue in need of further research because it has strong implications on determining whether a radial velocity (RV) signal is a potential close-in planet or stellar activity.

Reiners et al. (2018) report the $\upsilon \sin i$ of GJ 3270 to be 35.3 ± 3.5 km s^{-1} and Kesseli et al. (2018) report a $\upsilon \sin i$ value of 37.3 ± 1.3 km s^{-1}. In this work, we adopt the more conservative estimate by Reiners et al., but we note that using the Kesseli et al. values does not appreciably alter the results of this paper[3]. Combining the $\upsilon \sin i$ with the photometric rotation period, , the value for the stellar radius can be constrained as follows:

$$R = \frac{P_{rot} \upsilon \sin i}{2\pi \sin i} \geq \frac{P_{rot} \upsilon \sin i}{2\pi} . \tag{7.2}$$

This yields a lower radius limit of $0.26 \pm 0.05\, R_{\odot}$, which is consistent with the $0.278 \pm 0.009\, R_{\odot}$ determined by Cifuentes et al. (2020). Out of an abundance of caution we doubled the

[3]The $\upsilon \sin i$ value of 190.3 km s^{-1} reported by Jeffers et al. (2018) was incorrect.

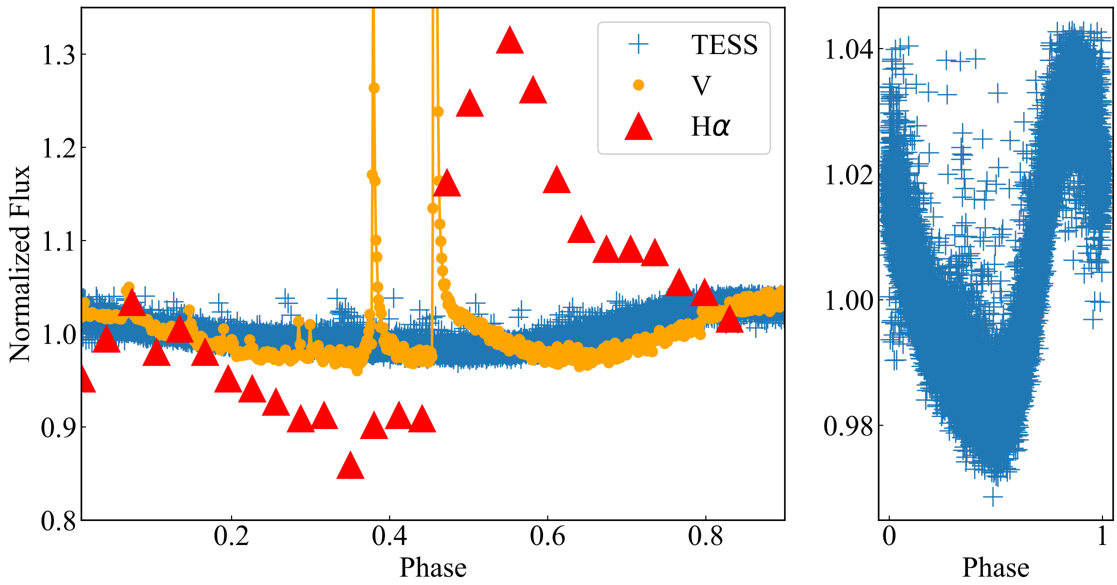

Figure 7.4.: *Left*: Comparison of the phase-folded *TESS* flare-removed light curve (blue crosses) and SNO V (orange circles) photometric data with CARMENES Hα I/I_r (red triangles) for flares 1 and 2. The Hα values have been normalized by their median value to properly relate them to the *TESS* and SNO V values. *Right*: Phase-folded, flare-removed light curve of *TESS* observations of GJ 3270.

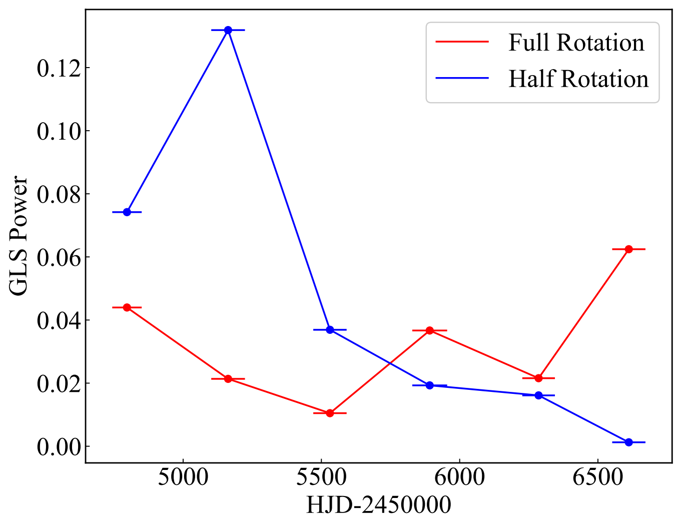

Figure 7.5.: Comparison of the GLS power (Zechmeister & Kürster 2009) of the full- and half-rotation period of GJ 3270 from SuperWASP data. The error bars denote observing seasons from which the GLS periodograms were generated.

Table 7.2.: GJ 3270 basic properties.

Parameters	LSPM J0417+0849	Ref.
Karmna	J04173+088	Cab16
α (J2000)	04:17:18.52	*Gaia*
δ (J2000)	+08:49:22.10	*Gaia*
d [pc]	14.59±0.02	*Gaia*
G [mag]	11.3537±0.0013	*Gaia*
Sp. type	M4.5 V	PMSU
$T_{\rm eff}$ [K]	3100±200	This workb
L [$L_\odot$]	0.00642±0.00003	Cif20
R [$R_\odot$]	0.278±0.009	Cif20
$M_\star$ [$M_\odot$]	0.269±0.013	Cif20
pEW (Hα) [Å]	−11.5 ± 0.015	Schf19
$P_{\rm rot}$ [d]	0.369829±0.0000036	This work
$v \sin i$ [km s^{-1}]	35.3±3.5	Rei18
v [km s^{-1}]	38.0±1.2	This work
i [deg]	68±15	This work
U [km s^{-1}]	−7.75 ± 4.7	CC16
V [km s^{-1}]	−27.03 ± 0.38	CC16
W [km s^{-1}]	−15.13 ± 2.57	CC16

References: *Gaia*: Gaia Collaboration et al. (2018); Cab16: Caballero et al. (2016) Cif20: Cifuentes et al. (2020); PMSU: Hawley et al. (1996); Schf19: Schöfer et al. (2019); Rei18: Reiners et al. (2018); CC16: Cortés-Contreras et al. (2017b). **Notes.** [(a)] CARMENES identifier. [(b)] Based on original $T_{\rm eff}$ determination by Cifuentes et al. (2020).

error bars we had initially calculated owing to the youth of GJ 3270. This radius determination lends support to the conclusion that the 0.1848 d period is a semi-period of the 0.3698 d period.

Adopting the latter radius allows us to estimate the inclination of the stellar rotation axis, which yields a best estimate of 68 ± 15 deg for the inclination and a value of 38 ± 1.2 km s^{-1} for the equatorial rotation velocity. We present these and other known parameters of GJ 3270 in Table 7.2.

7.4. Analysis

In this section we lay out the methods to be used in the analysis of the photometric and spectroscopic data.

7.4.1. Flare energy estimation

Our normalized multiband light curves show easily recognizable flare signatures above the underlying photospheric background, but these light curves lack an absolute calibration because no photometric standard stars were available in our FOV. To obtain fluxes and luminosities for the flares, we used a PHOENIX model spectrum (see Sect. 7.3) as an absolute reference for the photospheric spectrum. We obtained band-specific stellar surface fluxes, f_b, by folding the PHOENIX spectrum with the respective filter transmission curves. Multiplication with the stellar surface area (see Sect. 7.3) then yielded the band-specific photospheric luminosity, L_b, against which the flare is observed.

To study the flare parameters, we set up a light curve model with an exponential form. The free parameters are the flare start time, t_0, the peak, l_p, and the (exponential) decay time, τ. We also include an offset, which we consider a nuisance parameter. As in particular the *TESS* light curves show relatively long integration times per photometric data point, we used an oversampled model light curve, which we subsequently binned to the temporal resolution of the respective measurement (e.g., Kipping 2010). We then obtained best-fit parameters with a χ^2 minimization. The model provided our normalized photometric light curve $l_b(t_i)$ at time t_i. We obtained flare luminosities, by

$$L_{F,b}(t_i) = L_b \cdot l_b(t_i) \; . \tag{7.3}$$

The total flare energy in the band, E_b, is obtained by integration of luminosity over the flare period. Assuming an exponential form for the flare light curve, the peak luminosity, $L_{\mathrm{peak,b}} = l_p \cdot L_b$, and total flare energy are related to the e-folding time, τ_b, through

$$\tau_b = \frac{E_b}{L_{\mathrm{peak,b}}} \; . \tag{7.4}$$

We estimate that the relative uncertainty of the total energy amounts to about 10 %, primarily caused by the systematic error induced by using the synthetic template.

7.4.2. Flare model

As we have simultaneous multiband light curves, an estimation of the temperature and the size of the flaring region can be attempted. We first degraded the time resolution of the individual light curves to align their time binning with that of the V-band light curve. To that end, we averaged all r, i, and z-band photometric data points falling into the respective V-band time bin and linearly interpolated the B-band light curve.

In our modeling, we adopt a single blackbody with a temperature T_{bb} for the flare spectrum. By scaling the flare spectrum with the flare area, A_f, and folding with the filter transmission curves, we simulated the response of the different photometric bands.

For each time bin of the rebinned light curve, we estimate values for the blackbody flare temperature, T_{bb}, and its area, A_f, by fitting the model to the five available band fluxes. In the fit, we gave equal weight in the individual light curves by assuming a signal-to-noise ratio (S/N) of 100 for all of them. The fits in the individual time bins are independent, with the exception that we demand that the blackbody temperature does not rise after the flare peak.

7.4.3. Spectroscopic index definition

We employed the following lines as chromospheric activity indicators: He I D3 λ5877.2 Å (henceforth He I D_3), Na D2 λ5891.5 Å (henceforth Na I D_2), Na D1 λ5897.5 Å (henceforth Na I D_1), Hα λ6564.6 Å, and the Ca II infrared triplet B line at 8500.4 Å (henceforth Ca II IRT). We focused on the latter component because the Ca II IRT A & C lines are closer to the edge of the CCD and subject to greater uncertainty. The He I λ10 830 Å triplet lines are heavily affected by telluric OH emission lines and are, therefore, not suitable for our analysis. The Na D lines also show some telluric contamination, which mainly affects the last hour of our observations because GJ 3270 was low on the horizon, but this does not impede our analysis.

We used the index method as described by Kürster et al. (2003) to quantify the state of the chromospheric indicators. For each line, L, index values, I_L, are calculated for all spectra according to

$$I_L = \frac{\overline{F_{T,L}}}{\frac{1}{2}(\overline{F_{R_{L,1}}} + \overline{F_{R_{L,2}}})} . \tag{7.5}$$

In this equation, $\overline{F_{T,L}}$ denotes the average flux density over a target region, covering the respective line core, and $\overline{F_{R_{L,1}}}$ and $\overline{F_{R_{L,2}}}$ indicate averages over reference regions of pseudo-continuum. We adopted the same width of 5 Å for all regions. Details are given in Table 7.3.

The relatively broad target regions account for the strong rotational line broadening and additional broadening of the chromospheric line cores during flares. Uncertainties on the index values were obtained by error propagation as follows:

$$\sigma_I = I \times \sqrt{\left(\frac{\delta\overline{F_T}}{\overline{F_T}}\right)^2 + \left(\frac{\delta\overline{F_{R_1}}}{\overline{F_{R_1}} + \overline{F_{R_2}}}\right)^2 + \left(\frac{\delta\overline{F_{R_2}}}{\overline{F_{R_2}} + \overline{F_{R_1}}}\right)^2} , \tag{7.6}$$

where $\delta\overline{F_T}$, $\delta\overline{F_{R_1}}$, and $\delta\overline{F_{R_2}}$ denote the uncertainties of the respective mean, and the line index, L, was dropped for readability. All index values and uncertainties are listed in Table **??**.

Table 7.3.: Vacuum wavelength ranges adopted for index definition

Indicator	Target [Å]	Reference 1 [Å]	Reference 2 [Å]
Hα Index	6562–6567	6550–6555	6570-6575
Hα Broad	6550–6575	6520–6545	6580-6605
Hα BWI	6558–6563	6540–6545	6580-6585
Hα RWI	6566–6571	6540–6545	6580-6585
Hα BWI-e	6556–6561	6540–6545	6580-6585
Hα RWI-e	6568–6573	6540–6545	6580-6585
He I D_3	5875–5880	5869–5874	5905-5910
Na I D_2	5889–5894	5869–5874	5905-5910
Na I D_1	5896–5901	5869–5874	5905-5910
Ca II IRT	8497.5–8502.5	8490–8495	8505-8510

To better study the relation between the activity indices, we created a relative index (henceforth I/I_r) for every line, L, such that

$$I_{r,L}(t_i) = \frac{I_L(t_i)}{I_L(t_{\mathrm{low}})}, \tag{7.7}$$

where t_{low} denotes the minimum activity state, corresponding to the spectrum with the lowest observed Hα index value (observation no. 13). This was also the case for all the other activity indicators except for He I D_3, which had the first exposure, of our observation period, as its lowest value.

7.5. Results

We applied the methods discussed in Sect. 7.4 to the photometric (Sect. 7.5.1) and spectroscopic (Sect. 7.5.2) data. In Sect. 7.5.3 we compared these results with emphasis on timing and energy differences of the effect of the flare in the photometric and spectroscopic data.

7.5.1. Photometry

We present the results from analyzing the photometric data from SNO and MuSCAT2 (Sect. 7.5.1.1) and *TESS* (Sect. 7.5.1.2). We emphasize the determination of the energy, peak luminosity, and *e*-folding decay time of the flares. This allows us to determine that the flares that we observed on 15 December 2018 do not differ greatly when compared to the characteristics of the flares *TESS* observed the month prior.

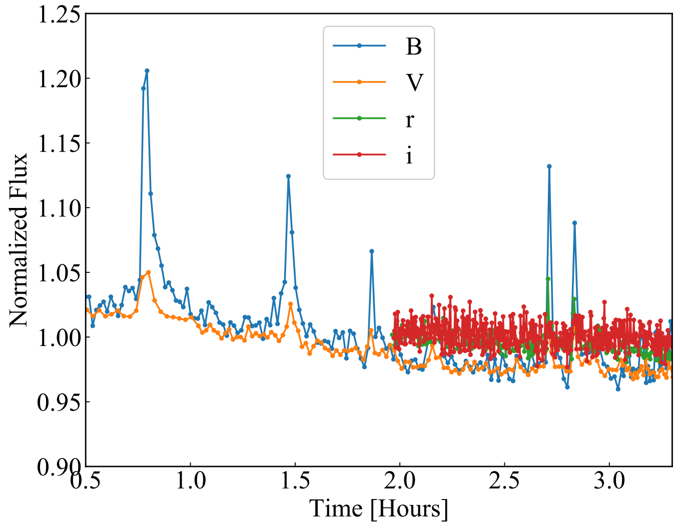

Figure 7.6.: Minor flaring in B, V, r, and i bands that occurred at the beginning of the observation run.

7.5.1.1. SNO and MuSCAT2

The light curves in Fig. 7.1 show two prominent flare-like events at relative times close to 3.6 h (henceforth flare 1) and 4.2 h (henceforth flare 2), of which the latter shows higher peak flux in all bands. At least five weaker flares were observed in the B and V bands, primarily early in the observing run (Fig. 7.6).

The different exposure times and relative offsets in cadence complicate the determination of the instant of flare onset. We normalized the flare light curves by the peak flux (Fig. 7.7). This allowed us to identify a 2.6 s window of overlap between the first bins, which consider to show elevated flux due to flaring. Therefore we determined that the onset of flare 2 occurred at UT 15-12-2018 23:47:33 (4.2167 h into the observations, JD 2458468.49135 ±1.3 s), which is consistent with simultaneous onset in all light curves. While we consider this strong evidence that a simultaneous onset occurred, it does not eliminate the possibility of a delayed onset. We are able to constrain any such delay to a maximum of 25 s between onset in B and onset in z, which would still satisfy the observed light curves.

We applied the methods described in Sect. 7.4.1 to determine the band energy, peak luminosity, and e-folding decay time. We present these values in Table 7.4. The results for the z band in flare 1 remain insignificant and are, therefore, not listed in the table. The e-folding decay times are presented in Table 7.4.

Flaring is generally more pronounced in the bluer bands, which is a consequence of the higher temperature flare spectra contrasting against the cooler stellar spectra (McMillan & Herbst 1991; Rockenfeller et al. 2005). This behavior is also exhibited by flare 2 as shown in Fig. 7.1. This effect is so pronounced that flare 1 becomes essentially undetectable in

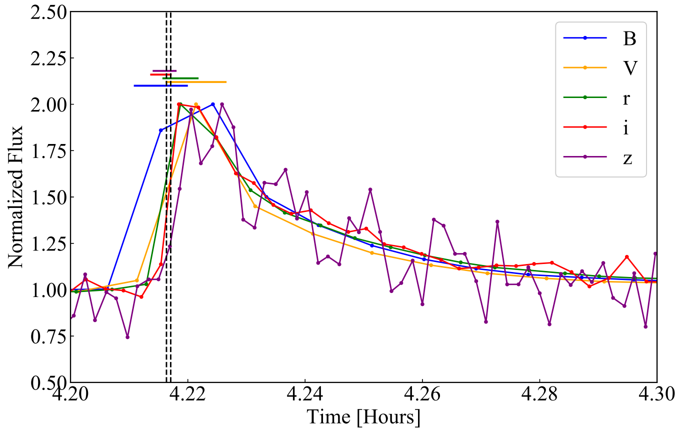

Figure 7.7.: Multiband light curve of flare 2 normalized by peak flare flux. The horizontal bars indicate the integration time of the flare onset observation for each band. Because of the low S/N of the z-band observations, we extended the possible onset time of the flare by an additional exposure. The dashed lines represent the onset window for flare 2 that would satisfy the onset conditions of all the photometric bands.

the z band. From our best-fit model (see Sect. 7.4.2) we determine the peak temperature of flare 2 to be ~10,000±1500 K, covering an area of $(1.35\pm0.39)\times10^{19}$ cm^2. Using the same procedure to calculate the total bolometric luminosity assuming the flare is a blackbody as in Günther et al. (2020) and Shibayama et al. (2013), we estimate the total energy to be $(6.3 \pm 3.2) \times 10^{32}$ erg, which is consistent with the sum of B,V,R,i, and z band energies of 3.6×10^{32} erg. This puts flare 2 close to the superflare regime of flares with bolometric energy greater than about 10^{33} erg (Shibayama et al. 2013).

However, while the model fits well to the peak and early decay phase, it does not reproduce the onset or late decay phase. For the onset we suspect that the issue lies in the aforementioned differences in cadence and exposure and the swift development of the flare. For the late decay phase the parameters become degenerate as the flare-affected region cools and, therefore, are no longer reliable. In our energy calculation we omit these degenerate values but nevertheless we assign a conservative 20 % error on the energy estimate.

7.5.1.2. *TESS*

We carried out a search for flares in the *TESS* light curve. To that end, we classified any photometric excursion as a flare if it peaked more than 3.6σ above the noise (determined by comparing lowest detectable injected flare to the noise background) and consisted of more than three consecutive data points. As the data set is inherently skewed owing to the presence of flares, we used the robust median deviation about the median to estimate the standard deviation of noise (e.g., Rousseeuw, P. J. & Croux, C. 1993). With our criterion, we identified 22 flare events in the 26 day observational period. Our detection threshold

Table 7.4.: Parameters of flares 1 and 2a.

Band	E_b [10^{31} erg]	$L_{\mathrm{peak},b}$ [10^{29} erg s^{-1}]	τ_b [s]	$\frac{E_b}{\Delta\lambda_b}$ [10^{29} erg Å^{-1}]
		Flare 1		
B	3.19	3.63	88	0.41
V	1.86	1.98	99	0.19
r	1.56	1.34	116	0.12
i	1.18	0.68	85	0.09
z	...	...	...	...
		Flare 2		
B	12.95	19.79	65	1.66
V	7.14	11.46	62	0.72
r	6.12	7.17	85	0.48
i	3.65	3.87	94	0.28
z	5.89	7.19	82	0.22

Note: $^{(a)}$ $\Delta\lambda$ in the fourth column denotes FWHM of the filter. Values given in Section 7.2.1.

for these flare events is ~10^{31}erg. By visual inspection, we determined that 15 of these are isolated events, with a single distinct peak followed by a decay. The remaining seven events were part of three different features consisting of multiple peaks. This occurs when a new event begins prior to the end of the decay phase of the previous event. Whether the events are physically related or are aligned by chance is unclear. Of these seven events, three were rejected from processing. One of these was rejected because if it been an isolated event, it would not have met the 3.6σ criterion. Two others were rejected as their profiles were not able to be fit with an exponential owing to an unusually long decay time or confounding behavior of the continuum. Likewise, one isolated event was rejected for the same issue. The parameters of the remaining flares are given in Table 7.5.

For individual flare events (IFEs) the peak luminosities, energies, and e-folding decay times were calculated in the same manner as that described in Sect. 7.4.1 for the SNO and MuSCAT2 data. The flares in the multi-flare events (MFEs) were a bit more complicated in that the decay curves of the individual events were disrupted by the curve of the following event. To estimate the energy, we fit an exponential decay curve based on the peak flux and the data points that existed prior to the next flare occurrence. The same procedure was done for the second and third flare in the sequence, only now subtracting the curve of the prior events. This allowed us to integrate under the curves and get an approximation for the energy output in each flare as if they were individual events. The values of these calculations are given in Table 7.5.

In Fig. 7.8, we show the flare peak luminosity as a function of flare energy. In comparing the data on the flares observed by *TESS* to those of flares 1 and 2, we opted to use the values in the i band and r band, added together. We opted to not use the z band as well

Table 7.5.: Parameters of *TESS* flares.

Type	E_T [10^{31} erg]	$L_{\mathrm{peak},T}$ [10^{29} erg s^{-1}]	τ_T [s]	Onset timea [d]
S	6.70	6.32	106	1.2917
S	33.68	4.63	721	3.9806
S	4.83	7.10	68	6.1001
S	58.25	7.53	774	7.7682
S	6.96	3.12	223	7.8668
S	10.22	5.03	203	9.4015
S	11.57	3.49	332	13.9043
S	38.07	21.28	179	15.1598
S	30.72	26.69	115	17.4195
S	15.02	3.02	498	21.0736
S	12.34	1.96	628	21.6111
S	3.01	2.49	121	22.6402
S	8.15	3.88	210	24.0666
S	24.01	13.55	177	24.2305
M	14.22	14.79	96	2.6334
M	18.85	8.32	222	2.6403
M	10.69	2.36	452	3.6528
M	12.74	13.27	96	11.0556

Notes. [(a)] Time given in days since beginning of *TESS* observations, sector 5 (JD 2458437.997). S indicates the flare was an isolated event, whereas M indicates the flare was part of a MFE event. Values represent the output of the *TESS* band only.

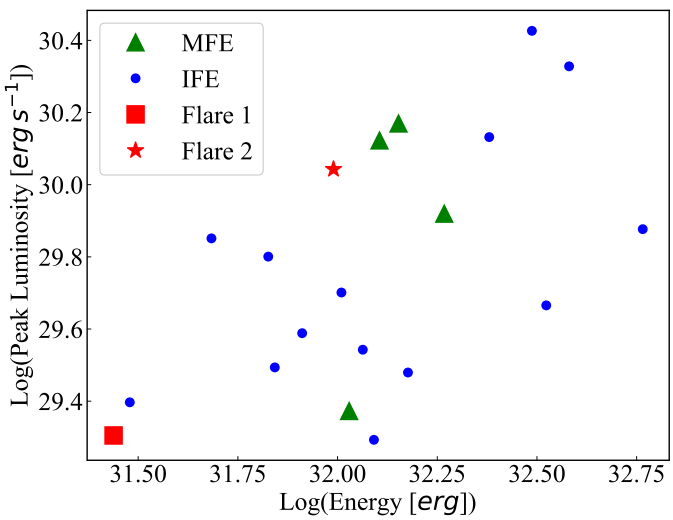

Figure 7.8.: Flare peak flux as a function of total energy for flares 1 and 2 (red square and star, respectively) as well as multiple (green triangles: MFE) and individual flare (blue circles: IFE) events observed by *TESS*.

because only flare 2 was detected in this band.

Isolated and MFEs behave similarly in this diagram, albeit the number of MFEs remain low. While others have identified these MFEs (Tsang et al. 2012; Vida et al. 2019b; Günther et al. 2020), also referred to as outbursts, there is to our knowledge no direct comparison of the parameters of single versus multiple events. Taken in total, however, the data show a statistically significant relation between peak luminosity and energy (p-value of $4.96{\times}10^{-6}$).

7.5.2. Spectroscopy

We present the results of analyzing the CARMENES spectroscopic data. The descriptions of the indicators used can be found in Sect. 7.4.3. First, we present the response of the chromospheric activity indicators (Sect. 7.5.2.1). These give broad outlines of the activity state of the star at any given time during the observations. Following this, we use the same methodology to examine the asymmetry of the Hα line (Sect. 7.5.2.2). In Sect. 7.5.2.3 we show that the blue asymmetry in Hα is caused by blue-shifted emission feature that is strongly correlated with those of the other activity indicators.

7.5.2.1. Chromospheric index time series

In Fig. 7.9, we show the time evolution of chromospheric indices. Prior to flare 1 (at about 3.6 h), all the activity indices remained roughly constant with the exception of that of Hα, which showed a decline. Flare 1 did not elicit a strong response from any activity indicators. If not for the photometric signature, flare 1 would have remained undetected. Interestingly, the sodium indices seemed to respond the most, in relation to the response of other indicators, to flare 1 (Fig. 7.9). In contrast, all indicators showed a pronounced flare signature that is consistent with the timing of photometric flare 2, with a characteristic fast rise and subsequent longer decay phase (Fuhrmeister et al. 2018; Reiners & Basri 2008; Honda et al. 2018; Schmidt et al. 2019).

The most prominent flare 2 response was observed in the Hα line, for which the rise to the peak index value lasted about 45 min. The following decay phase slowed after another 45 min essentially developing a plateau, followed by a moderate linear decay lasting beyond the end of the observations. In comparison to Hα, Ca ii IRT reacted the least but reached its peak faster. However, similar to Hα this flare did not fully return to its pre-flare values before the end of observations.

The He i D_3 and Na i indices showed similar temporal behavior, marked by a swift (unresolved by 15 min cadence) rise phase followed by a 45 min plateau. After this plateau, the He i D_3 and the sodium line indices showed a decay back to pre-flare levels, which appears to proceed the most rapidly in the He i D_3 line index. Close to the 6 h mark, the lines showed another enhancement in activity, which coincided with the plateau-like

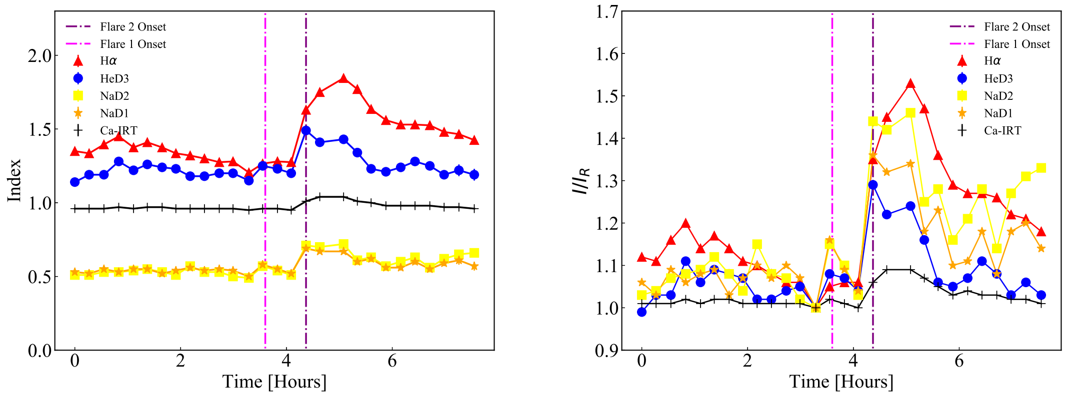

Figure 7.9.: *Left:* Index for Hα (red triangles), He I D_3 (blue circles), Na I D_2 (yellow squares), Na I D_1(orange stars), and Ca II IRT (black crosses) for all observations. Flare 2 occurs at 4.3 h. Hα is scaled down by factor of 2.5. *Right:* I/I_r for Hα (red triangles), He I D_3 (blue circles), Na I D_2 (yellow squares), Na I D_1 (orange stars), and Ca II IRT (black crosses) for all observations. Vertical lines in both plots indicate onset times of flares 1 and 2.

feature seen in the Hα index. The pattern of Ca II IRT decaying slower than He I D_3 has been previously noted with other M dwarf flares (Fuhrmeister et al. 2008, 2011).

The Na I D_1 and Na I D_2 indices showed an apparent increase in activity level after 6.5 h into the observations. This period coincided with increased telluric contamination of the sodium lines (Fig. 7.14).

7.5.2.2. Hα wing indices

Flare 2 had effects beyond the core of the Hα line profile with an increase in flux being detected from −10 Å to +5 Å. We show this in Fig. 7.10 with line fit parameters given in Table 7.6. Moreover, we quantified the effects in the Hα wings, including asymmetries, by measuring an index on both sides of the core index: the red wing index (RWI) and blue wing index (BWI).

Additionally, we took the index of a broad region that included the line core (Broad Index). The definitions of these indices can be found in Table 7.3. We plot these new indices along with the original Hα index in Fig. 7.11.

At the beginning of the observations, the RWI was enhanced over that of the BWI, but by 2 h into the observations the two indices equalized. Neither index reacted to the onset of flare 1. The BWI showed a sharp rise at the onset time of flare 2 followed by an exponential decay with an *e*-folding time of about 30 min. The RWI also showed a rapid increase at the time of the onset of flare 2 followed by a decay. This decay was interrupted, however, and a secondary rise was detected shortly after 5 h into the observations. The

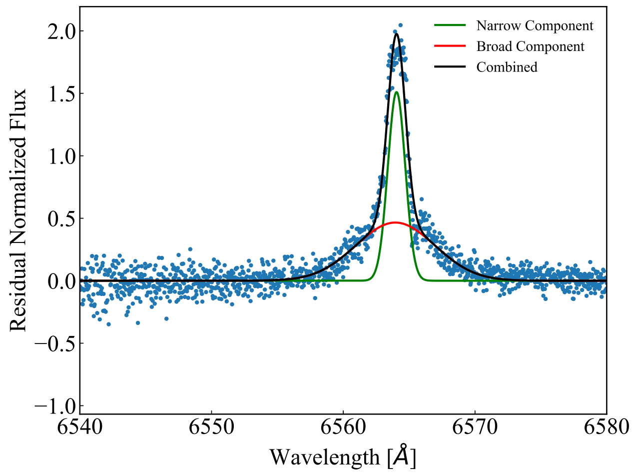

Figure 7.10.: Hα double Gaussian fit for the onset of flare 2. The narrow component (green line) has a shift of $-25.12\,\mathrm{km\,s^{-1}}$ and the broad component (red line) has a shift of $-29.68\,\mathrm{km\,s^{-1}}$ from the line core. The combined fit is given by the solid black line.

Table 7.6.: Parameters of double Gaussian fit.

Parameter	Narrow component	Broad component
Amp. [Å]	1.51	0.47
δ Amp. [Å]	0.03	0.03
μ^a [Å]	6564.05 (-25.12)	6563.95 (-29.68)
$\delta\,\mu^a$ [Å]	0.01 (0.46)	0.01 (0.46)
σ [Å]	0.66	3.0
$\delta\,\sigma$ [Å]	0.02	0.13

[a] Figures in parenthesis denote the Doppler shift in $\mathrm{km\,s^{-1}}$.

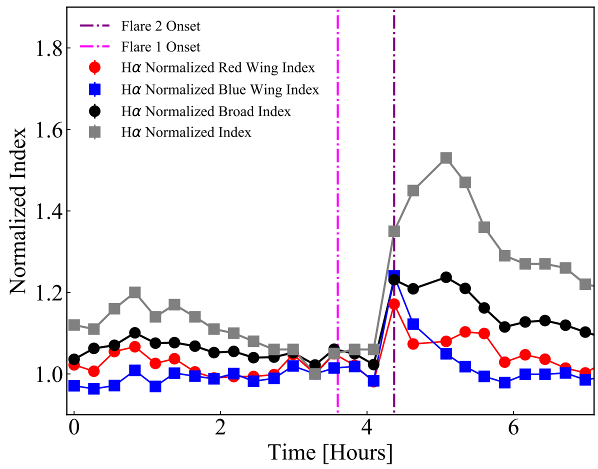

Figure 7.11.: Hα red (RWI) and blue (BWI) wing indices. Hα I/I_r and broad index are shown in gray and black, respectively. The vertical lines indicate onset times of flares 1 and 2.

RWI remained elevated over that of the BWI for the remainder of observations. This indicates that the BWI was primarily affected by the events around the flare onset.

Initially the flare onset appeared in the Hα line as a large asymmetry on the blue wing of the line. When subtracting the minimum activity spectrum (Fig. 7.12) this blue asymmetry is the summation of two features: a narrow and broad component (Fig. 7.10). We fit a double Gaussian profile to these components, the result of which is given in Table 7.6.

For the broad component, the fit yielded a shift of $-29.7\,\mathrm{km\,s^{-1}}$ from the line core and a narrow component shifted by $-25.1\,\mathrm{km\,s^{-1}}$. This broad component was only strong enough to be fit with a Gaussian at the flare onset, but indices placed even further from the line core than the BWI and RWI indicate that this component lasted for a total of 30 min. This also suggests that the narrow component was limited to the 7 Å nearest the line core as it persisted in the BWI for much longer. The red extreme index did not show as much of an enhancement after 5 h as the RWI, suggesting that the asymmetry detected by the RWI was also confined to within 7 Å of the Hα line core.

The narrow component, represented by the BWI, persisted for at least 90 min while decreasing in strength. This can be seen in the activity minimum subtracted spectrum as the narrow component decreasing in amplitude and shifting toward the line core.

7.5.2.3. Doppler shifted emission

The initial displacement and subsequent shift toward the line core seen in Hα can also be observed in the other activity indicator line profiles (Fig. 7.13). To more clearly illustrate this, we compiled all of the available spectra for each indicator into a series of “heatmaps” (Fig. 7.14). These heatmaps show the temporal evolution of the normalized flux density

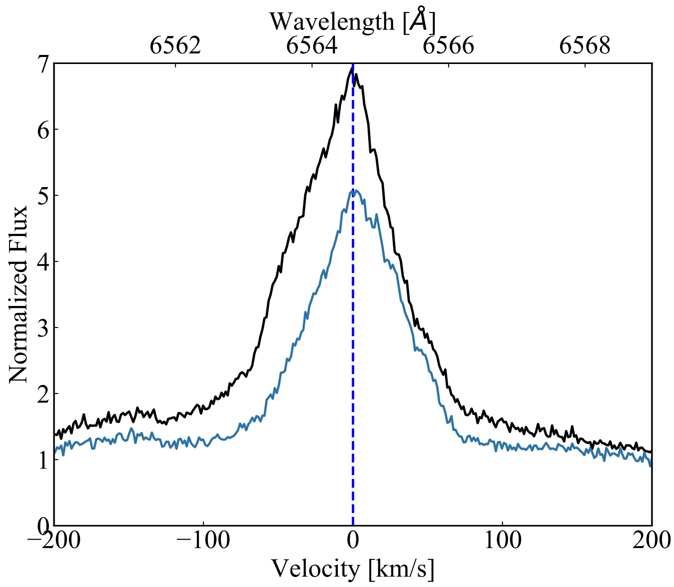

Figure 7.12.: Hα at flare onset (solid black, observation 17) and at activity minimum (solid gray, observation 13). The dashed vertical line indicates the rest wavelength.

for these lines. The clearest example of the shift is given by the Ca II IRT line because it has the highest S/N. Notably, none of the activity indicator lines have Doppler displacements that exceed the projected rotational velocity of the star. In this picture, the shift in Hα is actually the least obvious owing to the preexisting emission in the line core.

By subtracting the minimum activity spectrum, we can generate a set of residual spectra in which deviations from the quasi-quiescent state can be analyzed. To these residual spectra we fit a Gaussian profile, thereby determining the Doppler displacement from the line core (Fig. 7.15).

All of the Doppler shift values at the onset of flare 2 are between $-27\,\mathrm{km\,s^{-1}}$and $-21\,\mathrm{km\,s^{-1}}$. The flare onset values of the Hα single Gaussian fit are comparable to the results of the narrow component in the double Gaussian fit.

Prior to flare 1, the Gaussian fits to the Hα and He I D_3 residual spectra show predominantly redshifted values, whereas the sodium residuals are either neutral or blueshifted. We attribute these, along with the sporadic shifts exhibited by the sodium lines, to the low amplitude of the signals, telluric interference, and systematic uncertainty caused by the selection of the minimum activity spectrum.

As the onset of flare 1 approached, the Hα residuals became increasingly redshifted. At the onset of flare 1 the Hα shift decreased almost to neutrality and He I D_3 appeared blueshifted. After the onset of flare 1 but prior to flare 2 Hα, He I D_3, and the sodium lines all appeared blueshifted with a shift of between -20 and $-10\,\mathrm{km\,s^{-1}}$. After the onset of flare 2 the shifts of all chromospheric residuals were strongly correlated. Over the subsequent ~2 h, the residuals shifted toward longer wavelengths. Formally, the He I D_3

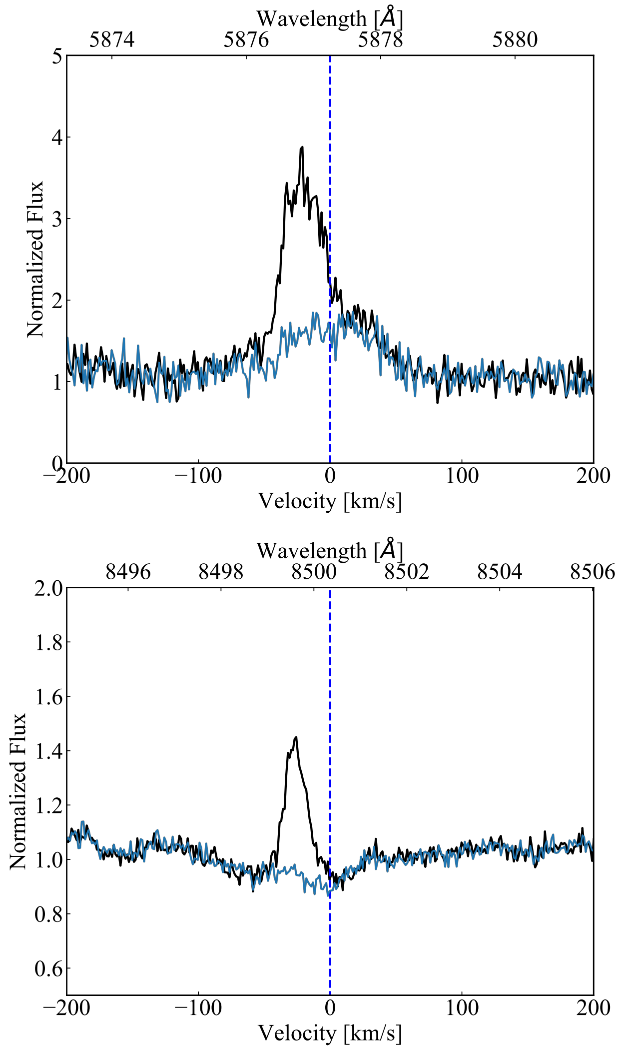

Figure 7.13.: Flare emission from the He I D_3 (top) and Ca II IRT lines (bottom) during flare onset (solid black, observation 17), activity minimum spectra (solid gray, observation 13). The dashed vertical line indicates the rest wavelength.

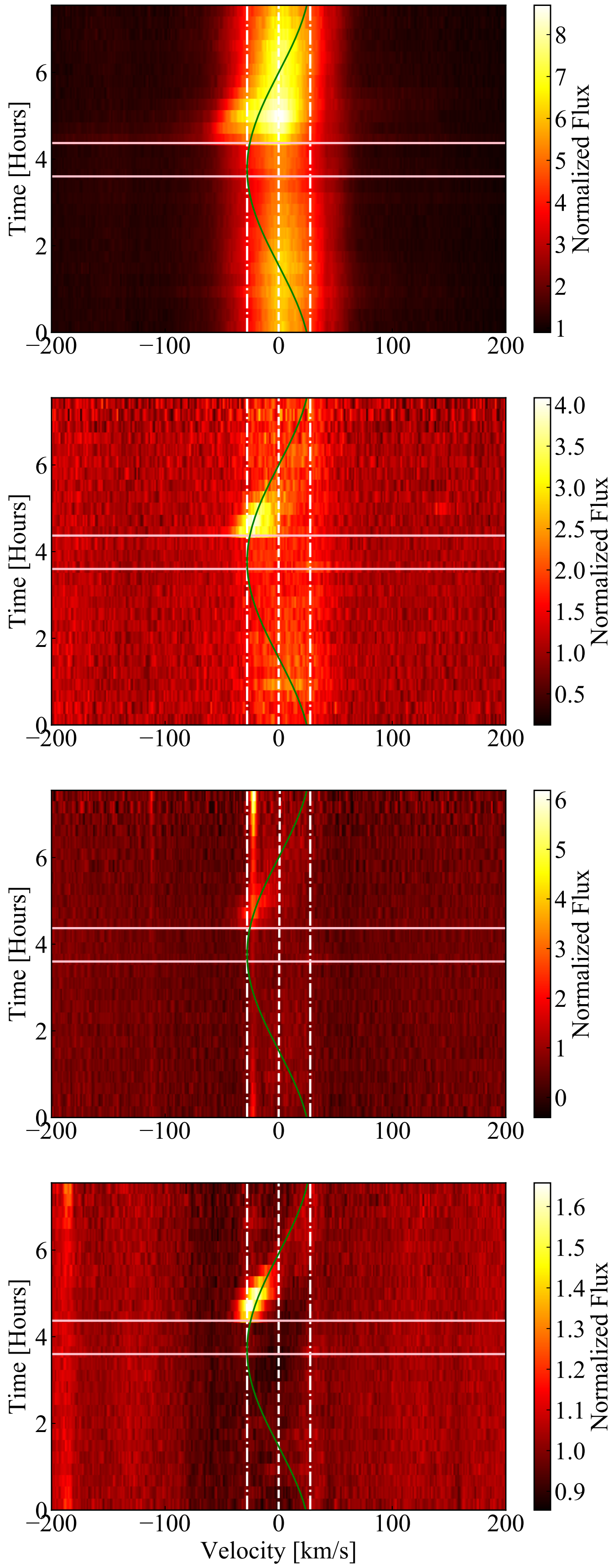

Figure 7.14.: From top to bottom: Hα, He I D$_3$, Ca II IRT, and Na I D$_2$ flux density evolution during our observing run. The central dashed line indicates the nominal rest-frame wavelength and the outer two dash-dotted lines denote the maximum Doppler shift for a corotating object at 43 deg latitude (28.6 km s^{-1}). The green line represents the expected Doppler shift of such an object if it were to emerge onto the blue limb of the disk 3.72 h into the observation run. Horizontal solid white lines indicate onset times of flares 1 and 2.

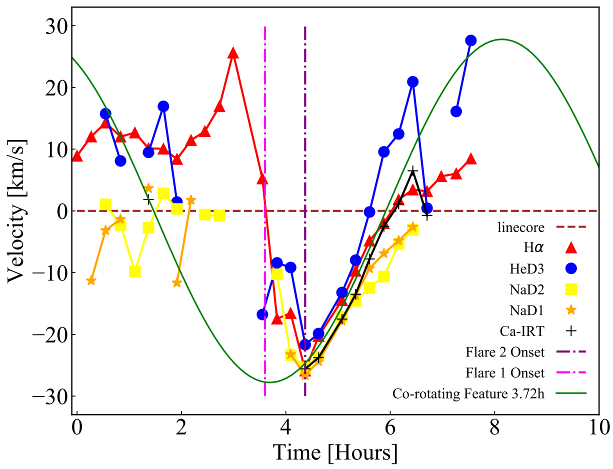

Figure 7.15.: Doppler shift of excess flare emission of the line cores. The missing data points indicate that a Gaussian fit was impossible, which causes the gap at about 3 h, where the minimum activity spectrum is located. All of the activity indicators shift to the blue before the flare onset (noted by vertical dotted line). Green line represents the expected Doppler shift of such an object, at 43 deg latitude, if it were to emerge onto the blue limb of the disk 3.72 h into the observation run.

residual emission was the first to return to its rest wavelength and then became increasingly redshifted. Shortly after followed the shifts of the residual Hα and Ca II IRT line cores. For the sodium lines the return to neutrality could not be observed, probably because of telluric interference.

7.5.3. Spectroscopy versus photometry

In Fig. 7.4 we juxtapose the phase-folded *TESS* light curve (with flare events subtracted) with the SNO V band light curve and the Hα index time series; the latter two are scaled. The Hα index data shows a decline prior to flare 2.

Similar behavior is exhibited by our B, V, r band light curves, but it is not detectable in the i and z bands, possibly owing to poorer S/N (Fig. 7.1). Although the *TESS* light curve was not taken simultaneously, the narrow gap of only about four days, combined with the relative stability of the rotational signal during the TESS observing window, suggests that the source of the decline in Fig. 7.4 is rotational variability. This rotational variability is likely caused by corotating active regions, which is also consistent with the effect being more pronounced at shorter wavelengths. This implies that the modulation of the Hα index prior to flare 2 is also, primarily, driven by rotational effects.

The decay times of the activity indicators for flare 2 are, at a minimum, two times longer than those observed in the photometric bands. The e-folding duration of Hα, for instance,

Table 7.7.: Indicator energies for flare 2.

Indicator	Band L [10^{27} erg s^{-1}]	Peak L [10^{26} erg s^{-1}]	Energy [10^{29} erg]	τa [s]
Hα Index	3.57	45.55	136.33	2993
Hα Broad	17.41	50.12	371.98	...
Hα BW	3.70	9.83	11.68	1188
Hα RW	3.62	6.27	23.20	3700
Hα EBW	3.50	3.86	1.76	458
Hα ERW	3.49	2.65	5.40	2038
He I D_3	1.07	3.61	16.96	4697
Na I D_1	0.42	7.70	4.93	6400
Na I D_2	0.35	7.93	5.80	7304
Ca II IRT	6.54	5.90	34.67	5878

Notes. [(a)] *e*-folding decay time (see Sect. 7.4.1), Hα broad component does not have a decay value as it does not exhibit an exponential-like decay profile.

is ~3000 s, whereas the longest *e*-folding duration of a photometric indicator is 1320 s and nearly exponential in nature. The decay phase of Hα appears to be complex with an initial exponential decay followed by a plateau and a later linear decay that lasts until the end of observations. Since the non-exponential decay phase of Hα occurred over a period of time when the photometric flare had already returned to quiescent level, the transition between the phases in the activity indicators is likely due to phenomena that affected the chromosphere but not the photosphere.

Table 7.7 shows the energies involved for each activity indicator used in this study. Hα, one of the principal cooling lines of the chromosphere, puts out an energy equivalent to ~22 % of the *r* band. However it takes Hα 30 times as long to emit that energy. This contrast in the rate of output between Hα and the *r* band is clear when looking at the peak luminosity. The photometric value is 148 times larger than the Hα spectroscopic value. The other spectroscopic indicators have similar ratios to the photometric bands in which they occur. The activity indicators (He I D_3 and the sodium lines) in the *V* band are slightly more contrasted (2.5 % of the energy output of the *V* band) as a consequence of the higher temperature of the flare material in comparison to the photospheric background.

7.6. Discussion

We present our interpretation and extrapolation of the data above. In Sect. 7.6.1 we compare the flares observed with SNO and *TESS* to other flaring M dwarfs. In Sect. 7.6.2 we interpret the Doppler shifts of the activity indicators as evidence for a corotating feature and isolate the location of it to a latitude of43 deg and a longitude of –70 deg. In Sect. 7.6.3 we look at the beginning of the observations when sustained minor flaring is associated with a persistent redshift in the Hα line. We find that the data are consistent with an active region, separate from that of flare 2, which was in the process of rotating off the observable disk at that time. In Sect. 7.6.4 we look at evidence for rotational modulation and find that our data are consistent with Hα being rotationally modulated. Additionally we discuss the Doppler shifts of the activity indicators and find that both major flares likely originate from a similar location on the stellar surface. Additionally, the red excess seen in the Hα wing index is consistently elevated, suggesting ejected material reentering the lower atmosphere. We then compare, in Sect. 7.6.5, the response of the activity indicators to flares 1 and 2. We present a series of possible scenarios as to why there was such a difference in reaction to the two events. Lastly, we explore the possibility of a CME being associated with the blue asymmetry of flare 2. We find, however, that our data do not support any successful mass ejection of material, but there is some evidence for a failed ejection that later reenters the lower atmosphere causing a disruption to the chromospheric indices.

7.6.1. Flaring rates and energies

Given the *TESS* observation period and the observed flare count we calculate a flare rate of 0.818 flares per day. The sum of their decay times was 5,221 s for a duty cycle (time flaring divided by non-flaring time) of 0.23 %. Figure 7.8 shows that flare 1 and 2, which we covered with multiband, ground-based photometry, have similar energies and peak luminosities as the *TESS* flares observed the month prior. There may be a small separation between high energy, long-duration flares, of which flare 2 is a member, and lower energy flares, of which flare 1 is a member. Whether this gap corresponds to some physical property or mechanism remains speculative.

Vida et al. 2019b, using *TESS*, measure a flare rate of 1.49 per day on Proxima Centauri with a duty cycle of 7.2 %. The average energy output of the 72 events observed on Proxima Centauri is 11.5×10^{30} erg while the average for our observations is 17.8×10^{31} erg, that is, about an order of magnitude more, which is in line with a higher cadence and duty cycle for the events identified on Proxima Centauri. In a larger study of flares observed by *TESS*, Günther et al. 2020 find that for M dwarfs, with rotation periods < 0.3 d, the flare frequency was between 0.1 and 0.5 per day. In a similar study with Sloan Digital Sky Survey, Hilton et al. 2010 find that for M0 to M1 dwarfs the flare duty cycle was 0.02 % but went up to 3 % for M dwarfs M7 to M9. Although direct comparisons remain difficult owing to different sensitivities and flare detection methodology, our findings are generally consistent with those in comparable stars.

7.6.2. Localization of flare 2 region

With the information on the Doppler shifts of the chromospheric lines, we can estimate the latitude and longitude of the flaring region. The (rotational) RV(t) of a surface element as a function of time, Δt, and stellar latitude, ϕ, is given by

$$\mathrm{RV}(t) = v \sin i \cos\phi \sin\left(2\pi\left(\frac{(t-t_0)}{P} + \frac{3}{4}\right)\right) , \tag{7.8}$$

where $v \sin i$ is the projected equatorial rotation speed, P is the stellar rotation period, and t_0 is the instance of minimum RV. For a large inclination, this corresponds well to the instant of appearance of a feature at the limb.

We fit the expression in Eq. 7.8 to the Hα, He I D_3, Na I D_1, and Ca II IRT shifts of observations no. 18 to 22, treating ϕ and t_0 as free parameters. In this way, we obtained a latitude of 43 ± 10 deg and a value of 3.73 ± 0.12 h for t_0, where the error is estimated using the jackknife method (e.g., Efron & Stein 1981). We did not use the two observations during and after flare onset as these are the most likely to be contaminated by radial bulk motions, as indicated in Fig. 7.11.

Given the onset time of flare 2, we estimate that the flare started 70 ± 5 deg from the center of the disk. At this instance, Eq. 7.8 yields a shift of $-26 \pm 4\,\mathrm{km\,s^{-1}}$, which agrees well with the observed RV shift.

The agreement of these two values indicates that the majority of the blueshift of the narrow components originates from the displacement of the active region from the center of the disk and the resulting rotational RV shift rather than bulk motions of flaring material (Figs.7.14 and 7.15). It is likely that the bulk motions are better represented by the broad component featured in Fig. 7.10. The observed data and the corotating aspect are similar to an active region with post-flare arcadal loops on our Sun.

7.6.3. Minor flares

Prior to flare 1, Fig. 7.15 shows that the Hα line is shifted to the red. These redshifts coincide with a series of small flare-like events (Fig. 7.6). Concurrently with these small flares, the wing index measurement (Fig. 7.11) of Hα shows an enhancement in the red wing over that of the blue wing. While there are multiple situations in which chromospheric lines can exhibit asymmetries, these red wing enhancements are frequently associated with coronal rain in which the down-falling material emits Hα as it heats up upon reentry of the lower atmosphere (Fuhrmeister et al. 2018).

Starting at two hours into the observation, this redward shift quickly ascends from $+10\mathrm{km\,s^{-1}}$ to a peak of $+26\mathrm{km\,s^{-1}}$ within about one hour. This maximum occurs just after the last of the minor flare-like events. It is immediately followed by the activity minimum spectrum and for the rest of the observing run there are no further small flare events. For the rest of our observations, the Hα velocity shift value never again reaches the $10\,\mathrm{km\,s^{-1}}$ value. Additionally the slope of the increasing redshift of the Hα asymmetry is consistent with a corotating feature. This implies that these minor flares and increasing red asymmetry may be due to an active region moving over the limb of the star just prior to or concurrent with the activity minimum observation. Unfortunately, without data spanning multiple rotation periods, we could not confirm this. We can, however, conclusively rule out any association of the minor flares with flare 1 and 2. If the minor flares were part of the same active region as flare 1 and 2, then they would have occurred while the active region was on the far side of the star and therefore unobservable.

When comparing the minor flaring across photometric bands (Fig. 7.6), the minor flares are only discernible at short wavelengths (*B* and *V* specifically). In the longer wavelength ranges they become indistinguishable from the background. Therefore, if further work is to be done to disentangle possible rotation modulation of Hα from the effect of minor flaring (bulk vertical motion; i.e., coronal rain), it should be done with high cadence, simultaneous spectroscopic and photometric (*B* and *V*) observations.

7.6.4. Rotational modulation and Doppler shifts of activity indicators

In Fig. 7.4, the trend of Hα in the first half of the observing run is similar, if more exaggerated, to that of the light curve of *TESS*, suggesting that the Hα index is modulated by rotation. However owing to the onset of flare 2 in the second half of the data set we could not confirm this. There also exists the possibility that Hα index has a periodicity twice that of the rotational period of the star as seen in other active M dwarfs (Schöfer et al. 2019).

An alternative scenario for the pre-flare absorption dip in Hα is supplied by Jardine et al. (2020). They argue that rapidly rotating and young (< 800 Myr) stars (such as GJ 3270) are prone to having slingshot prominences. Slingshot prominences are comprised of trapped, cool, gas and appear as absorption transients in Hα. Slingshot prominences are thought to be most common around zero age main-sequence stars (Jardine et al. 2020; Cang et al. 2020). If such a prominence was present prior to flare 2, it was likely disrupted or ejected by that flare because no similarly sized absorption transients are seen for the rest of our observational period. Whether this absorption feature in Hα is due to a prominence or the rotational modulation of Hα is unclear.

For two hours after flare 1 (this time frame includes flare 2) all indicators are closely correlated (Fig. 7.15). This suggests that flare 1 and 2 are related and likely originate from the same active region. Therefore, given the determined onset position of flare 2, flare 1 would have occurred at or just over the limb of the star.

After flare 2, the Doppler shifts are consistent with a corotating feature, as detailed in Sect. 7.6.2. At ~6 h into the observations, all of the Doppler shifts of the activity indicators have returned to their line cores and from this point forward become redshifted (Fig. 7.15). Simultaneously, the activity indicator Doppler shifts diverge from that expected of a corotating feature, suggesting that the post-flare effects in the active region have subsided or are no longer the dominant feature of activity on the disk. Additionally,

Table 7.8.: Enhancement factor of flare 2 from flare 1 by photometric band.

B	V	r	i	z	mean
3.36	2.6	1.9	1.19	...	2.26

all the activity indices increase except for Hα, which halts its decay and plateaus for ~45 min (Fig. 7.9). The wing index (Fig. 7.11) shows a larger red enhancement at this time than it did during the period of minor flaring. We find these data are consistent with a period of coronal rain, possibly the result of material partially ejected during the onset of flare 2, returning to the star.

7.6.5. Comparison of flare 1 and 2

While the position of flare 2 can be calculated by its after effects, flare 1 is considerably less intense (Table 7.8, Fig. 7.1) and has no discernible after effects. We must therefore infer its relation to flare 2.

Just prior to flare 1, the Hα line had reached its maximum redshift value of ~25 km s^{-1} (Fig. 7.15). We previously surmised that this may be the signature of an active region ˜30 min from going over the limb of the star. At the onset of flare 1, all Doppler shifts of the activity indicators shift toward the blue. After flare 1, these shifts increase until the maximum blueshift occurs at the onset of flare 2. The Doppler shifts of all the activity indicators are well correlated from flare 1 onset to ~90 min after flare 2 onset, indicating that the source of this shift is the dominant chromospheric feature on the star.

The calculated location of the active region that spawned flare 2 at the time of the onset of flare 2 is 70±5 deg from disk center. It would have taken this active region ~30±8 min to arrive at this location from the limb. The timing uncertainty and longer visibility of higher latitudes inclined toward the observer allow that flare 1 originated from the same active region as flare 2. If this active region were the source of flare 1 then flare 1 would have occurred at or near the limb of the star. That we did not see the full blueshifted value of this active region, at that time, could have been due to either a lack of a strong signal or possibly to residual, contaminating effects of the other active region moving over the far limb. This would have been the same active region from whence the minor flares had occurred earlier in the observation period.

This positional argument is supported by the response of the activity indicators (Fig. 7.9). We conservatively took the flare 2 onset values for I/I_r and divided them by the V-band flare 2 over flare 1 enhancement (2.6, Table 7.8) giving us a list of expected activity indicator values for the response to flare 1 if it were proportional to flare 2 (Table 7.9). This allowed us to compare the expected with the observed indicator values of flare 1. We found that Na I D_2, Na I D_1 , and Ca II IRT responded to flare 1 in proportion to their response to flare 2. Hα and He I D_3 however, did not. Both of these indicators were

Table 7.9.: Expected vs. observed activity indicator response to flare 1

	Hα	He I D_3	Na I D_2	Na I D_1	Ca II IRT
Flare 2 obs	1.35	1.29	1.44	1.36	1.06
Flare 1 exp	1.13	1.12	1.17	1.14	1.02
Flare 1 obs	1.05	1.08	1.15	1.16	1.02

Note: Error on figures: 0.02.

somewhat weaker in flare 1 than would be expected. A possible explanation for this is preferential absorption.

Preferential absorption could arise from an extended light path through the mid-upper atmosphere in which Hα and He I D_3 form. In these regions the temperatures are too hot for the ground states of the sodium and calcium lines, thereby allowing the Na I D_2, Na I D_1 , and Ca II IRT lines through unhindered whilst absorbing some of the Hα and He I D_3. This extended path would be expected for a source near the limb of the star. While we cannot say for certain that flare 1 occurred on the limb or that it is associated with flare 2, we find the evidence for this case plausible. In this case the observed differences in activity indicator response between flare 1 and 2 would be due to a viewing angle effect.

7.6.6. Ejection of material

In our observations we do see a large blue asymmetry that has a broad, asymmetric component. This indicates that some bulk plasma motion was occurring during our observations. However the velocity of these plasma motions was at most 30 km s^{-1}, which is only 5% of the escape velocity. Additionally if this material originated from the same active region as the narrow component then it should also have a $\sim$25 km s^{-1} blueshift due to rotation. We therefore conclude that the detected bulk plasma motions did not result in a CME. However, as we already noted in Section 7.5.2, about 90 min after the onset of flare 2 there was a change in the decay trend of all chromospheric activity indicators into an increasing trend (except for Hα which halts its decay and enters a plateau for $\sim$45 min). During this time the red wing enhancement is at its peak, superseding that of the earlier flaring period. This would indicate, with the assumption that this red wing enhancement is due to an increase in coronal rain, that a considerable amount of material is falling through the chromosphere. During this same time period there were no indications in the photometric data of further flaring activity. We find our data consistent for either a failed loop ejection or a failed CME. In this scenario material from this event rises into the upper atmosphere before raining down and releasing the kinetic energy into the chromosphere, thereby triggering the increase in activity that we observe.

7.7. Conclusions

We report a series of flares, including a large flare that was followed by a corotating feature, on the ultra-fast-rotating M4.5 V star GJ 3270. We analyzed 27 spectra taken with CARMENES on 15 December 2018. Simultaneous to these observations, photometric observations out in B and V bands from Sierra Nevada and observations in the r, i, and z bands by MuSCAT2 from Teide were carried out. Just prior to our ground-based observations, *TESS* monitored GJ 3270 for 26 d in a row.

Early in the CARMENES+SNO+MuSCAT2 observing period, a series of minor flaring events were observed along with associated red asymmetries in the Hα line. This is consistent with the interpretation that these flares were inducing coronal rain. Just prior to the cessation of minor flaring, these red asymmetries increased to the point that the Doppler shift of the residual flux in the Hα had nearly reached the $v \sin i$ of the star. No further minor flares were detected for the rest of the observation period. This is consistent with the interpretation that an active region was rotating off the observable disk.

A flare that was larger than those seen during the earlier period of minor flaring occurred 45 min later. This flare (flare 1) had an unusual reaction from the chromospheric activity indicators. Typically Hα is the most sensitive line in flaring situations. In this case, however, the sodium D lines appeared to be the most sensitive followed by He I D_3. This unusual reaction coupled with the location of the next, larger flare (flare 2) suggests that flare 1 occurred at or just over the limb of the star. This difference in reaction of the activity indicators, coupled with the position of the flare, can be due to a number of different scenarios. While preferential absorption through a light path containing more stellar atmosphere is a likely explanation, more such situations would have to be observed to come to any firm conclusions.

Flare 2 had energies on the order of 10^{32} erg s^{-1}. This is comparable to the events detected during the *TESS* observation period. The most noticeable feature of flare 2 is the strong blue asymmetry in Hα that persisted for ~90 min. At flare onset this asymmetry could be separated into a narrow component and a broad component. The broad component was ~15 Å wide, asymmetric and blueshifted by 30 km s^{-1} from the line core. This broad component was visually evident only at the flare onset and may have persisted into the next exposure at a minimal level for a total duration of ~30 min. We associate this broad component as indicative of bulk plasma motion. The narrow component was blueshifted by 25.9 km s^{-1} from the line core. This component is what persisted for the ~90 min for which the blue asymmetry was observed. In other activity indicators (sodium D lines, He I D_3, Ca II IRT) an emission peak was observed that is blueshifted by ~25 km s^{-1} as well. These features then proceeded, well correlated to one another, to shift toward the line core over the subsequent 90 min, while the amplitude of the shifting component decreased. The rate of this shift is consistent with a corotating surface feature that originates at ~65 deg away from disk center with a latitude of ~40 deg. To our knowledge this is the first time such a feature has been observed on an M dwarf. The data are consistent with the solar analogy of an active region experiencing arcadal loops.

Approximately 6 h into the observations and 2 h after flare 2 onset, an increase in chromospheric activity indicators occurred. Associated with this increase was also an elevated period of red asymmetries associated with many of the activity lines. These red asymmetries were larger than those observed earlier during the period of minor flaring. During this same time period, however, no flaring activity was detected in any of the photometric bands. Given that bulk plasma motions were detected during the onset of flare 2, these data are consistent with a period of intense coronal rain, possibly resulting from the reentry of ejected material.

We conclude that the main phenomenon behind our observations was a corotating feature analogous to an active region with arcadal loops. Beyond that, while we have not conclusively shown that a failed CME occurred or that flare regions have a temperature stratification, we have seen sufficient suggestive evidence to warrant further simultaneous, spectroscopic, and photometric observations of fast-rotating M dwarfs.

8. Summary & future work

This work was organized into two distinct sections. The first section dealt with the difficulties in measuring chromospheric features with a molecule-dominated photospheric backdrop. This was particularly necessary in low-activity M dwarf stars that do not have the chomospheric activity indicators in emission. The second section dealt with the opposite activity regime, namely a series of flares on the fast-rotating star GJ 3270.

In the first section we introduced the Molecular Normalized Index(MNI) as an improved index. The MNI normalizes out the effect of the molecular continuum on the index. Being an Index of indexes, when used on a earlier type star, not dominated by molecular features, the MNI is indistinguishable from the original index method. When comparing to the Kürster index we found the MNI counters the molecular absorption past M3V and the Kürster index was more suitable to comparing stars of different spectral types than was originally suspected. In addition to the MNI, we also formulated a modification of the FWHM, which we named the pseudo FWHM (pFWHM).

When we applied the MNI to Hα and Ca II IRT, we found that, for the least active M dwarfs in the CARMENES sample, the chromospheric absorption in these lines was not due to stellar activity but rather correlated very well with the stellar effective temperature. This implies that the heating of this quiet chromosphere is due to another process not associated with magnetic stellar activity. We also found that the absorption in these lines decreased with decreasing effective temperature implying that the temperature of the quiet chromosphere was also decreasing, although still hotter than the photosphere. Additionally, we observed no supporting evidence of Hα first increasing in absorption with increasing activity.

We discussed how Hα can be modeled as a two component system with one component being an active, emission profile while the other is a quiet, absorption profile. We also noted that the emission profile was always much broader than the absorption profile and the addition of these two profiles is what leads to the classic active M dwarf Hα line profile of a large emission line with a substantial central reversal. We postulated that these different components corresponded to the ratio of quiet to active chromosphere on the star and that the asymmetries frequently observed in Hα are due to a non-symmetric distribution of active and quiet regions on the observed side of the star. We observed a gap between the low-activity sample of stars and the more active sample, which is suggestive that this gap represents a rapid transition from being a younger, active, Hα emissive star to a quieter, older, Hα absorptive star.

As for Ca ii IRT, we observed that the line starts out, at M0.0V, as broad and shallow. It deepens and thins until M3.0V then rapidly retreats before becoming indistinguishable with the continuum at M5.0V. We proposed that this was due to the differing line formation processes in a simultaneously cooling photosphere and chromosphere over spectral subtypes M0.0V to M5.0V. Additionally, we discussed how this process made it difficult to use Ca ii IRT as an activity indicator for quiescent to low activity stars. The line tends to fill in rather than, like Hα lift up. This causes a low activity star to look like a colder, quiescent star with less absorption. We therefore concluded that Hα still serves as the best activity indicator for M dwarfs.

We assembled these observations into a proposed, updated, model of line formation in M dwarf chromospheres. This model describes how, for each activity indicator except for He i D_3 and, potentially, Ca ii HK, there is a effective temperature correlated amount of absorption that is not due to stellar activity. We proposed that Ca ii HK has emission correlated to the effective temperature due to pumping of its excited levels by Ca ii IRT. As activity increases, Ca ii IRT fills in and the pumping mechanism becomes progressively less important to the emission strength of Ca ii HK. Hα absorption profile gets combined with a wide emission profile. We suggest that this should be modeled by NLTE chromospheric models to confirm this mechanism as a possible explanation. Observationally this is first noticed with emission wings but as activity levels continue to increase the entire line goes into emission.

In the second section we discussed the use of simultaneous photometric and spectroscopic observations of a series of flares on the ultra-fast rotating, M4.5V, M dwarf, GJ 3270. We also added to these observations with 26 days of TESS observations. Initially we saw the asymmetries of the Hα line red shift which we interpreted as an active region rotating off the observable disk of the star. 45 minutes later we observed a large flare in which only some of the activity indicators reacted. We interpreted this as a new active region that was just over the limb of the star and this extreme viewing angle made for different absorption paths through the atmosphere for the different activity indicators resulting in the observed behavior.

Subsequently we observed a 10^{32} ergs flare which was immediately followed by large blue asymmetries in all activity indicators. These asymmetries were as much as 30 km s^{-1}offset from the line core. Over the next 90 minutes we observed these asymmetries weaken and shift back toward the line core. We interpreted this as the signature of an active region with post-flare arcadal loops co-rotating with star at a latitude of 40 degrees and starting at 65 degrees away from the disk center. 6 hours into the observations we observed a large increase in redshifted lines and we postulated that this might be coronal rain from a failed CME but we did not have sufficient evidence to back this conclusion.

These results give us additional research opportunities in a number of potential future projects. We briefly describe these below:

1. Expansion of the MNI to other activity indicators

2. Calibration of RV jitter to the Hα profile asymmetries in active M dwarfs. Using the hypothesis that asymmetries arise from the asymmetric distribution of active regions, and thereby spots, it should be possible to infer an expected RV deviation by observing the Hα profile asymmetry.
3. Investigate if force fitting of activity based RV jitter compensation techniques on M dwarfs in the quiet and ultra quiet regime would yield spurious results.
4. Determine if the methods used to track the active region on GJ 3270 can be improved to detect transiting active regions in similar stars during non-flaring periods.
5. With the criteria for quiescence determined in this work we can attempt to isolate quiescent M6+ stars in order to test the predictions we laid out. Additionally observations on M dwarfs from M0 to M8 that include both Ca II HK and Ca II IRT can determine if the modeled constraints of Ca II IRT pumping are correct.

A. Appendix

A.1. Wavelength ranges for index and MNI

Table A.1.: Hα wavelength ranges of concern

Index	Target Range (Å)	Reference Range 1 (Å)	Reference Range 2 (Å)
Hα $\widetilde{I}_T$	6563-6566	6552-6555	6577.5-6580.5
Hα $\widetilde{I}_{R_1}$	6552-6555	6549-6552	6577.5-6580.5
Hα $\widetilde{I}_{R_2}$	6577.5-6580.5	6552-6555	6583.5-6586.5

Table A.2.: Ca II IRT wavelength ranges of concern

Index	Target Range(Å)	R_1 Range(Å)	R_2 Range(Å)
Ca II IRT $\widetilde{I}_T$	8499.5-8501.24	8490-8494	8506-8510
Ca II IRT $\widetilde{I}_{R_1}$	8490-8494	8481-8485	8506-8510
Ca II IRT $\widetilde{I}_{R_2}$	8506-8510	8490-8494	8522-8526

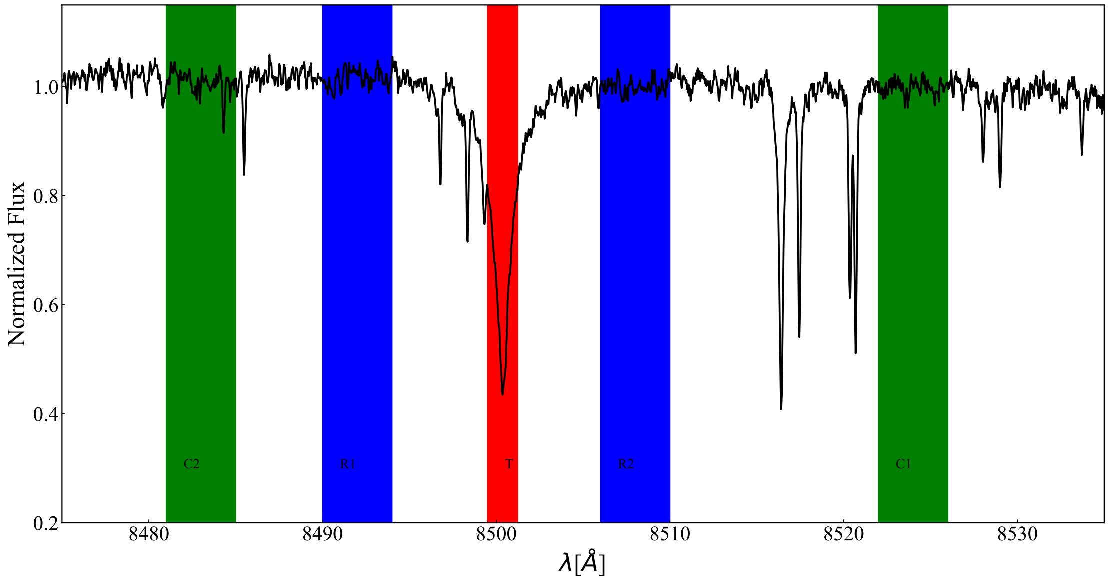

Figure A.1.: Display of the calculation regions used in this work for Ca II IRT. Red is the Ca II IRT measurement region. Blue denotes the regions that the Ca II IRT index is referenced to. Green represents the regions used for calculating the index of the reference regions.

Table A.3.: Na I D_1 wavelength ranges of concern

Index	Target Range(Å)	R_1 Range(Å)	R_2 Range(Å)
Na I D_1 $\widetilde{I}_T$	5897.3-5897.9	5896-5897	5898.5-5899.5
Na I D_1 $\widetilde{I}_{R_1}$	5896-5897	5871.5-5874	5898.5-5899.5
Na I D_1 $\widetilde{I}_{R_2}$	5898.5-5899.5.5	5896-5897	5911-5913.5

Table A.4.: Na I D_2 , wavelength ranges of concern

Index	Target Range(Å)	R_1 Range(Å)	R_2 Range(Å)
Na I D_2 $\widetilde{I}_T$	5891.3-5891.9	5889.7-5890.7	5892.5-5893.5
Na I D_2 $\widetilde{I}_{R_1}$	5889.7-5890.7	5871.5-5874	5892.5-5893.5
Na I D_2 $\widetilde{I}_{R_2}$	5892.5-5893.5	5889.7-5890.7	5911-5913.5

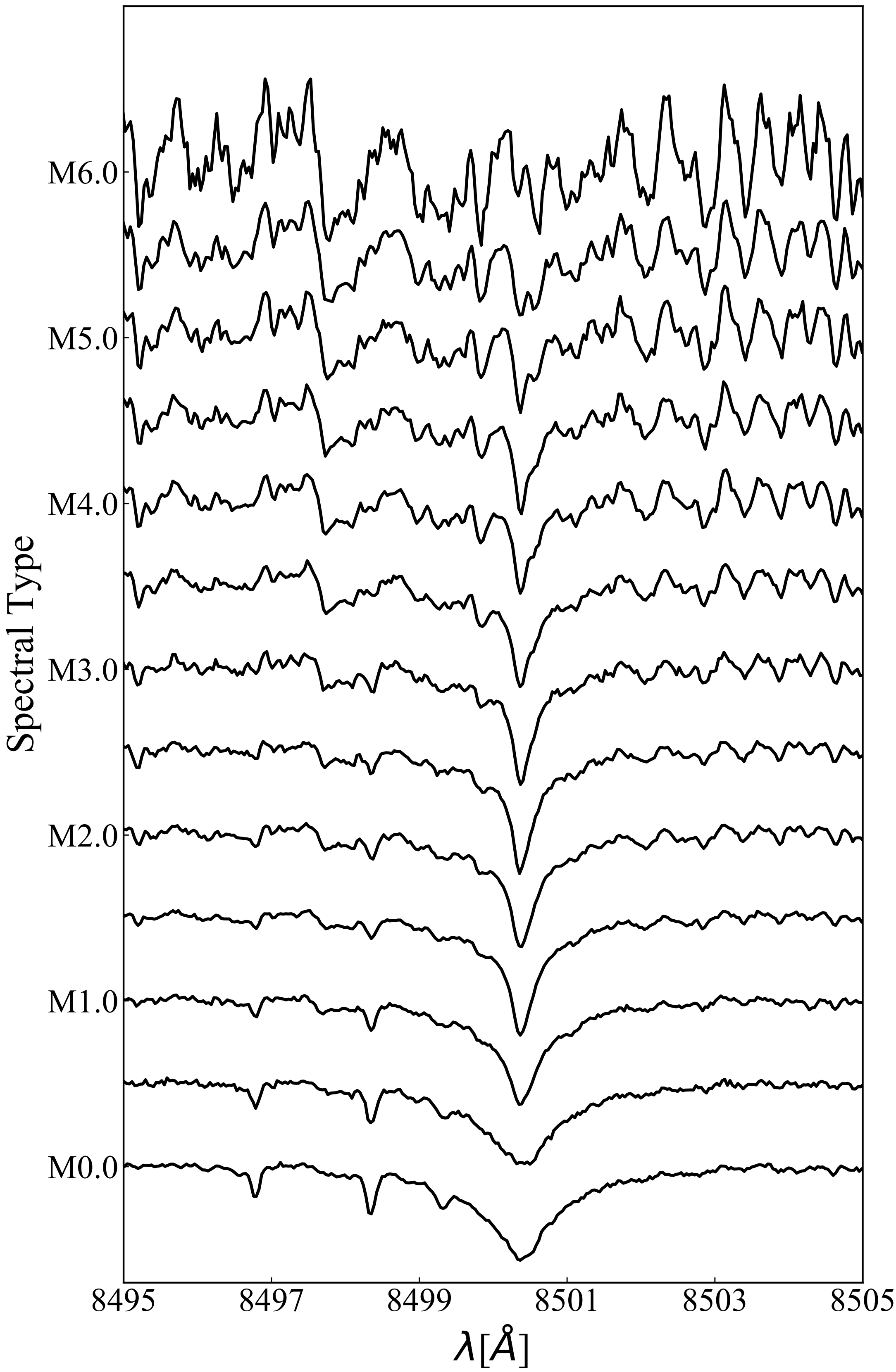

Figure A.2.: Progression of CARMENES reference M dwarf Ca II IRT spectra from M0.0V at the bottom to M6.0V at the top.

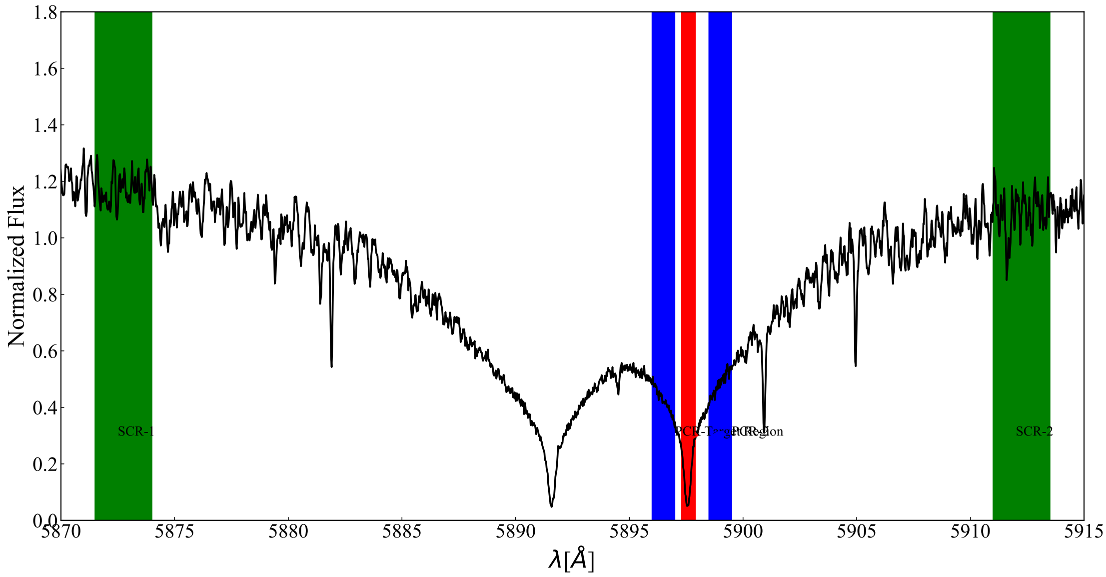

Figure A.3.: Display of the calculation regions used in this work for Na I D_1. Red is the Na I D_1 measurement region. Blue denotes the regions that the Na I D_1 index is referenced to. Green represents the regions used for calculating the index of the reference regions. Similar regions are used for Na I D_2.

Table A.5.: He I D_3 wavelength ranges of concern

Index	Target Range(Å)	R_1 Range(Å)	R_2 Range(Å)
He I D_3 $\widetilde{I}_T$	5876.7-5878.2	5872.5-5873.5	5879-5880
He I D_3 $\widetilde{I}_{R_1}$	5872.5-5873.5	5863.1-5864.5	5879-5880
He I D_3 $\widetilde{I}_{R_2}$	5879-5880	5872.5-5873.5	5882.6-5884

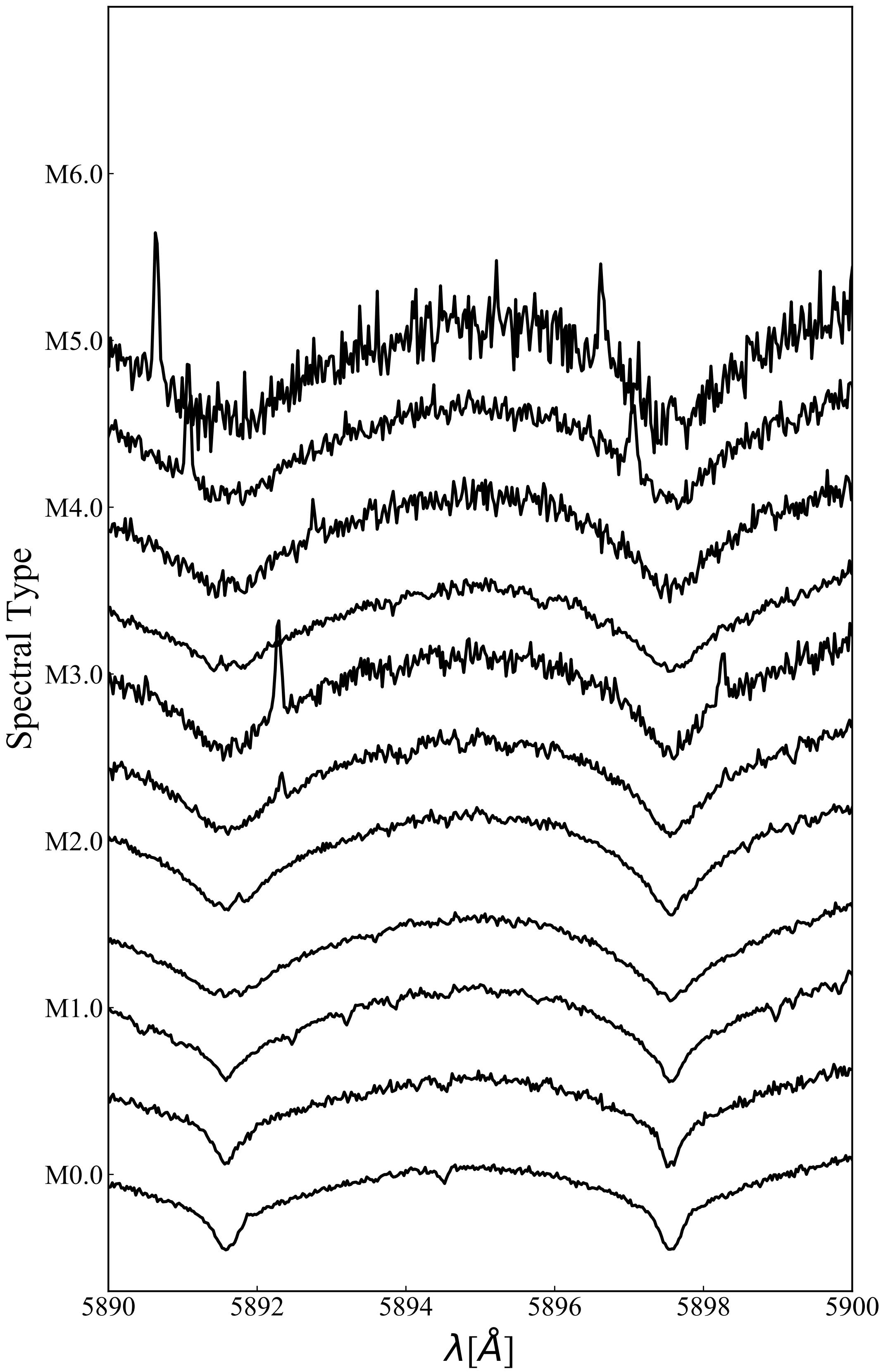

Figure A.4.: Progression of CARMENES reference M dwarf Na I $D_{1\&2}$ spectra from M0.0V at the bottom to M6.0V at the top. The thin emission lines are due to telluric emission.

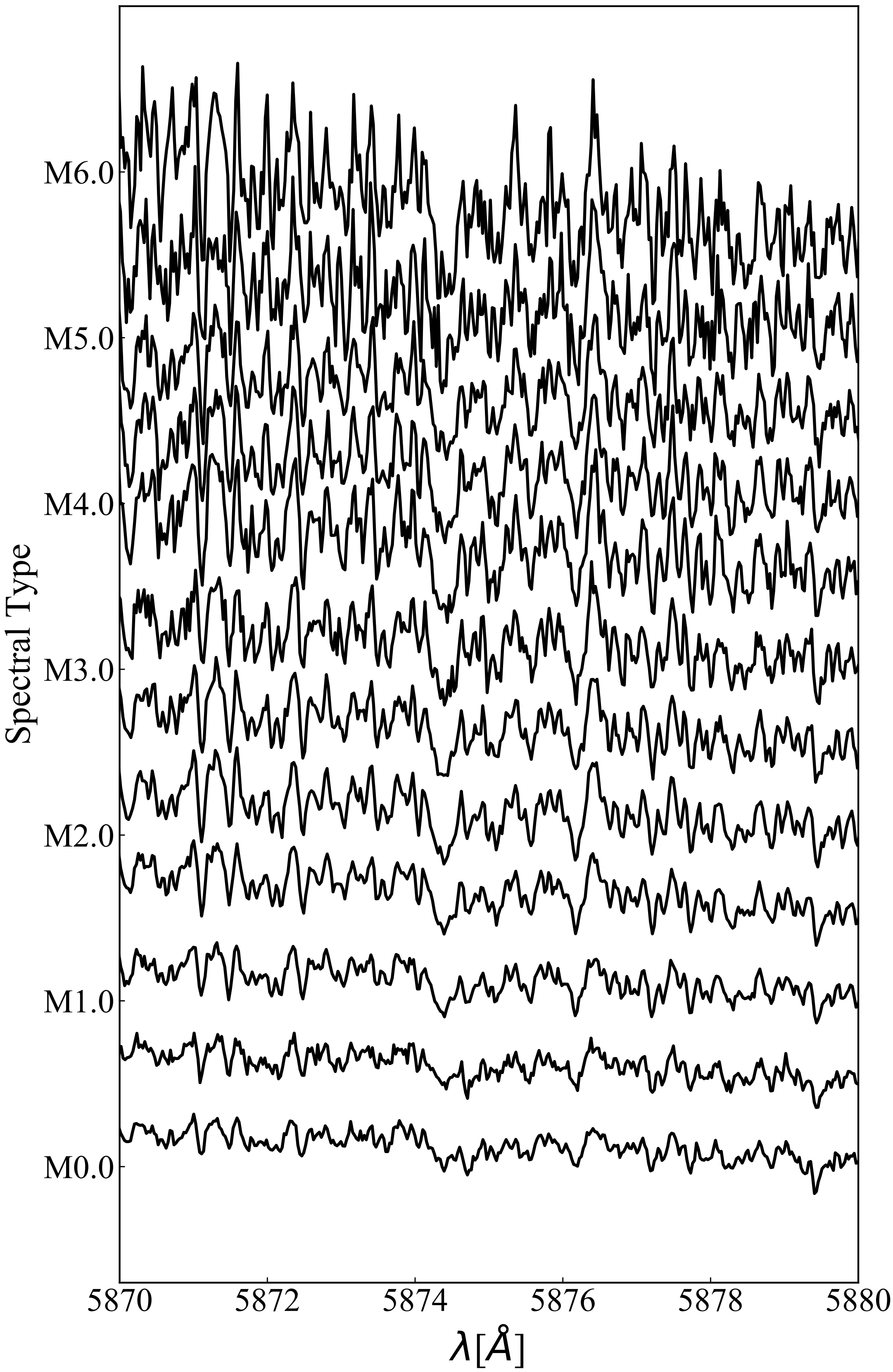

Figure A.5.: Progression of CARMENES reference M dwarf He I D_3 spectra from M0.0V at the bottom to M6.0V at the top.

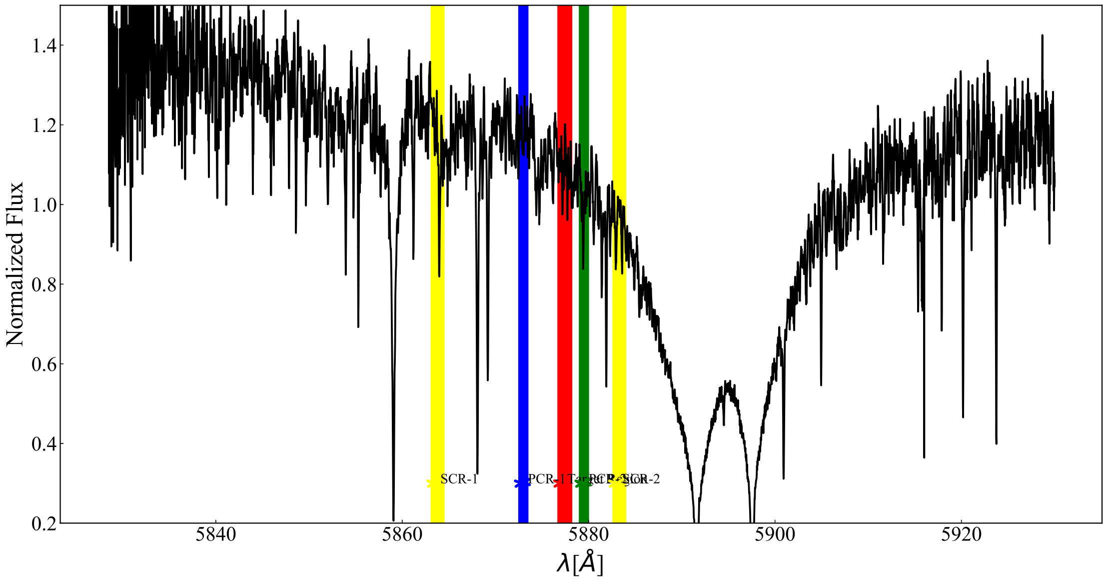

Figure A.6.: Display of the calculation regions used in this work for He I D_3. Red is the He I D_3 measurement region. Blue and green denote the regions that the He I D_3 index is referenced to. Yellow represents the regions used for calculating the index of the reference regions.

A.2. Median Activity Indicator Table

Table A.6.: Activity indicator MNI values 1.

KARMN	SPT	Hα	δHα	Ca II IRT	δCa II IRT	Na I D_1	δNa I D_1	He I D_3	δHe I D_3
J00051+457	1.0	0.88	0.01	0.71	0.01	0.6	0.01	0.95	0.01
J00067-075	5.5	1.05	0.01	0.87	0.01	0.49	0.02	...	0.01
J00162+198E	4.0	0.98	0.01	0.81	0.01	0.29	0.01	0.94	0.01
J00162+198W	4.0	2.53	0.01	0.92	0.01	1.34	0.02	1.03	0.01
J00183+440	1.0	0.89	0.01	0.69	0.01	0.41	0.01	0.95	0.01
J00184+440	3.5	0.97	0.01	0.79	0.01	0.33	0.01	0.9	0.01
J00286-066	4.0	0.97	0.01	0.78	0.01	0.3	0.01	0.93	0.01
J00389+306	2.5	0.91	0.01	0.72	0.01	0.41	0.01	0.94	0.01
J00570+450	3.0	0.97	0.01	0.75	0.01	0.4	0.01	0.93	0.01
J01013+613	2.0	0.92	0.01	0.71	0.01	0.47	0.01	0.92	0.01
J01019+541	5.0	2.78	0.02	0.92	0.01	2.35	0.13	...	0.04
J01025+716	3.0	0.92	0.01	0.73	0.01	0.4	0.01	0.94	0.01
J01026+623	1.5	0.92	0.01	0.72	0.01	0.61	0.01	0.95	0.01
J01033+623	5.0	4.18	0.01	1.05	0.01	3.55	0.07	1.18	0.02
J01048-181	5.0	1.02	0.01	0.88	0.01	...	...	...	...
J01056+284	5.0	1.07	0.01	0.88	0.01	...	...	...	...
J01125-169	4.5	1.45	0.01	0.83	0.01	...	...	...	0.01
J01339-176	4.0	1.61	0.01	0.82	0.01	1.13	0.02	0.96	0.01
J01352-072	4.0	3.15	0.01	1.01	0.01	1.28	0.02	1.39	0.02
J01433+043	2.0	0.93	0.01	0.71	0.01	0.42	0.01	0.94	0.01
J01518+644	2.5	0.9	0.01	0.72	0.01	0.52	0.01	0.94	0.01
J02002+130	3.5	1.74	0.01	0.85	0.01	2.08	0.03	0.96	0.01
J02015+637	3.0	0.94	0.01	0.74	0.01	0.36	0.01	0.95	0.01
J02070+496	3.5	1.13	0.01	0.75	0.01	0.54	0.01	0.92	0.01
J02088+494	3.5	3.03	0.01	0.93	0.01	1.84	0.02	1.1	0.01
J02123+035	1.5	0.89	0.01	0.68	0.01	0.39	0.01	0.95	0.01
J02222+478	0.5	0.83	0.01	0.68	0.01	0.6	0.01	0.95	0.01
J02336+249	4.0	1.99	0.01	0.87	0.01	1.39	0.02	0.99	0.01
J02358+202	2.0	0.87	0.01	0.71	0.01	0.53	0.01	0.94	0.01
J02362+068	4.0	0.97	0.01	0.81	0.01	0.27	0.01	0.92	0.01
J02442+255	3.0	0.94	0.01	0.74	0.01	0.33	0.01	0.93	0.01
J02519+224	4.0	2.92	0.01	0.91	0.01	1.19	0.02	1.12	0.01
J02530+168	7.0	1.14	0.01	0.92	0.01	...	...	...	...
J02565+554W	1.0	0.83	0.01	0.66	0.01	0.51	0.01	0.97	0.01
J03133+047	5.0	1.03	0.01	0.89	0.01	...	...	...	...
J03181+382	1.5	0.84	0.01	0.68	0.01	0.53	0.01	0.94	0.01
J03213+799	2.0	0.91	0.01	0.71	0.01	0.48	0.01	0.94	0.01
J03217-066	2.0	1.02	0.01	0.75	0.01	0.65	0.01	0.94	0.01
J03463+262	0.0	0.86	0.01	0.68	0.01	0.61	0.01	0.95	0.01
J03473-019	3.0	2.28	0.01	0.97	0.01	1.86	0.02	1.03	0.01
J03531+625	3.0	0.93	0.01	0.72	0.01	0.31	0.01	0.94	0.01
J04153-076	4.5	2.28	0.01	0.84	0.01	1.4	0.03	1.01	0.01
J04219+213	0.0	0.8	0.01	0.66	0.01	0.3	0.01	0.98	0.01
J04225+105	3.5	0.94	0.01	0.78	0.01	0.38	0.01	0.95	0.01
J04290+219	0.5	0.79	0.01	0.62	0.01	0.59	0.01	0.95	0.01
J04311+589	4.0	1.0	0.01	0.84	0.01	0.26	0.01	0.95	0.01
J04376-110	1.5	0.88	0.01	0.69	0.01	0.44	0.01	0.94	0.01
J04376+528	0.0	0.83	0.01	0.67	0.01	0.55	0.01	0.97	0.01
J04429+189	2.0	0.89	0.01	0.72	0.01	0.52	0.01	0.95	0.01
J04429+214	3.5	0.96	0.01	0.76	0.01	0.37	0.01	0.95	0.01

Table A.7.: Activity indicator MNI values 2.

KARMN	SPT	Hα	δHα	Ca II IRT	δCa II IRT	Na I D_1	δNa I D_1	He I D_3	δHe I D_3
J04472+206	5.0	3.97	0.02	0.92	0.01	1.81	0.05	1.31	0.03
J04520+064	3.5	0.97	0.01	0.79	0.01	0.32	0.01	0.94	0.01
J04538-177	2.0	0.9	0.01	0.7	0.01	0.43	0.01	0.94	0.01
J04588+498	0.0	0.85	0.01	0.68	0.01	0.61	0.01	0.96	0.01
J05019-069	4.0	1.22	0.01	0.82	0.01	0.95	0.02	0.93	0.01
J05019+011	4.0	3.34	0.01	0.96	0.01	1.51	0.03	1.1	0.01
J05033-173	3.0	0.94	0.01	0.75	0.01	0.34	0.01	0.92	0.01
J05062+046	4.0	3.33	0.01	0.93	0.01	1.5	0.03	1.21	0.02
J05084-210	5.0	5.29	0.05	0.96	0.01	...	...	...	...
J05127+196	2.0	0.89	0.01	0.7	0.01	0.41	0.01	0.94	0.01
J05280+096	3.5	0.98	0.01	0.77	0.01	0.18	0.01	0.93	0.01
J05314-036	1.5	0.87	0.01	0.69	0.01	0.57	0.01	0.94	0.01
J05337+019	2.5	2.55	0.01	0.97	0.01	2.37	0.02	1.04	0.01
J05348+138	3.5	0.95	0.01	0.77	0.01	0.32	0.01	0.95	0.01
J05360-076	4.0	0.98	0.01	0.83	0.01	0.16	0.01	0.95	0.01
J05365+113	0.0	0.96	0.01	0.74	0.01	0.63	0.01	0.96	0.01
J05366+112	4.0	2.0	0.01	0.84	0.01	1.08	0.01	0.99	0.01
J05415+534	1.0	0.87	0.01	0.7	0.01	0.59	0.01	0.95	0.01
J05421+124	4.0	0.97	0.01	0.81	0.01	0.21	0.01	0.93	0.01
J05532+242	1.5	0.87	0.01	0.69	0.01	0.5	0.01	0.95	0.01
J06000+027	4.0	2.0	0.01	0.85	0.01	1.39	0.02	0.99	0.01
J06011+595	3.5	0.97	0.01	0.8	0.01	0.33	0.01	0.93	0.01
J06024+498	5.0	1.03	0.01	0.87	0.01	0.11	0.04	0.89	0.02
J06103+821	2.0	0.9	0.01	0.71	0.01	0.41	0.01	0.94	0.01
J06105-218	0.5	0.84	0.01	0.69	0.01	0.59	0.01	0.95	0.01
J06246+234	4.0	0.98	0.01	0.8	0.01	0.44	0.01	0.9	0.01
J06318+414	5.0	4.14	0.02	0.94	0.01	...	...	1.39	0.04
J06371+175	0.0	0.86	0.01	0.69	0.01	0.54	0.01	0.97	0.01
J06396-210	4.0	1.04	0.01	0.8	0.01	0.59	0.01	0.94	0.01
J06421+035	3.5	0.94	0.01	0.75	0.01	0.27	0.01	0.94	0.01
J06548+332	3.0	0.94	0.01	0.75	0.01	0.29	0.01	0.9	0.01
J06574+740	4.0	2.84	0.01	0.9	0.01	1.69	0.02	1.13	0.01
J06594+193	5.0	1.12	0.01	0.91	0.01	...	...	...	...
J07001-190	5.0	3.65	0.02	1.01	0.01	3.79	0.11	1.2	0.03
J07033+346	4.0	2.25	0.01	0.86	0.01	1.47	0.02	1.0	0.01
J07044+682	3.0	0.92	0.01	0.75	0.01	0.33	0.01	0.94	0.01
J07274+052	3.5	0.97	0.01	0.79	0.01	0.25	0.01	0.96	0.01
J07287-032	3.0	0.93	0.01	0.75	0.01	0.3	0.01	0.94	0.01
J07319+362N	3.5	1.99	0.01	0.84	0.01	0.94	0.01	0.98	0.01
J07353+548	2.0	0.92	0.01	0.71	0.01	0.38	0.01	0.93	0.01
J07361-031	1.0	1.15	0.01	0.81	0.01	0.76	0.01	0.96	0.01
J07386-212	3.0	0.94	0.01	0.75	0.01	0.22	0.01	0.94	0.01
J07393+021	0.01	0.82	0.01	0.66	0.01	0.59	0.01	0.96	0.01
J07403-174	6.0	1.14	0.05	0.9	0.01	...	...	...	...
J07446+035	4.5	3.71	0.01	0.99	0.01	2.18	0.03	1.12	0.01
J07472+503	4.0	2.19	0.01	0.86	0.01	1.34	0.02	1.01	0.01
J07558+833	4.5	2.74	0.01	0.91	0.01	2.23	0.04	1.08	0.01
J07582+413	3.5	0.97	0.01	0.81	0.01	0.25	0.01	0.93	0.01
J08119+087	4.5	1.0	0.01	0.78	0.01	0.98	0.01	0.9	0.01
J08126-215	4.0	0.99	0.01	0.85	0.01	0.38	0.01	0.94	0.01

Table A.8.: Activity indicator MNI values 3.

KARMN	SPT	Hα	δHα	Ca II IRT	δCa II IRT	Na I D_1	δNa I D_1	He I D_3	δHe I D_3
J08161+013	2.0	0.9	0.01	0.71	0.01	0.44	0.01	0.95	0.01
J08293+039	2.5	0.9	0.01	0.72	0.01	0.54	0.01	0.94	0.01
J08298+267	6.5	2.91	0.02	0.94	0.01	...	...	...	...
J08315+730	4.0	0.97	0.01	0.79	0.01	0.27	0.01	0.95	0.01
J08358+680	2.5	0.99	0.01	0.73	0.01	0.42	0.01	0.94	0.01
J08402+314	3.5	0.96	0.01	0.78	0.01	0.25	0.01	0.93	0.01
J08409-234	3.5	0.94	0.01	0.77	0.01	0.3	0.01	0.96	0.01
J08413+594	5.5	1.32	0.01	0.89	0.01	...	...	...	...
J08526+283	4.5	1.0	0.01	0.86	0.01	0.32	0.01	0.96	0.01
J09003+218	6.5	3.77	0.06	0.95	0.01	...	...	...	...
J09005+465	4.5	1.4	0.01	0.85	0.01	0.91	0.02	0.96	0.01
J09028+680	4.0	0.97	0.01	0.79	0.01	0.28	0.01	0.93	0.01
J09033+056	7.0	2.72	...	0.91	0.01	...	...	...	...
J09133+688	2.5	1.11	0.01	0.77	0.01	0.77	0.01	0.95	0.01
J09140+196	3.0	0.98	0.01	0.75	0.01	0.62	0.01	0.95	0.01
J09143+526	0.0	0.83	0.01	0.68	0.01	0.56	0.01	0.97	0.01
J09144+526	0.0	0.83	0.01	0.67	0.01	0.5	0.01	0.97	0.01
J09161+018	4.0	2.64	0.01	0.88	0.01	1.72	0.02	1.04	0.01
J09163-186	1.5	1.0	0.01	0.73	0.01	0.67	0.01	0.95	0.01
J09307+003	3.5	0.97	0.01	0.76	0.01	0.27	0.01	0.94	0.01
J09360-216	2.5	0.92	0.01	0.72	0.01	0.32	0.01	0.94	0.01
J09411+132	1.5	0.91	0.01	0.7	0.01	0.52	0.01	0.94	0.01
J09423+559	3.5	0.97	0.01	0.79	0.01	0.28	0.01	0.95	0.01
J09425+700	2.0	1.11	0.01	0.76	0.01	0.67	0.01	0.95	0.01
J09428+700	3.0	1.21	0.01	0.78	0.01	0.62	0.01	0.95	0.01
J09439+269	3.5	0.94	0.01	0.77	0.01	0.48	0.01	0.95	0.01
J09447-182	4.0	0.97	0.01	0.81	0.01	0.36	0.01	0.94	0.01
J09449-123	5.0	5.83	0.02	1.01	0.01	1.48	0.05	1.64	...
J09468+760	1.5	0.87	0.01	0.69	0.01	0.47	0.01	0.96	0.01
J09511-123	0.5	0.87	0.01	0.68	0.01	0.5	0.01	0.97	0.01
J09561+627	0.0	0.85	0.01	0.68	0.01	0.62	0.01	0.95	0.01
J10023+480	1.0	0.84	0.01	0.68	0.01	0.53	0.01	0.96	0.01
J10122-037	1.5	0.91	0.01	0.72	0.01	0.59	0.01	0.95	0.01
J10125+570	3.5	0.97	0.01	0.77	0.01	0.33	0.01	0.93	0.01
J10167-119	3.0	0.91	0.01	0.72	0.01	0.39	0.01	0.95	0.01
J10182-204	4.5	3.89	0.02	1.05	0.01	2.23	0.07	1.27	0.02
J10196+198	3.0	2.43	0.01	0.92	0.01	1.78	0.02	1.02	0.01
J10251-102	1.0	0.88	0.01	0.7	0.01	0.6	0.01	0.95	0.01
J10289+008	2.0	0.9	0.01	0.7	0.01	0.46	0.01	0.94	0.01
J10350-094	3.0	0.93	0.01	0.75	0.01	0.37	0.01	0.94	0.01
J10354+694	3.5	0.97	0.01	0.76	0.01	0.26	0.01	0.94	0.01
J10360+051	3.5	2.83	0.01	0.86	0.01	1.64	0.02	1.02	0.01
J10396-069	2.5	0.91	0.01	0.73	0.01	0.44	0.01	0.95	0.01
J10416+376	4.5	0.98	0.01	0.82	0.01	0.25	0.01	0.93	0.01
J10482-113	6.5	2.08	0.02	0.91	0.01	...	...	...	...
J10504+331	4.0	0.96	0.01	0.79	0.01	0.3	0.01	0.96	0.01
J10508+068	4.0	0.97	0.01	0.82	0.01	0.3	0.01	0.94	0.01
J10564+070	6.0	4.33	0.01	1.0	0.01	...	...	...	...
J10584-107	5.0	2.99	0.02	0.91	0.01	...	...	1.03	0.03
J11000+228	2.5	0.92	0.01	0.72	0.01	0.39	0.01	0.94	0.01

Table A.9.: Activity indicator MNI values 4.

KARMN	SPT	Hα	δHα	Ca II IRT	δCa II IRT	Na I D_1	δNa I D_1	He I D_3	δHe I D_3
J11026+219	1.0	1.02	0.01	0.77	0.01	0.67	0.01	0.96	0.01
J11033+359	1.5	0.94	0.01	0.69	0.01	...	0.01	0.94	0.01
J11054+435	1.0	0.91	0.01	0.69	0.01	0.36	0.01	0.94	0.01
J11055+435	5.5	4.73	0.02	0.93	0.01	8.48	0.29	1.64	0.03
J11126+189	1.5	0.87	0.01	0.71	0.01	0.57	0.01	0.95	0.01
J11201-104	2.0	1.53	0.01	0.89	0.01	1.03	0.01	0.99	0.01
J11289+101	3.5	0.96	0.01	0.78	0.01	0.28	0.01	0.94	0.01
J11302+076	2.5	0.9	0.01	0.72	0.01	0.41	0.01	0.95	0.01
J11306-080	3.5	0.96	0.01	0.76	0.01	0.35	0.01	0.93	0.01
J11417+427	4.0	0.96	0.01	0.79	0.01	0.26	0.01	0.9	0.01
J11421+267	2.5	0.92	0.01	0.72	0.01	0.25	0.01	...	...
J11467-140	3.0	0.91	0.01	0.73	0.01	0.45	0.01	0.94	0.01
J11474+667	5.0	3.61	0.02	0.95	0.01	2.81	0.12	1.13	0.03
J11476+002	4.0	2.68	0.01	0.89	0.01	1.51	0.04	1.02	0.02
J11476+786	3.5	0.97	0.01	0.77	0.01	0.24	0.01	0.94	0.01
J11477+008	4.0	0.99	0.01	0.83	0.01	0.34	0.01	0.93	0.01
J11509+483	4.5	1.04	0.01	0.85	0.01	0.47	0.01	0.92	0.01
J11511+352	1.5	0.93	0.01	0.7	0.01	0.56	0.01	0.95	0.01
J12054+695	4.0	1.0	0.01	0.81	0.01	0.31	0.01	0.95	0.01
J12100-150	3.5	0.97	0.01	0.81	0.01	0.21	0.01	0.96	0.01
J12111-199	3.0	0.94	0.01	0.74	0.01	0.36	0.01	0.94	0.01
J12123+544S	0.0	0.82	0.01	0.66	0.01	0.54	0.01	0.97	0.01
J12156+526	4.0	2.8	0.01	0.91	0.01	1.66	0.02	1.17	0.01
J12189+111	5.0	2.98	0.01	0.96	0.01	2.86	0.07	1.06	0.02
J12230+640	3.0	0.9	0.01	0.71	0.01	0.39	0.01	0.91	...
J12248-182	2.0	0.92	0.01	0.71	0.01	0.3	0.01	0.93	0.01
J12312+086	0.5	0.85	0.01	0.68	0.01	0.6	0.01	0.96	0.01
J12350+098	2.5	0.89	0.01	0.71	0.01	0.41	0.01	0.95	0.01
J12373-208	4.0	0.96	0.01	0.81	0.01	0.16	0.01	0.95	0.01
J12388+116	3.0	0.95	0.01	0.76	0.01	0.39	0.01	0.96	0.01
J12428+418	4.0	1.96	0.01	0.84	0.01	1.08	0.01	0.98	0.01
J12479+097	3.5	0.96	0.01	0.79	0.01	0.23	0.01	0.94	0.01
J13005+056	4.5	2.82	0.01	0.94	0.01	2.8	0.07	1.0	0.02
J13102+477	5.0	2.33	0.01	0.9	0.01	1.66	0.07	1.02	0.02
J13196+333	1.5	0.85	0.01	0.68	0.01	0.51	0.01	0.94	0.01
J13209+342	1.0	0.87	0.01	0.69	0.01	0.51	0.01	0.96	0.01
J13229+244	4.0	0.98	0.01	0.79	0.01	0.27	0.01	0.93	0.01
J13283-023W	3.0	0.93	0.01	0.74	0.01	0.38	0.01	0.95	0.01
J13293+114	3.5	0.93	0.01	0.74	0.01	0.32	0.01	0.94	0.01
J13299+102	0.5	0.85	0.01	0.68	0.01	0.53	0.01	0.95	0.01
J13427+332	3.5	0.97	0.01	0.8	0.01	0.3	0.01	0.94	0.01
J13450+176	0.0	0.86	0.01	0.67	0.01	0.41	0.01	0.98	0.01
J13457+148	1.5	0.87	0.01	0.69	0.01	0.46	0.01	0.95	0.01
J13458-179	3.5	0.95	0.01	0.77	0.01	0.24	0.01	0.94	0.01
J13536+776	4.0	2.3	0.01	0.85	0.01	1.4	0.02	1.0	0.01
J13582+125	3.0	0.96	0.01	0.76	0.01	0.45	0.01	0.91	0.01
J13591-198	4.0	2.16	0.01	0.89	0.01	0.87	0.02	0.99	0.01
J14010-026	1.0	0.86	0.01	0.69	0.01	0.5	0.01	0.96	0.01
J14082+805	1.0	0.85	0.01	0.69	0.01	0.55	0.01	0.96	0.01
J14152+450	3.0	0.92	0.01	0.73	0.01	0.36	0.01	0.95	0.01

Table A.10.: Activity indicator MNI values 5.

KARMN	SPT	Hα	δHα	Ca II IRT	δCa II IRT	Na I D_1	δNa I D_1	He I D_3	δHe I D_3
J14155+046	5.0	1.0	0.01	0.83	0.01	0.47	0.02	0.93	0.02
J14173+454	5.0	2.37	0.01	0.87	0.01	2.77	0.08	...	0.02
J14251+518	2.5	0.92	0.01	0.72	0.01	0.38	0.01	0.94	0.01
J14257+236E	0.5	0.84	0.01	0.68	0.01	0.59	0.01	0.95	0.01
J14257+236W	0.0	0.82	0.01	0.65	0.01	0.6	0.01	0.95	0.01
J14294+155	2.0	0.88	0.01	0.7	0.01	0.51	0.01	0.95	0.01
J14307-086	0.5	0.8	0.01	0.62	0.01	0.57	0.01	0.96	0.01
J14310-122	3.5	0.96	0.01	0.78	0.01	0.2	0.01	0.93	0.01
J14321+081	6.0	2.94	0.05	0.97	0.01	...	...	...	...
J14342-125	4.0	0.99	0.01	0.84	0.01	0.22	0.01	0.94	0.01
J14524+123	2.0	0.92	0.01	0.74	0.01	0.58	0.01	0.95	0.01
J14544+355	3.5	0.96	0.01	0.77	0.01	0.26	0.01	0.95	0.01
J15013+055	3.0	0.96	0.01	0.76	0.01	0.4	0.01	0.93	0.01
J15095+031	3.0	0.92	0.01	0.73	0.01	0.35	0.01	0.95	0.01
J15194-077	3.0	0.95	0.01	0.75	0.01	0.29	0.01	0.93	0.01
J15218+209	1.5	1.86	0.01	0.95	0.01	1.35	0.01	1.0	0.01
J15305+094	5.5	2.53	0.02	0.91	0.01	...	...	...	...
J15369-141	4.0	0.97	0.01	0.8	0.01	0.32	0.01	0.95	0.01
J15412+759	3.0	0.95	0.01	0.75	0.01	0.32	0.01	0.93	0.01
J15474-108	2.0	0.91	0.01	0.73	0.01	0.43	0.01	0.94	0.01
J15499+796	5.0	2.78	0.02	0.9	0.01	1.92	0.08	1.13	0.03
J15598-082	1.0	0.91	0.01	0.71	0.01	0.58	0.01	0.95	0.01
J16028+205	4.0	0.99	0.01	0.81	0.01	0.29	0.01	0.93	0.01
J16092+093	3.0	0.98	0.01	0.73	0.01	0.39	0.01	0.94	0.01
J16167+672N	3.0	0.92	0.01	0.74	0.01	0.44	0.01	0.95	0.01
J16167+672S	0.0	0.8	0.01	0.64	0.01	0.6	0.01	0.95	0.01
J16254+543	1.5	0.91	0.01	0.7	0.01	0.41	0.01	0.93	0.01
J16303-126	3.5	0.96	0.01	0.79	0.01	0.2	...	0.89	...
J16313+408	5.0	3.69	0.02	1.0	0.01	...	...	...	...
J16327+126	3.0	0.92	0.01	0.72	0.01	0.27	0.01	0.94	0.01
J16462+164	2.5	0.91	0.01	0.73	0.01	0.37	0.01	0.94	0.01
J16554-083N	3.5	0.96	0.01	0.79	0.01	0.29	0.01	0.93	0.01
J16555-083	7.0	...	...	0.92	0.01	...	...	...	...
J16570-043	3.5	2.44	0.01	0.86	0.01	1.61	...	1.0	...
J16581+257	1.0	0.88	0.01	0.7	0.01	0.6	0.01	0.95	0.01
J17033+514	4.5	1.01	0.01	0.86	0.01	0.24	0.01	0.93	0.01
J17052-050	1.5	0.87	0.01	0.69	0.01	0.42	0.01	0.95	0.01
J17071+215	3.0	0.93	0.01	0.74	0.01	0.33	0.01	0.94	0.01
J17115+384	3.5	0.93	0.01	0.76	0.01	0.26	0.01	0.94	0.01
J17166+080	2.0	0.91	0.01	0.71	0.01	0.38	0.01	0.93	0.01
J17198+417	2.5	0.92	0.01	0.73	0.01	0.33	0.01	0.93	0.01
J17303+055	0.0	0.84	0.01	0.68	0.01	0.58	0.01	0.96	0.01
J17338+169	5.5	4.92	0.03	0.96	0.01	1.41	0.04	1.63	0.03
J17355+616	0.5	0.87	0.01	0.69	0.01	0.6	0.01	0.95	0.01
J17378+185	1.0	0.89	0.01	0.68	0.01	0.43	0.01	0.94	0.01
J17542+073	4.0	1.01	0.01	0.81	0.01	0.29	0.01	0.94	0.01
J17578+046	3.5	0.97	0.01	0.77	0.01	0.2	0.01	0.91	0.01
J17578+465	2.5	0.97	0.01	0.75	0.01	0.4	0.01	0.94	0.01
J18022+642	5.0	2.75	0.01	0.89	0.01	2.89	0.07	1.05	0.02
J18027+375	5.0	1.01	0.01	0.88	0.01	...	...	...	...

Table A.11.: Activity indicator MNI values 6.

KARMN	SPT	Hα	δHα	Ca II IRT	δCa II IRT	Na I D_1	δNa I D_1	He I D_3	δHe I D_3
J18051-030	1.0	0.86	0.01	0.69	0.01	0.52	0.01	0.95	0.0 1
J18075-159	4.5	2.41	0.01	0.88	0.01	...	...	...	...
J18131+260	4.0	3.15	0.01	0.92	0.01	1.81	0.02	1.06	0.01
J18165+048	5.0	1.01	0.01	0.87	0.01	0.46	0.02	...	0.02
J18174+483	2.0	1.49	0.01	0.84	0.01	0.95	0.01	0.97	0.0
J18180+387E	3.0	0.94	0.01	0.74	0.01	0.31	0.01	0.93	0.01
J18189+661	4.5	1.84	0.01	0.84	0.01	3.08	0.06	0.99	0.01
J18221+063	4.0	0.96	0.01	0.75	0.01	0.21	0.01	0.92	0.01
J18224+620	4.0	1.01	0.01	0.85	0.01	0.43	0.01	0.91	0.01
J18319+406	3.5	0.99	0.01	0.77	0.01	0.41	0.01	0.93	0.01
J18346+401	3.5	0.98	0.01	0.82	0.01	0.39	0.01	0.95	0.01
J18353+457	0.5	0.82	0.01	0.65	0.01	0.54	0.01	0.97	0.01
J18363+136	4.0	1.32	0.01	0.78	0.01	0.53	0.01	0.95	0.01
J18409-133	1.0	0.85	0.01	0.69	0.01	0.57	0.01	0.94	0.01
J18419+318	3.0	0.94	0.01	0.73	0.01	0.31	0.01	0.93	0.01
J18480-145	2.5	0.91	0.01	0.72	0.01	0.42	0.01	0.92	0.01
J18482+076	5.0	2.32	0.01	0.94	0.01	2.24	0.08	1.02	0.02
J18498-238	3.5	1.76	0.01	0.82	0.01	1.88	0.02	0.95	0.01
J18580+059	0.5	0.85	0.01	0.68	0.01	0.61	0.01	0.95	0.01
J19070+208	2.0	0.95	0.01	0.7	0.01	0.21	0.01	0.94	0.01
J19072+208	2.0	0.95	0.01	0.71	0.01	0.23	0.01	0.94	0.01
J19084+322	3.0	0.93	0.01	0.75	0.01	0.31	0.01	0.92	0.01
J19098+176	4.5	1.0	0.01	0.86	0.01	0.33	0.01	0.93	0.01
J19169+051N	2.5	0.9	0.01	0.72	0.01	0.43	0.01	0.95	0.01
J19169+051S	8.0	...	...	0.94	0.01	...	...	...	...
J19216+208	4.5	1.0	0.01	0.84	0.01	0.35	0.01	0.92	0.01
J19251+283	3.0	0.97	0.01	0.78	0.01	0.31	0.01	0.93	0.01
J19346+045	0.0	0.81	0.01	0.66	0.01	0.5	0.01	0.98	0.01
J19422-207	5.0	3.18	0.02	0.94	0.01	2.79	0.11	1.13	0.03
J19511+464	4.0	2.55	0.01	0.87	0.01	1.69	0.03	1.07	0.01
J20093-012	5.0	3.14	0.01	0.93	0.01	2.36	0.07	1.09	0.03
J20198+229	3.0	2.32	0.01	1.03	0.01	1.92	0.03	1.03	0.01
J20260+585	5.0	1.06	0.01	0.89	0.01	...	...	...	...
J20305+654	2.5	0.99	0.01	0.74	0.01	0.46	0.01	0.93	0.01
J20336+617	4.0	0.98	0.01	0.8	0.01	0.26	0.01	0.95	0.01
J20405+154	4.5	1.1	0.01	0.87	0.01	0.45	0.01	0.94	0.01
J20450+444	1.5	0.89	0.01	0.7	0.01	0.45	0.01	0.94	0.01
J20525-169	4.0	0.99	0.01	0.82	0.01	0.39	0.01	0.91	0.01
J20533+621	1.0	0.86	0.01	0.68	0.01	0.57	0.01	0.95	0.01
J20556-140N	4.0	0.98	0.01	0.81	0.01	0.3	0.01	0.94	0.01
J20556-140S	5.0	1.02	0.01	0.86	0.01	0.42	0.03	0.92	0.02
J20567-104	2.5	0.91	0.01	0.73	0.01	0.43	0.01	0.94	0.01
J21019-063	2.5	0.91	0.01	0.73	0.01	0.45	0.01	0.93	0.01
J21152+257	3.0	0.9	0.01	0.73	0.01	0.44	0.01	0.96	0.01
J21164+025	3.0	0.91	0.01	0.74	0.01	0.42	0.01	0.89	0.01
J21221+229	1.0	0.88	0.01	0.7	0.01	0.59	0.01	0.95	0.01
J21348+515	3.0	0.92	0.01	0.72	0.01	0.36	0.01	0.95	0.01
J21463+382	4.0	0.98	0.01	0.78	0.01	0.22	0.01	0.92	0.01
J21466-001	4.0	0.97	0.01	0.81	0.01	0.27	0.01	0.93	0.01
J21466+668	4.0	0.98	0.01	0.8	0.01	-1.57	0.01	0.9	0.01

Table A.12.: Activity indicator MNI values 7.

KARMN	SPT	Hα	δHα	Ca II IRT	δCa II IRT	Na I D_1	δNa I D_1	He I D_3	δHe I D_3
J22012+283	4.0	3.1	0.01	0.92	0.01	1.59	0.02	1.24	0.01
J22020-194	3.5	0.95	0.01	0.77	0.01	0.25	0.01	0.92	0.01
J22021+014	0.5	0.84	0.01	0.69	0.01	0.62	0.01	0.95	0.01
J22057+656	1.5	0.87	0.01	0.7	0.01	0.53	0.01	0.96	0.01
J22096-046	3.5	0.91	0.01	0.75	0.01	0.4	0.01	0.95	0.01
J22114+409	5.5	3.11	0.03	0.95	0.01	...	...	...	...
J22115+184	2.0	0.89	0.01	0.73	0.01	0.54	0.01	0.95	0.01
J22125+085	3.0	0.93	0.01	0.73	0.01	0.33	0.01	0.93	0.01
J22137-176	4.5	0.99	0.01	0.83	0.01	...	...	...	...
J22231-176	4.5	2.28	0.01	0.93	0.01	2.65	0.12	0.96	0.02
J22252+594	4.0	0.97	0.01	0.78	0.01	0.33	0.01	0.94	0.01
J22298+414	4.0	0.98	0.01	0.82	0.01	0.29	0.01	0.93	0.01
J22330+093	1.0	0.88	0.01	0.7	0.01	0.56	0.01	0.95	0.01
J22468+443	3.5	2.8	0.01	0.88	0.01	1.42	0.02	0.98	0.01
J22503-070	0.5	0.85	0.01	0.68	0.01	0.58	0.01	0.96	0.01
J22518+317	3.0	2.64	0.01	1.0	0.01	1.95	0.02	1.08	0.01
J22532-142	4.0	0.97	0.01	0.81	0.01	0.29	0.01	0.94	0.01
J22559+178	1.0	0.87	0.01	0.71	0.01	0.62	0.01	0.95	0.01
J22565+165	1.5	0.88	0.01	0.71	0.01	0.58	0.01	0.9	0.01
J23113+085	3.5	0.95	0.01	0.79	0.01	...	...	0.94	...
J23216+172	4.0	0.99	0.01	0.8	0.01	0.29	0.01	0.96	0.01
J23245+578	1.0	0.87	0.01	0.7	0.01	0.59	0.01	0.94	0.01
J23340+001	2.5	0.9	0.01	0.71	0.01	0.37	0.01	0.94	0.01
J23351-023	5.5	1.24	0.01	0.89	0.01	1.26	0.05	0.95	0.03
J23381-162	2.0	0.89	0.01	0.7	0.01	0.36	0.01	0.94	0.01
J23419+441	5.0	1.19	0.01	0.91	0.01	0.22	...	0.94	...
J23431+365	4.0	1.36	0.01	0.84	0.01	0.75	0.01	0.95	0.01
J23492+024	1.0	0.9	0.01	0.68	0.01	0.35	0.01	0.97	0.01
J23505-095	4.0	1.01	0.01	0.83	0.01	0.54	0.01	0.95	0.01
J23548+385	4.0	2.86	0.01	0.88	0.01	2.1	0.03	1.05	0.01
J23556-061	2.5	0.89	0.01	0.72	0.01	0.49	0.01	0.94	0.01
J23585+076	3.0	0.93	0.01	0.74	0.01	0.38	0.01	0.94	0.01
J04173+088	4.5	3.88	0.03	0.96	0.01	...	...	...	...

Bibliography

Abbett, W. P. & Hawley, S. L. 1999, ApJ, 521, 906

Adelberger, E. G., García, A., Robertson, R. G. H., et al. 2011, Reviews of Modern Physics, 83, 195

Alfvén, H. & Lindblad, B. 1947, Monthly Notices of the Royal Astronomical Society, 107, 211

Allard, F. & Hauschildt, P. H. 1995, ApJ, 445, 433

Alonso-Floriano, F. J., Morales, J. C., Caballero, J. A., et al. 2015, A&A, 577, A128

An, J. H., Evans, N. W., Kerins, E., et al. 2004, ApJ, 601, 845

Andretta, V., Doyle, J., & Byrne, P. 1997, Astronomy and Astrophysics, 322, 266

Appenzeller, I. & Mundt, R. 1989, A&A Rev., 1, 291

Astudillo-Defru, N., Delfosse, X., Bonfils, X., et al. 2017, A&A, 600, A13

Athay, R. G. & Warwick, C. S. 1961, in (Elsevier), 1–83

Atkins, P., De Paula, J., & Keeler, J. 2018, Atkins' Physical Chemistry (Oxford University Press)

Aulanier, G., Démoulin, P., Schrijver, C. J., et al. 2013, A&A, 549, A66

Baliunas, S. L. & Vaughan, A. H. 1985, ARA&A, 23, 379

Baranne, A., Queloz, D., Mayor, M., et al. 1996, A&AS, 119, 373

Barnes, J., Jeffers, S., Jones, H., et al. 2015, The Astrophysical Journal, 812

Barnes, S. A. 2003, ApJ, 586, 464

Basri, G. & Nguyen, H. T. 2018, ApJ, 863, 190

Bauer, F. F., Zechmeister, M., & Reiners, A. 2015, A&A, 581, A117

Bell, C. P. M., Mamajek, E. E., & Naylor, T. 2015, MNRAS, 454, 593

Benz, A. O., Conway, J., & Gudel, M. 1998, A&A, 331, 596

Benz, A. O. & Güdel, M. 2010, ARA&A, 48, 241

Berdyugina, S. V. 2005, Living Reviews in Solar Physics, 2, 8

Berger, T. E., Title, A. M., Tarbell, T., et al. 2007, in Astronomical Society of the Pacific Conference Series, Vol. 369, New Solar Physics with Solar-B Mission, ed. K. Shibata, S. Nagata, & T. Sakurai, 103

Berta, Z. K., Irwin, J., Charbonneau, D., Burke, C. J., & Falco, E. E. 2012, AJ, 144, 145

Bethe, H. A. 1939, Physical Review, 55, 103

Biermann, L. 1946, Naturwissenschaften, 33, 118

Böhm-Vitense, E. 1992, Introduction to Stellar Astrophysics

Bohr, N. 1913, The London, Edinburgh, and Dublin Philosophical Magazine and Journal of Science, 26, 1

Boudreaux, T. M., Newton, E. R., Mondrik, N., Charbonneau, D., & Irwin, J. 2022, ApJ, 929, 80

Bowen, I. S. 1927, Nature, 120, 473

Boyajian, T. S., von Braun, K., van Belle, G., et al. 2012, The Astrophysical Journal, 757, 112

Bozza, V., Mancini, L., & Sozzetti, A. 2016, Methods of Detecting Exoplanets: 1st Advanced School on Exoplanetary Science

Bradt, H. 2008, Astrophysics Processes

Branscomb, L. M. & Pagel, B. E. J. 1958, MNRAS, 118, 258

Budding, E. 1977, Ap&SS, 48, 207

Caballero, J. A., Cortés-Contreras, M., Alonso-Floriano, F. J., et al. 2016, in 19th Cambridge Workshop on Cool Stars, Stellar Systems, and the Sun (CS19), Cambridge Workshop on Cool Stars, Stellar Systems, and the Sun, 148

Caballero, J. A., Guàrdia, J., del Fresno, M. L., et al. 2016, in Observatory Operations: Strategies, Processes, and Systems VI, ed. A. B. Peck, R. L. Seaman, & C. R. Benn, Vol. 9910, International Society for Optics and Photonics (SPIE), 110 – 127

Campbell, B. & Walker, G. A. H. 1979, Publications of the Astronomical Society of the Pacific, 91, 540

Campbell, B., Walker, G. A. H., & Yang, S. 1988, ApJ, 331, 902

Cang, T. Q., Petit, P., Donati, J. F., et al. 2020, A&A, 643, A39

Cannon, A. J. & Pickering, E. C. 1912, Annals of Harvard College Observatory, 56, 115

Carrington, R. C. 1859, MNRAS, 20, 13

Carroll, B. & Ostlie, D. 2014, An Introduction to Modern Astrophysics, Pearson custom library (Pearson)

Chabrier, G. & Baraffe, I. 1997, A&A, 327, 1039

Chabrier, G. & Baraffe, I. 2000, ARA&A, 38, 337

Chabrier, G. & Küker, M. 2006, A&A, 446, 1027

Cho, K., Lee, J., Chae, J., et al. 2016, Solar Physics, 291

Chugainov, P. F. 1966, Information Bulletin on Variable Stars, 122, 1

Cifuentes, C., Caballero, J. A., Cortés-Contreras, M., et al. 2020, A&A, 642, A115

Colloquium, I. A. U., Aime, C., & Vakili, F. 2006, Direct Imaging of Exoplanets (IAU C200): Science and Techniques, IAU colloquium (Cambridge University Press)

Cortés-Contreras, M., Béjar, V. J. S., Caballero, J. A., et al. 2017a, A&A, 597, A47

Cortés-Contreras, M., Béjar, V. J. S., Caballero, J. A., et al. 2017b, A&A, 597, A47

Council, N. R. 2008, Severe Space Weather Events: Understanding Societal and Economic Impacts: A Workshop Report (Washington, DC: The National Academies Press)

Cox, A. N. 2000, Allen's astrophysical quantities

Cram, L. E. & Mullan, D. J. 1979, ApJ, 234, 579

Crespo-Chacón, I., Montes, D., García-Alvarez, D., et al. 2006, A&A, 452, 987

Dai, X. & Guerras, E. 2018, ApJ, 853, L27

Debus, M., Huke, P., Meyer, D., & Reiners, A. 2021, Journal of Astronomical Telescopes, Instruments, and Systems, 7, 025005

Dekker, H., D'Odorico, S., Kaufer, A., Delabre, B., & Kotzlowski, H. 2000, in Society of Photo-Optical Instrumentation Engineers (SPIE) Conference Series, Vol. 4008, Optical and IR Telescope Instrumentation and Detectors, ed. M. Iye & A. F. Moorwood, 534–545

Díaz, R. F., Cincunegui, C., & Mauas, P. J. D. 2007, MNRAS, 378, 1007

Donati, J.-F., Kouach, D., Lacombe, M., et al. 2018, in Handbook of Exoplanets, ed. H. J. Deeg & J. A. Belmonte, 107

Donati, J. F., Morin, J., Petit, P., et al. 2008, MNRAS, 390, 545

Doppler, C. 1842, Ueber das farbige Licht der Doppelsterne und einiger anderer Gestirne des Himmels: Versuch einer das Bradley'sche Aberrations-Theorem als integrirenden Theil in sich schliessenden allgemeineren Theorie, Abhandlungen einer Privatgesellschaft in Böhmen. NF.5,2 (In Commission bei Borrosch & André)

Dorn, R. J., Follert, R., Bristow, P., et al. 2016, in Society of Photo-Optical Instrumentation Engineers (SPIE) Conference Series, Vol. 9908, Ground-based and Airborne Instrumentation for Astronomy VI, ed. C. J. Evans, L. Simard, & H. Takami, 99080I

Drake, G. 2006, High Precision Calculations for Helium, ed. G. Drake (New York, NY: Springer New York), 199–219

Dunlap, R. A. 2021, Energy from Nuclear Fusion, 2053-2563 (IOP Publishing)

Eberhard, G. & Schwarzschild, K. 1913, ApJ, 38, 292

Efron, B. & Stein, C. 1981, The Annals of Statistics, 9, 586

Eggen, O. J. 1983, Monthly Notices of the Royal Astronomical Society, 204, 377

Endl, M., Kürster, M., Rouesnel, F., et al. 2003, in Astronomical Society of the Pacific Conference Series, Vol. 294, Scientific Frontiers in Research on Extrasolar Planets, ed. D. Deming & S. Seager, 75–78

Feigelson, E. D. & Babu, G. J. 2012, Modern Statistical Methods for Astronomy

Fisher, G. H., Canfield, R. C., & McClymont, A. N. 1985, ApJ, 289, 425

Foukal, P. V. 2004, Solar Astrophysics, 2nd, Revised Edition

Fraunhofer, J. 1817, Annalen der Physik, 56, 264

Fuhrmeister, B., Czesla, S., Perdelwitz, V., et al. 2023, A&A, 670, A71

Fuhrmeister, B., Czesla, S., Schmitt, J. H. M. M., et al. 2018, A&A, 615, A14

Fuhrmeister, B., Lalitha, S., Poppenhaeger, K., et al. 2011, A&A, 534, A133

Fuhrmeister, B., Liefke, C., Schmitt, J. H. M. M., & Reiners, A. 2008, A&A, 487, 293

Fulcher, G. S. 1915, ApJ, 41, 359

Gaia Collaboration, Brown, A. G. A., Vallenari, A., et al. 2018, A&A, 616, A1

Gaidos, E., Mann, A. W., Kraus, A. L., & Ireland, M. 2016, Monthly Notices of the Royal Astronomical Society, 457, 2877

Gaidos, E., Mann, A. W., Lépine, S., et al. 2014, MNRAS, 443, 2561

Giampapa, M. S., Linsky, J. L., Schneeberger, T. J., & Worden, S. P. 1978, ApJ, 226, 144

Gizis, J. E., Monet, D. G., Reid, I. N., et al. 2000, The Astronomical Journal, 120, 1085–1099

Golimowski, D. A., Leggett, S. K., Marley, M. S., et al. 2004, AJ, 127, 3516

Gomes da Silva, J., Santos, N. C., Bonfils, X., et al. 2011, A&A, 534, A30

Gopalswamy, N. 2015, in Astrophysics and Space Science Library, Vol. 415, Solar Prominences, ed. J.-C. Vial & O. Engvold, 381

Gould, A. 2000, ApJ, 542, 785

Gray, D. F. 2008, The Observation and Analysis of Stellar Photospheres

Griffin, R. & Griffin, R. 1973, MNRAS, 162, 255

Guarcello, M. G., Micela, G., Sciortino, S., et al. 2019, A&A, 622, A210

Günther, M. N., Zhan, Z., Seager, S., et al. 2020, AJ, 159, 60

Gustafsson, B., Edvardsson, B., Eriksson, K., et al. 2008, A&A, 486, 951

Haisch, B., Strong, K. T., & Rodono, M. 1991, ARA&A, 29, 275

Hale, G. E. 1908, ApJ, 28, 315

Hall. 2008, Living Reviews in Solar Physics, 5

Hatzes, A. P., Cochran, W. D., Endl, M., et al. 2003, ApJ, 599, 1383

Hawley, S. L., Gizis, J. E., & Reid, I. N. 1996, AJ, 112, 2799

Hawley, S. L. & Pettersen, B. R. 1991, ApJ, 378, 725

Haynes, W. 2016, CRC Handbook of Chemistry and Physics (CRC Press)

Henry, T. J., Jao, W.-C., Winters, J. G., et al. 2018, The Astronomical Journal, 155, 265

Herschel, W. 1800, Philosophical Transactions of the Royal Society of London Series I, 90, 284

Hertzsprung, E. 1909, Astronomische Nachrichten, 179, 373

Heyvaerts, J. 1990, in Basic Plasma Processes on the Sun, ed. E. R. Priest & V. Krishan, Vol. 142, 207

Hilton, E. J., West, A. A., Hawley, S. L., & Kowalski, A. F. 2010, AJ, 140, 1402

Hintz, D., Fuhrmeister, B., Czesla, S., et al. 2019, A&A, 623, A136

Hirayama, T. 1971, Sol. Phys., 19, 384

Hodgkin, S. T., Jameson, R. F., & Steele, I. A. 1995, MNRAS, 274, 869

Honda, S., Notsu, Y., Namekata, K., et al. 2018, PASJ, 70, 62

Houdebine. 2012, Monthly Notices of the Royal Astronomical Society, 421, 3189

Houdebine, E. R., Junghans, K., Heanue, M. C., & Andrews, A. D. 2009, A&A, 503, 929

Hubeny, I. & Mihalas, D. 2015, Theory of Stellar Atmospheres. An Introduction to Astrophysical Non-equilibrium Quantitative Spectroscopic Analysis

Huggins, W. & Miller, W. A. 1864, Philosophical Transactions of the Royal Society of London Series I, 154, 437

Husser, T. O., Wende-von Berg, S., Dreizler, S., et al. 2013, A&A, 553, A6

Hyde Wollaston, W. 1802, Philosophical Transactions of the Royal Society of London Series I, 92, 365

Jacquinot, P. 1954, J. Opt. Soc. Am., 44, 761

Jardine, M., Collier Cameron, A., Donati, J. F., & Hussain, G. A. J. 2020, MNRAS, 491, 4076

Jefferies, J. T. 1968, Spectral line formation

Jefferies, S. M., McIntosh, S. W., Armstrong, J. D., et al. 2006, ApJ, 648, L151

Jeffers, S. V., Barnes, J. R., & Collier Cameron, A. 2002, MNRAS, 331, 666

Jeffers, S. V., Schöfer, P., Lamert, A., et al. 2018, A&A, 614, A76

Jenkins, J. M., Twicken, J. D., McCauliff, S., et al. 2016, in Society of Photo-Optical Instrumentation Engineers (SPIE) Conference Series, Vol. 9913, Software and Cyberinfrastructure for Astronomy IV, ed. G. Chiozzi & J. C. Guzman, 99133E

Jess, D. B., Morton, R. J., Verth, G., et al. 2015, Space Sci. Rev., 190, 103

Jitrik, O. & Bunge, C. 2004, Journal of Physical and Chemical Reference Data - J PHYS CHEM REF DATA, 33

Johnson, E. N., Czesla, S., Fuhrmeister, B., et al. 2021, A&A, 651, A105

Johnson, H. L. & Morgan, W. W. 1953, ApJ, 117, 313

Johnstone, C. P., Khodachenko, M. L., Lüftinger, T., et al. 2019, A&A, 624, L10

Jouve, L., Lignières, F., & Gaurat, M. 2020, A&A, 641, A13

Joy, A. H. 1947, ApJ, 105, 96

Judge, P. G. & Carpenter, K. G. 1998, ApJ, 494, 828

Juncar, P., Pinard, J., Hamon, J., & Chartier, A. 1981, Metrologia, 17, 77

Kane, S. R., McTiernan, J. M., & Hurley, K. 2005, A&A, 433, 1133

Karttunen, H., Kröger, P., Oja, H., Poutanen, M., & Donner, K. 2014, Fundamental Astronomy (Springer Berlin Heidelberg)

Kasting, J. F., Whitmire, D. P., & Reynolds, R. T. 1993, Icarus, 101, 108

Kenyon, S. J. & Hartmann, L. 1995, ApJS, 101, 117

Kesseli, A. Y., Muirhead, P. S., Mann, A. W., & Mace, G. 2018, AJ, 155, 225

Khodachenko, M. L., Terrada, N., Lammer, H., et al. 2007, in European Planetary Science Congress 2007, 561

Kippenhahn, R. & Weigert, A. 1990, Stellar Structure and Evolution

Kipping, D. M. 2010, MNRAS, 408, 1758

Kiraga, M. & Stepien, K. 2007, Acta Astron., 57, 149

Kirchhoff, G. 1860, Annalen der Physik, 185, 275

Kirkpatrick, J. D., Henry, T. J., & McCarthy, Donald W., J. 1991, ApJS, 77, 417

Konacki, M., Torres, G., Jha, S., & Sasselov, D. D. 2003, Nature, 421, 507

Kopparapu, R. K., Ramirez, R., Kasting, J. F., et al. 2013, ApJ, 765, 131

Kowalski, A. F., Mathioudakis, M., & Hawley, S. L. 2018, in 20th Cambridge Workshop on Cool Stars, Stellar Systems and the Sun, Cambridge Workshop on Cool Stars, Stellar Systems, and the Sun, 42

Kramida, A. E. 2010, Atomic Data and Nuclear Data Tables, 96, 586

Kron, G. E. 1947, PASP, 59, 261

Kron, G. E. 1952, ApJ, 115, 301

Kuerster, M. & Schmitt, J. H. M. M. 1996, A&A, 311, 211

Kuerster, M., Schmitt, J. H. M. M., & Cutispoto, G. 1994, A&A, 289, 899

Kürster, M., Endl, M., Rouesnel, F., et al. 2003, A&A, 403, 1077

Lagrange, A. M., Gratadour, D., Chauvin, G., et al. 2009, A&A, 493, L21

Landman, D. A. 1981, ApJ, 244, 345

Laughlin, G., Bodenheimer, P., & Adams, F. C. 1997, The Astrophysical Journal, 482, 420

Leenaarts, J., Carlsson, M., Hansteen, V., & Gudiksen, B. V. 2011, A&A, 530, A124

Leibacher, J. & Stein, R. F. 1982, SAO Special Report, 1, A.23

Leitzinger, M., Odert, P., Greimel, R., et al. 2020, MNRAS, 493, 4570

Lépine, S., Hilton, E. J., Mann, A. W., et al. 2013, AJ, 145, 102

Lingam, M. & Loeb, A. 2017, ApJ, 848, 41

Linsky, J. L. 2017, Annual Review of Astronomy and Astrophysics, 55, 159

Linsky, J. L., Hunten, D. M., Sowell, R., Glackin, D. L., & Kelch, W. L. 1979, ApJS, 41, 481

Livingston, W., Wallace, L., White, O. R., & Giampapa, M. S. 2007, ApJ, 657, 1137

Livshits, M. A., Urnov, A. M., Goryaev, F. F., et al. 2011, Astronomy Reports, 55, 918

Magain, P. 1986, A&A, 163, 135

Mallik, S. V. 1997, A&AS, 124, 359

Marcy, G. W. & Butler, R. P. 1992, PASP, 104, 270

Mariska, J. T. 1986, ARA&A, 24, 23

Mariska, J. T. 1992, The Solar Transition Region

Martin, J., Fuhrmeister, B., Mittag, M., et al. 2017, arXiv e-prints, arXiv:1708.04895

Martin, W. C. 1973, Journal of Physical and Chemical Reference Data, 2, 257

Mayor, M., Pepe, F., Queloz, D., et al. 2003, The Messenger, 114, 20

Mayor, M. & Queloz, D. 1995, Nature, 378, 355

McLean, M., Berger, E., & Reiners, A. 2012, ApJ, 746, 23

McMillan, J. D. & Herbst, W. 1991, AJ, 101, 1788

Mihalas, D. 1978, Stellar atmospheres

Milkey, R. W., Heasley, J. N., & Beebe, H. A. 1973, ApJ, 186, 1043

Montes, D., Fernandez-Figueroa, M., Castro, E., & Sanz-Forcada, J. 1997, Astronomy and Astrophysics Supplement Series, 125, 263

Morgan, W. W., Keenan, P. C., & Kellman, E. 1943, An atlas of stellar spectra, with an outline of spectral classification

Morton, D. C. 1990, in 3rd International Collogium of the Royal Netherlands Academy of Arts and Sciences, 88

Munro, R. H., Gosling, J. T., Hildner, E., et al. 1979, Solar Physics, 61, 201

Narita, N., Fukui, A., Kusakabe, N., et al. 2019, Journal of Astronomical Telescopes, Instruments, and Systems, 5, 015001

Newton, E. R., Irwin, J., Charbonneau, D., et al. 2017, The Astrophysical Journal, 834, 85

Newton, E. R., Irwin, J., Charbonneau, D., et al. 2016, ApJ, 821, 93

Newton, I. & Innys, W. 1730, Opticks:: Or, A Treatise of the Reflections, Refractions, Inflections and Colours of Light, Opticks:: Or, A Treatise of the Reflections, Refractions, Inflections and Colours of Light (William Innys at the West-End of St. Paul's.)

Okamoto, T. J. & Sakurai, T. 2018, The Astrophysical Journal Letters, 852, L16

Oláh, K., K"ovári, Zs., Petrovay, K., et al. 2016, A&A, 590, A133

O'Malley-James, J. T. & Kaltenegger, L. 2017, MNRAS, 469, L26

Osten, R. A., Kowalski, A., Drake, S. A., et al. 2016, ApJ, 832, 174

Parker, E. N. 1955, ApJ, 122, 293

Parker, E. N. 1988, ApJ, 330, 474

Parnell, C. E. & Jupp, P. E. 2000, ApJ, 529, 554

Parviainen, H., Pallé, E., Zapatero Osorio, M. R., et al. 2020, A&A, 633, A28

Passegger, V. M., Bello-García, A., Ordieres-Meré, J., et al. 2022, A&A, 658, A194

Pecaut, M. J. & Mamajek, E. E. 2013, ApJS, 208, 9

Pepe, F., Cristiani, S., Rebolo, R., et al. 2021, A&A, 645, A96

Perryman, M. 2018, The Exoplanet Handbook

Petrovay, K. & van Driel-Gesztelyi, L. 1997, Sol. Phys., 176, 249

Planck, M. 1900, Ueber eine Verbesserung der Wien'schen Spectral-Gleichung (J.A. Barth)

Plez, B. 2012a, (PP2012)

Plez, B. 2012b, (PPN2012)

Podsiadlowski, P. 1993, in Astronomical Society of the Pacific Conference Series, Vol. 36, Planets Around Pulsars, ed. J. A. Phillips, S. E. Thorsett, & S. R. Kulkarni, 149–165

Pollacco, D. L., Skillen, I., Collier Cameron, A., et al. 2006, PASP, 118, 1407

Popinchalk, M., Faherty, J. K., Kiman, R., et al. 2021, The Astrophysical Journal, 916, 77

Quirrenbach, A., Amado, P. J., Caballero, J. A., et al. 2016, Society of Photo-Optical Instrumentation Engineers (SPIE) Conference Series, Vol. 9908, CARMENES: an overview six months after first light, 990812

Quirrenbach, A., Amado, P. J., Mandel, H., et al. 2010, Astronomical Society of the Pacific Conference Series, Vol. 430, CARMENES: Calar Alto High-Resolution Search for M Dwarfs with Exo-earths with a Near-infrared Echelle Spectrograph, ed. V. Coudé du Foresto, D. M. Gelino, & I. Ribas, 521

Quirrenbach, A., Amado, P. J., Seifert, W., et al. 2012, in Ground-based and Airborne Instrumentation for Astronomy IV, ed. I. S. McLean, S. K. Ramsay, & H. Takami, Vol. 8446, International Society for Optics and Photonics (SPIE), 84460R

Radick, R. R., Lockwood, G. W., Skiff, B. A., & Baliunas, S. L. 1998, ApJS, 118, 239

Rajpurohit, Allard, F., Rajpurohit, S., et al. 2018, A&A, 620, A180

Rauscher, E. & Marcy, G. W. 2006, PASP, 118, 617

Reader, J., Corliss, C. H., Wiese, W. L., & Martin, G. A. 1980, Wavelengths and transition probabilities for atoms and atomic ions: Part 1. Wavelengths, part 2. Transition probabilities

Reid, I. N. & Hawley, S. L. 2005a, New light on dark stars : red dwarfs, low-mass stars, brown dwarfs

Reid, I. N. & Hawley, S. L. 2005b, New light on dark stars : red dwarfs, low-mass stars, brown dwarfs

Reid, N., Hawley, S. L., & Mateo, M. 1995, MNRAS, 272, 828

Reiners, A. & Basri, G. 2008, ApJ, 684, 1390

Reiners, A. & Basri, G. 2010, ApJ, 710, 924

Reiners, A., Joshi, N., & Goldman, B. 2012, AJ, 143, 93

Reiners, A. & Mohanty, S. 2012, ApJ, 746, 43

Reiners, A., Zechmeister, M., Caballero, J. A., et al. 2018, A&A, 612, A49

Ribas, I., Reiners, A., Zechmeister, M., et al. 2023, A&A, 670, A139

Ricker, G. R., Winn, J., & Vanderspek, R. 2022, in Bulletin of the American Astronomical Society, Vol. 54, 406.02

Ricker, G. R., Winn, J. N., Vanderspek, R., et al. 2015, Journal of Astronomical Telescopes, Instruments, and Systems, 1, 014003

Robinson, C. R., Baliunas, S. L., Bennett, W., et al. 1989, in Bulletin of the American Astronomical Society, Vol. 21, 1115

Robinson, R. D., J. 1980, ApJ, 239, 961

Rockenfeller, B., Bailer-Jones, C., Mundt, R., & Ibrahimov, M. 2005, MNRAS, 367

Rodríguez, E., García, J. M., Costa, V., et al. 2010, MNRAS, 408, 2149

Rousseeuw, P. J. & Croux, C. 1993, Journal of the American Statistical Association, 88, 1273

Russell, H. N. 1914, Popular Astronomy, 22, 331

Rutten, R. J. 2003, Radiative Transfer in Stellar Atmospheres

Rutten, R. J. 2012, Philosophical Transactions of the Royal Society of London Series A, 370, 3129

Ryabchikova, T., Piskunov, N., Kurucz, R. L., et al. 2015, Phys. Scr, 90, 054005

Rydberg, J. 1890, Recherches sur la constitution des spectres d'émission des éléments chimiques, Kungliga vetenskapsakademiens handlingar No. 11 (Kungliga Vetenskapsakademien)

Saar, S. H. 1988, in The Impact of Very High S/N Spectroscopy on Stellar Physics, ed. G. Cayrel de Strobel & M. Spite, Vol. 132, 295

Saar, S. H., Huovelin, J., Osten, R. A., & Shcherbakov, A. G. 1997, A&A, 326, 741

Schmidt, S. J., Kowalski, A. F., Hawley, S. L., et al. 2011, The Astrophysical Journal, 745, 14

Schmidt, S. J., Shappee, B. J., van Saders, J. L., et al. 2019, ApJ, 876, 115

Schöfer, P., Jeffers, S. V., Reiners, A., et al. 2019, A&A, 623, A44

Schrijver, C. J. 1987, A&A, 172, 111

Schwabe, H. 1844, Astronomische Nachrichten, 21, 233

Schwarzschild, M. 1948, ApJ, 107, 1

Schweitzer, A., Passegger, V. M., Cifuentes, C., et al. 2019, A&A, 625, A68

Schwenke, D. W. 1998, Faraday Discussions, 109, 321

Seager, S. 2010, Exoplanets

Segura, A., Walkowicz, L. M., Meadows, V., Kasting, J., & Hawley, S. 2010, Astrobiology, 10, 751, pMID: 20879863

Shibayama, T., Maehara, H., Notsu, S., et al. 2013, The Astrophysical Journal Supplement Series, 209, 5

Shine, R. A. & Linsky, J. L. 1972, Sol. Phys., 25, 357

Shopov, Y., Stoykova, D., Stoitchkova, K., et al. 2008, Journal of Atmospheric and Solar-Terrestrial Physics, 70, 356, recent Observations and Simulations of the Sun-Earth System

Short, C. & Doyle, J. 1998, Astronomy and Astrophysics, 336, 613

Shulyak, D., Reiners, A., Engeln, A., et al. 2017, Nature Astronomy, 1, 0184

Shulyak, D., Reiners, A., Nagel, E., et al. 2019, A&A, 626, A86

Simon, T., Ayres, T. R., Redfield, S., & Linsky, J. L. 2002, The Astrophysical Journal, 579, 800

Slee, O. B. & Stewart, R. T. 1989, Monthly Notices of the Royal Astronomical Society, 236, 129

Sobel'Man, I. I., Vainshtein, L. A., & Yukov, E. A. 1995, Excitation of Atoms and Broadening of Spectral Lines

Socas-Navarro, H. & Asensio Ramos, A. 2021, A&A, 652, A78

Solanki, S. K. 2003, A&A Rev., 11, 153

Spruit, H. C. 1976, Sol. Phys., 50, 269

Spruit, H. C. 2011, in The Sun, the Solar Wind, and the Heliosphere, ed. M. P. Miralles & J. Sánchez Almeida, Vol. 4, 39

Stauffer, J. R. & Hartmann, L. W. 1986, ApJS, 61, 531

Strassmeier, K. G. 1993, in Astronomical Society of the Pacific Conference Series, Vol. 40, IAU Colloq. 137: Inside the Stars, ed. W. W. Weiss & A. Baglin, 605–619

Strassmeier, K. G., Rice, J. B., Wehlau, W. H., et al. 1991, A&A, 247, 130

Stuart, A., Ord, J. K., & Arnold, S. 1999, Kendall's advanced theory of statistics. Vol.2A: Classical inference and the linear model

Sugar, J., Corliss, C., & of Standards, U. S. N. B. 1985, Atomic Energy Levels of the Iron-period Elements, Potassium Through Nickel, Journal of physical and chemical reference data (American Chemical Society and the American Institute of Physics)

Tamuz, O., Mazeh, T., & Zucker, S. 2005, MNRAS, 356, 1466

Thomson, W. 1871, Nature, 4, 261

Tilley, M. A., Segura, A., Meadows, V., Hawley, S., & Davenport, J. 2019, Astrobiology, 19, 64, pMID: 30070900

Tsang, B. T. H., Pun, C. S. J., Stefano, R. D., Li, K. L., & Kong, A. K. H. 2012, ApJ, 754, 107

Vernazza, J. E., Avrett, E. H., & Loeser, R. 1981, ApJS, 45, 635

Vida, K., Leitzinger, M., Kriskovics, L., et al. 2019a, A&A, 623, A49

Vida, K., Oláh, K., Kővári, Z., et al. 2019b, ApJ, 884, 160

Villarreal D'Angelo, C., Jardine, M., & See, V. 2018, MNRAS, 475, L25

Voges, W., Aschenbach, B., Boller, T., et al. 1999, A&A, 349, 389

Vogt, S. S., Allen, S. L., Bigelow, B. C., et al. 1994, in Society of Photo-Optical Instrumentation Engineers (SPIE) Conference Series, Vol. 2198, Instrumentation in Astronomy VIII, ed. D. L. Crawford & E. R. Craine, 362

Volz, U., Majerus, M., Liebel, H., Schmitt, A., & Schmoranzer, H. 1996, Phys. Rev. Lett., 76, 2862

Walton, S. R., Preminger, D. G., & Chapman, G. A. 2003, ApJ, 590, 1088

Wedemeyer-Böhm, S., Steiner, O., Bruls, J., & Rammacher, W. 2007, in Astronomical Society of the Pacific Conference Series, Vol. 368, The Physics of Chromospheric Plasmas, ed. P. Heinzel, I. Dorotovič, & R. J. Rutten, 93

Weiss, N. O. 1990, Philosophical Transactions of the Royal Society of London Series A, 330, 617

West, A. A., Hawley, S. L., Bochanski, J. J., et al. 2008, AJ, 135, 785

West, A. A., Hawley, S. L., Walkowicz, L. M., et al. 2004, The Astronomical Journal, 128, 426

West, A. A., Weisenburger, K. L., Irwin, J., et al. 2015, ApJ, 812, 3

Wildt, R. 1939, ApJ, 90, 611

Williams, D., Marton, L., & Marton, C. 1962, Methods of Experimental Physics: Molecular physics ; edited by Dudley Williams No. v. 3 (Academic P)

Willson, R. C. & Hudson, H. S. 1991, Nature, 351, 42

Wilson, O. C. 1968, ApJ, 153, 221

Wilson, O. C. & Vainu Bappu, M. K. 1957, ApJ, 125, 661

Wolf, R. 1852, Astronomische Nachrichten, 35, 369

Wolszczan, A. & Frail, D. A. 1992, Nature, 355, 145

Wright, N. J., Newton, E. R., Williams, P. K. G., Drake, J. J., & Yadav, R. K. 2018, MNRAS, 479, 2351

Yelle, R., Lammer, H., & Ip, W.-H. 2008, Space Sci. Rev., 139, 437

Young, A., Skumanich, A., Stauffer, J. R., Bopp, B. W., & Harlan, E. 1989, ApJ, 344, 427

Young, C. A. 1872, American Journal of Science, 4, 356

Zacharias, N., Finch, C. T., Girard, T. M., et al. 2013, AJ, 145, 44

Zechmeister, M. 2010, PhD thesis, Ruprecht-Karls University of Heidelberg, Germany

Zechmeister, M., Anglada-Escudé, G., & Reiners, A. 2014, A&A, 561, A59

Zechmeister, M. & Kürster, M. 2009, A&A, 496, 577

Zeeman, P. 1896, Verslagen en Mededeelingen der Kon. Academie van Wetenschappen, Afd. Natuurkunde, 5, 181

Zickgraf, F. J., Krautter, J., Reffert, S., et al. 2006, VizieR Online Data Catalog, J/A+A/433/151

Zirin, H. 1957, ApJ, 126, 159

Zirin, H. 1975, ApJ, 199, L63

Acknowledgements

Due to many contributing variables my time as a Ph.D. student has not been particularly easy. I, therefore, would like to thank those that made the experience just a bit easier and more enjoyable.

A special thanks to Artie Hatzes, for all the guidance and mentorship. Additionally I would also like to thank him for having my back when it really mattered. I also extend my heartfelt thanks to Stefan Dreizler for stepping in when needed. I would also like to thank the rest of my defense committee.

I am also extremely grateful to Stefan Czesla for the feedback and discussions on both my paper and thesis. His input and friendship has been invaluable. A special thanks to Martin Kürster for advice regarding the methodology. I would also like to extend my heartfelt thanks to Urs Mall for his invaluable advice and guidance. Thanks also to Laurent Gizon for his comments and time. I would like to thank Mathias Zechmeister and Sebastian Schäfer for their very helpful advice and support.

A very special thanks to Yaiza Thiele for her constant level-headed support on all things. Also a thanks to Patrick Schöfer for the many discussions and debates over the years. I would like to extend a thanks to all those in CARMENES but particularly to Birgit, Lev, Mathias and Sebastian for their frequent feedback, encouragement and discussions.

I am supremely grateful to my mom for her unconditional understanding and love, no matter what the issue. The deepest appreciation, gratitude and love to my wonderful girlfriend, Gurmeet. Without you writing this thesis and life itself would have been impossible. You are my world. Lastly to my father, who was my hero and inspiration. I wish you could be here.